Reference dosimetry of static, nonstandard radiation therapy fields:

application to biology-guided radiotherapy and cranial radiosurgery generators

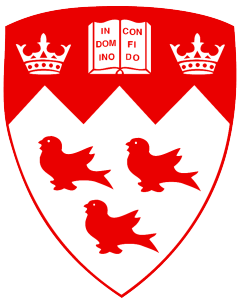

Lalageh Mirzakhanian

Department of Physics
McGill University, Montreal

A thesis submitted to McGill University in partial fulfillment of the requirements of the degree of
Doctor of Philosophy

 December 2019

To Dikran …

Acknowledgements

I am sincerely grateful to my supervisor Dr. Jan Seuntjens for sharing his expertise in dosimetry with me and always supporting me during the graduate studies. He gave me the opportunity to come to Canada, join the McGill medical physics program, grow both personally and professionally and become an independent researcher.

I also would like to thank my committee meeting members Dr. Frederic Tessier, Dr. Saiful Huq and Dr. Pavlos Papaconstadopoulos for their insightful comments and suggestions. I am also grateful to Dr. Stephen Davis who was kindly sharing his knowledge in dosimetry with me and giving me access to clinical equipment. I am very thankful to Dr. Arman Sarfehnia who spent his time doing measurements with me on multiple weekends. I would like to thank our other great collaborators that I had the chance to work with Dr. Hamza Benmakhlouf, Dr. Rostem Bassalow and Calvin Huntzinger. Thank you to Dr. Peter Watson for carefully reviewing this thesis and Véronique Fortier for translation of the thesis abstract into French. Thank you to Margery Knewstubb and Tatjana Nisic for always helping with the administrative issues. Thank you to Joe Larkin and Bhavan Siva for manufacturing and repairing my experimental equipment. Thank you to Michael Evans for giving advice on the radiation safety and enabling the use of clinical equipment. In addition, I am grateful to my colleagues Stella Xing, Véronique Fortier, Zaki Ahmed, James Renaud, Peter Truong, Peter Watson, Kyle O'Grady and many others for their friendship, many productive and enjoyable discussions we had in the last four years.

Thank you to my parents Vazgen and Emma, my sisters Erebooni, Biayna and Anasheh for their unconditional love, encouragement and support during my studies. Finally, I like to thank Dikran, my husband who supported me in every challenge I faced studying abroad.

Abstract

In radiotherapy, radiation field sizes smaller than 3×3 cm^2 have been widely used, however, dosimetry of small fields is very complex and requires calibration methodologies that are different than the calibration methodologies used for the radiotherapy machines with conventional field size. To provide recommendations on dosimetry of small fields, a working group was formed by the International Atomic Energy Agency (IAEA) in collaboration with the American Association of Physicists in Medicine (AAPM). In 2017, the working group published a new Code of Practice (COP) termed the IAEA-AAPM Technical Report Series (TRS) No 483 (TRS-483). The TRS-483 defines a formalism for the dosimetry of static small and nonstandard fields used in radiotherapy and introduces the correction factor $k_{Q_{msr},Q_0}^{f_{msr},f_{ref}}$ for calibration purposes.

One example of the use of small and nonstandard fields in radiotherapy is the Leksell Gamma Knife®(LGK). The LGK is a cranial radiosurgery generator containing 192 ^{60}Co sources arranged in a cone section configuration which delivers small radiation fields with the maximum field size of 16 mm diameter (Perfexion model). The $k_{Q_{msr},Q_0}^{f_{msr},f_{ref}}$ values for calibration of LGK are tabulated in TRS-483. However, these data are limited to a few chamber types, a single orientation of the chamber, and only two phantom materials. Moreover, the $k_{Q_{msr},Q_0}^{f_{msr},f_{ref}}$ values in TRS-483 have not been validated experimentally for the LGK.

The first aim of this thesis was to provide the data for reference dosimetry of LGK for different chamber types, phantoms and orientations of chambers. First the $k_{Q_{msr},Q_0}^{f_{msr},f_{ref}}$ values for 9 common ionization chamber types and 6 phantom materials used in the calibration of LGK Perfexion model were calculated using Monte Carlo (MC). A relationship was derived between the $k_{Q_{msr},Q_0}^{f_{msr},f_{ref}}$ values and the electron density of the phantom material. Therefore, $k_{Q_{msr},Q_0}^{f_{msr},f_{ref}}$ for any phantom material type of known electron density can be determined. Secondly, the calculated $k_{Q_{msr},Q_0}^{f_{msr},f_{ref}}$ factors for the calibration of the LGK unit were experimentally validated. The TRS-483 with the aforementioned correction factors was compared to two other calibration protocols of

the LGK. Applying the $k_{Q_{\text{msr}},Q_0}^{f_{\text{msr}},f_{\text{ref}}}$ values to the measured dose rates using the LGK unit resulted in dose rates that were consistent to within 0.4%.

A second radiation therapy unit that uses nonstandard fields is the recently developed RefleXion$^{\text{TM}}$ biology-guided radiotherapy (BgRT) machine which combines stereotactic radiotherapy with positron-emission tomography (PET) and computed tomography (CT) imaging systems. The closest possible field size to a reference field in this system is 10×2 cm^2 or possibly 10×3 cm^2 at the isocenter. The BgRT is a new machine and there is no available data on its reference dosimetry. The calibration of this machine is challenging and the TRS-483 cannot be directly applied.

The goal of this thesis in chapters 5 and 6 was therefore to provide a methodology for reference dosimetry of machines with fields as small as 10×2 cm^2 and to provide the data for calibration of BgRT. We extended the TRS-483 methodology to 10×2 cm^2 field size and provided 2 calibration methods. We recommended using the 1st approach, however, if the $k_{Q_{\text{A}},Q_0}^{f_{\text{A}},f_{\text{ref}}}$ values are not available, the second calibration method can be used to predict the $k_{Q_{\text{A}},Q_0}^{f_{\text{A}},f_{\text{ref}}}$ factors. However, the second methodology should not be used for chambers with electrode materials of high atomic number Z. Next, we provided the data for calibration of the BgRT using the 2 methodologies. The $k_{Q_{\text{A}},Q_0}^{f_{\text{A}},f_{\text{ref}}}$ values calculated using the two approaches were within $\pm 0.27\%$ for all chambers except the IBA CC01, which has an electrode made of high Z material. We provided the $k_{Q_{\text{A}},Q_0}^{f_{\text{A}},f_{\text{ref}}}$ values as a function of the beam quality specifier at the BgRT for 6 chamber types.

The first part of this thesis provided data for reference dosimetry of LGK. The second part provided 2 calibration approaches and data for the BgRT. Overall this work contributed to improved accuracy in reference dosimetry of nonstandard beams.

Résumé

En radiothérapie, un champ plus petit que 3×3 cm^2 est généralement considéré comme petit. Cependant, la dosimétrie de ces petits champs est très complexe et requiert des méthodes de calibration différentes de celles utilisées pour les champs conventionnels. Afin de fournir des recommandations sur la dosimétrie des petits champs, un groupe a été formé par l'agence internationale de l'énergie atomique (IAEA) en collaboration avec l'association américaine des physiciens en médecine (AAPM). En 2017, ce groupe a publié un nouveau code de pratiques (COP), le IAEA-AAPM Technical Report Series (TRS) No 483 (TRS-483), afin de proposer un formalisme de dosimétrie pour les petits champs statiques utilisés en radiothérapie. Le TRS-483 présente le facteur de correction $k_{Q_{\text{msr}},Q_0}^{f_{\text{msr}},f_{\text{ref}}}$ pour des fins de calibration.

Le Leksell Gamma Knife (LGK) est une machine de radiothérapie qui contient des sources 192 ^{60}Co installées en une configuration de cône, permettant de générer des petits champs de radiation, avec un diamètre maximal de 16 mm (modèle Perfexion). Les valeurs de $k_{Q_{\text{msr}},Q_0}^{f_{\text{msr}},f_{\text{ref}}}$ pour la calibration du LGK sont présentées dans le rapport TRS-483. Cependant, les valeurs reportées sont limitées à seulement quelques types de chambre à ionisation, de même qu'à une seule orientation de la chambre et 2 matériaux de fantôme. De plus, les valeurs de $k_{Q_{\text{msr}},Q_0}^{f_{\text{msr}},f_{\text{ref}}}$ dans le TRS-483 n'ont pas été validées expérimentalement.

Le premier objectif de cette thèse était de fournir et valider les données pour la dosimétrie de référence du LGK. Premièrement, les valeurs de $k_{Q_{\text{msr}},Q_0}^{f_{\text{msr}},f_{\text{ref}}}$ pour 9 types de chambre à ionisation et 6 matériaux de fantôme utilisés pour la calibration du LGK ont été calculées par la methode Monte Carlo (MC). Une relation a été dérivée entre les valeurs de $k_{Q_{\text{msr}},Q_0}^{f_{\text{msr}},f_{\text{ref}}}$ et la densité d'électron du matériau de fantôme. Cette relation permet de prédire la valeur de $k_{Q_{\text{msr}},Q_0}^{f_{\text{msr}},f_{\text{ref}}}$ pour différent types de matériau de fantôme à partir de la densité électronique. Deuxièmement, les valeurs de $k_{Q_{\text{msr}},Q_0}^{f_{\text{msr}},f_{\text{ref}}}$ calculées pour la calibration du LGK Perfexion ont été validées expérimentalement. Le TRS-483 avec les facteurs de correction calculés a été comparé à 2 autres protocoles. En

appliquant les valeurs de $k_{Q_{msr},Q_0}^{f_{msr},f_{ref}}$ aux débits de dose mesurés avec le LGK, une précision de 0.4% a été obtenue pour les débits de dose.

Une autre machine qui utilise des petits champs est le système de radiothérapie guidée par la biologie RefleXion (BgRT). Le BgRT combine la radiothérapie stéréotaxique avec un système d'imagerie de tomographie par émission de positrons (TEP) et de tomodensitométrie (TDM). Le champ le plus près d'un champ conventionnel de référence qui peut être obtenu avec le BgRT est un champ de 10×2 cm^2. Le BgRT est un nouveau système pour lequel il n'existe pour l'instant pas de données pour sa dosimétrie de référence. La calibration de ce système est complexe et le TRS-483 ne peut être appliqué directement.

Le second objectif de cette thèse, présenté aux chapitres 5 et 6, était de présenter une méthode de dosimétrie de référence pour les machines de radiothérapie avec des champs, aussi petit que 10×2 cm^2, ainsi que de fournir des données pour la calibration du BgRT. Nous avons développé davantage la méthode du TRS-483 pour l'appliquer à des champs de 10×2 cm^2 et présenté 2 méthodes de calibration. Nous avons aussi fourni des données de calibration pour le BgRT pour ces 2 méthodes proposées. Le facteur $k_{Q_A,Q_0}^{f_A,f_{ref}}$ calculé avec ces 2 méthodes étaient cohérents ($\pm$ 0.27%) pour toutes les chambres à ionisation, sauf pour la IBA CC01 qui possède une électrode fabriquée avec un matériau à nombre Z élevé. Nous avons présenté les valeurs de $k_{Q_A,Q_0}^{f_A,f_{ref}}$ en fonction du facteur de qualité du rayonnement pour le BgRT pour 6 types de chambres.

La première partie de cette thèse présente des données pour la dosimétrie de référence du LGK. La deuxième partie présente 2 méthodes de calibration de même que des données de calibration pour le BgRT. En somme, ce travail contribue à améliorer la précision de la dosimétrie de référence pour des faisceaux non standards.

Contents

List of Figures

List of Tables

List of Abbreviations

AAPM	American Association of Physicists in Medicine
ABS	acrylonitrile butadiene styrene
BgRT	biology-guided radiotherapy
BIPM	Bureau international des poids et mesures
CBCT	cone-beam computed tomography
CM	component module
COP	Code of Practice
CPD	cumulative probability distribution function
CPE	charged particle equilibrium
CT	computed tomography
CTV	clinical target volume
DBS	directional bremsstrahlung splitting
EBRT	external beam radiation therapy
FDG	fluorodeoxyglucose
FFF	flattening filter free
FOI	field of interest
FWHM	full width at half maximum

GTV	gross tumor volume
GUM	Guide to the Expression of Uncertainty in Measurement
IAEA	International Atomic Energy Agency
IEC	International Electronic Commission
IFMM	intra-fraction motion management
IMRT	intensity modulated radiotherapy
kerma	kinetic energy released per unit mass
kV	kilovoltage
LCPE	lateral charged particle equilibrium
LGK	Leksell Gamma Knife
linac	linear accelerator
MC	Monte Carlo
mfp	mean free path
MLC	multileaf collimator
MR	magnetic resonance
MRI	magnetic resonance imaging
msr	machine specific reference
MU	monitor unit
MV	megavoltage
NRC	National Research Council
OAR	organs at risk
PCPE	partial charged particle equilibrium

PDD	percentage depth dose
PDF	probability distribution function
PET	positron-emission tomography
PMMA	polymethylmetacrylate
PTV	planning target volume
QA	quality assurance
%RMS	percentage root-mean-square
RR	Russian roulette
RT	radiation therapy
SAD	source-to-axis distance
SBRT	stereotactic body radiation therapy
SDD	source-to-detector distance
SRS	stereotactic radiosurgery
SSD	source-to-surface distance
SW	solid water
TCPE	transient charged particle equilibrium
3D	three-dimensional
TG	Task Group
TPR	tissue phantom ratio
TRS	Technical Report Series
VRT	variance reduction technique
WFF	with flattening filter
XCSE	photon cross-section enhancement

Preface and Contribution of Authors

This thesis consists of four manuscripts, one published (chapter 4) and three submitted (chapters 5, 6 and 7). My and my co-authors contribution to each manuscripts is outlined below.

1. Determination of $k_{Q_{msr},Q_0}^{f_{msr},f_{ref}}$ factors for ion chambers used in the calibration of Leksell Gamma Knife Perfexion model using `EGSnrc` and `PENELOPE` Monte Carlo codes. Lalageh Mirzakhanian, Hamza Benmakhlouf, Frederic Tessier, Jan Seuntjens, Medical physics 45.4 (2018): 1748-1757

   I modeled some of the ionization chambers in `EGSnrc`, ran all the `EGSnrc` simulations, analyzed the data and wrote the manuscript. Hamza Benmakhlouf modeled the ionization chambers in `PENELOPE` and ran the `PENELOPE` simulations. Frederic Tessier provided some of the chambers models in `EGSnrc`. Jan Seuntjens defined the project and supervised the study. All co-authors reviewed the manuscript.

2. Experimental validation of recommended *msr*-correction factors for the calibration of Leksell Gamma Knife® Icon™ Unit following IAEA TRS-483. Lalageh Mirzakhanian, Arman Sarfehnia, Jan Seuntjens, submitted to Physics in Medicine and Biology, August 2019.

   I performed the measurements, analyzed the data, and wrote the manuscript. Arman Sarfehnia provided the measurement equipment and assisted with the measurements. Jan Seuntjens helped with the measurements and supervised the study. All co-authors reviewed the manuscript.

3. Extending the IAEA-AAPM TRS-483 methodology for radiation therapy machines with field sizes down to 10×2 cm^2, Lalageh Mirzakhanian, Rostem Bassalow, Calvin Huntzinger, Jan Seuntjens, submitted to Medical physics, July 2019

I modeled the chambers, ran the simulations, performed the measurements, analyzed the data, and wrote the manuscript. Rostem Bassalow and Calvin Huntzinger provided the Exradin A26 chamber and contributed to the original idea. Jan Seuntjens provided guidance and supervision. All co-authors reviewed the manuscript.

4. IAEA-AAPM TRS-483-based reference dosimetry of the new RefleXion^{TM} biology-guided radiotherapy (BgRT) machine, Lalageh Mirzakhanian, Rostem Bassalow, Daniel Zaks, Calvin Huntzinger, Jan Seuntjens, submitted to Medical physics, July 2019

   I modeled the chambers, ran the simulation, analyzed the data and wrote the manuscript. Rostem Bassalow performed the measurements, developed the beam model and reviewed the manuscript. Daniel Zaks assisted with the measurements and developing the beam model. Calvin Huntzinger contributed to the original idea and reviewed the manuscript. Jan Seuntjens provided guidance on the project and reviewed the manuscript.

Chapter 1

Introduction

1.1 Radiation therapy

Cancer is the rapid creation of abnormal cells that grow beyond their usual boundaries, and which can then invade adjoining parts of the body and spread to other organs (defined by World Health Organization). The latter process is referred to as metastasizing. Cancer is a major public health problem throughout the world. One in five men and one in six women worldwide get cancer during their lifetime, and one in eight men and one in eleven women die from it [1].

Radiation therapy (also referred to as radiotherapy) is one of the major and most effective cancer treatment modalities besides the other two common modalities chemotherapy, and surgery [2]. The use of each modality or any combination of them depends on different factors, for example the type and stage of cancer. The utilization rate of radiation therapy is also different in various countries, for example for new cancer cases it varies from 20 to 55% in Australia, the United States, Canada, and the Nordic countries [3].

In general, radiation can be non-ionizing or ionizing. Non-ionizing radiation does not have the required energy to ionize the medium, while ionizing radiation can since its energy is greater than the ionization potential of atoms or molecules of the medium [2].

Ionizing radiation can transfer its energy to the medium directly or indirectly. Charged particles such as electrons, protons, alpha particles and heavy ions transfer their energy to the medium using direct Coulomb interactions between the charged particle and orbital electrons of atoms and the nucleus in the medium. However, uncharged particles such as photons and neutrons deposit their energy in the medium first by creating charged particles in the medium

(photons release electrons or electron/positron pairs, and neutrons release protons or heavier ions). Afterwards the charged particle transfers energy to the medium using direct Coulomb interactions [4]. Radiotherapy is applied clinically with electrons, photons, neutrons and heavy charged particles.

Radiation therapy uses ionizing radiation to kill cancer cells and reduce the tumor size while attempting to protect the healthy tissue. The main target in radiation-induced cell killing is thought to be the DNA molecule although other targets in the cell have also been coined. When cells are exposed to ionizing radiation, the radiation can damage the cell directly or indirectly. In the direct damage, the radiation hits the DNA molecule directly altering the molecular structure resulting in cell damage or cell death. Indirect damage is damage caused by radiation hitting water molecules, the major constituents of the cell, and causing radiolysis leading to free radicals. Free radicals then react with DNA molecules and cause a structural molecular damage. This also results in the impairment of cellular function or death of the cell [5].

In conventional radiation therapy, radiation dose is given over a period of weeks instead of a single session which is called fractionation. Fractionation provides time to the healthy tissue to repair from the sublethal damage and allows cells to repopulate. It also increases the damage to the tumor since the hypoxic cells reoxigenate and become more sensitive to radiation. Furthermore, fractionation redistributes cells. Cells pass through a series of stages/phases for duplication and division known as the cell cycle. Radiosensitivity of the cells varies in different phases. Redistribution makes the cell population more sensitive to fractionated treatment by redistributing the surviving cells into more sensitive parts of the cell cycle as compared with a single dose, which increases the cell kill [2].

Radiation therapy is delivered in two ways: internal radiation therapy (also known as brachytherapy) and external beam radiation therapy (EBRT). In brachytherapy, the radiation source (sealed or unsealed) is placed near or inside the volume to be treated, while in EBRT the radiation source is located outside of the patient. The choice of radiation beam and dose prescription depends on many factors such as medical patient-related factors, physician-related factors, availability of equipment, physical properties of the radiation beam to be used in treatment and biological factors produced in tissue by the radiation beam [6].

1.2 Medical linear accelerators

Prior to use of medical linear accelerators (linac), the cobalt-60 teletherapy machine had been widely used for radiation therapy. Cobalt-60 teletherapy machine was developed in Canada in the early 1950s by medical physicist Harold E. Johns. In the late 1990s, the cobalt-60 machine has been gradually replaced by medical linacs. Since then, linacs have undergone different developments. Currently in developed countries, linacs are the most widely used radiation sources/devices used in EBRT. Medical linacs can deliver photons with nominal energies between ^{60}Co-50 megavoltage (MV) or electrons with nominal energies between 4-50 megaelectron-volt (MeV). The production process of a photon beam using a conventional medical linac is summarized below.

The schematic diagram of a Varian Clinac® accelerator and its collimation system are shown in figure 1.1. First, electrons are created using an electrostatic accelerator called an electron gun. The electron gun has a heated filament cathode and a grounded electrode creating an electric field. The heated cathode emits electrons thermionically. The electron beam is focused and accelerated towards the waveguide. Electrons are accelerated using a radiofrequency system and transported in vacuum in the accelerating waveguide. The electron beam path is modified using bending magnets and guided to the bremsstrahlung target. The electron beam hits the target and interacts with the target nuclei. The electrons are decelerated and they lose part of their kinetic energy which is converted to bremsstrahlung photons. The resulting photon beam is collimated using the primary collimator. Primary collimator defines the maximum field size available on the linac. The angular distribution of the photon beam created in the bremsstrahlung target peaks in a forward direction (forward peaked), therefore in some linear accelerators flattening filters are placed in the path of the beam to produce a uniform dose distribution at reference depth (10 cm) in water. This type of beam is called "with flattening filter" (WFF) beams. However, some recent linacs do not have a flattening filter or have a mode of operation where the flattening filter is removed referred as "flattening filter free" (FFF). Afterwards, the beam passes through the dose monitor chamber. The monitor chamber registers the output, flatness, symmetry and energy of the beam during irradiation. The photon beam is collimated using the upper and lower collimator made of high Z material (jaws). The jaws can be adjusted to create square or rectangular radiation fields. In conventional linacs, the maximum field dimension is usually 40×40 cm^2 at the isocenter. Isocenter is a point in space around which the linac head rotates. In conventional

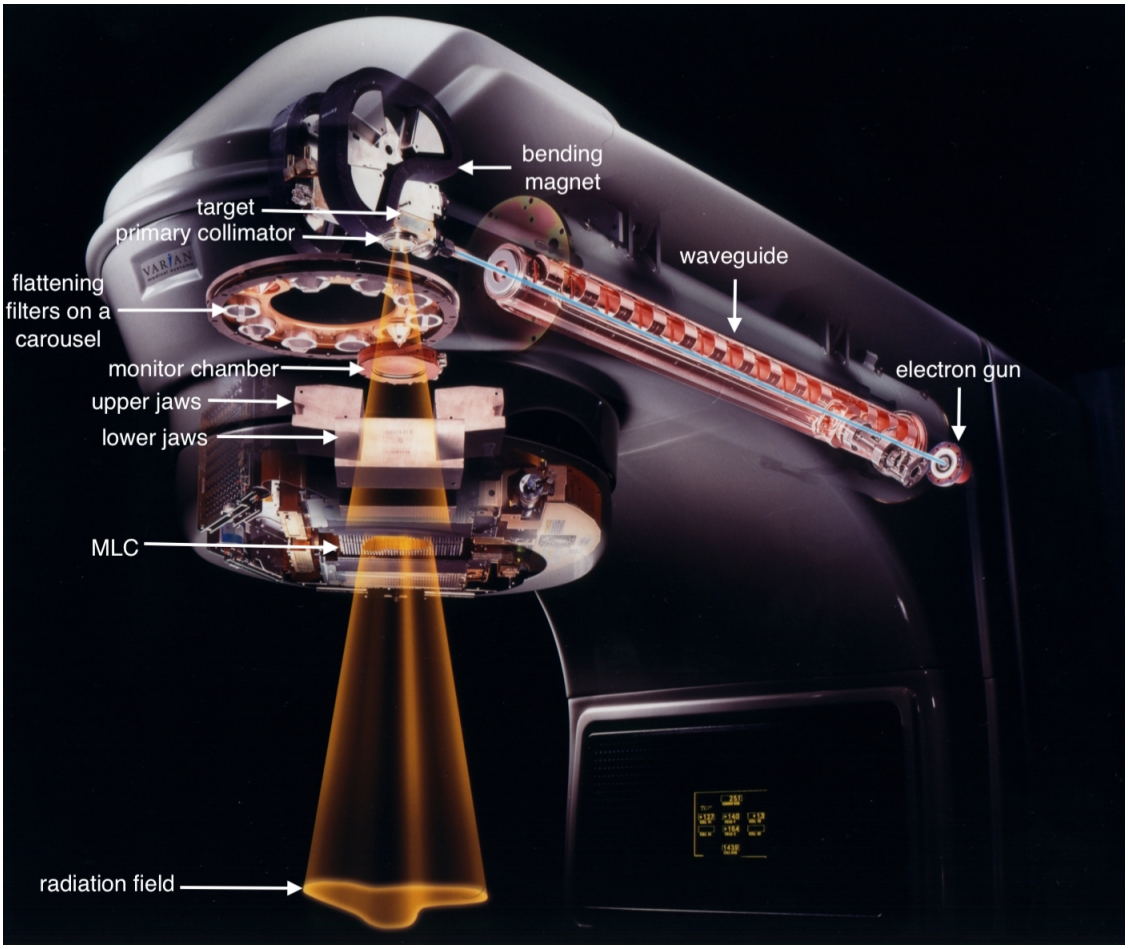

Figure 1.1 A schematic diagram of inside a Varian linear accelerator and its collimation system. Image courtesy of Varian Medical Systems, Inc. All rights reserved.

linacs, isocenter is 100 cm from the target. To produce irregular shaped radiation fields, the multileaf collimator (MLC) is put in the beam path. It consists of an array of narrow collimator leaf pairs (high Z material that blocks some parts of the radiation beam), each leaf controlled with its own miniature motor [7].

1.3 Introduction to reference and relative dosimetry

Prior to using any radiotherapy machine in the clinic to treat patients, the output of the machine must be calibrated. Output in this context represents absorbed dose to water under

clinical reference conditions. Absorbed dose is a fundamental physical quantity of interest for relating radiation treatment to its outcome. The absorbed dose is defined as the mean energy imparted by ionizing radiation to matter of mass per unit mass (the absorbed dose and the mean energy imparted are explained further in section 2.1.9). The determination of the output of a radiotherapy machine in the clinic using a detector (usually an air-filled ionization chamber) that is traceable to a primary standards laboratory is termed "reference dosimetry". The International Atomic Energy Agency (IAEA) and the Radiation Therapy Committee of the American Association of Physicists in Medicine (AAPM) are the two main associations that provide guidance on reference dosimetry of radiotherapy machines. Chapter 3 describes the concepts of primary standards, ionization chambers and different dosimetry protocols or Codes of Practice (COP) used in the calibration of high-energy photon beams in detail.

Relative dosimetry involves the measurements of beam profiles and field output factors in a water tank (or a solid phantom: a designed object made of tissue-equivalent material) using an appropriate detector. A field output factor is defined as the ratio of absorbed dose to water in any non-reference field to that in a reference field (10×10 cm^2) at a given depth. Relative dosimetry measurements are used as an input in treatment planning systems during a process that is called commissioning after installation of the radiotherapy machine.

The focus of this thesis is on reference dosimetry rather than relative dosimetry.

1.4 Workflow in radiation therapy

In EBRT the patient will go through several workflow steps as follows [8].

1.4.1 Simulation and contouring

Simulation is a step that is intended to “simulate” the radiation therapy delivery and to decide the treatment beams to be used and where to place them, relative to the tumor. Simulation is conventionally carried out on a kilovoltage (kV) device called a simulator, and nowadays takes place on a computed tomography (CT)-simulator or magnetic resonance (MR)-simulator. First, the patient is immobilized using immobilization devices such as masks, frames or molds. The treatment positions (the treatment plan field center, edge or other reference point) are determined by skin marks or sometimes by tattoo marks. The marks are used to reproduce the positioning of the patient during the treatment such that same area is irradiated

during different radiation therapy sessions. Afterwards, volumetric images of the areas to be treated are acquired using CT, magnetic resonance imaging (MRI) and/or positron-emission tomography (PET) to build the patient anatomical model. The three imaging techniques CT, PET and MRI are briefly described below.

CT is a three-dimensional (3D) imaging technique that provides the body's anatomical information. In CT, an X-ray generator rotates around the patient. The intensity of photons transmitted through the patient are measured by X-ray detectors positioned opposite the X-ray source. The intensity is converted to a corresponding electronic signal. From this data, the image is generated using mathematical processes called image reconstruction techniques. The contrast in CT images is due to the differences in attenuation of X-ray beam by different regions of the body. PET is an imaging technique which provides information on the metabolic function of organs or tissues. The basic principle in PET is that the patient is injected with a radioactive tracer isotope. The radionuclide used in the radioactive tracer is a positron emitter. The most commonly used PET radioactive tracer is fluorodeoxyglucose (FDG). Most cancer cells metabolize FDG at a much higher rate than normal tissues [2]. The uptake of FDG also varies greatly for different tumor types. High uptake is usually due to a high number of viable tumor cells and/or rapidly proliferating cells [9]. The radioisotope undergoes positron emission decay and emits a positron. The emitted positron interacts with an electron in the tissue and goes through annihilation. It emits two photons traveling approximately in opposite directions. The photons are detected by the detection instruments. By detecting these photons, PET identifies cancerous cells, even at an early stage, when other imaging modalities may miss them [2]. MRI is another imaging technique which provides 3D anatomical images using strong magnetic field and radio waves. When the patient is placed inside the MRI scanner, the MRI scanner applies a strong magnetic field around the area to be imaged. The protons' axes (human body is mostly made of water and water molecules contain hydrogen nuclei (protons)) all line up creating a magnetic vector oriented along the axis of the MRI scanner. When additional energy in the form of a radio wave is added to the magnetic field, the magnetic vector is deflected. When the radiofrequency source is switched off the magnetic vector returns to its resting state, and this causes a signal (also a radio wave) to be emitted. This signal is used to create the MR images [10].

For multiple imaging studies, the images are geometrically registered to each other to produce a self-consistent image of the patient. After image acquisition and registration, the target volume and its surrounding features are defined. First, the visible primary tumor volume

called the gross tumor volume (GTV) is contoured. The second contouring volume is the clinical target volume (CTV) which contains the GTV and a margin to take into account the sub-clinical microscopic malignant disease. The third volume is the planning target volume (PTV) for set-up uncertainties, machine tolerances and intratreatment variations. The definition of the GTV, CTV and PTV is a clinical assessment made by radiation oncologist. The critical normal tissue structures, organs at risk (OAR), are also contoured. The maximum permissible dose that can be received by the OARs is determined.

1.4.2 Treatment planning and delivery

Prior to the actual treatment delivery, the treatment must be planned and simulated, a process termed virtual simulation. In EBRT, medical physicists use computerized treatment planning systems to design the treatment plan by interactively changing the number, angles and energies of external high-energy photon beams, electrons or other particles to achieve the desired dose distribution in patient. As part of the quality assurance (QA), the dose distribution or points in the dose distribution is evaluated before the treatment delivery.

Once the treatment plan is approved, the data is transferred from the treatment planning to the treatment machine. Sometimes, patient-specific QA is performed by delivering the treatment plan to a test phantom and measuring the dose using dose measurement devices. The measured data is compared to the treatment plan. The acceptability criteria or the tolerance limits are different depending on the treatment technique, treatment machines, planning system and measurement devices. Once it is approved, the treatment plan is delivered to the patient.

1.5 Introduction to small field dosimetry

For an external photon beam to be considered small, at least one of the following three physical conditions should be met. The first two conditions are beam-related, while the third condition is detector-related [11].

1. **There is a loss of lateral charged particle equilibrium (LCPE) on the beam axis**

   Charged particle equilibrium (CPE) occurs when the charged particles of a given energy from regions outside the beam central axis are scattered toward the central region and compensate for charged particles of the same energy leaving the central region. Lack

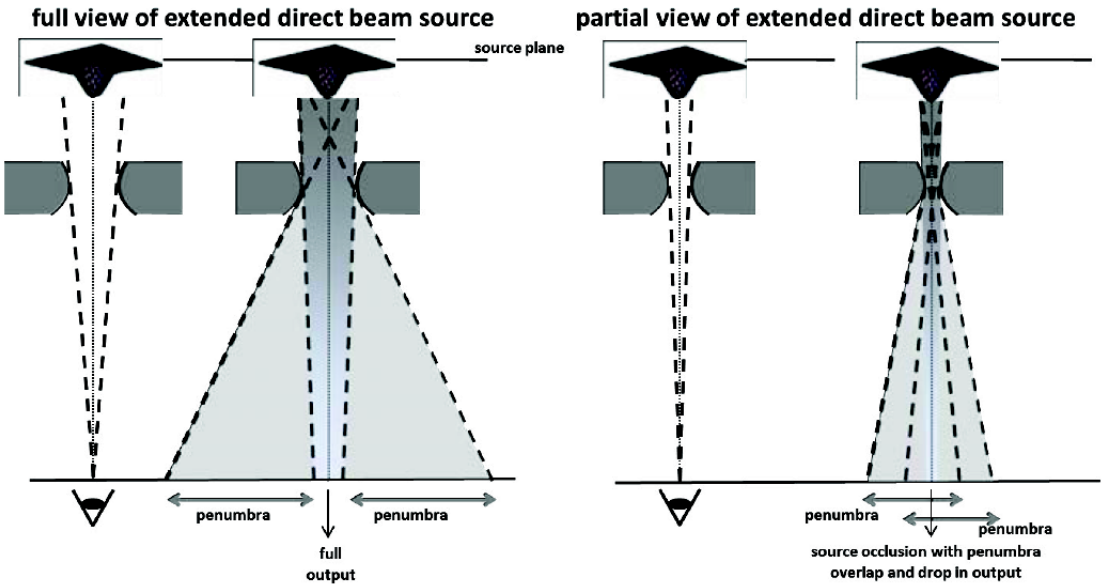

Figure 1.2 A schematic diagram of the source occlusion effect. Adapted from Palmans et al. [11]

of CPE can be mainly in the lateral direction, perpendicular to the beam axis. Loss of CPE happens in photon beams when the beam half width or radius is smaller than the maximum range of secondary electrons that contribute to the absorbed dose [4]. The parameter lateral charged particle equilibrium range (r_{LCPE}) is used to determine if the field size is small. The concepts of CPE and r_{LCPE} are explained further in sections 2.1.11 and 2.1.13 respectively.

2. **There is partial occlusion of the primary photon source by the collimating devices on the beam axis**

   Below a certain field size, only a part of the source area can be seen from a detector's point of view [12]. The partial source occlusion can result in overlap of the penumbra, reduction of the machine output and field widening, which causes a mismatch between the full width at half maximum (FWHM) and the collimator setting [13]. A schematic illustration of the source occlusion effect is shown in figure 1.2

3. **The size of the detector is similar or large compared to the beam dimensions**

   The signal of the detector is averaged over its volume, which is proportional to the energy deposited in the sensitive volume of the detector. If the field size is smaller than

the chamber dimensions or if the fluence over the detector is not uniform (FFF beams) the detector signal averaged over its volume will not be correct [13].

Further developments in radiation therapy techniques such as stereotactic radiosurgery (SRS), intensity modulated radiotherapy (IMRT), and stereotactic body radiation therapy (SBRT) have led to a rapid increase of the use of small fields.

SRS is a radiation therapy technique that uses externally generated ionizing radiation to inactivate or destroy defined targets in the head or spine without the need to do a surgical cut. The radiotherapy machines that use the SRS technology are linacs, particle beam accelerators and Gamma Knife [14]. Gamma Knife is described in more details in section 1.6.1. IMRT is another radiation therapy technique that deliberately delivers a non-uniform intensity to the target using multiple intensity-modulated beams [15]. SBRT is a radiation therapy technique that delivers larger doses in fewer fractions compared to conventional radiation therapy. It is very effective in controlling early stage primary and oligometastatic cancers at locations throughout the abdominopelvic and thoracic cavities, and at spinal and paraspinal sites [16].

The use of large and inappropriate chambers in small fields can result in overdose of patients. For example, an unfortunate accident occurred in 2006-2007 in France where 145 patients were overdosed due to use of an inappropriate detector during the commissioning of the installation of a MLC-based linac [17].

1.6 Applications of small fields

1.6.1 Leksell Gamma Knife

One example of the use of small fields and the SRS technology is the Leksell Gamma Knife® (LGK) machine (Elekta Instruments AB, Stockholm, Sweden). LGK is a cranial radiosurgery generator. It had applications for almost all intracranial tumors, either as a primary strategy or adjunctive therapy since mid-20th century [18]. LGK radiosurgery has also had a significant impact on treatment of brain metastases [18].

LGK was developed in 1968 by Lars Leksell from Karolinska Institute, Stockholm, Sweden and Borge Larsson from Uppsala University, Sweden. The first LGK unit was installed at the Sophiahemmet Hospital in 1968 [19]. Since then, this device has undergone several improvements with the advancement in technology. The latest version of this device, the LGK Perfexion™ was introduced in 2006 [20]. The beam delivery system consists of 192 ^{60}Co

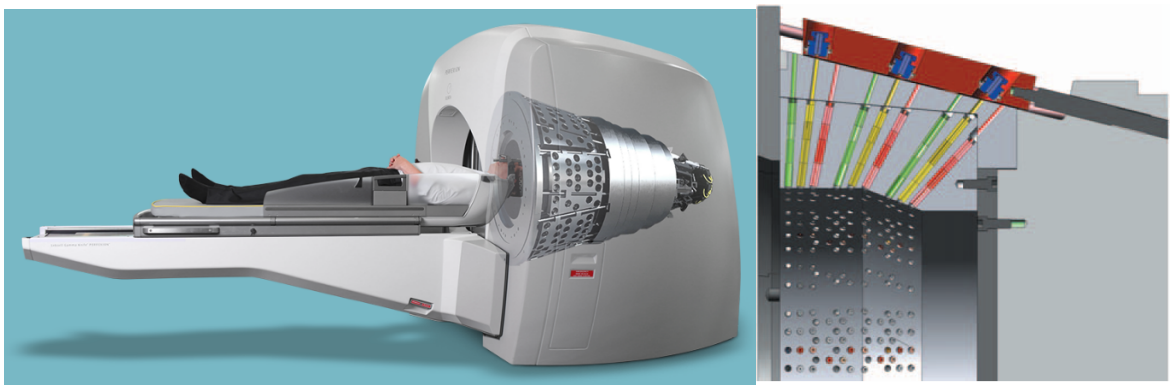

a b

Figure 1.3 (a) A schematic diagram of the LGK Perfexion unit and (b) its longitudinal section showing three sources (colored blue) in the 4 mm beam position. The source tray (colored red) can move along its longitudinal axis to dock with other beam collimator channels. The yellow, green, and red colored tubes correspond to 4, 8 and 16 mm collimators respectively [20]. Adapted from Elekta Instruments AB.

sources arranged in a cone configuration. The beams cross each other at the focal point. The source to focus distance varies from 374 to 433 mm. Radiosurgery is performed by moving the patient's head to the correct position around the focal point. The target inside the head of the patient is kept in position for suitable duration [21]. A schematic diagram of the LGK Perfexion unit is shown in figure 1.3a.

Treatment occurs inside a 12-cm thick tungsten mass through which 192 collimator channels have been drilled. The collimators are arranged in a series of five concentric rings [20]. The sources are mounted on 8 movable sectors, each containing 24 sources, for a total of 192 sources [21]. Beam diameters can be automatically changed to 4, 8 and 16 mm (defined at isocenter) by moving the sources over the selected collimator set [20] (see figure 1.3b). Therefore, the maximum field size achievable in this unit is 16 mm diameter.

In 2016, the LGK Perfexion model was upgraded to the LGK Icon^{TM} model. The Icon unit has the same radiation unit as the Perfexion model, however it differs from the Perfexion unit by an additional cone-beam computed tomography (CBCT) imaging system and a motion tracking system (intra-fraction motion management, IFMM) [22].

1.6.2 RefleXion biology-guided radiotherapy

Another application of the use of small fields is the recent RefleXion^{TM} biology-guided radiotherapy (BgRT) machine (Hayward, CA, USA). The RefleXion BgRT machine combines stereotactic radiotherapy with PET and fan-beam CT imaging systems (PET/CT) for better localization and tracking of the tumor during the treatment delivery. It delivers a high dose of radiation to the tumor while sparing the healthy tissue based on the patient's individual biology monitored during the treatment (intra-fraction) using PET emissions in real-time [23]. The PET image that guides BgRT delivery is different than a diagnostic PET image. Instead of waiting for the generation of a full diagnostic image, the PET system on the RefleXion machine continuously acquires images during the treatment delivery and continuously broadcasts the location of the tumor even while in motion [24].

The RefleXion BgRT was founded in 2009 by Samuel Mazin and Akshay Nanduri, co-founders of RefleXion Medical, a biotargeting oncology company based in Hayward, California. At the time of writing, the machine is in the process of gaining approval and has not yet been used for treating patients. Figure 1.4 shows a schematic diagram of the RefleXion BgRT machine.

Major components of the BgRT machine are the linear accelerator, the collimation system, the PET detector arcs, the fan-beam kV CT system and the MV X-ray detectors (see figure 1.5).

The energy of the linear accelerator is 6 MV and the beam is FFF. The collimation system consists of the primary collimator, the upper jaws, the MLC and the lower jaws. The MLC is sandwiched between the upper and lower jaws. The maximum field size achievable in this machine is 2 or 3 cm in the Y dimension and 40 cm in the X dimension (X and Y coordinates have the same origin as the International Electronic Commission (IEC)-61217 coordinates [25] shown in figure 1.5) at the source-to-axis distance (SAD) of 85 cm.

Two symmetric sets of PET detectors are mounted in an arc shape opposite to each other in the same rotating plane as the radiotherapy treatment beam. The two arcs detect the photons emitted by the annihilation of a positron-electron pair (the patient is previously injected with the PET tracer as discussed in section 1.4.1).

The MV detector system is used to perform QA on the beam generation and collimation systems to confirm the operation of beam energy, MLC and output consistency.

The fan beam kVCT system is used to image the patient in the target area to confirm that the tumor is in the correct position relative to the radiotherapy beam prior to the treatment.

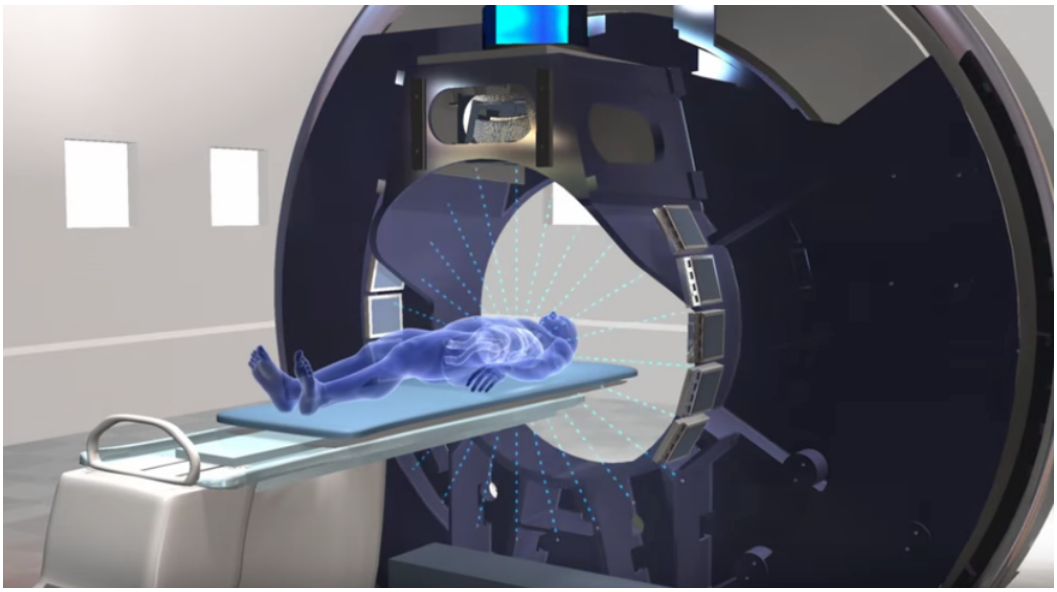

Figure 1.4 A schematic diagram of the RefleXion BgRT machine. Adapted from RefleXion Medical.

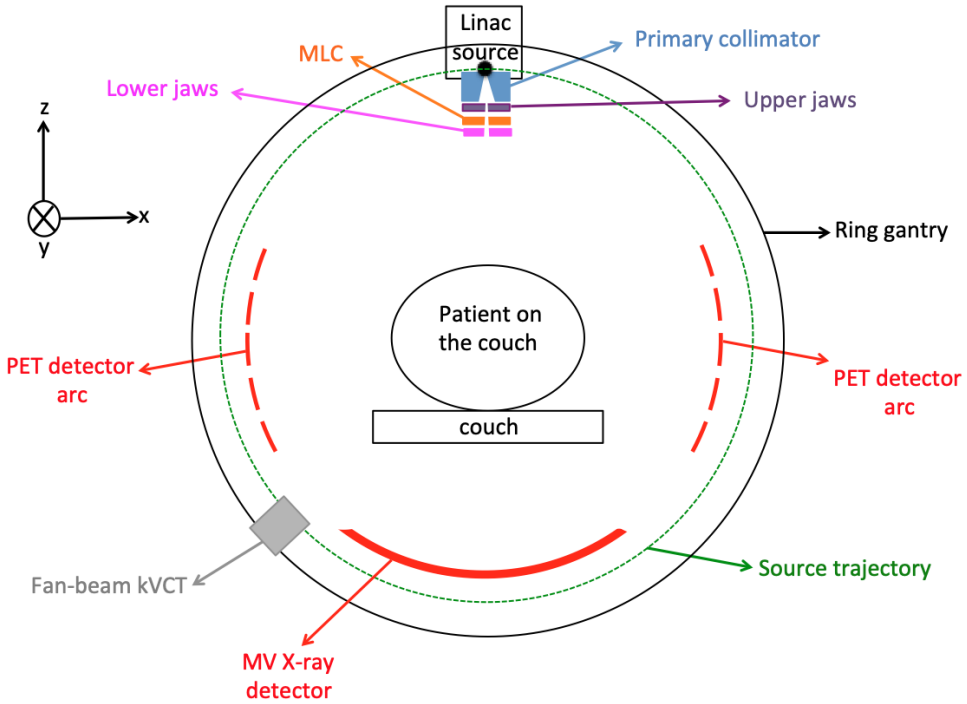

Figure 1.5 A schematic cross section view of the RefleXion BgRT machine. Recreated from figure 1 of Fan et al. [23]

The main components of the RefleXion BgRT are mounted on a ring gantry rotating continuously at 60 revolutions per minute.

The RefleXion BgRT machine uses functional imaging data from PET and anatomic data from CT to detect cancer cells and guide radiation treatment in real time. This enables the radiation therapy to treat multiple targets (cancers that have metastasized) in the same treatment session. Furthermore, the machine can be used for standard CT-guided treatment, IMRT or SBRT without using PET.

1.7 Thesis objectives and hypotheses

Despite the fact that LGK is a common and well-established radiotherapy machine, currently most clinics calibrate the machine using an older protocol (AAPM Task Group 21 report (TG-21) [26]). TG-21 is based on air-kerma standards requiring a complicated conversion process resulting in an increase in the possibility of errors in the clinic. Little data is available on reference dosimetry of LGK using the recent COP, IAEA-AAPM Technical Report Series No. 483 (TRS-483) [11, 27–29] (the air-kerma standards, TG-21 and TRS-483 are explained in chapter 3). The first two objectives in this thesis are as follows:

1. To provide data for reference dosimetry of LGK for different ionization chamber types, phantom materials and orientations of chambers with respect to LGK in the context of TRS-483 and to come up with a methodology to predict correction factors for these chambers for any phantom type of known electron density (chapter 4).

2. To validate the data provided in objective 1 experimentally, and to compare different protocols used in reference dosimetry of LGK (chapter 5).

RefleXion BgRT is a new machine and currently there is no available data on its reference dosimetry. The field size closest to the reference field (10×10 cm^2) produced by this machine is 10×2 cm^2 or 10×3 cm^2. The reference dosimetry of this machine is challenging since the 10×2 cm^2 does not meet the so-called machine specific reference field (*msr*) requirement of TRS-483 for calibration (the concept of *msr* is explained in chapter 3). The second two objectives in this thesis are as follows:

3. To provide a general methodology for reference dosimetry of machines with field sizes down to 10×2 cm^2 (chapter 6).

4. To provide data for reference dosimetry of RefleXion BgRT (chapter 7).

The two main hypotheses in this thesis are as follows:

1. The correction factors ($k_{Q_{msr},Q_0}^{f_{msr},f_{ref}}$) for different ionization chambers in calibration of LGK can be predicted for any phantom material only knowing the electron density of a phantom material.

   This hypothesis is supported by the fact that the photon energy fluence ratios water-to-phantom material (plastic) changes almost linearly with electron density. This is described further in chapter 4.

2. For the 10×2 cm^2 field size of RefleXion BgRT, depending on the detector used, appropriate correction factors determined for reference detectors can still be applied for the purpose of reference dosimetry.

   This hypothesis is supported by the well-established practice, recommended in TRS-483 for the LGK unit. In that case, depending on the detector used, the collimator field sizes of 16 mm (Perfexion) may not meet the CPE conditions. Further support for this hypothesis stems from the fact that the literature and TRS-483 has published highly accurate field output correction factors for small fields for a wide variety of ionization chambers (and other detectors), supporting the idea that for fields comparable or slightly below LCPE conditions accurate dose determination is possible.

Bibliography

[1] World Health Organization. Latest global cancer data: Cancer burden rises to 18.1 million new cases and 9.6 million cancer deaths in 2018. *International Agency for Research on Cancer,* 2018.

[2] Podgorsak EB. Radiation oncology physics: A handbook for teachers and students. *Vienna: International Atomic Energy Agency,* 2005.

[3] Delaney G, Jacob S, Featherstone C, Barton M. The role of radiotherapy in cancer treatment: estimating optimal utilization from a review of evidence-based clinical guidelines. *Cancer: Interdisciplinary International Journal of the American Cancer Society*, 104(6), 1129-1137, 2005.

[4] Andreo P, Burns DT, Nahum AE, Seuntjens J, Attix FH. Fundamentals of Ionizing Radiation Dosimetry. *Wiley*, 2017.

[5] Desouky O, Ding N, Zhou G. Targeted and non-targeted effects of ionizing radiation. *Journal of Radiation Research and Applied Sciences*, 8(2), 247-254, 2015.

[6] Podgorsak EB. Radiation Physics for Medical Physicists. *Springer Science Business Media*, 2010.

[7] Podgorsak EB. Compendium to Radiation Physics for Medical Physicists. *Springer*, 2014.

[8] McShan DL. Workflow and Clinical Decision Support for Radiation Oncology. Efficient Decision Support Systems-Practice and Challenges in Biomedical Related Domain. *IntechOpen*, 2011.

[9] Baert AL. Diagnostic nuclear medicine. *Springer Science & Business Media*, 2006.

[10] Berger A. How does it work?: Magnetic resonance imaging. *BMJ: British Medical Journal*, 324(7328):35, 2002.

[11] Palmans H, Andreo P, Christaki K, Huq MS, Seuntjens J. TRS-483: Dosimetry of small static fields used in external beam radiotherapy: an international code of practice for reference and relative dose determination. *International Atomic Energy Agency, Vienna*, 2017.

[12] Das IJ, Ding GX, Ahnesjö A. Small fields: nonequilibrium radiation dosimetry. *Medical physics*, 35(1), 206–215, 2008.

[13] Andreo P. The physics of small megavoltage photon beam dosimetry. *Radiotherapy and Oncology*, 126(2), 205–213, 2018.

[14] Barnett GH, Linskey ME, Adler JR, Cozzens JW, Friedman WA, Heilbrun MP, Lunsford LD, Schulder M, Sloan AE. Stereotactic radiosurgery—an organized neurosurgery-sanctioned definition. *Journal of neurosurgery*, 106(1), 1-5, 2007.

[15] Bortfeld T. IMRT: a review and preview. *Physics in Medicine & Biology*, 51(13), R363, 2006.

[16] Benedict SH, Yenice KM, Followill D, Galvin JM, Hinson W, Kavanagh B, Keall P, Lovelock M, Meeks S, Papiez L, Purdie T. Stereotactic body radiation therapy: the report of AAPM Task Group 101. *Medical physics*, 37(8), 4078–4101, 2010.

[17] Derreumaux S, Boisserie G, Brunet G, Buchheit I, Sarrazin T. Concerns in France about the dose delivered to the patients in stereotactic radiation therapy. No. IAEA-CN–182, 2010.

[18] Monaco EA, Grandhi R, Niranjan A, Lunsford LD. The past, present and future of Gamma Knife radiosurgery for brain tumors: the Pittsburgh experience. *Expert review of neurotherapeutics*, 12(4), 437–445, 2012.

[19] Leksell L. Stereotactic radiosurgery. *Journal of Neurology, Neurosurgery & Psychiatry*, 46(9), 797–803, 1983.

[20] Lindquist C, Paddick I. The Leksell Gamma Knife Perfexion and comparisons with its predecessors. *Neurosurgery*, 61(suppl_3), ONS–130, 2007.

[21] Ganz J. Gamma Knife neurosurgery. *Springer Science & Business Media*, 2010.

[22] Zeverino M, Jaccard M, Patin D, Ryckx N, Marguet M, Tuleasca C, Schiappacasse L, Bourhis J, Levivier M, Bochud FO, Moeckli R. Commissioning of the Leksell Gamma Knife® Icon™. *Medical physics*, 44(2), 355–363, 2017.

[23] Fan Q, Nanduri A, Mazin S, Zhu L. Emission guided radiation therapy for lung and prostate cancers: A feasibility study on a digital patient. *Medical physics*, 39(11), 7140–7152, 2012.

[24] Silva A, Mazin S. Treatment planning and delivery overview of biology-guided radiotherapy. *American Society for Radiation Oncology (ASTRO)*, 2019.

[25] IE Commission. Radiotherapy equipment—coordinates, movements and scales. *IEC1217*, 1996.

[26] AAPM Task Group 21, Radiation Therapy Committee. A protocol for the determination of absorbed dose from high-energy photon and electron beams. *Medical Physics*, 10(6): 741–771, 1983.

[27] Johansson J, Gorka B, Novotny Jr, Bourland JD, Bhatnagar J, Bednarz G, Best RCM, Persson L, Nordström H, Svärm O. *Plenary Oral Presentation at the 16th International Meeting of the Leksell Gamma Knife® Society;* 69, 2012.

[28] Zoros E, Moutsatsos A, Pappas EP, Georgiou E, Kollias G, Karaiskos P, Pantelis E. Monte Carlo and experimental determination of correction factors for gamma knife perfexion small field dosimetry measurements. *Physics in Medicine & Biology,* 62(18), 7532, 2017.

[29] Andreo P, Benmakhlouf H. Improved reference and relative dosimetry of small radiation therapy photon beams. Strålsäkerhetsmyndigheten, 2014.

Chapter 2

Dosimetric principles and quantities

This chapter summarizes some fundamental dosimetric concepts and Monte Carlo (MC) methods that will appear in this thesis.

2.1 Fundamental concepts in dosimetry

2.1.1 Radiant energy

The radiant energy (R) is the energy of N number of particles with energy E. The unit of R is joule (J). For particle of energy E, R is defined below [1].

$$R = NE \tag{2.1}$$

2.1.2 Fluence and energy fluence

The fluence Φ is the quotient of dN by da where dN is the number of particles incident on a sphere of cross-sectional area da [1]. The unit of fluence is m^{-2}.

$$\Phi = \frac{\mathrm{d}N}{\mathrm{d}a} \tag{2.2}$$

The energy fluence Ψ takes into account the energy of the particles scored. It is defined as the quotient of dR by da where dR is the radiant energy incident on the sphere of cross-sectional

area da [1]. The unit of energy fluence is J m^{-2}.

$$\Psi = \frac{\mathrm{d}R}{\mathrm{d}a} \tag{2.3}$$

If the particles are monoenergetic, then Ψ is:

$$\Psi = \Phi E \tag{2.4}$$

2.1.3 Photon interactions

When photons traverse the medium there are four main interaction mechanisms that can occur: photoelectric absorption, Compton effect, pair production and Rayleigh scattering.

Photoelectric absorption happens when a photon interacts with an inner shell electron, the photon gets absorbed completely and the orbital electron (called photoelectron) is ejected.

The Compton effect occurs between a photon and a loosely bound ("free") electron. In Compton effect, the photon interacts with a free electron, producing a scattered photon and ejecting the electron from the atom.

Pair production can only occur if the incident photon has energy greater than 1.02 MeV. In this process, the photon interacts with a charged particle and converts into an electron-positron pair. Pair production can only happen in the Coulomb field of an atomic nucleus or orbital electron (triplet production). When pair production happens in the field of an orbital electron, three particles (an electron-positron pair and the orbital electron) are created, this effect is called triplet production.

Rayleigh scattering occurs when a photon interacts with the bound atomic electrons of an absorber atom. The photon is then elastically scattered (i.e. has the same incoming and outgoing energy) [2].

Among the photon interaction mechanisms discussed, photoelectric effect, Compton scattering and triplet production can produce a vacancy in one of the inner shells or the outer shell of the atom. An atom with a vacancy in its inner shell is in an excited state and returns to its ground state through electronic transitions by emitting characteristic radiation (fluorescence) or by transferring the energy to a higher shell electron and ejecting the electron from the atom. These ejected electrons are termed Auger electrons [2].

The interaction probability of the photoelectric effect, Compton effect, and pair production depends both on the photon energy and the atomic number of the absorbing medium [1].

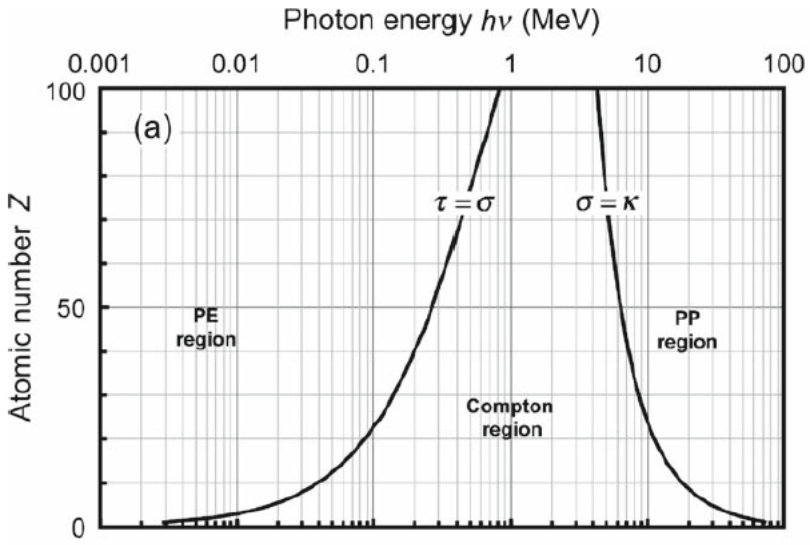

Figure 2.1 Relative importance of the photoelectric effect (PE), Compton effect and pair production (PP). Adapted from Podgorsak [2].

Figure 2.1 represents the relative predominance of each three main processes as a function of atomic number and photon energy. The photoelectric effect is dominant at low photon energies, Compton effect occurs at intermediate energies and pair production effect is dominant at high photon energies (greater than 1.02 MeV).

2.1.4 Charged particles interactions

When an energetic charged particle (e.g an electron) traverses the medium, it can interact with matter through Coulomb interaction with orbital electrons and atomic nuclei. Three types of interaction can occur depending on the size of the impact parameter (b) of the interaction (the perpendicular distance between the initial velocity of the charged particle before the interaction and the atomic nucleus) relative to the size of the atomic radius of the medium (a) [2]. The three types of interaction are shown in figure 2.2.

1. If $b \approx a$, the charged particle interacts with a single atomic electron using Coulomb interaction. The electron is ejected with significant kinetic energy. The ejected electron is called a "secondary electron" or a "delta ray" and the interaction is referred as "hard collision".

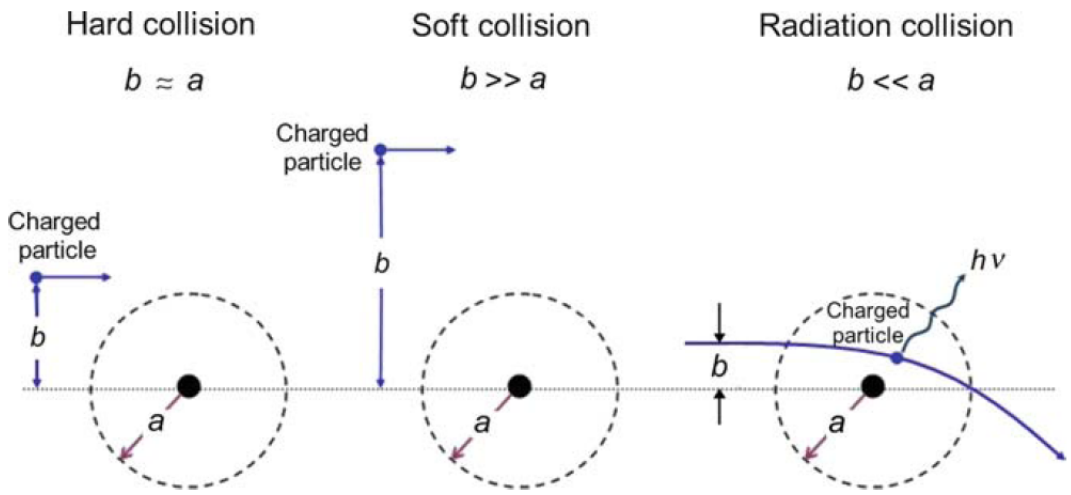

Figure 2.2 Three types of interaction of a charged particle with an atom. Adapted from Podgorsak [2].

2. If $b \gg a$, the charged particle Coulomb force interacts with the atom as a whole resulting in excitation or ionization through ejection of an electron from valence shell. This interaction is referred as "soft collision".

3. If $b \ll a$, the charged particle interacts mainly with the nucleus and undergoes either elastic or inelastic scattering. The interaction probability of elastic interaction is higher than inelastic interaction. In the elastic interaction, the charged particle is scattered by the nucleus and loses a negligible amount of its energy. However, in the inelastic interaction, the charged particle (an electron or a positron) interacts with the nucleus and loses a significant amount of its energy by emitting photons called "bremsstrahlung photons".

   In addition to bremsstrahlung effect, annihilation can occur when a positron encounters an orbital electron. The positron loses its kinetic energy and undergoes annihilation with the orbital electron resulting in two photons each with energy of 0.511 MeV. Another interaction which is less frequent is in-flight annihilation. In this process, the positron interacts with a tightly bound electron or a free electron. The positron gives its kinetic energy to one or both of the annihilation photons (their individual energies will exceed 0.511 MeV) [1].

2.1.5 Interaction coefficient for photon beams

Linear attenuation coefficient

The attenuation coefficient represents the ability of a material to attenuate the intensity of a photon beam. The linear attenuation coefficient μ of a material is the quotient of $\frac{\mathrm{d}N}{N}$ by $\mathrm{d}l$. That is, $\frac{\mathrm{d}N}{N}$ is the mean fraction of particles that go through interactions when traveling a distance $\mathrm{d}l$ in the medium [1]. The unit of μ is m^{-1}.

$$\mu = \frac{1}{\mathrm{d}l}\frac{\mathrm{d}N}{N} \tag{2.5}$$

The attenuation coefficient μ is related to the photon mean free path (mfp) $\bar{x}$. The photon mfp is the average distance a photon travels in the medium before undergoing an interaction [2]. It is related to the μ as follows:

$$\bar{x} = \frac{1}{\mu} \tag{2.6}$$

Mass attenuation coefficient

The linear attenuation coefficient μ depends on the density of the medium. To remove the density dependency, the mass attenuation coefficient ($\frac{\mu}{\rho}$) is defined as follows:

$$\frac{\mu}{\rho} = \frac{1}{\rho\mathrm{d}l}\frac{\mathrm{d}N}{N} \tag{2.7}$$

where ρ is the density of the medium. The unit of $\frac{\mu}{\rho}$ is $\mathrm{m}^2\mathrm{kg}^{-1}$.

The mass attenuation coefficient provides information on how particles interact. For photons with energies above 1 keV, the dominant interactions of photons with atoms are the photoelectric absorption, Compton (incoherent) scattering, pair production and Rayleigh (coherent) scattering. The mass attenuation coefficient can be related to the interaction cross section of the individual processes of photoelectric absorption ($\frac{\tau}{\rho}$), Compton scattering ($\frac{\sigma_{incoh}}{\rho}$), pair production ($\frac{k}{\rho}$) and Rayleigh scattering ($\frac{\sigma_{coh}}{\rho}$) as follows:

$$\frac{\mu}{\rho} = \frac{\tau}{\rho} + \frac{\sigma_{incoh}}{\rho} + \frac{k}{\rho} + \frac{\sigma_{coh}}{\rho} \tag{2.8}$$

Mass energy transfer coefficient

The mass energy transfer coefficient provides information on how much energy is transferred by photons to charged particles by photoelectric effect, Compton effect, and pair production. The mass energy transfer coefficient $\frac{\mu_{tr}}{\rho}$ for a material of density ρ is defined as follows:

$$\frac{\mu_{tr}}{\rho} = \frac{1}{\rho \mathrm{d}l} \frac{\mathrm{d}R_{tr}}{R} \tag{2.9}$$

where $\mathrm{d}R_{tr}$ is the mean energy transferred to kinetic energy of charged particles due to the interaction of the uncharged particles of incident radiant energy R in traversing the distance $\mathrm{d}l$ in the medium [1]. The mass energy transfer coefficient is related to the interaction cross section of individual processes (photoelectric effect, Compton effect, and pair production) that result in energy transfer (Rayleigh scattering is not included since the photon is elasticity scattered without transferring energy).

$$\frac{\mu_{tr}}{\rho} = \frac{\tau_{tr}}{\rho} + \frac{\sigma_{tr}}{\rho} + \frac{k_{tr}}{\rho} \tag{2.10}$$

Mass energy absorption coefficient

The mass energy absorption coefficient ($\frac{\mu_{en}}{\rho}$) describes the fraction of photon energy transferred and subsequently resulting in local dose deposition (excluding the radiative energy losses by charged particles which leave the local region and deposit energy elsewhere) [1]. The mass energy absorption coefficient is related to mass energy transfer coefficient by

$$\frac{\mu_{en}}{\rho} = \frac{\mu_{tr}}{\rho}(1-g) \tag{2.11}$$

where g is the average fraction of secondary electrons energy that is lost in radiative interactions (bremsstrahlung or in-flight annihilation).

2.1.6 Interaction coefficients for charged particles

Linear stopping power

Linear stopping power (S) is the rate of mean energy loss ($\mathrm{d}E$) of a charged particle per traversing distance ($\mathrm{d}l$) in a medium. The unit of S is J m^{-1}.

$$S = \frac{\mathrm{d}E}{\mathrm{d}l} \tag{2.12}$$

Mass stopping power

Linear stopping power S depends on the density of the material. This dependency is largely removed by expressing the thickness of the material in mass unit (kg/m^2). The quantity is called mass stopping power (S/ρ). Its unit is J m^2 kg^{-1}.

$$\frac{S}{\rho} = \frac{1}{\rho}\frac{\mathrm{d}E}{\mathrm{d}l} \tag{2.13}$$

The mass stopping power can be split into three components: mass electronic stopping power ($\frac{S_{\mathrm{el}}}{\rho}$ also called mass collision stopping power), the mass radiative stopping power ($\frac{S_{\mathrm{rad}}}{\rho}$) and the mass nuclear stopping power ($\frac{S_{\mathrm{nuc}}}{\rho}$).

$$\frac{S}{\rho} = \frac{S_{\mathrm{el}}}{\rho} + \frac{S_{\mathrm{rad}}}{\rho} + \frac{S_{\mathrm{nuc}}}{\rho} \tag{2.14}$$

The mass electronic stopping power is due to the energy transfer from collisions resulting in ionization or excitation. The mass radiative stopping power is due to the energy transfer to the bremsstrahlung emission in the electric field of atomic nuclei or atomic electrons. The mass nuclear stopping power is due to the energy transfer from elastic Coulomb interactions (the term nuclear stopping power is traditionally used for interactions where charged particles lose some energy in elastic collision with atom and deflect considerably, however these are not nuclear reactions in a proper sense) [1].

Restricted mass electronic stopping power

In radiation therapy, we are often interested in determining the dose deposited locally in a region of interest. The use of mass electronic stopping power in determining the energy transfer to the region of interest might overestimate the dose since the secondary electrons created by ionization might have enough energy to travel and carry their energy outside the region of interest. Therefore, these energetic secondary electrons must be excluded when calculating the energy deposition. The restricted mass electronic stopping power ($\frac{L}{\rho}$) is defined to address this issue. The restricted mass electronic stopping power is the mass electronic stopping power that excludes energy transfer above an energy threshold Δ. Δ must be larger

than the binding energy of the atomic electrons in the medium. The choice of the energy threshold depends on the problem. For example, for ionization chambers assuming a threshold energy of 10 keV is reasonable. A 10 keV electron in air has a range of the order of 2 mm [2].

2.1.7 Kerma

For uncharged particles, the quantity kerma (acronym for kinetic energy released per unit mass) K is defined as the kinetic energy released ($\mathrm{d}E_{\mathrm{tr}}$) per unit mass $\mathrm{d}m$. The unit of K is J kg^{-1} or Gy (Gray).

$$K = \frac{\mathrm{d}E_{\mathrm{tr}}}{\mathrm{d}m} \tag{2.15}$$

Kerma focuses on the energy transferred to charged particles only. Kerma K has two components electronic (or collision) kerma (K_{el}) and radiative kerma (K_{rad}).

$$K = K_{\mathrm{el}} + K_{\mathrm{rad}} \tag{2.16}$$

The K_{el} includes that part of kerma that results in local energy deposition. The K_{rad} includes the portion of kerma that is due to the radiative energy losses by charged particles which leave the local region and deposit their energy elsewhere.

Kerma and electronic kerma at a point in a medium (K_{med} and $[K_{\mathrm{el}}]_{\mathrm{med}}$ respectively) can be related to the photon energy fluence spectrum in the medium $[\Psi(E)]_{\mathrm{med}}$ using equations 2.17 and 2.18 respectively.

$$K_{\mathrm{med}} = \int_0^{E_{\mathrm{max}}} [\Psi(E)]_{\mathrm{med}} [\frac{\mu_{tr}}{\rho}(E)]_{\mathrm{med}} \mathrm{d}E \tag{2.17}$$

$$[K_{\mathrm{el}}]_{\mathrm{med}} = \int_0^{E_{\mathrm{max}}} [\Psi(E)]_{\mathrm{med}} [\frac{\mu_{en}}{\rho}(E)]_{\mathrm{med}} \mathrm{d}E \tag{2.18}$$

2.1.8 Exposure

The exposure X is the quotient of $\mathrm{d}q$ by $\mathrm{d}m$. $\mathrm{d}q$ is the amount of charge produced when all of the charged particles liberated by the photons incident on a mass $\mathrm{d}m$ of dry air are completely stopped in dry air [1]. Exposure is only used for photons. The unit of exposure is C Kg^{-1}

$$X = \frac{\mathrm{d}q}{\mathrm{d}m} \tag{2.19}$$

Exposure is the ionization equivalent of electronic air kerma, except that the ionization arising from the absorption of bremsstrahlung emitted by the electrons is not to be included in dq. Exposure is directly related to air kerma (K_{air}) as follows:

$$X = (\frac{e}{W})K_{\text{air}}(1-g) \tag{2.20}$$

where g is the fraction of the energy released that is dissipated as bremsstrahlung and W/e is the mean energy expended per ion pair produced in air and per electron charge.

2.1.9 Absorbed dose

The absorbed dose D is defined as the quotient of d$\bar{\varepsilon}$ by dm, where d$\bar{\varepsilon}$ is the mean energy imparted by ionizing radiation to matter of mass dm. The unit of D is J kg^{-1} or Gy.

$$D = \frac{\mathrm{d}\bar{\varepsilon}}{\mathrm{d}m} \tag{2.21}$$

The mean energy imparted in a volume ($\bar{\varepsilon}$) is defined as:

$$\bar{\varepsilon} = R_{\text{in}} - R_{\text{out}} + \Sigma M' \tag{2.22}$$

where R_{in} and R_{out} are the mean total radiant energy of the ionizing particles entering and leaving the volume respectively. $\Sigma M'$ is the mean total decrease in the rest energies of the nuclei and elementary particles in the volume [1].

The absorbed dose to medium D_{med} is related to the charged particle fluence in the medium $[\Phi(E)]_{\text{med}}$ (equation 2.23) provided that the radiative photons escape the volume of interest and secondary electrons are absorbed on the spot [3].

$$D_{\text{med}} = \int_0^{E_{max}} [\Phi(E)]_{\text{med}} [\frac{S_{\text{el}}}{\rho}(E)]_{\text{med}} \mathrm{d}E \tag{2.23}$$

However, it is easier to characterize a given radiation beam with electrons of one energy instead of using an electron spectrum [2]. The mean electronic stopping power can be defined as below:

$$[\frac{\bar{S}_{\text{el}}}{\rho}]_{\text{med}} = \frac{\int_0^{E_{max}} [\Phi(E)]_{\text{med}} [\frac{S_{\text{el}}}{\rho}(E)]_{\text{med}} \mathrm{d}E}{\int_0^{E_{max}} [\Phi(E)]_{\text{med}} \mathrm{d}E} \tag{2.24}$$

Therefore, equation 2.23 can be written as follows with Φ_{med} being the total particle fluence in the medium:

$$D_{\text{med}} = \Phi_{\text{med}}[\frac{\bar{S}_{\text{el}}}{\rho}]_{\text{med}} \tag{2.25}$$

2.1.10 Range of charged particles

There are different definitions of range used in radiation physics. It can be defined as the thickness of an absorber that the charged particle can penetrate in an absorbing medium [2]. It can be also defined as the expectation value of the path length that a charged particle follows in the absorbing medium until it comes to rest [1]. Another common definition is the *continuous-slowing-down range* (R_{CSDA}). R_{CSDA} of a charged particle is the average path length traveled by a particle when it slows down from an initial energy E_0 down to zero [1].

$$R_{\text{CSDA}} = \rho \int_0^{E_0} \frac{\mathrm{d}E}{S(E)} \tag{2.26}$$

The R_{CSDA} unit is kg m^{-2}.

2.1.11 Charged particle equilibrium (CPE)

Charged particle equilibrium (CPE) occurs when the number of charged particles scattered toward the central region from regions outside the beam central axis is equal to the number of charged charged particles of the same energy leaving the central region [1]. A simplified illustration of CPE is shown in figure 2.3a. Figure 2.3a shows photons interacting at different depths (shown as bins) starting from surface to several mean free paths in water. Photon gets absorbed at different bins and creates an electron. It is assumed that electron tracks are straight and the range of all secondary electrons is four depth units. From the fourth bin onward, the total number of track segments within each bin remains constant (four). Thus, beyond the range of secondary electrons or the so-called electron build-up depth in photon beams CPE condition exists [1]. However, this is a very simplified illustration since photons are attenuated and the number and energy of electrons created by each photon is not the same at each bin.

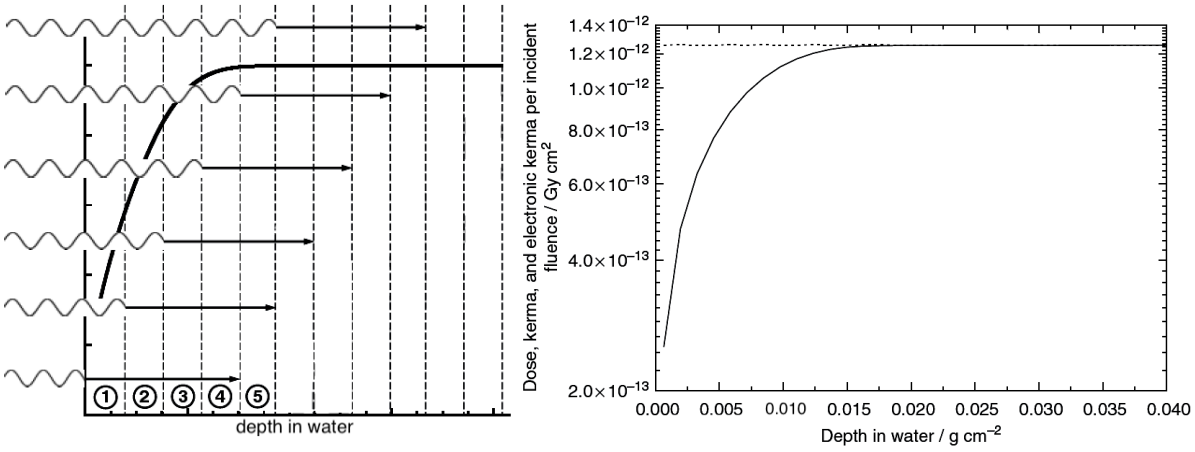

a b

Figure 2.3 (a) A schematic illustration of photon interactions at different depths in water. At bin 4 and beyond the condition of CPE exists. Reproduced from Andreo et al. [1]. (b) Depth dose dependency of absorbed dose (full curve), kerma (dotted curve) and electronic kerma (dotted curve indistinguishable from kerma) per incident fluence for a 250 keV photon broad beam incident on a water phantom (MC calculated). Reproduced from Kumar et al. [4] and Andreo et al. [1].

Under CPE conditions, the absorbed dose to the medium is equal to electronic kerma in the medium.

$$D_{\text{med}} \overset{\text{CPE}}{=} [K_{\text{el}}]_{\text{med}} \tag{2.27}$$

Using equations 2.18 and 2.27 we can write:

$$D_{\text{med}} \overset{\text{CPE}}{=} \int_0^{E_{\max}} [\Psi(E)]_{\text{med}} [\frac{\mu_{en}}{\rho}(E)]_{\text{med}} \mathrm{d}E \tag{2.28}$$

Equation 2.28 is the basis of cavity theory, explained in section 2.1.15.

Figure 2.3b shows the depth dependency of absorbed dose, kerma and electronic kerma for a 250 keV photon beam incident on a water phantom. Beyond the build-up depth, electronic kerma and dose are identical. In this energy range, radiative losses are negligible therefore kerma and electronic kerma are also indistinguishable.

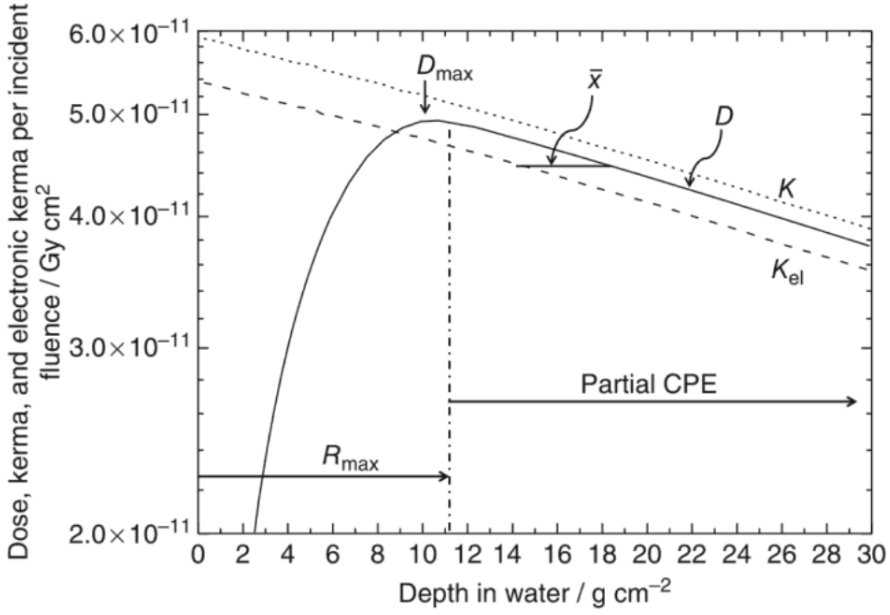

Figure 2.4 Depth dependency of absorbed dose (D), kerma (K) and electronic kerma (K_{el}) per incident fluence for a 25 MeV photon broad beam incident on a water phantom (MC calculated). The R_{max} is the depth of maximum secondary electron range, D_{max} is the depth of maximum dose and $\bar{X}$ is the displacement between the D and K_{el}. Adapted from Kumar et al. [4] and Andreo et al. [1].

2.1.12 Partial charged particle equilibrium (PCPE)

At high-energy photon beams, CPE approximation fails due to greater photon attenuation and scattering in the medium. This relatively minor CPE failure is termed *Partial charged particle equilibrium (PCPE)* or *transient charged particle equilibrium (TCPE)*. In general, the absorbed dose to the medium is related to electronic kerma in the medium as follows:

$$D_{med} = \beta_{med}[K_{el}]_{med} \tag{2.29}$$

where β is a constant and $\beta < 1$ in the build-up region, $\beta = 1$ under the CPE condition and $\beta > 1$ when there is PCPE. Figure 2.4 shows the depth dependency of absorbed dose, kerma and electronic kerma for a 25 MeV photon beam incident on a water phantom. The PCPE region beyond the depth of maximum secondary electron range (R_{max}) is shown. In this region absorbed dose is larger than electronic kerma ($\beta > 1$).

2.1.13 Lateral charged particle equilibrium (LCPE) range

LCPE is a term given to CPE when associated with the lateral (perpendicular to beam axis) movement of charged particles in laterally limited beam conditions. The LCPE range (r_{LCPE}) is a practical parameter used to determine if a radiation field size is small. The r_{LCPE} is the minimum radius of a circular photon field for which collision kerma in water and absorbed dose to water are equal at the centre of the field.

2.1.14 Beam quality

Most radiation beams are not mono-energetic, therefore the spectrum of the beam or the dosimetric effectiveness of the beam needs to be specified. This specification is called beam quality and is commonly represented by the variable Q. The two common beam quality specifiers ($\%\mathrm{dd}(10)_X$ and $TPR_{20,10}$) are explained in chapter 3.

2.1.15 Cavity theory

Ionization chambers are devices used in measuring absorbed dose in the medium (described in section 3.1). However, these detectors cannot be placed in the patient. In the clinic the measurement of absorbed dose is performed in a liquid (a water tank) or a solid mass, termed a phantom consisting of tissue-equivalent material that can model the properties of human body. The signal of the ionization chamber is proportional to the mean absorbed dose in the sensitive volume of the chamber. However, the sensitive volume of the detector (usually air) is not the same material as the surrounding medium (water or a tissue equivalent plastic). It is then necessary to convert the absorbed dose in air to absorbed dose in water. Cavity theory relates the mean absorbed dose in the sensitive material of the detector (D_{det}) to the absorbed dose at the reference point in the undisturbed medium (D_{med}) (in the absence of the detector) for beam quality Q using the conversion parameter $f_{\mathrm{med,det},Q}$. A schematic illustration is shown in figure 2.5.

$$f_{\mathrm{med,det},Q} = \left(\frac{D_{\mathrm{med}}}{D_{\mathrm{det}}}\right)_Q \tag{2.30}$$

Using equation 2.23, equation 2.30 can be written as

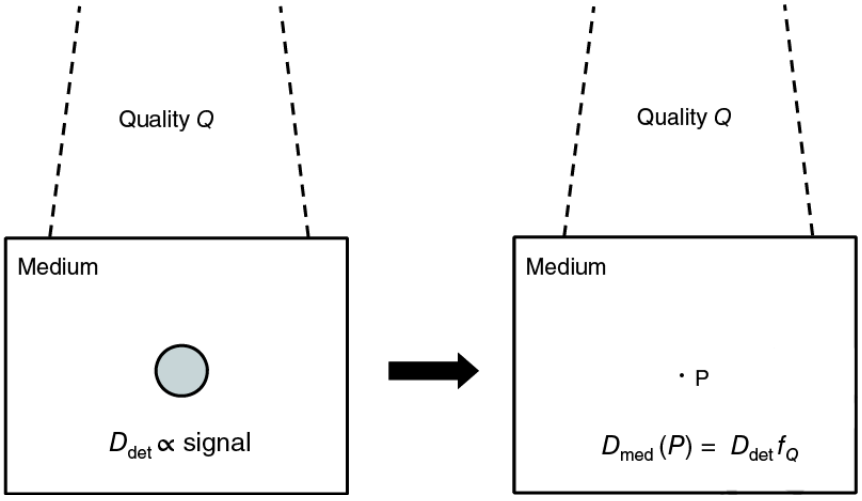

Figure 2.5 An illustration of the mean absorbed dose in the sensitive material of the detector (D_{det}) and the absorbed dose at point P in the undisturbed medium (D_{med}) for beam quality Q. The cavity-theory factor f_Q relates the D_{det} to D_{med}. Adapted from Andreo et al. [1].

$$f_{\text{med,det},Q} = \frac{\int_0^{E_{max}} [\Phi(E)]_{\text{med}} [\frac{S_{\text{el}}}{\rho}(E)]_{\text{med}} \mathrm{d}E}{\int_0^{E_{max}} [\Phi(E)]_{\text{det}} [\frac{S_{\text{el}}}{\rho}(E)]_{\text{det}} \mathrm{d}E} \tag{2.31}$$

Depending on the size of cavity compared to the range of the secondary charged particles in the cavity, different cavity theories have been developed.

Cavities that are small compared to secondary electron ranges

For small cavities the Bragg-Gray and Spencer-Attix theories have been developed [3].

Bragg-Gray cavity theory: To use the Bragg-Gray theory there are two conditions that must be met. The first condition is that the cavity size must be smaller than the range of secondary particles incident on it. Therefore, it can be assumed that the presence of the cavity does not disturb the fluence of charged particles and the electron fluence in the medium and the cavity are equal. The second condition is that the absorbed dose to the cavity is deposited only by charged particles crossing the cavity. This means that no photon interactions happens inside the cavity and no secondary electrons are created inside the cavity [3]. Therefore in equation 2.31, the particle fluence in the medium and cavity are assumed to be equal. For Bragg-Gray cavity theory, equation 2.31 can be expressed as follows:

$$f^{\mathrm{BG}}_{\mathrm{med,det},Q} = \frac{\int_0^{E_{max}} [\Phi(E)^{\mathrm{prim}}]_{\mathrm{med}} [\frac{S_{\mathrm{el}}}{\rho}(E)]_{\mathrm{med}} \mathrm{d}E}{\int_0^{E_{max}} [\Phi(E)^{\mathrm{prim}}]_{\mathrm{med}} [\frac{S_{\mathrm{el}}}{\rho}(E)]_{\mathrm{det}} \mathrm{d}E} \tag{2.32}$$

where $\Phi(E)^{\mathrm{prim}}$ is the primary charged particle fluence. $\Phi(E)^{\mathrm{prim}}$ excludes the δ ray.

Spencer–Attix cavity theory: The Spencer–Attix cavity theory is more general compared to the Bragg-Gray cavity theory. Unlike Bragg-Gray cavity theory, Spencer–Attix cavity theory takes into account the secondary electrons created as a result of hard collisions in the slowing down of the primary electrons in the sensitive volume of the dosimeter. Some of these electrons have energies larger than or equal to the threshold energy Δ (considered fast) and some of them have energies lower than Δ (considered slow). The slow electrons deposit their energy locally while the fast electrons have enough energy to cross the cavity, carry some of their energy with them and are set in motion in the medium (not in the cavity). The energy deposition of all electrons (primary and secondary) is determined using the restricted mass electronic stopping power, so that energies below Δ are locally deposited.

For Spencer–Attix cavity theory, the relation between the dose to the medium and dose to the cavity becomes (for derivation please see Andreo et al. [1]):

$$f^{\mathrm{SP}}_{\mathrm{med,det},Q} = \frac{\int_\Delta^{E_{max}} [\Phi_E^{\mathrm{tot}}]_{\mathrm{med}} [\frac{L_\Delta}{\rho}(E)]_{\mathrm{med}} \mathrm{d}E + [\Phi_E(\Delta)^{\mathrm{tot}}]_{\mathrm{med}} [\frac{S_{el}}{\rho}(\Delta)]_{\mathrm{med}} \Delta}{\int_\Delta^{E_{max}} [\Phi_E^{\mathrm{tot}}]_{\mathrm{med}} [\frac{L_\Delta}{\rho}(E)]_{\mathrm{det}} \mathrm{d}E + [\Phi_E(\Delta)^{\mathrm{tot}}]_{\mathrm{med}} [\frac{S_{el}}{\rho}(\Delta)]_{\mathrm{det}} \Delta} \tag{2.33}$$

where $[\Phi_E^{\mathrm{tot}}]$ is the electron fluence without any detector being present, Δ is the cut-off energy, $\frac{L_\Delta}{\rho}(E)$ and $\frac{S_{el}}{\rho}(\Delta)$ are the restricted and unrestricted mass electronic stopping powers respectively. In equation 2.33, the first terms in the numerator and denominator are the energy deposition due to all electrons down to the threshold energy Δ in the cavity of the detector and the reference point in the undisturbed medium respectively. The second terms in the numerator and denominator (also called track-end term [5]) are the energy deposition in the reference point and the cavity of the detector as the electron energy drops from Δ to zero respectively [6, 1].

Cavities that are large compared to secondary electron ranges

When the detector/cavity dimensions are large compared to the secondary electron range, the cavity is referred as "large". This situation has fewer applications in dosimetry of high-energy photon beams compared to Bragg-Gray and Spencer-Attix cavity theories. Assuming there is

PCPE in the detector, the conversion parameter $f_{\text{med,det},Q}$ for large cavities is determined as follows:

$$f_{\text{med,det},Q} = \frac{\int_0^{E_{\max}} [\Psi(E)]_{\text{med}} [\frac{\mu_{en}}{\rho}(E)]_{\text{med}} \mathrm{d}E}{\int_0^{E_{\max}} [\Psi(E)]_{\text{med}} [\frac{\mu_{en}}{\rho}(E)]_{\text{det}} \mathrm{d}E} \tag{2.34}$$

where $\Psi(E)$ is the photon energy fluence in the undisturbed medium and $\frac{\mu_{en}}{\rho}(E)$ is the mass energy absorption coefficient in the medium.

Burlin cavity theory

Burlin extended the Bragg-Gray and Spencer-Attix cavity theories to cavities of intermediate dimensions [7]. The Burlin cavity theory can be written as follows:

$$\frac{D_{\text{det}}}{D_{\text{med}}} = \omega_{\text{BG}} [\frac{\bar{L}_{\Delta}}{\rho}]^{\text{det}}_{\text{med}} + (1 - \omega_{\text{BG}}) [\frac{\bar{\mu}_{\text{en}}}{\rho}]^{\text{det}}_{\text{med}} \tag{2.35}$$

where ω_{BG} is a weighting factor that varies between zero (for large cavities) and one (for small cavities). $[\frac{\bar{L}_{\Delta}}{\rho}]^{\text{det}}_{\text{med}}$ is the mean restricted mass electronic stopping power ratio detector to medium and $[\frac{\bar{\mu}_{\text{en}}}{\rho}]^{\text{det}}_{\text{med}}$ is the mean mass energy absorption coefficient ratio detector to medium.

2.2 Monte Carlo methods

The term *Monte Carlo* was first used as a class of numerical methods by scientists working on the development of nuclear weapons in Los Alamos in the 1940s [8]. MC methods are games of chance or random sampling whose outcome can be used to study different phenomena. One of the earliest examples of the use of random sampling was in evaluating integrals. In 1777, Leclerc et al. [9] proposed a MC-like method to determine the outcome of an experiment consisted of a needle of length L dropped randomly on a horizontal plane ruled with parallel straight lines a distance d ($d > L$) apart (known as Buffon's needle problem). They showed that the probability that the needle will cross one of the lines was $2L/\pi d$, both experimentally and mathematically.

The main components of MC methods are random numbers, probability distributions and sampling methods to get randomized values from the probability distributions [1].

2.2.1 Pseudo random numbers

Pseudo random numbers are usually distributed uniformly between [0,1]. Pseudo random numbers should be uncorrelated and should not be repeated. The algorithms used in generating random numbers are called random number generators. The pseudo random numbers should be generated in large amounts and at a speed that current computers can process. The algorithms used in generating random numbers for particle transport purposes are numerical. Since these algorithms are deterministic (an algorithm that given the same input, will always produce the same output), the generated random numbers are not really random. These numbers are referred as "pseudo random numbers" [1].

2.2.2 Probability distribution and inverse sampling

For a variable x in the interval $[x_{\min}, x_{\max}]$, the probability distribution function (PDF) (also called probability density function), $f(x)$ gives the likelihood of obtaining a value x in the interval. The probability of obtaining x in a differential interval $\mathrm{d}x$ is $f(x)\mathrm{d}x$.

Since probabilities are always positive, the PDF is positive ($f(x) \geq 0$) and normalized to unity:

$$\int_{x_{\min}}^{x_{\max}} f(x)\mathrm{d}x = 1 \tag{2.36}$$

The mean or the expectation value of variable x is:

$$E[x] = \int_{x_{\min}}^{x_{\max}} x f(x)\mathrm{d}x \tag{2.37}$$

The variance of the distribution of the values of x (σ_{x}^2) represent the width of the PDF:

$$\sigma_{\mathrm{x}}^2 = E[x^2] - E[x]^2 = \int_{x_{\min}}^{x_{\max}} (x - E[x])^2 f(x)\mathrm{d}x \tag{2.38}$$

The cumulative probability distribution function (CPD) can be defined for each PDF:

$$F(x) = \int_{x_{\min}}^{x} f(x')dx', \text{with x} \in [x_{\min}, x_{\max}] \tag{2.39}$$

where $F(x_{\min}) = 0$ and $F(x_{\max}) = 1$, that is $F(x) \in [0, 1]$.

There are different sampling methods. One of the common and straightforward sampling methods is the inverse sampling. The random number ξ in the interval $[0,1]$ can be related to $F(x)$ such that

$$\xi \equiv F(x) \text{ and } x = F^{-1}(\xi) \tag{2.40}$$

where $F^{-1}(x)$ is the inverse of the function $F(x)$ and x becomes a random sample from the distribution $f(x)$. This method is called inverse-transform sampling [1].

One of the most typical examples of the inverse-transform sampling in radiation transport is sampling from an exponential distribution. For a PDF $f(y) = Ae^{-Ay}$, the CPD will be $F(y) = \xi = 1 - e^{-Ay}$ which yields:

$$y = -\frac{1}{A} ln(1-\xi) \tag{2.41}$$

For a photon interaction with the photon attenuation coefficient μ, the distance to the next interaction (x) will be:

$$x = -\frac{1}{\mu} ln(1-\xi) \tag{2.42}$$

where $\frac{1}{\mu}$ is the mfp (defined in section 2.1.5) and $-ln(1-\xi)$ is the number of mfps (n_{mfp}).

2.2.3 Monte Carlo codes for particle transport

MC methods can be used in radiation transport to model the random trajectories of individual particles since the different interaction mechanisms of radiation with matter follow probability distributions. MC techniques use machine-generated random numbers to sample from these probability distributions [10]. First, particles are created according to probability distributions describing the radiation source. Then, the distance that the particles travel to the next interaction and the type of interaction (e.g. photoelectric, Compton, pair production for photons) are determined using a probability distribution depending on the total interaction cross section. Subsequently, the particle is scattered into another energy and/or direction following the corresponding differential cross section [11].

However, in case of electron transport, due to the large number of Coulomb interactions that happen in a short path length an event-by-event simulation would be very time consuming. To address this issue, the condensed history technique was developed by Berger [12]. In the

condensed history technique, the path of the electron is decomposed into a series of steps for which the effects of the large number of collisions happening during the step are grouped together [10]. The change of particle's energy and direction is sampled at the end of the step using multiple scattering distributions.

EGSnrc is a general-purpose MC code used to model the transport of photons, electrons and positrons with kinetic energies between 1 keV and several hundred GeV through matter [13]. The EGSnrc is maintained by the National Research Council (NRC) of Canada, however it is based on the EGS code developed initially at the Stanford Linear Accelerator Center in the 1970s. Over the years, NRC has also developed and released a series of user codes based on the EGSnrc system (e.g. BEAMnrc, egs_chamber, DOSXYZnrc, DOSRZnrc, SPRRZnrc, g) [14, 15].

Another available MC particle transport code is PENELOPE. PENELOPE is a general-purpose code for simulation of electron, positron and photon transport applicable to energies from 50 eV to 1 GeV [16].

The focus of this thesis is on EGSnrc. The EGSnrc user codes used in this thesis are briefly explained below.

BEAMnrc

BEAMnrc is an EGSnrc MC user code for modelling radiotherapy sources such as ^{60}Co units, x-ray systems, electron and photon beams [15]. BEAMnrc is built on the EGSnrc code system and it consists of a series of component modules (CMs). The users can set the dimensions and material of each CM, and combine them to model different parts of the accelerator such as the target, primary collimator, jaws, MLC and other components. The main output of BEAMnrc is a phase space file which contains data on the position, direction, energy, and charge for every particle crossing a defined scoring plane.

egs_chamber

The egs_chamber user code is used for ionization chamber calculations [17, 13]. It is used to calculate the dose to the cavity of an ionization chamber and the dose ratios of two correlated geometries used for the computation of perturbation factors for different components of an ionization chamber (perturbation factors are defined in section 3.3.3). Correlated geometries allow us to do the dose calculations in the region of interest for different cases (materials) with

a single execution of the code instead of performing the entire region calculation multiple times for different materials [18].

DOSXYZnrc

The DOSXYZnrc user code is used to calculate the 3-dimensional absorbed dose distributions in a rectilinear voxel phantom [19]. The voxel dimensions are variable in all three directions. The code scores the energy deposition in the designated voxels and outputs the dose distribution arrays.

DOSRZnrc

The DOSRZnrc user code is used to score dose in a generalised cylindrical geometry [14]. The energy deposition can be scored in the user-defined regions. It is used for dose and kerma calculations.

SPRRZnrc

The SPRRZnrc user code calculates restricted mass electronic stopping power ratios in each region in a cylindrical geometry for arbitrary media [14].

g

The g user code is used to calculate quantities such as μ_{tr}, μ_{en} and g (average fraction of secondary-electron energy that is lost in radiative interactions).

2.2.4 Variance reduction techniques

Monte Carlo calculations might require large CPU times, especially when used in radiation therapy. To address this issue, different variance reduction techniques (VRTs) have been developed. The goal of any VRT is to improve the calculation efficiency without introducing a systematic error in the calculation. The calculation efficiency ε is defined as below:

$$\varepsilon = \frac{1}{\sigma^2 T} \tag{2.43}$$

where σ^2 is the statistical variance of the quantity of interest and T is the CPU computation time. Statistics depend on the number of independent events (N_{events}):

$$\sigma^2 \propto \frac{1}{N_{\text{events}}} \tag{2.44}$$

N_{events} is proportional to the number of histories, area and thickness of scoring region. However, the area and thickness of scoring region cannot be so large as to no longer represents the dose at the point of interest. To improve the efficiency, the uncertainty or/and the computation time should be reduced. The `EGSnrc` VRTs used in this thesis are summarized below.

Russian roulette

When a Russian roulette (RR) with a survival probability p is played on a particle with statistical weight w, the particle trajectory can get killed/terminated with probability $1-p$ or can survive with probability p. If the particle survives, it is assigned a statistical weight of $\frac{w}{p}$ (its statistical weight is increased by $\frac{1}{p}$). Therefore, the weight of the particle is preserved before and after applying the RR. The main applications of RR in radiation transport is to avoid transporting of particles that contribute nothing or very little to the quantity of interest.

Particle splitting

Particle splitting is the reverse of RR. A particle can split into N identical particles. Each of the daughter particles gets $\frac{1}{N}$ of the statistical weight of the initial particle. Each daughter particle is transported separately therefore improving the information gain. However, tracking the secondary electrons created by split-photon interactions can become time consuming. Therefore, particle splitting is often combined with RR. Particle splitting is used in situations where particle arrives in a region that is rarely visited during the simulation.

Photon cross-section enhancement

Photon cross-section enhancement (XCSE) is used in different `EGSnrc` user codes such as `egs_chamber` and `DOSRZnrc` as a VRT [17]. The XCSE technique increases the photon cross section (Σ) by an enhancement factor $b > 1$, therefore decreasing the mean free path length of the photons and generating more secondary electrons along the photon path. If the real interaction cross section is Σ, the total interaction cross section after cross section enhancement would be $\Sigma_{\text{tot}} = b\Sigma$. This leads to a fictitious interaction cross ($\Sigma(b-1)$) such that:

$$\Sigma_{\text{tot}} = \Sigma + \Sigma(b-1) = b\Sigma \tag{2.45}$$

At an interaction site, the photon is split into a portion that undergoes a real interaction and a portion that undergoes a fictitious interaction (non-interacting portion). The interacting portion is $\frac{\Sigma}{b\Sigma} = \frac{1}{b}$ and the non-interacting portion is $\frac{(b-1)\Sigma}{b\Sigma} = 1 - \frac{1}{b}$. Assuming the statistical weight of the incident photon is w_0, the interacting photon will set in motion electrons and/or scattered photons all carrying a statistical weight of $\frac{w_0}{b}$. A RR game is played with a survival probability of $\frac{1}{b}$ for scattered photons and $1 - \frac{1}{b}$ for the non-interacting portion of the incident photon so that all surviving photons carry again the initial weight w_0. The user in `egs_chamber` can set different enhancement factors in different regions. For a NE2571 Farmer chamber dose calculations in `egs_chamber`, a 1 cm cylindrical water shell surrounding the chamber with XCSE factor of 256 for a beam quality %dd(10) of 63.4 (high-energy photon beams) increases the gain in efficiency of about a factor of 300 [17].

Photon forcing

Photon forcing is a VRT which forces an interaction to happen within the geometry between the current point and the point where the photon leaves the geometry [14, 1]. In general when a photon interaction is not forced, the number of mfps is selected from $n_{\text{mfp}} = -ln(1-\xi)$ (see section 2.2.2). When the photon interaction is forced in a geometry with thickness of X mfp, the fraction of photons interacting in the geometry will be $1 - e^{-X}$ and the fraction of photons leaving the geometry will be e^{-X}. The number of mfps (n_{mfp}) to the next generation is selected from:

$$n_{\text{mfp}} = -ln(1 - \xi(1 - e^{-X})) \tag{2.46}$$

Photon forcing is used in `BEAMnrc` to force photons to interact in a specified CM. It improves the statistics and is essential for calculations in very thin geometries where photon interactions are sparse [15]. Photon forcing is also used in other user codes, such as `DOSRZnrc`.

Directional bremsstrahlung splitting

The directional bremsstrahlung splitting (DBS) is a VRT used in `BEAMnrc` which splits the bremsstrahlung photons directed toward a field of interest (FOI) at the time of creation. The

user defines a FOI, a circle surrounding the treatment field with sufficiently large margins. The bremsstrahlung photons that are aimed away from the FOI are not split and RR is played for all these photons not directed towards the FOI. However, the bremsstrahlung photons directed toward the FOI are split *NBRSPL* times at the time of creation. Each photon will have a corresponding weight of $\frac{1}{NBRSPL}$. DBS improves the statistics of bremsstrahlung photons resulting from electron interactions [15].

Bibliography

[1] Andreo P, Burns D, Nahum A, Seuntjens J, Attix F. Fundamentals of Ionizing Radiation Dosimetry. *Weinheim: Wiley*, 2017.

[2] Podgorsak EB. Radiation Physics for Medical Physicists. *Springer Science & Business Media*, 2010.

[3] Podgorsak EB. Radiation oncology physics: A handbook for teachers and students. *Vienna: International Atomic Energy Agency*, 2005.

[4] Kumar S, Deshpande DD, Nahum AE. Monte-Carlo-derived insights into dose–kerma–collision kerma inter-relationships for 50 keV–25 MeV photon beams in water, aluminum and copper. *Physics in Medicine & Biology*, 60(2), 501, 2014.

[5] Nahum AE. Calculations of electron flux spectra in water irradiated with megavoltage electron and photon beams with applications to dosimetry. *Doctoral dissertation, University of Edinburgh*, 1976.

[6] Bouchard H. A theoretical re-examination of Spencer–Attix cavity theory. *Physics in Medicine & Biology*, 57(11), 3333, 2012.

[7] Burlin TE. A general theory of cavity ionisation. *The British journal of radiology*, 39(466), 727-734, 1966.

[8] Kalos MH, Whitlock PA. Monte carlo methods. *John Wiley & Sons*, 2009.

[9] Leclerc GL, De Buffon C. Essai d'arithmétique morale. *Supplément à l'Histoire Naturelle*, 4, 1777.

[10] Rogers DWO, Bielajew AF. Monte Carlo techniques of electron and photon transport for radiation dosimetry. *The dosimetry of ionizing radiation*, 3, 427–539, 1990.

[11] Kawrakow I. Accurate condensed history Monte Carlo simulation of electron transport. I. `EGSnrc`, the new `EGS4` version. *Medical physics*, 27(3), 485–498, 2000.

[12] Berger MJ. Monte Carlo calculation of the penetration and diffusion of fast charged particles. *No. PRINT-91-0305,* 1963.

[13] Kawrakow I, Mainegra-Hing E, Rogers DWO, Tessier F, Walters BRB. The `EGSnrc` code system: Monte Carlo simulation of electron and photon transport, NRCC Report PIRS-701. *National Research Council of Canada*, 2019.

[14] Rogers DWO, Kawrakow I, Seuntjens JP, Walters BRB, Mainegra-Hing E. NRC user codes for `EGSnrc`, NRCC Report PIRS-702(revC). *National Research Council of Canada*, 2019.

[15] Rogers DWO, Walters B, Kawrakow I. `BEAMnrc` users manual, NRCC Report PIRS-0509(A)revL. *National Research Council of Canada*, 2019.

[16] Salvat F, Fernández-Varea JM, Sempau J. PENELOPE-2008: A code system for Monte Carlo simulation of electron and photon transport. *In Workshop Proceedings*, 4, 6222, 2006.

[17] Wulff J, Zink K, Kawrakow I. Efficiency improvements for ion chamber calculations in high energy photon beams. *Medical physics*, 35(4), 1328–1336, 2008.

[18] De Almeida CE. An Efficiency Studying of an Ion Chamber Simulation Using Vriance Reduction Techniques with `EGSnrc`. *Journal of Biomedical Physics & Engineering*, 9(3):259, 2019.

[19] Walters B, Kawrakow I, Rogers DWO. `DOSXYZnrc` users manual, NRCC Report PIRS-794revB. *National Research Council of Canada*, 2019.

Chapter 3

Reference dosimetry in high-energy photon beams

This chapter summarizes how an ionization chamber works, and the primary standards and dosimetry protocols for reference dosimetry of high-energy photon beams used in this thesis.

3.1 Ionization chamber

Ionization chambers (also known as ion chambers), usually air-filled, are the most common devices used to determine absorbed dose in radiation therapy. Typically, a cylindrical ionization chamber consists of a central electrode, a wall and a stem. A voltage (usually between 100 V and 400 V depending on the chamber type) is applied between two conductors to create an electric field. When an ion chamber is irradiated, ion pairs (electron and positively charged atoms) are created in the gas - typically air - in the sensitive volume of the chamber. The ion pairs within the sensitive volume are collected by the conductors under the influence of the electric field. The signal of the chamber (charge) is read out using an electrometer, and the typical charge measured amounts up to a few tens of nC for radiation therapy doses. The signal of the ionization chamber is proportional to the absorbed dose in the sensitive air volume of the chamber. Using the cavity theory explained in section 2.1.15, absorbed dose in the sensitive volume can be converted into absorbed dose in water. One of the most commonly used ionization chambers is the cylindrical (or thimble) ionization chamber. A cylindrical chamber has a cylindrical geometry with central electrode and outer cylindrical wall acting as the conductors. Figure 3.1 shows an image of a cylindrical chamber, Exradin A12. The main

Figure 3.1 An image of a cylindrical chamber (Exradin A12). Adapted from Standard Imaging.

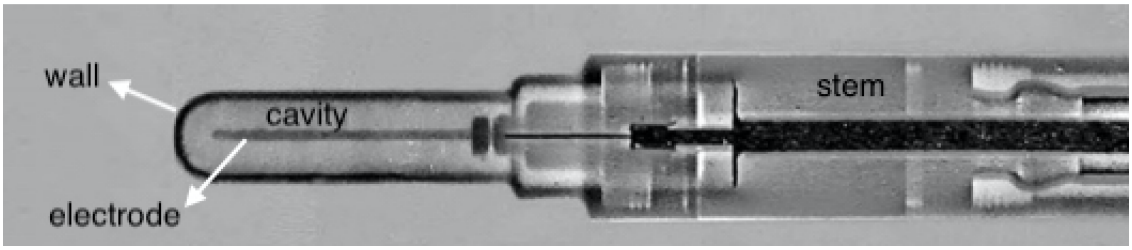

Figure 3.2 A radiograph image of Exradin A12. Adapted from McCaffrey et al. [1] with the wall, electrode, cavity and stem labeled.

components including wall, central electrode, cavity (sensitive volume) and stem are labeled in the radiograph image (Figure 3.2).

3.2 Primary standards for megavoltage beams

Since radiation treatments must be comparable between institutions, ionization chambers used in hospitals for reference dosimetry of radiation therapy machines must have a calibration traceable to a primary standard. Primary standards are instruments/measurements of the highest metrological quality and the quantity determined by primary standard is accepted without reference to other standards of same quantity [2]. Primary standards are realized by the primary standards dosimetry laboratories. In Canada, the NRC develops and maintains the primary standards. In Canadian hospitals, the reference ionization chambers are sent to the NRC standards laboratory and returned with calibration coefficients. Primary standards can be for the quantity air-kerma (or exposure) or can be for absorbed dose to water described below.

3.2.1 Air-kerma (or exposure) based standards

At primary standards laboratories, the exposure (X) or air kerma (K_{air}) is determined at a point in air for a collimated beam of photons (1.17 MeV and 1.33 MeV) emitted by radioactive ^{60}Co. The air kerma standard consists of a graphite thick-walled cavity ionization chamber. Subsequently, the center of the user's ionization chamber is placed at the same location as the standards laboratory graphite cavity chamber and exposed to the known exposure X or the known air kerma K_{air}. Since the measurements are in air, a build up cap is used for most chambers to provide PCPE in the wall of the ionization chamber. This condition allows the measurement of the charge produced in the air of the ionization chamber to be converted to absorbed dose to the wall using cavity theory. Absorbed dose to the wall is related to air kerma free in air using mass energy absorption coefficient ratios. The set-up is shown in figure 3.3. The charge is recorded for the user's ionization chamber using an electrometer and normalized to temperature of 22 °C and a pressure of one standard atmosphere. The standards laboratory provides the users the ^{60}Co exposure calibration coefficient (N_X) or air kerma calibration coefficient (N_k) defined below.

$$N_X = XM^{-1} \tag{3.1}$$

$$N_K = K_{\text{air}}M^{-1} \tag{3.2}$$

Where M is the measured charge using the user's ionization chamber corrected for temperature and pressure.

3.2.2 Absorbed dose to water standards

The primary absorbed dose to water in high-energy photon beams can be determined using an ionization chamber, chemical dosimetry or calorimetry [4].

Absorbed dose standards using ionization chambers

This standard has been mainly implemented at the Bureau international des poids et mesures (BIPM). A graphite cavity ionization chamber is irradiated in a cubic water phantom. Measurements are performed in a 10×10 cm^2 field with the center of the chamber at a reference depth (5 g cm^2) at a distance 100 cm from the source (see figure 3.4). The absorbed dose to

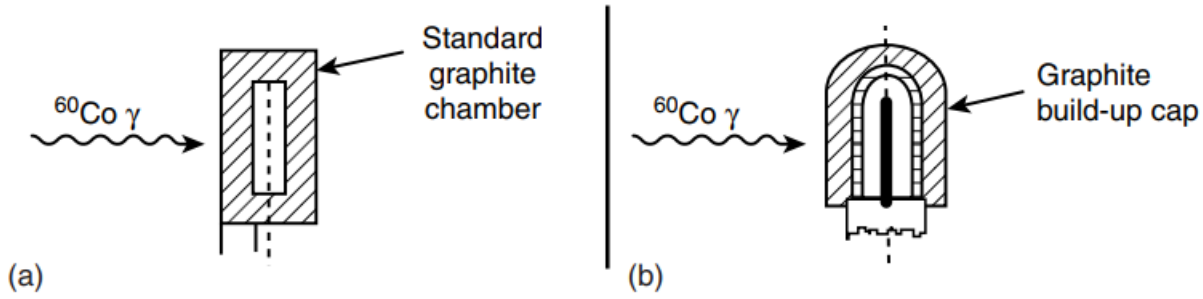

Figure 3.3 The setup for air kerma determination. (a) a graphite thick-walled ionization chamber is exposed to the beam (b) the user's ionization chamber with the build-up cap is placed at the same location as the standards laboratory graphite cavity chamber and exposed to the same known exposure/air kerma. Adapted from Andreo et al. [3].

water is determined using the Spencer-Attix cavity theory with MC determined correction factors.

Absorbed dose standards using the Fricke chemical dosimeter

The most common chemical dosimeter is the ferrous sulphate dosimeter, also known as the Fricke dosimeter consisting of the aqueous ferrous sulphate solution. When the ferrous sulphate solution is irradiated, ferrous ions Fe^{2+} oxidize into ferric ions Fe^{3+}. The absorbed dose can be determined by measuring the concentration of Fe^{3+}. Since Fe^{3+} shows a strong absorption peak at a wavelength of 304 nm, the absorbance (optical density) of the solutions before and after the irradiation (electron beam) is measured using spectrophotometry. The net optical density is proportional to the absorbed dose. A conversion factor, determined using MC calculations, is used to transfer the absorbed dose in the Fricke solution (the sensitive volume of the dosimeter) to the absorbed dose to water at the reference point in a water phantom [6].

Absorbed dose standards using calorimetry

The main principle of calorimetry is that the energy imparted in the medium by ionizing radiation causes a temperature rise in the medium. The temperature rise can be measured and related to the absorbed dose. Currently, calorimeters used at standards laboratories are either graphite or water calorimeters [4]. Graphite has a low atomic number making it a suitable material for calorimetry from a radiological perspective [6]. Graphite is a suitable material

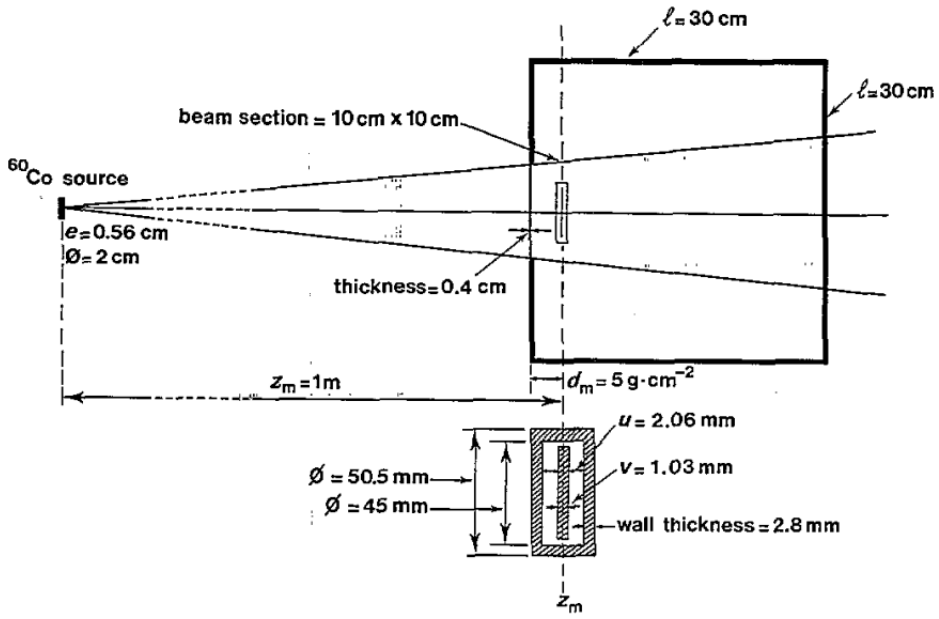

Figure 3.4 A schematic view of the experimental set-up for determination of absorbed dose to water and the ionization chamber at BIPM. Adapted from Boutillon et al. [5]

also from the perspective of heat dissipation, as the energy absorbed is quickly averaged out in the individual bodies of the calorimeter. Despite this, a correction is needed to convert the absorbed dose in graphite to absorbed dose in water. Water calorimetry in stagnant water is also possible since the thermal diffusivity of water is so low that the temperature distribution stays in place for accurate point measurements [4]. In stagnant water calorimeters, the absorbed dose to water (D_{m}) can be directly determined as follows:

$$D_{\mathrm{m}} = \Delta T_{\mathrm{m}} c_{\mathrm{m}} \tag{3.3}$$

where ΔT_{m} is the temperature rise measured at a point and c_{m} is the specific heat capacity of water. Different water calorimeters have been designed and used world wide. Figure 3.5 shows a schematic drawing of the NRC primary standard water calorimeter.

The standards laboratory provides the user with the absorbed dose to water calibration coefficient $N_{D,w}^{Q}$ for the user's ionization chamber. The user's detector is placed at the reference depth (usually 5 g cm^2 or 10 g cm^2) at beam quality Q (usually ^{60}Co) at a specific source-to-detector distance (SDD) of 80 cm or 100 cm. The charge is measured using the user's electrometer and corrected for temperature and pressure.

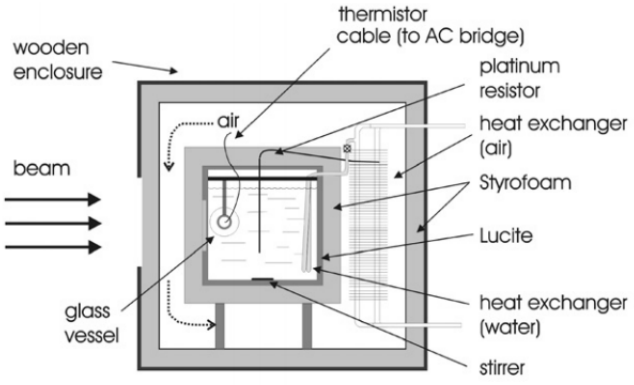

Figure 3.5 A schematic view of the water calorimeter at NRC primary standards laboratory. Adapted from Seuntjens et al. [4]

The $N^{Q}_{D,w}$ is determined as follows:

$$N^{Q}_{D,w} = D_w M^{-1} \tag{3.4}$$

Where, D_w is the absorbed dose to water determined using an ionization chamber, Fricke dosimeter or water calorimeter and M is the charge reading for the user's ionization chamber at standards laboratory corrected for temperature and pressure.

3.3 Dosimetry protocols for reference dosimetry of high-energy photon beams used in this thesis

3.3.1 AAPM TG-21

The AAPM TG-21 is a protocol published in 1983 providing guidelines on determining dose to water for ^{60}Co gamma rays, photon beams (energy range of 2-50 MeV) and electron beams (energy range of 5-50 MeV) used in radiation therapy [7]. The TG-21 is based on exposure (or air kerma) standards. For the calibration of photon beams, the procedure recommended in TG-21 is summarized below.

Beam quality specifier

For photon beams, the ratio of ionization measurements at 20 cm depth and 10 cm depth with a fixed SDD is used as the beam quality specifier in TG-21. The ionization ratio is also related to the nominal accelerating potential of the x-ray source.

Absorbed dose to water

The users send their ionization chamber and electrometer to a standards laboratory. As described in section 3.2.1, the standards laboratories provide the N_X for the user's detector. A quantity called the cavity-gas calibration factor (N_{gas}) is defined as the dose to gas (D_{gas}) in the chamber per electrometer reading M[1]. N_{gas} is usually not provided by the standards laboratory, but the user can calculate N_{gas} from N_X theoretically using the expression below (for derivation please see TG-21 [7])

$$N_{gas} = \frac{N_X k (W/e) A_{ion} A_{wall} \beta_{wall}}{\alpha (\bar{L}/\rho)^{wall}_{air} (\bar{\mu}_{en}/\rho)^{air}_{wall} + (1-\alpha)(\bar{L}/\rho)^{cap}_{air} (\bar{\mu}_{en}/\rho)^{air}_{cap}} \tag{3.5}$$

Where k is the charged produced in air per unit mass per unit exposure ($k = 2.58 \times 10^{-4}$ C/kg R), W/e is the mean energy expended per unit charge in air at usual humidity (W/e = 33.7 J/C) and A_{ion} is the ionization collection efficiency in the user's chamber at the time of calibration at the primary standards laboratory. A_{wall} corrects for the attenuation and scatter in the wall and build up cap of the user's chamber. A_{wall} values are provided in TG-21 as a function of the internal dimensions of the chamber. β_{wall} is the quotient of absorbed dose by the collision fraction of kerma in the chamber wall (β_{wall}=1.005) and α is the fraction of ionization due to electrons from the chamber wall. The values for α are provided in TG-21 as a function of chamber wall thickness. The $(\bar{L}/\rho)$ and $(\bar{\mu}_{en}/\rho)$ are the mean restricted mass electronic stopping power and the mean mass energy absorption coefficient respectively given in TG-21 for different materials for ^{60}Co gamma rays. The "wall", "air" and "cap" refer to the chamber wall, chamber cavity and buildup cap material respectively.

In the clinic, the users might choose phantom materials other than water for calibration such as solid water (a plastic radiologically equivalent to water), polymethylmetacrylate (PMMA, also known as acrylic or Lucite), polystyrene or acrylonitrile butadiene styrene (ABS).

[1]Note that because $N_{\text{gas}} = \frac{D_{\text{gas}}}{M} = \frac{W/e}{m_{\text{air}}}$, N_{gas} is a representation of the effective mass of air (m_{air}) responsible for signal generation in the ionization chamber

The dose to phantom material per monitor unit (D_{med}/U) that replaces the chamber when it is removed is determined by

$$D_{med}/U = (\overline{M/U})N_{gas}(\overline{L}/\rho)^{med}_{air}P_{wall}P_{ion}P_{repl} \tag{3.6}$$

Where M is the chamber signal normalized to the temperature of 22°C and pressure of 760 mm Hg and U represents the monitor units for linacs or time for ^{60}Co unit. P_{repl} is the replacement correction that corrects for the replacement of phantom material by an ionization chamber. The users can find the values of P_{repl} in TG-21 as a function of inner diameter of the chamber and beam quality. P_{ion} corrects for the ionization recombination. P_{ion} can be calculated using two sets of measurements one with the normal bias voltage and the other one with bias voltage reduced by half. P_{wall} correction is calculated using equation 3.7 for photon beams, when the chamber wall composition is different than the dosimetry phantom composition.

$$P_{wall} = \frac{\alpha(\bar{L}/\rho)^{wall}_{air}(\bar{\mu}_{en}/\rho)^{med}_{wall} + (1-\alpha)(\bar{L}/\rho)^{med}_{air}}{(\bar{L}/\rho)^{med}_{air}} \tag{3.7}$$

Where α is the fraction of the total ionization produced by electrons arising in the chamber wall, $(1-\alpha)$ is the fraction of the total ionization produced by electrons arising in the dosimetry phantom, $(\bar{\mu}_{en}/\rho)^{med}_{wall}$ is the ratio of mean mass energy absorption coefficient for the dosimetry phantom to that of the chamber wall for the user's photon beam. The users can find the values of $(\bar{\mu}_{en}/\rho)$ and $(\bar{L}/\rho)$ in TG-21 for different materials as a function of beam quality.

Absorbed dose to medium (D_{med}) must be converted to absorbed dose to water (D_{water}). D_{water} can be related to the D_{med} as follows:

$$D_{water} = (D_{med})(\bar{\mu}_{en}/\rho)^{water}_{med} \tag{3.8}$$

where $(\bar{\mu}_{en}/\rho)^{water}_{med}$ is the ratio of mean mass energy absorption coefficient for water to that of the user's phantom material.

In summary, clinics send their reference ionization chamber to a standards laboratory to be calibrated. The standards laboratory provides the clinic with N_X (and sometimes N_{gas}). The user calculates the N_{gas} and performs the measurement at their photon beam possibly using plastic phantoms. The user determines the absorbed dose to the plastic, applies the proper corrections and calculates the absorbed dose to water. The relative standard uncertainty on

the absorbed dose to water determined using TG-21 is estimated to be 1.5% [8]. TG-21 is a well established and common protocol, however as shown it requires complex calculations with many parameters involved. This increases the possibility of making mistakes in the clinic. Additionally, the TG-21 protocol is based on the exposure (air-kerma) standards which then needs to be converted into absorbed dose to water.

Another protocol that is based on air-kerma (or exposure) is the IAEA TRS-277 published in 1987 (first edition). It provided recommendations for the determination of absorbed dose to water for low-energy X-rays (tube potentials below 100 kV), medium-energy X-rays (above 100 kV), high-energy photon beams (energies above 0.66 MeV) and high-energy electron beams (energy ranges of 5-50 MeV) [9]. The principles behind the TRS-277 protocol are the same as those behind the TG-21 protocol, although the nomenclature used is different.

3.3.2 AAPM TG-51

The AAPM TG-51 is a protocol published in 1999 providing recommendations on determining absorbed dose to water for photon beams with energies between ^{60}Co gamma rays and 50 MV and electron beams with energies between 4-50 MeV [10]. TG-51 is based on standards of the absorbed dose to water and compared to TG-21, TG-51 is easier to implement. The formalism recommended in TG-51 for reference dosimetry of photon beams is outlined below.

Beam quality specifier

The percentage depth dose (PDD) at 10 cm depth in a water phantom due to photons only $\%dd(10)_X$, is used as the beam quality specifier for high-energy photon beams in TG-51. $\%dd(10)_X$ is defined for a 10 $\times$ 10 cm^2 field size at the phantom surface at source-to-surface distance (SSD) of 100 cm.

Absorbed dose to water

The users in the clinic send their reference ionization chamber and electrometer to standards laboratory. As explained in section 3.2.2, the standards laboratory provides the users with the $N_{D,w}^{Q}$ for their chamber. In the clinic, the absorbed dose to water D_w^Q (in Gy) per monitor unit is determined under reference conditions (at depth 10 cm in water with a 10 $\times$10 cm^2 field size at an SSD of 100 cm). The D_w^Q for the beam quality Q under reference conditions is determined as follows:

$$D_w^Q = M k_Q N_{D,w}^Q \tag{3.9}$$

where M is the chamber reading at the reference depth in water corrected for the influence quantities such as polarity, ion recombination, electrometer calibration effects and corrected to standard environmental conditions of temperature and pressure. k_Q is the beam quality conversion factor that corrects for the differences in the absorbed dose to water calibration factor between the user's beam quality Q and the beam quality for which the absorbed dose calibration coefficient applies. k_Q is chamber dependent and is provided in TG-51 as a function of beam quality.

In 2014, an addendum to TG-51 was published [11]. A new set of k_Q data was provided for high-energy photon beams. An uncertainty budget on determination of absorbed dose to water was also added.

3.3.3 IAEA TRS-398

The IAEA TRS-398 is a COP used for external beam radiotherapy dosimetry developed in 2000 by the IAEA, in collaboration with World Health Organization, Pan American Health Organization and European Society for Radiotherapy and Oncology [12]. The TRS-398 is based on standards of absorbed dose to water and is used for low-and medium-energy x-rays, ^{60}Co gamma-rays, high-energy photons, electrons, protons and heavy ions [13]. The TRS-398 is also based on standards of absorbed dose to water. The formalism for calibration of high-energy photon beams is summarized below.

Beam quality specifier

The tissue-phantom ratio $TPR_{20,10}$, is used as the beam quality specifier for high-energy photons beam in TRS-398. $TPR_{20,10}$ is the ratio of the absorbed doses at depths of 20 cm and 10 cm in a water phantom, measured with a constant SDD of 100 cm and a field size of 10 $\times$ 10 cm^2 at the plane of the ionization chamber. One advantage of using $TPR_{20,10}$ over %dd(10)$_X$ is that $TPR_{20,10}$ is independent of electron contamination (unwanted electrons in the beam due to the photon interactions in the beam accelerator head or in the phantom). The use of $TPR_{20,10}$ also avoids the systematic errors in positioning the chamber since the settings at both depths 10 and 20 cm will be affected in a similar way [12].

Absorbed dose to water

In the clinic, the absorbed dose to water ($D_{w,Q}$) at the reference depth (z_{ref}) in water for the beam of quality Q and in the absence of ionization chamber is determined using equation 3.10. This is similar to TG-51 (equation 3.9) but with slightly different notations:

$$D_{w,Q} = M_Q N_{D,w,Q_o} k_{Q,Q_0} \tag{3.10}$$

where M_Q is the reading of the chamber corrected for influence quantities, N_{D,w,Q_o} is the chamber calibration coefficient provided by the standards laboratory, k_{Q,Q_0} is a correction factor that takes into account the difference between the reference beam quality Q_0 and the user's beam quality Q. The k_{Q,Q_0} is unity if the ionization chamber is used in the same beam quality that is used during the calibration at the standards laboratory.

The k_{Q,Q_0} is defined as the ratio at the qualities Q and Q_0 of the calibration factors in terms of absorbed dose to water of the ionization chamber [12].

$$k_{Q,Q_0} = \frac{N_{D,w,Q}}{N_{D,w,Q_0}} = \frac{D_{w,Q}/M_Q}{D_{w,Q_0}/M_{Q_0}} \tag{3.11}$$

Preferably, the k_{Q,Q_0} should be directly measured for each chamber. However, when there is no available experimental data, the k_{Q,Q_0} can be determined theoretically using the Bragg–Gray theory. The theoretical expression for k_{Q,Q_0} is:

$$k_{Q,Q_0} = \frac{(s_{w,air})_Q (W_{air})_Q P_Q}{(s_{w,air})_{Q_0} (W_{air})_{Q_0} P_{Q_0}} \tag{3.12}$$

$$P_Q = P_{cav} P_{dis} P_{wall} P_{cel} \tag{3.13}$$

where, $s_{w,air}$ is the Spencer-Attix water to air stopping power ratios and the W_{air} is the mean energy expended in air per ion pair formed (this is the same W/e term introduced in TG-21 with a different notation). P_Q is the overall perturbation factor including the cavity correction (P_{cav}), the displacement correction (P_{dis}), the wall correction (P_{wall}) and the central electrode correction (P_{cel}) in beam qualities Q. P_{cav} accounts for the perturbation of the electron fluence due to scattering differences between the air cavity and the medium. P_{dis} corrects for the fact that a cylindrical chamber cavity with its centre at z_{ref} samples the electron fluence at a point which is closer to the radiation source than z_{ref}. P_{wall} accounts for differences in the photon mass energy absorption coefficients and electron stopping powers of the chamber

wall material and the medium. P_{cel} corrects for the lack of air equivalence of the central electrode [12]. The users can determine the values of each of these parameters using the equations and tables provided in TRS-398. Note that the change in W_{air} between calibration and users beam quality is often neglected, an assumption that is justified for high-energy photon and electron beams, but not for proton beams.

The difference between TG-51 and TRS-398 is that TG-51 is used mainly in North America while TRS-398 is used in the rest of the world, especially in Europe [13]. In TRS-398, $TPR_{20,10}$ is used as the beam quality specifier, however TG-51 recommends to use $\%dd(10)_X$ as the beam quality specifier. The two protocols also use slightly different notations. Although different beam quality specifiers are used in the two protocols, the k_Q or k_{Q,Q_0} values agree within $\pm 0.2\%$ for almost the entire range of clinical photon beam qualities for most chambers [13].

3.3.4 IAEA-AAPM TRS-483

The TRS-398 and TG-51 are widely used in reference dosimetry of conventional radiotherapy beams where the reference condition of 10×10 cm^2 field size at SSD of 100 cm is achievable on the machine. However, these protocols cannot be used for radiotherapy machines that use small and nonstandard fields (such as treatment machines using MLCs or LGK). The use of these machines can increase the uncertainty of clinical dosimetry. The IAEA-AAPM TRS-483 is a COP published in 2017 giving recommendations for reference and relative dosimetry of small static and nonstandard fields used for external beam photon radiotherapy of energies with nominal accelerating potential up to 10 MV [14]. In this section, first the concept of the *msr* introduced in the TRS-483 (initially introduced by Alfonso et al. [15]) is explained, followed by the equivalent square *msr* field size and beam quality specifier determination. Afterwards, the three approaches recommended in TRS-483 for reference dosimetry of high-energy photon beams are described.

The machine specific reference field (*msr*)

The *msr* field has dimensions as close as possible to the conventional reference field (10×10 cm^2). In some machines it is the maximum field size achievable on the machine. The *msr* field has to extend at least a distance r_{LCPE} beyond the outer boundaries of the reference ionization

chamber, or its FWHM has to satisfy the following condition [14]:

$$FWHM \geq 2r_{\mathrm{LCPE}} + d \tag{3.14}$$

where d is the greatest distance between two points on the outer boundary of detector. r_{LCPE} is the lateral charge particle equilibrium range. For example the *msr* field in LGK Perfexion is a 16 mm diameter collimator field . In the RefleXion BgRT machine, it is a 10×2 cm^2 or 10×3 cm^2 field size.

Equivalent square *msr* field size

The equivalent field is defined as the standard field that has the same depth dose characteristics (or scatter component) as the non-standard field [16]. If the *msr* field is not a standard WFF square field, then an equivalent square field size needs to be determined. The equivalent field determination is based on Clarkson's method [17]. Clarkson [17] and Meredith et al. [18] showed that the dose deposited at a point due to photons in a photon beam can be determined by integrating over a scatter function. The scatter function s is a function of radius r given by

$$s = \frac{SC(r)}{SC(\infty)} = 1 - e^{\lambda r} - \mu\lambda r e^{-\lambda r} \tag{3.15}$$

where μ=0.5 and λ=0.18 are parameters obtained by fitting the equation 3.15 to experimental data. $SC(r)$ is the scatter component of a circular field with radius r and $SC(\infty)$ is the scatter component of a circular field with infinite radius.

For WFF beams the integration over the scatter function becomes

$$SC_{field} = \frac{1}{2\pi} \iint_{\text{field area}} [\lambda(1-\mu)\frac{e^{-\lambda r}}{r} + \mu\lambda^2 e^{-\lambda r}] r \,\mathrm{d}r \,\mathrm{d}\theta \tag{3.16}$$

For FFF beams, the scatter for a given field size is smaller than in WFF beams due to the non-uniform lateral beam profile. This is taken into account by using a function $F(r)$ describing the radial dependence of the lateral beam profile. Therefore, equation 3.16 becomes

$$SC_{field} = \frac{1}{2\pi} \iint [\lambda(1-\mu)\frac{e^{-\lambda r}}{r} + \mu\lambda^2 e^{-\lambda r}] F(r) r \,\mathrm{d}r \,\mathrm{d}\theta \tag{3.17}$$

By equating the scatter component for the equivalent square field size and the scatter component for the non-standard field, the equivalent field size S can be determined. For

example, for a 10 × 2 cm^2 FFF field size, the equivalent field size S can be determined using the following condition (in Cartesian coordinate).

$$(SC_{field})_{\text{FFF } 10\times2\ cm^2} = (SC_{field})_{\text{WFF } S\times S\ cm^2} \tag{3.18}$$

$$\int_{-5}^{+5}\int_{-1}^{+1}[\lambda(1-\mu)\frac{e^{-\lambda\sqrt{x^2+y^2}}}{\sqrt{x^2+y^2}}+\mu\lambda^2 e^{-\lambda\sqrt{x^2+y^2}}]F(\sqrt{x^2+y^2})\,\mathrm{d}x\,\mathrm{d}y = \int_{-S/2}^{+S/2}\int_{-S/2}^{+S/2}[\lambda(1-\mu)\frac{e^{-\lambda\sqrt{x^2+y^2}}}{\sqrt{x^2+y^2}}+\mu\lambda^2 e^{-\lambda\sqrt{x^2+y^2}}]\,\mathrm{d}x\,\mathrm{d}y$$

Beam quality specifier

As explained in sections 3.3.3 and 3.3.2, the two beam quality specifiers for a 10 × 10 cm^2 reference field in high-energy photon beams are $TPR_{20,10}(10)$ and %dd(10)$_X$ (denoted as $\%dd(10,10)_X$ in TRS-483). For machines where the reference 10 × 10 cm^2 field size cannot be established, the users first measure the beam quality specifier for their machine's *msr* field, either the $TPR_{20,10}(S)$ or $\%dd(10,S)_X$. $TPR_{20,10}(S)$ is the tissue phantom ratio in water at the depths of 20 and 10 g/cm^2, for an equivalent field size of S × S cm^2 defined at an SDD of 100 cm. The $\%dd(10,S)_X$ is the percentage depth dose at 10 cm depth in a water phantom due to photons only for an equivalent square field size of S × S cm^2 at an SSD of 100 cm. The set-up to measure the $TPR_{20,10}(S)$ and $\%dd(10,S)$ are shown in figure 3.6a and 3.6b respectively.

After measuring the $TPR_{20,10}(S)$ or $\%dd(10,10)_S$, the equations 3.19 and 3.20 are used to derive the beam quality specifier for a hypothetical 10 × 10 cm^2 field size for the same machine as for the *msr* field ($TPR_{20,10}(10)$ or $\%dd(10,10)_X$) from $TPR_{20,10}(S)$ or $\%dd(10,S)$ respectively.

$$TPR_{20,10}(10) = \frac{TPR_{20,10}(S)+c(10-S)}{1+c(10-S)} \tag{3.19}$$

where c = (16.15 ± 0.12) × 10^{-3}, valid for $4 \le S \le 12$, S in cm,

$$\%dd(10,10) = \frac{\%dd(10,S)+80c(10-S)}{1+c(10-S)} \tag{3.20}$$

where c = (53.4 ± 1.1) × 10^{-3}, valid for $4 \le S \le 12$, S in cm.

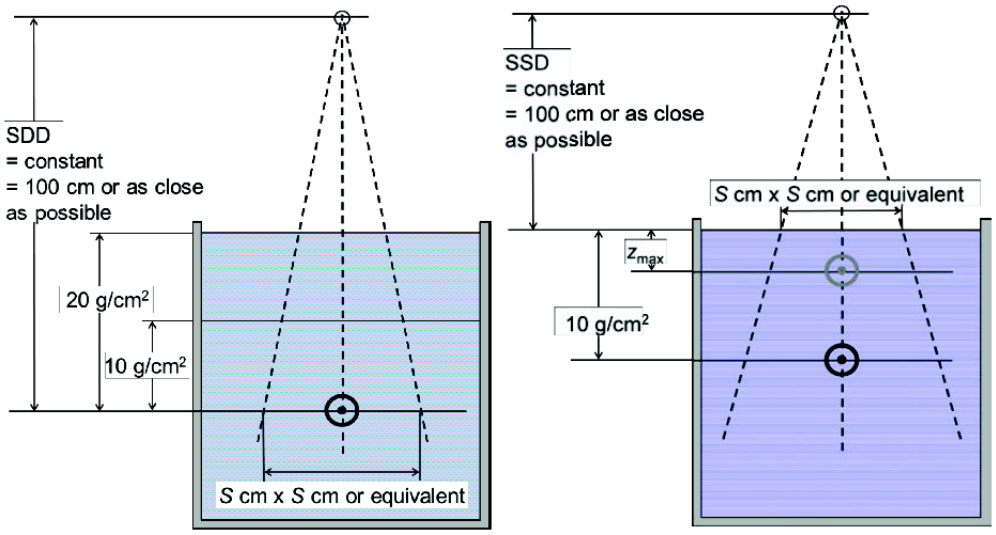

Figure 3.6 The measurement setup for determination of beam quality specifiers (a) $TPR_{20,10}(S)$ and (b) $\%dd(10,S)$. Adapted from Palmans et al. [14]

Equations 3.19 and 3.20 are based on previous studies by Palmans [19] and Sauer [20] where an analytical relationship was proposed between the beam quality specifier and field size. The measured beam quality specifier for different beam qualities were plotted as a function of field size. The proposed model was fitted to the measured data, resulting in equations 3.19 and 3.20.

Three approaches recommended in TRS-483 for reference dosimetry of high-energy photon beams

Three approaches for the calibration of *msr* fields have been formulated in the TRS-483:

1. **The ionization chamber is calibrated by the standards laboratory for the user's *msr* field:**

   The standards laboratory provides the user a calibration coefficient for an ionization chamber measured directly for the user's *msr* field. This is the preferred, as yet theoretical approach, as these calibrations are currently not available. The absorbed dose to water at the reference depth in the *msr* field in the absence of the ionization chamber ($D^{f_{\text{msr}}}_{\text{w},Q_{\text{msr}}}$) is determined by:

$$D^{f_{\text{msr}}}_{\text{w},Q_{\text{msr}}} = M^{f_{\text{msr}}}_{Q_{\text{msr}}} N^{f_{\text{msr}}}_{D,\text{w},Q_{\text{msr}}} \tag{3.21}$$

where $M_{Q_{\mathrm{msr}}}^{f_{\mathrm{msr}}}$ is the chamber reading in the *msr* field corrected for influences quantities. $N_{D,\mathrm{w},Q_{\mathrm{msr}}}^{f_{\mathrm{msr}}}$ is the calibration coefficient in terms of absorbed dose to water of the ionization chamber measured at the standards laboratory for the *msr* field f_{msr} of quality Q_{msr}. Therefore, there is no need for the beam quality correction factors.

2. **The ionization chamber is calibrated by the standards laboratory for a conventional reference field, with generic values of beam quality correction factors available:**

   This is the most common approach. The standards laboratory provides the user a calibration coefficient in terms of absorbed dose to water ($N_{D,\mathrm{w},Q_0}^{f_{\mathrm{ref}}}$) of the ionization chamber measured for the beam quality Q_0 (usually ^{60}Co) for a conventional 10×10 cm^2 reference field (f_{ref}). The absorbed dose to water for the *msr* field and beam quality Q_{msr} ($D_{\mathrm{w},Q_{\mathrm{msr}}}^{f_{\mathrm{msr}}}$) is determined by:

$$D_{\mathrm{w},Q_{\mathrm{msr}}}^{f_{\mathrm{msr}}} = M_{Q_{\mathrm{msr}}}^{f_{\mathrm{msr}}} N_{D,\mathrm{w},Q_0}^{f_{\mathrm{ref}}} k_{Q_{\mathrm{msr}},Q_0}^{f_{\mathrm{msr}},f_{\mathrm{ref}}} \tag{3.22}$$

   where the $M_{Q_{\mathrm{msr}}}^{f_{\mathrm{msr}}}$ is the chamber reading corrected for influence quantities in the *msr* field and beam quality Q_{msr}. The beam quality conversion factor $k_{Q_{\mathrm{msr}},Q_0}^{f_{\mathrm{msr}},f_{\mathrm{ref}}}$ is used to correct for the differences between the response of the chamber in the conventional reference calibration field f_{ref} with beam quality Q_0 at the standards laboratory and the response of the chamber in the user's *msr* field f_{msr} with beam quality Q_{msr}. The $k_{Q_{\mathrm{msr}},Q_0}^{f_{\mathrm{msr}},f_{\mathrm{ref}}}$ can be determined experimentally or by using MC simulations. For example, the data for LGK for a few types of ionization chambers are tabulated in TRS-483. This approach is used when the $k_{Q_{\mathrm{msr}},Q_0}^{f_{\mathrm{msr}},f_{\mathrm{ref}}}$ factors for the ionization chambers and beam qualities are available.

3. **The ionization chamber is calibrated by the standards laboratory for a conventional reference field without generic values of beam quality correction factors available**

   This approach is used when the $k_{Q_{\mathrm{msr}},Q_0}^{f_{\mathrm{msr}},f_{\mathrm{ref}}}$ factors are not available. The absorbed dose to water for the *msr* field and beam quality Q_{msr} ($D_{\mathrm{w},Q_{\mathrm{msr}}}^{f_{\mathrm{msr}}}$) is given by:

$$D_{\mathrm{w},Q_{\mathrm{msr}}}^{f_{\mathrm{msr}}} = M_{Q_{\mathrm{msr}}}^{f_{\mathrm{msr}}} N_{D,\mathrm{w},Q_0}^{f_{\mathrm{ref}}} k_{Q,Q_0}^{f_{\mathrm{ref}}} k_{Q_{\mathrm{msr}},Q}^{f_{\mathrm{msr}},f_{\mathrm{ref}}} \tag{3.23}$$

where $M_{Q_{\text{msr}}}^{f_{\text{msr}}}$ is the chamber reading corrected for influences quantities in the *msr* field and beam quality Q_{msr}. $N_{D,\text{w},Q_0}^{f_{\text{ref}}}$ is the calibration coefficient in terms of absorbed dose to water of the ionization chamber measured for the beam quality Q_0 for a conventional 10×10 cm^2 reference field (f_{ref}) at the standards laboratory.

The $k_{Q,Q_0}^{f_{\text{ref}}}$ correction corrects for the difference between the response of the ionization chamber in the conventional 10×10 cm^2 reference field (f_{ref}) with a beam quality Q_0 at standards laboratory and the response of the ionization chamber in a conventional 10×10 cm^2 reference field f_{ref} with a beam quality Q using the same machine as the *msr* field f_{msr} (Q is the beam quality of the user beam if the machine could produce a 10×10 cm^2 field size). Knowing the beam quality specifier for the hypothetical 10×10 cm^2 field ($TPR_{20,10}(10)$ or $\%dd(10,10)_X$), the $k_{Q,Q_0}^{f_{\text{ref}}}$ for the user's chamber can be looked up from the tabulated values in TRS-483, TG-51 or TRS-398.

The $k_{Q_{\text{msr}},Q}^{f_{\text{msr}},f_{\text{ref}}}$ correction factor corrects for the difference between the response of the ionization chamber in a conventional 10×10 cm^2 reference field with beam quality Q at the same machine as the *msr* field and the response of the ionization chamber in the *msr* field with beam quality Q_{msr}. $k_{Q_{\text{msr}},Q}^{f_{\text{msr}},f_{\text{ref}}}$ is assumed to be unity in TRS-483 for most detectors recommended in TRS-483.

However, to apply this approach to FFF beams, the values for $k_{Q,Q_0}^{f_{\text{ref}}}$ may be different from the values reported in the existing protocols such as TG-51 or TRS-398. Therefore, the $k_{Q,Q_0}^{f_{\text{ref}}}$ is replaced by the product of two factors. For a FFF beam, the absorbed dose to water for the *msr* field and beam quality $Q_{\text{msr}}^{\text{FFF}}$ ($D_{\text{w},Q_{\text{msr}}^{\text{FFF}}}^{f_{\text{msr}}}$) is given by:

$$D_{\text{w},Q_{\text{msr}}^{\text{FFF}}}^{f_{\text{msr}}} = M_{Q_{\text{msr}}^{\text{FFF}}}^{f_{\text{msr}}} N_{D,\text{w},Q_0}^{f_{\text{ref}}} k_{Q^{\text{WFF}},Q_0}^{f_{\text{ref}}} k_{Q^{\text{FFF}},Q^{\text{WFF}}}^{f_{\text{ref}}} k_{Q_{\text{msr}}^{\text{FFF}},Q^{\text{FFF}}}^{f_{\text{msr}},f_{\text{ref}}} \tag{3.24}$$

where, $M_{Q_{\text{msr}}^{\text{FFF}}}^{f_{\text{msr}}}$ is the chamber reading corrected for influence quantities in the *msr* field and beam quality $Q_{\text{msr}}^{\text{FFF}}$. $N_{D,\text{w},Q_0}^{f_{\text{ref}}}$ is the absorbed dose to water calibration coefficient of the ionization chamber measured at the standards laboratory for a conventional 10×10 cm^2 reference field in beam quality Q_0. The $k_{Q^{\text{WFF}},Q_0}^{f_{\text{ref}}}$ is the beam quality correction factor obtained from TRS-398 or TG-51 for a WFF beam with the same beam quality specifier as the one determined for FFF beam. The $k_{Q^{\text{FFF}},Q^{\text{WFF}}}^{f_{\text{ref}}}$ factor takes into account the difference in response of the ionization chamber between WFF and FFF beams. The $k_{Q_{\text{msr}}^{\text{FFF}},Q^{\text{FFF}}}^{f_{\text{msr}},f_{\text{ref}}}$ corrects for the different response of the ionization chamber in a hypothetical

10×10 cm^2 field with beam quality Q^{FFF} using the same machine as *msr* field and the response of the ionization chamber in the *msr* field with beam quality $Q^{\text{FFF}}_{\text{msr}}$.

Bibliography

[1] McCaffrey JP, Downton B, Shen H, Niven D, McEwen M. Pre-irradiation effects on ionization chambers used in radiation therapy. *Physics in Medicine & Biology,* 50(13), N121, 2005.

[2] Izewska JO, Rajan G. Radiation dosimeters. Radiation oncology physics: a handbook for teachers and students. *Vienna, International Atomic Energy Agency,* 71–99, 2005.

[3] Andreo P, Nahum A. Absolute dose determination under reference conditions. Handbook of Radiotherapy Physics-Theory and Practice ed P Mayles, JC Rosenwald and AE Nahum. *(New York and London: Taylor Francis),* 333-365, 2007.

[4] Seuntjens J, Duane S. Photon absorbed dose standards. *Metrologia,* 46(2), S39, 2009.

[5] Boutillon M, Perroche AM. Ionometric determination of absorbed dose to water for cobalt-60 gamma rays. *Physics in Medicine & Biology*, 38(3), 439–454, 1993.

[6] Podgorsak EB. Radiation oncology physics: A handbook for teachers and students. *Vienna: International Atomic Energy Agency,* 2005.

[7] AAPM Task Group 21, Radiation Therapy Committee. A protocol for the determination of absorbed dose from high-energy photon and electron beams. *Medical Physics*, 10(6): 741–771, 1983.

[8] Huq MS, Andreo P. Reference dosimetry in clinical high-energy photon beams: Comparison of the AAPM TG-51 and AAPM TG-21 dosimetry protocols. *Medical physics*, 28(1), 46–54, 2001.

[9] TRS-277 : Absorbed dose determination in photon and electron beams. An international Code of Practice. *International Atomic Energy Agency*, 1997.

[10] Almond PR, Biggs PJ, Coursey BM, Hanson WF, Huq MS, Nath R, Rogers DW. AAPM's TG-51 protocol for clinical reference dosimetry of high-energy photon and electron beams. *Medical physics*, 26(9):1847–1870, 1999.

[11] McEwen M, DeWerd L, Ibbott G, Followill D, Rogers DW, Seltzer S, Seuntjens J. Addendum to the AAPMs TG-51 protocol for clinical reference dosimetry of high-energy photon beam. *Medical physics*, 41(4), 2014.

[12] Andreo P, Burns DT, Hohlfeld K, Huq MS, Kanai T, Laitano F, Smyth V, Vynckier S. TRS-398: Absorbed dose determination in external beam radiotherapy: an international code of practice for dosimetry based on standards of absorbed dose to water. *International Atomic Energy Agency*, 2000.

[13] Huq MS, Andreo P, Song H. Comparison of the IAEA TRS-398 and AAPM TG-51 absorbed dose to water protocols in the dosimetry of high-energy photon and electron beams. *Physics in Medicine & Biology*, 46(11), 2985, 2001.

[14] Palmans H, Andreo P, Christaki K, Huq MS, Seuntjens J. TRS-483: Dosimetry of small static fields used in external beam radiotherapy: an international code of practice for reference and relative dose determination. *International Atomic Energy Agency, Vienna*, 2017.

[15] Alfonso R, Andreo P, Capote R, Huq MS, Kilby W, Kjäll P, Mackie TR, Palmans H, Rosser K, Seuntjens J, Ullrich W. A new formalism for reference dosimetry of small and nonstandard fields. *Medical physics*, 35(11), 5179–5186, 2008.

[16] Burns JE. BJR Supplement 25: Central axis depth dose data for use in radiotherapy. *British Institute of Radiology, London: England*, 1996.

[17] Clarkson JR. A note on depth doses in fields of irregular shape. *The British Institute of Radiology*, 14(164), 265–268, 1941.

[18] Meredith WJ, Neary GJ. The production of isodose curves and the calculation of energy absorption from standard depth dose data. *The British Journal of Radiology*, 17(195), 75–82, 1944.

[19] Palmans H. Determination of the beam quality index of high-energy photon beams under nonstandard reference conditions. *Medical physics*, 39(9), 5513–5519, 2012.

[20] Sauer OA. Determination of the quality index for photon beams at arbitrary field sizes. *Medical physics*, 36(9Part1), 4168–4172, 2009.

Chapter 4

Determination of $k_{Q_{\mathbf{msr}},Q_{\mathbf{0}}}^{f_{\mathbf{msr}},f_{\mathbf{ref}}}$ factors for ion chambers used in the calibration of Leksell Gamma Knife Perfexion model using EGSnrc and PENELOPE Monte Carlo codes

Lalageh Mirzakhanian[a)], Hamza Benmakhlouf, Frederic Tessier and Jan Seuntjens

Published in: Medical physics 45.4 (2018): 1748-1757 (Editor's Choice).

4.1 Preface

The first goal of this thesis was to provide the data for reference dosimetry of LGK for different ionization chamber types, phantom materials and orientation of chambers. In this paper, the beam source, ionization chambers and phantoms were modeled in MC. Afterwards, the $k_{Q_{\mathrm{msr}},Q_0}^{f_{\mathrm{msr}},f_{\mathrm{ref}}}$ values were calculated for each ionization chambers and phantom materials in MC. The influence of two MC codes (EGSnrc and PENELOPE), ionization chamber type, chamber orientation and phantom electron density on $k_{Q_{\mathrm{msr}},Q_0}^{f_{\mathrm{msr}},f_{\mathrm{ref}}}$ was also studied.

Abstract

Purpose: To calculate the $k_{Q_{msr},Q_0}^{f_{msr},f_{ref}}$ factors for nine common ionization chamber types following the small fields dosimetry formalism for the calibration of the Leksell Gamma Knife®(LGK) Perfexion™ using Monte Carlo simulation. This study also provides the first independent comparison of EGSnrc and PENELOPE for the calculation of $k_{Q_{msr},Q_0}^{f_{msr},f_{ref}}$ correction factors and proposes a practical method to predict these factors based on chamber type, chamber orientation and phantom electron density.

Methods: The ionization chambers are modeled using the EGSnrc and PENELOPE Monte Carlo codes based on the blueprints provided by the manufacturers. The chambers are placed in a half-sphere water phantom and five spherical phantoms made of liquid water, solid water, ABS, polystyrene and PMMA, respectively. Dose averaged over the air cavity of the chambers and a small water volume are calculated using EGSnrc and PENELOPE Monte Carlo codes for both conventional and machine specific reference (*msr*) set-ups. Using the calculated dose-ratio, the $k_{Q_{msr},Q_0}^{f_{msr},f_{ref}}$ factor is determined for all phantom materials and two possible orientations of chamber. The calculated $k_{Q_{msr},Q_0}^{f_{msr},f_{ref}}$ factors are compared to a previous Monte Carlo study [1, 2]. A relationship between the $k_{Q_{msr},Q_0}^{f_{msr},f_{ref}}$ factor and the electron density of the phantom material is derived to predict the $k_{Q_{msr},Q_0}^{f_{msr},f_{ref}}$ factor for any phantom material type. Applying the calculated $k_{Q_{msr},Q_0}^{f_{msr},f_{ref}}$ factors to the measured dose-rate of a recent round robin study [3] improves consistency of reference dosimetry of the Leksell Gamma Knife®(LGK) Perfexion™.

Results: Agreement within uncertainty is observed between $k_{Q_{msr},Q_0}^{f_{msr},f_{ref}}$ values determined in this study and the previous PEGASOS/PENELOPE study [1, 2] in a liquid water phantom. The difference between $k_{Q_{msr},Q_0}^{f_{msr},f_{ref}}$ values in parallel and perpendicular detector orientations is most significant for the PTW 31010 (1.8%) chamber. The percentage root-mean-square (%RMS) deviation between EGSnrc and PENELOPE calculated $k_{Q_{msr},Q_0}^{f_{msr},f_{ref}}$ values for Exradin-A1SL, A14 and A14SL chambers studies in this work was found to be 0.4%. The $k_{Q_{msr},Q_0}^{f_{msr},f_{ref}}$ values increase linearly with electron density of the phantom material for all chamber types mainly due to the linear dependency of photon energy fluence ratios on electron density. The average percentage difference between the calculated and predicted $k_{Q_{msr},Q_0}^{f_{msr},f_{ref}}$ values using two methods is found to be 0.15% and 0.16%. Previously measured dose-rates corrected with the $k_{Q_{msr},Q_0}^{f_{msr},f_{ref}}$ values determined in this work leads to absorbed dose values consistent to within 0.8%.

Conclusions: The calculated $k_{Q_{msr},Q_0}^{f_{msr},f_{ref}}$ values in this work will enable users to apply the appropriate correction for their own specific phantom material only knowing the electron density of the phantom material.

Key words: Leksell Gamma Knife perfexion, calibration, Monte Carlo, $k_{Q_{msr},Q_0}^{f_{msr},f_{ref}}$

4.2 Introduction

In recent years, the use of small and nonstandard fields in radiotherapy such as those used in Stereotactic Radiosurgery (Leksell Gamma Knife, CyberKnife and TomoTherapy) has increased significantly enabling a more precise delivery of radiation to the tumor volume while minimizing the exposure to the healthy tissue. Despite the superior dose conformity, dosimetry of these specialized machines is challenging leading to dosimetric errors mainly due to the beam and detector dependent complications [4]. Standardized recommendations have been developed on reference and relative dosimetry of small and nonstandard fields by the International Atomic Energy Agency (IAEA) [5] in cooperation with the American Association of Physicists in Medicine (AAPM) guided by a new dosimetry formalism introduced by Alfonso et al. [6] In this formalism, a new machine specific reference field (*msr*) is introduced for modalities that cannot establish conventional reference conditions. The *msr* field is a calibration field of size as close as possible to the conventional reference field. This formalism relates the calibration coefficient under reference conditions to the calibration coefficient under *msr* conditions using a factor $k_{Q_{msr},Q_0}^{f_{msr},f_{ref}}$ that corrects for the difference between the conditions of field size, geometry, phantom material, and beam quality of the conventional reference field and the *msr* field (reference dosimetry).

The LGK Perfexion^{TM} is an accurate radiosurgical device delivering small radiation fields in which an array of 192 ^{60}Co sources is arranged in a cone section configuration [7]. The nominal collimator field sizes available in LGK Perfexion^{TM} are 4, 8 and 16 mm. The *msr* field consists of all 192 sources emitting radiation all with the maximum achievable field sizes of 16 mm.

Only few published studies on reference dosimetry of LGK Perfexion^{TM} unit exist where the small fields formalism introduced by Alfonso et al. [6] is applied [1, 2, 8]. Johansson et al. [1] reported the $k_{Q_{msr},Q_0}^{f_{msr},f_{ref}}$ values for seven chamber types in three phantom materials using `PEGASOS` (a Monte Carlo system based on `PENELOPE`) in LGK unit. These corrections were applied in a Round Robin study [3] for two chambers and three phantoms. However,

these corrections were not calculated and verified for all possible phantom materials, chamber types and orientations. Therefore, there is a clear need for determining $k_{Q_{msr},Q_0}^{f_{msr},f_{ref}}$ factors for the potentially suitable ionization chambers and common phantoms in the calibration of LGK Perfexion^{TM} unit.

A second problem with Gamma Knife dosimetry is that measurements in water are uncommon since water phantoms are not supplied by the manufacturer. Plastic phantoms have been used routinely for reference dosimetry purposes. Plastic phantoms suffer from non-homogeneous density, possible air gaps between chamber and phantom material and the density and composition of a specific phantom may deviate from the nominal values.

The goal of this study is to derive the $k_{Q_{msr},Q_0}^{f_{msr},f_{ref}}$ factor introduced by Alfonso et al. [6] for nine common chamber types and six phantom materials used in the calibration of LGK Perfexion^{TM} model. This study provides the first independent comparison of `EGSnrc` and `PENELOPE` based $k_{Q_{msr},Q_0}^{f_{msr},f_{ref}}$ factors for the LGK Perfexion^{TM} and provides a method to predict these factors based on chamber type, chamber orientation, and phantom material.

4.3 Materials and Methods

4.3.1 Simulation set-up and parameters

Nine chamber types including Exradin-A1SL, A14SL, A14, A16, IBA-CC04, CC01, PTW 31010, 31014 and 31016 were modeled in the egs++ geometry package [9] of `EGSnrc` [10, 11] Monte Carlo code using the blueprints provided by the manufacturers. Exradin-A1SL, A14 and A14SL were also simulated using the `PENELOPE` code [12]. The characteristics of the chambers are given in table 4.1. These chambers are potentially suitable and recommended for reference dosimetry of the LGK [1, 2].

For the reference condition calculations, a $30\times30\times30$ cm^3 water phantom is modeled in `EGSnrc` and `PENELOPE`. The centroid of collecting volume of the chamber is positioned at 5 cm depth in water. The symmetry axis of the chamber is perpendicular to the ^{60}Co beam axis. The ^{60}Co beam is modeled using a previously tabulated spectrum [13]. The source is a point source collimated into a 10×10 cm^2 field size at the surface of the phantom with the Source Surface Distance (SSD) of 100 cm. For validation purposes the calculation for Exradin A1SL in reference condition was repeated using the phase space files of the ^{60}Co radiation unit used

Table 4.1 Chambers specifications used in this study.

Chamber type	Sensitive volume (cm^3)	Cavity length (mm)	Cavity radius (mm)	Electrode material
Exradin A1SL[a]	0.057	5.7	2.1	C-552
Exradin A14SL[a]	0.016	2.1	2.1	C-552
Exradin A14[a]	0.016	2.0	2.0	C-552
Exradin A16[b]	0.007	1.7	1.2	C-552
IBA CC04[b]	0.040	3.6	2.0	C-552
IBA CC01[b]	0.010	3.6	1.0	Steel
PTW 31010[b]	0.125	6.5	2.8	Aluminum
PTW 31014[b]	0.015	5.0	1.0	Aluminum
PTW 31016[b]	0.016	2.9	1.45	Aluminum

[a]Chambers modeled in both codes: `EGSnrc` and `PENELOPE`.
[b]Chambers modeled in `EGSnrc`.

by the secondary standard dosimetry laboratory at The Swedish Radiation Safety Authority (SSM) in Stockholm [14].

For the calculations with the *msr* field, the previously generated LGK Perfexion^{TM} phase space file [1] for *msr* field (16 mm size) is used as input radiation source in this study. The half-sphere water phantom designed by Drzymala et al. [15], the solid water LGK Dosimetry Phantom [16] and the Elekta acrylonitrile butadiene styrene (ABS) phantom used frequently in the calibration of LGK Perfexion^{TM} model were simulated in `EGSnrc` and `PENELOPE` Monte Carlo codes. The half-sphere water phantom is a hemispherical dome atop a 16-cm cylinder enclosed in a 2 mm thick urethane plastic shell [15]. The half-sphere water phantom was modeled in detail using the specifications provided in Drzymala et al. [15] study. The solid water and ABS were modeled as 16-cm diameter spheres made of solid water and ABS respectively. Polystyrene has an average atomic number and average mass density close to ABS. In some studies, because of the lack of information on Elekta ABS phantom, ABS phantom is treated to be made of Polystyrene instead of ABS [17, 18]. In our study, in addition to ABS phantom, the polystyrene phantom was modeled as a 16 cm diameter sphere made of polystyrene. For comparison purposes, a 16 cm diameter sphere made of liquid water termed the "theoretical liquid water phantom" was modeled as well. Moreover in order to provide $k_{Q_{msr},Q_0}^{f_{msr},f_{ref}}$ over a wider range of electron density, a 16 cm diameter spherical phantom made of

polymethylmetacrylate (PMMA) was also simulated in EGSnrc. In the Monte Carlo calculation of this study, phantoms were considered to be ideally homogeneous without any air gaps. The mounting frames in solid water and ABS phantoms were not modeled in this study.

The centroid of the chamber is placed at the center of each phantom. In the liquid water, ABS, polystyrene and PMMA phantoms, the calculations were performed for two possible orientations of chambers with the chamber stem positioned parallel figure 4.1(a) and perpendicular figure 4.1(b) to the symmetry axis of the collimator block (z-axis shown in figure 4.1). In the half-sphere water phantom and solid water phantom, the chamber stem was placed only parallel to the z-axis.

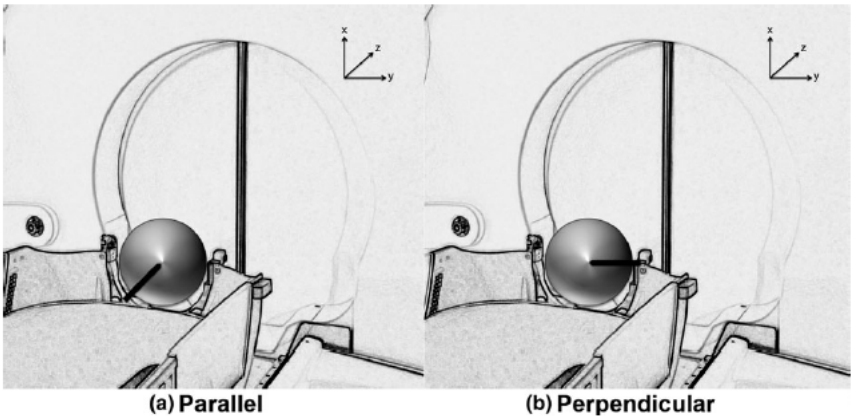

Figure 4.1 A schematic drawing of the chamber orientations, (a) parallel to the symmetry axis of the collimator block (z-axis) (b) perpendicular to the z-axis

The mass density of ABS is not well defined. However, Novotny Jr et al. [18] showed that the ABS phantom mass density can vary between 1.046 and 1.102 g/cm^3. For the solid water phantoms used, a certification document by the manufacturer does detail the composition for each specific phantom material used in the clinic. The specifications for ABS and solid water used in this study were taken from the Johansson et al. [1] study. The nominal electron densities for solid water, ABS, polystyrene and PMMA relative to water were taken as 1.0142, 1.0104, 1.0267 and 1.1563 respectively. For solid water and ABS, the density correction in EGSnrc were taken from estar NIST data [19].

The electron transport cut off energy (Global ECUT) and photon transport cut off energy (Global PCUT) in EGSnrc were set to 521 keV (including electron rest mass) and 10 keV respectively. The production thresholds for electrons (AE) is set to 521 keV and for photons (AP) is set to 10 keV.

Photon cross section enhancement (XCSE) was used as the variance reduction technique in EGSnrc/egs_chamber. The photon cross section is enhanced by a XCSE factor of 256 within a 1 cm cylindrical water shell surrounding the chamber to save computational time. Except for the use of XCOM photon cross section, default transport parameters were used in EGSnrc.

In PENELOPE/penEasy, the cutoff energy is set to 1 and 10 keV, for uncharged and charged particles, respectively in the *msr* set-up. For the reference set-up, the cutoff energy for photons is also set to 1 keV whereas it is made zone-dependent for charged particles. The cutoff energy is set to 10 keV for all charged particles inside a region of interest (ROI) (which includes the detector and 2 cm of its surroundings) and 200 keV outside the ROI. The elastic scattering parameters, C1 and C2, are both set to the conventional value of 0.1. The inelastic collision parameters, WCC and WCR, are set to equal the cutoff energies for charged and uncharged particles, respectively.

The EGSnrc calculations were carried out on Briaree and Guillimin clusters of Calcul Quebec operated under the Compute Canada Consortium. The computing time on one single CPU was between 88 and 2534 h for the reference setup and 9 and 226 h for the *msr* setup. In both setups reference and *msr*, the computations time was smallest for Exradin A1SL and largest for IBA CC01. Depending on the geometry in EGSnrc, the number of histories varied between 10^9 - 4×10^{10} in the reference setup and 3×10^7-2×10^9 in the *msr* setup.

In PENELOPE/penEasy, the simulations of reference setup is sped up by implementing conventional variance reduction techniques: interaction forcing, particle splitting and Russian roulette. Interaction forcing, with a factor of 100, is implemented for all particles inside the ionization chamber air cavity. Particle splitting, with a factor of 20, is implemented for all particles entering the ROI and Russian roulette, with a survival probability of 1/20, is implemented for particles coming out of the ROI.

4.3.2 Calculation of $k_{Q_{\mathbf{msr}},Q_{\mathbf{0}}}^{f_{\mathbf{msr}},f_{\mathbf{ref}}}$

The absorbed dose to water in the *msr* field $D_{w,Q_{\mathrm{msr}}}^{f_{\mathrm{msr}}}$ is determined using equation 4.1.

$$D_{w,Q_{\mathrm{msr}}}^{f_{\mathrm{msr}}} = M_{Q_{\mathrm{msr}}}^{f_{\mathrm{msr}}} N_{D,w,Q_0}^{f_{\mathrm{ref}}} k_{Q_{\mathrm{msr}},Q_0}^{f_{\mathrm{msr}},f_{\mathrm{ref}}} \tag{4.1}$$

Where $M_{Q_{\mathrm{msr}}}^{f_{\mathrm{msr}}}$ is the chamber reading corrected for the influence quantities including temperature, pressure, polarity effects, ion collection efficiency and electrometer accuracy in the *msr* field; $N_{D,w,Q_0}^{f_{\mathrm{ref}}}$ is the calibration coefficient at the standards laboratory; $k_{Q_{\mathrm{msr}},Q_0}^{f_{\mathrm{msr}},f_{\mathrm{ref}}}$ is a factor that

corrects for the differences between the conditions of field size, geometry, phantom material, and beam quality of the conventional reference field (f_{ref}) with calibration beam quality Q_0 and the machine-specific reference field (f_{msr}) with beam quality Q_{msr}. The definition equation of $k^{f_{msr},f_{ref}}_{Q_{msr},Q_0}$ is given by:

$$k^{f_{msr},f_{ref}}_{Q_{msr},Q_0} = \frac{D^{f_{msr}}_{w,Q_{msr}}/M^{f_{msr}}_{\text{plastic},Q_{msr}}}{D^{f_{ref}}_{w,Q_0}/M^{f_{ref}}_{w,Q_0}}, \tag{4.2}$$

where $D^{f_{ref}}_{w,Q_0}$ and $D^{f_{msr}}_{w,Q_{msr}}$ are the mean absorbed dose to water over a small volume in reference and *msr* fields, respectively. The $M^{f_{ref}}_{w,Q_0}$ and $M^{f_{msr}}_{\text{plastic},Q_{msr}}$ are the chamber readings in the reference and *msr* fields, respectively, both corrected for influence quantities. Note that the Eq. 4.2 includes the effect of the plastic phantom on the correction factor, also known as the phantom-dose conversion factor introduced by Seuntjens et al. [20] In Monte Carlo calculations, the chamber reading is assumed to be proportional to the mean absorbed dose to the air cavity of the ionization chamber. Therefore, equation 4.2 can be estimated by:

$$k^{f_{msr},f_{ref}}_{Q_{msr},Q_0} \approx \frac{D^{f_{msr}}_{w,Q_{msr}}/D^{f_{msr}}_{det,\text{plastic},Q_{msr}}}{D^{f_{ref}}_{w,Q_0}/D^{f_{ref}}_{det,w,Q_0}} \tag{4.3}$$

where $D^{f_{ref}}_{det,w,Q_0}$ and $D^{f_{msr}}_{det,\text{plastic},Q_{msr}}$ represent the mean absorbed dose to the air cavity of the ionization chamber in reference and *msr* fields respectively.

The effect of the plastic phantom can be uncoupled from a correction factor that would apply to water as phantom material as follows:

$$k^{f_{msr},f_{ref}}_{Q_{msr},Q_0} = \frac{D^{f_{msr}}_{w,Q_{msr}}/M^{f_{msr}}_{w,Q_{msr}}}{D^{f_{ref}}_{w,Q_0}/M^{f_{ref}}_{w,Q_0}} \left[\frac{M^{f_{msr}}_{w,Q_{msr}}}{M^{f_{msr}}_{\text{plastic},Q_{msr}}}\right], \tag{4.4}$$

where $M^{f_{msr}}_{w,Q_{msr}}$ is the chamber reading corrected for the influence quantities in the *msr* field in liquid water. The term on the right side of equation 4.4 outside the bracket can be defined as $k^{'f_{msr},f_{ref}}_{Q_{msr},Q_0}$ and that corrects for the differences between the conditions of field size, geometry, and beam quality. The term in square brackets is the phantom-dose conversion factor $k^{w,\text{plastic}}_{Q_{msr}}$ that corrects for the phantom material [20]. With this, equation 4.4 can be expressed as follows:

$$k^{f_{msr},f_{ref}}_{Q_{msr},Q_0} = k^{'f_{msr},f_{ref}}_{Q_{msr},Q_0} k^{w,\text{plastic}}_{Q_{msr}} \tag{4.5}$$

Assuming that the chamber reading is proportional to the absorbed dose in the detector, $k'^{f_{msr},f_{ref}}_{Q_{msr},Q_0}$ and $k^{w,plastic}_{Q_{msr}}$ can be estimated as follow:

$$k'^{f_{msr},f_{ref}}_{Q_{msr},Q_0} \approx \frac{D^{f_{msr}}_{w,Q_{msr}}/D^{f_{msr}}_{det,w,Q_{msr}}}{D^{f_{ref}}_{w,Q_0}/D^{f_{ref}}_{det,w,Q_0}} \tag{4.6}$$

$$k^{w,plastic}_{Q_{msr}} \approx \frac{D^{f_{msr}}_{det,w,Q_{msr}}}{D^{f_{msr}}_{det,plastic,Q_{msr}}} \tag{4.7}$$

$D^{f_{msr}}_{det,w,Q_{msr}}$ is the mean absorbed dose to the air cavity of ionization chamber in *msr* field in water. In this study, scaling of the depth as explained in Seuntjens et al. [20] is not considered since the measurement in solid water/ABS phantom is always performed at the center of the 8 cm radius phantom for LGK Perfexion^{TM} unit. The mean absorbed dose to the air cavity of chamber is calculated using `EGSnrc egs_chamber` [21] and `PENELOPE penEasy` user-codes for the reference setup ($D^{f_{ref}}_{det,w,Q_0}$). For the *msr* setup, the mean absorbed dose to the air cavity of chamber is also calculated for all phantoms: liquid water ($D^{f_{msr}}_{det,w,Q_{msr}}$) and plastic: solid water, ABS, polystyrene and PMMA ($D^{f_{msr}}_{det,plastic,Q_{msr}}$).

Absorbed dose at the position of the centre of the chamber in absence of the chamber was calculated by scoring in a 3 mm diameter sphere in both setups independently ($D^{f_{ref}}_{w,Q_0}$ for reference setup and $D^{f_{msr}}_{w,Q_{msr}}$ for *msr* setup). This scoring diameter was found to be adequate to represent the dose at a point. Using equations 4.3, 4.6, 4.7 the mentioned calculated quantities, $k^{f_{msr},f_{ref}}_{Q_{msr},Q_0}$, $k'^{f_{msr},f_{ref}}_{Q_{msr},Q_0}$, and $k^{w,plastic}_{Q_{msr}}$ were determined, respectively.

4.3.3 Calculation of perturbation factors in *msr* setup

To understand the origin of the differences between the $k^{f_{msr},f_{ref}}_{Q_{msr},Q_0}$ factors calculated in parallel and perpendicular orientations, the perturbation of each component of the chambers is calculated in the *msr* setup. The calculation is performed for one chamber PTW 31010 for both parallel and perpendicular orientations using `EGSnrc`. The perturbation effect of each component of the PTW 31010 including stem, wall, electrode and sensitive volume of the cavity was calculated for the *msr* setup using a similar methodology as in Bouchard et al. [22] Each detector material component was replaced gradually by the phantom material in our case ABS material, starting from the outermost layer down to the sensitive volume of chamber. The perturbation of each component layer is calculated as follow:

$$P_{stem} = \frac{D_{\text{without stem}}}{D} \tag{4.8}$$

$$P_{wall} = \frac{D_{\text{without stem and wall}}}{D_{\text{without stem}}} \tag{4.9}$$

$$P_{electrode} = \frac{D_{\text{without stem, wall and electrode}}}{D_{\text{without stem and wall}}} \tag{4.10}$$

$$P_{cavity} = \frac{D_{\text{plastic, point}}}{D_{\text{without stem, wall and electrode}}} \tag{4.11}$$

where D is the absorbed dose in the sensitive volume of air in the fully modeled chamber, $D_{\text{without stem}}$ is the absorbed dose in the sensitive volume of air with the chamber stem replaced by ABS. $D_{\text{without stem and wall}}$ is the absorbed dose in the sensitive volume of air in the chamber with stem and wall replaced by ABS. $D_{\text{without stem, wall and electrode}}$ is the absorbed dose in the sensitive volume of air in the chamber with stem, wall and electrode replaced by ABS. $D_{\text{plastic, point}}$ is the absorbed dose in a 3 mm diameter sphere of ABS at the centroid of the detector and representing absorbed dose at a point in ABS.

The volume averaging (P_{vol}) is also calculated by the ratio of the dose deposited in a point in ABS ($D_{\text{plastic, point}}$) and the dose deposited in the sensitive volume filled with ABS material ($D_{\text{plastic, volume}}$).

$$P_{vol} = \frac{D_{\text{plastic, point}}}{D_{\text{plastic, volume}}}. \tag{4.12}$$

It should be noted that there are differences between the way the perturbation corrections are defined in our study and Bouchard et al. [22] study. The order in which the two perturbation corrections P_{wall} and $P_{\text{electrode}}$ are defined in this study are reversed and in calculating the $P_{\text{electrode}}$ the electrode is replaced by the phantom material (ABS) instead of air.

These calculations are performed in the *msr* setup only for the purpose of comparing the parallel and perpendicular orientations and are not normalized to the reference setup since the same orientation of chamber is used in the reference setup. In order to study the contribution of different components of chamber on $k_{Q_{\text{msr}},Q_0}^{f_{\text{msr}},f_{\text{ref}}}$ factors, one should normalize the perturbation factors calculated in the *msr* setup to the perturbation factors calculated in the reference setup.

4.4 Results

4.4.1 Influence of Monte Carlo codes on $k^{f_{msr},f_{ref}}_{Q_{msr},Q_0}$

Figure 4.2 shows the comparison of EGSnrc and PENELOPE calculated $k^{f_{msr},f_{ref}}_{Q_{msr},Q_0}$ values with a previous PENELOPE/PEGASOS study [1, 2] for different chamber types in the theoretical liquid water phantom with the chamber stem positioned parallel to the z-axis. The uncertainties on $k^{f_{msr},f_{ref}}_{Q_{msr},Q_0}$ factors shown in figure 4.2 are type A, calculated using the uncertainty propagation method, and were less than 0.2% (k = 1) in all studies.

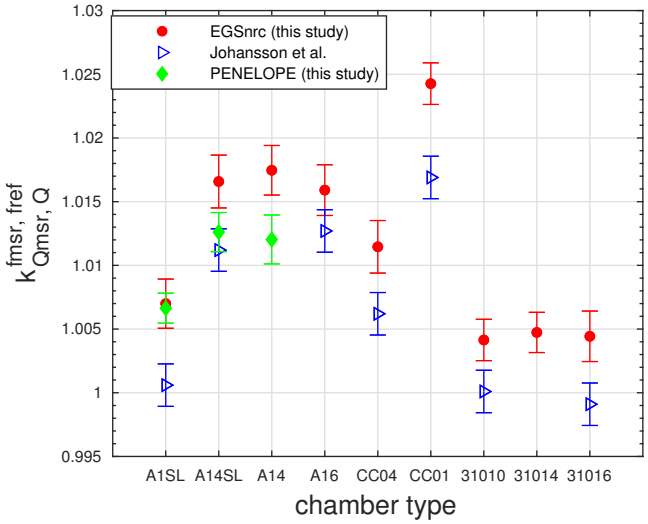

Figure 4.2 Comparison of EGSnrc and PENELOPE calculated $k^{f_{msr},f_{ref}}_{Q_{msr},Q_0}$ values with Johansson et al. [1] study for Exradin A1SL, A14SL, A14, A16, IBA CC04, CC01, PTW 31010, 31014 and 31016 in the theoretical liquid water phantom with the chamber stem placed in parallel to the z-axis. The quoted uncertainty on $k^{f_{msr},f_{ref}}_{Q_{msr},Q_0}$ is type A, and less than 0.2% (k = 1) in all studies

Depending on the chamber type, the difference between the correction values obtained with EGSnrc in this work and Johansson et al. [1] study varies between 0.32% and 0.72% in the liquid water phantom. Considering that in the liquid water phantom, there are no uncertainties associated with the phantom composition, phantom material electron density, phantom homogeneity, frames, air gaps and phantom inserts, these differences are exclusively due to differences in the chamber's material density, composition and the manner in which the chambers are modeled in two studies. Given that both codes EGSnrc and PENELOPE/PEGASOS are algorithmically self-consistent with respect to their own cross sections, i.e., they each satisfy the Fano test at the level of $\pm$ 0.2%, this difference is also due to slight cross section

differences, or differences in cross section implementation in both codes. The differences between the $k^{f_{msr},f_{ref}}_{Q_{msr},Q_0}$ values calculated with PENELOPE of this study and Johansson et al. [1] study are 0.14% for A14SL and 0.60% for A1SL. Since PENELOPE is used in both studies, this can be explained primarily by the differences in the ion chamber's dimensions, material density and composition used in the two studies.

4.4.2 Influence of chamber type and orientation on $k^{f_{msr},f_{ref}}_{Q_{msr},Q_0}$

The EGSnrc calculated $k^{f_{msr},f_{ref}}_{Q_{msr},Q_0}$ values for all chambers in the half-sphere water phantom, solid water, ABS and polystyrene phantoms for the nominal electron density of the phantoms are given in the Table 4.3 of Appendix. For ABS and polystyrene phantoms, data are provided for both possible orientations of chambers: parallel and perpendicular.

The $k^{f_{msr},f_{ref}}_{Q_{msr},Q_0}$ values for the ABS phantom is summarized in figure 4.3 for all chamber types with both orientations calculated using EGSnrc. The uncertainty on $k^{f_{msr},f_{ref}}_{Q_{msr},Q_0}$ represents type A and is less than 0.2% (k = 1).

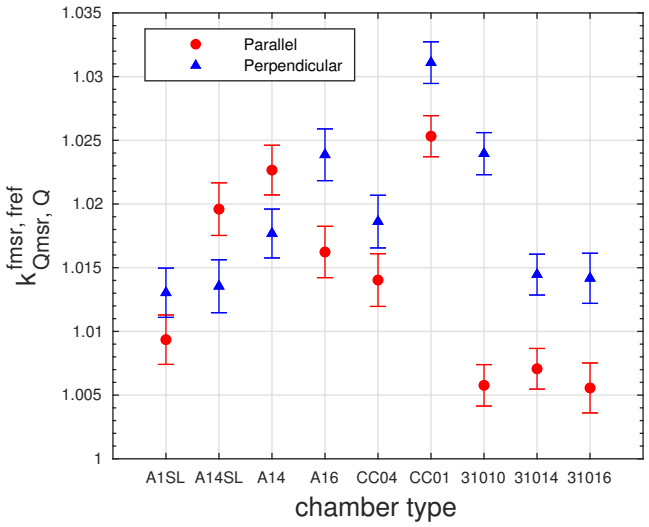

Figure 4.3 Comparison of $k^{f_{msr},f_{ref}}_{Q_{msr},Q_0}$ values in parallel and perpendicular orientation for Exradin A1SL, A14SL, A14, A16, IBA-CC04, CC01, PTW 31010, 31014 and 31016 in ABS phantom calculated by EGSnrc. The uncertainty on $k^{f_{msr},f_{ref}}_{Q_{msr},Q_0}$ represents type A and is less than 0.2% (k = 1).

Figure 4.3 shows that when the chamber is placed perpendicular to the z-axis, the Exradin A1SL model requires the smallest correction and the IBA CC01 model the largest correction.

However, when the chamber is positioned in the parallel orientation, PTW 31016 needs the smallest correction followed by PTW 31010 and 31014. A similar trend are observed for the other phantom materials.

The difference between $k_{Q_{msr},Q_0}^{f_{msr},f_{ref}}$ values in parallel and perpendicular orientations is the largest for the PTW-31010 (1.8%) chamber in the ABS phantom. It is the smallest for Exradin A1SL (0.4%), A14 (0.5%) and IBA-CC04 (0.5%) chambers (see figure 4.3). The magnitude of the correction factors is analyzed further by calculating component perturbation factors for different components of PTW-31010 chamber. Figure 4.4 shows these results in the ABS phantom for both the parallel and perpendicular orientations. The difference between perturbation factors in parallel and perpendicular orientation is more significant for the electrode (1.4%) and stem (0.4%) components.

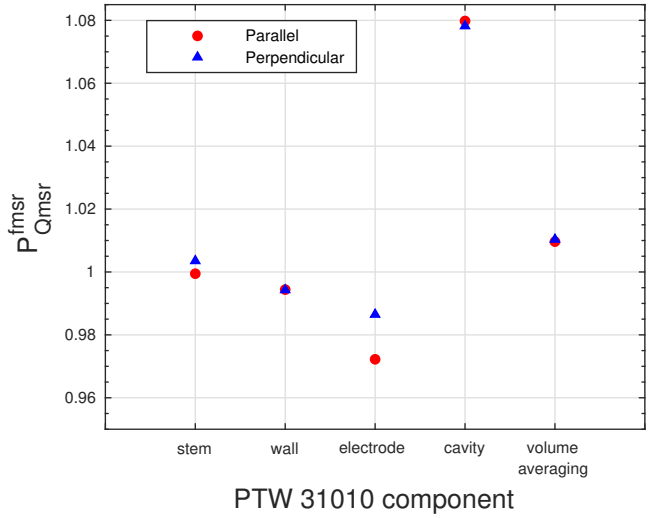

Figure 4.4 Perturbation factors for PTW-31010 in the ABS phantom *msr* field for both parallel and perpendicular orientations calculated by `EGSnrc`. The uncertainty is small and not shown (less than 0.1%).

4.4.3 Uncertainties

In this study, the type A uncertainty on $k_{Q_{msr},Q_0}^{f_{msr},f_{ref}}$ was calculated using the uncertainty propagation method as described in the Guide to the Expression of Uncertainty in Measurement (GUM) [23] and was less than 0.2% (k=1). In addition to the type A uncertainty, there are type B uncertainties including these on photon cross-sections, stopping powers, chamber materials and dimensions.

In this study, an overall type B uncertainty is estimated by calculating the percentage root-mean-square (%RMS) deviation between EGSnrc and PENELOPE $k_{Q_{msr},Q_0}^{f_{msr},f_{ref}}$ values for three chambers: Exradin A1SL, A14 and A14SL in theoretical liquid water phantom. The %RMS deviation between EGSnrc and PENELOPE calculated $k_{Q_{msr},Q_0}^{f_{msr},f_{ref}}$ values for three chambers in the theoretical liquid water in this study is found to be 0.4%. Considering 0.2% as our type A and 0.4% as our type B uncertainty the combined overall uncertainty (root-sum-of-squares) on the correction factor data presented in this work amounts to 0.45%.

4.4.4 Influence of phantom electron density on $k_{Q_{msr},Q_0}^{f_{msr},f_{ref}}$

Figure 4.5 shows the EGSnrc calculated $k_{Q_{msr},Q_0}^{f_{msr},f_{ref}}$ values plotted as a function of electron density of all phantom materials: the theoretical liquid water, ABS, solid water, polystyrene and PMMA for Exradin A1SL in parallel orientation. The $k_{Q_{msr},Q_0}^{f_{msr},f_{ref}}$ values increases linearly with electron density of the phantom material. This linear trend is also observed for all other chamber types in both orientations: parallel and perpendicular and is due to the linear dependence of photon energy fluence ratios on electron density. This linear trend enable the user to derive the $k_{Q_{msr},Q_0}^{f_{msr},f_{ref}}$ values from a nominal value of the correction factor for a given chamber type by only knowing the relative electron density of their phantom material. For this purpose, the slope of $k_{Q_{msr},Q_0}^{f_{msr},f_{ref}}$-electron density is given in table 4.2 for all chambers and the two orientations of chamber. For each chamber, eight data points (corresponding to eight different electron densities) are used for linear interpolation and calculating the slopes. Five of them correspond to the nominal electron densities (shown in figure 4.5) and three of them correspond to electron densities relative to water of 1.0128 (solid water), 1.0446 (ABS), and 1.0074 (Polystyrene). Equation 4.13 and table 4.2 are provided for the user to predict the $k_{Q_{msr},Q_0}^{f_{msr},f_{ref}}$ values for any phantom material.

$$k_{Q_{msr},Q_0}^{f_{msr},f_{ref}} = (\rho_e^{rel} - 1)a_{ch} + k_{Q_{msr},Q_0}^{'f_{msr},f_{ref}} \tag{4.13}$$

In equation 4.13, ρ_e^{rel} is the relative electron density of the phantom material, a_{ch} is the chamber-dependent slope of $k_{Q_{msr},Q_0}^{f_{msr},f_{ref}}$ vs electron density for each specific chamber and orientation provided in table 4.2 and $k_{Q_{msr},Q_0}^{'f_{msr},f_{ref}}$ is the correction factor in the spherical liquid water phantom calculated using equation 4.6 given in table 4.2. In equation 4.13, the spherical liquid water phantom with ρ_e^{rel} = 1 is chosen as the reference phantom. The accuracy of this method was tested by comparing $k_{Q_{msr},Q_0}^{f_{msr},f_{ref}}$ values predicted using equation 4.13 and $k_{Q_{msr},Q_0}^{f_{msr},f_{ref}}$

values calculated using equation 4.3 (the data is given in Appendix Table 4.3). The average relative percentage difference between the predicted and calculated $k_{Q_{msr},Q_0}^{f_{msr},f_{ref}}$ values for all phantom materials (theoretical liquid water, solid water, ABS, Polystyrene and PMMA) is found to be 0.15% for all nine chambers and orientations.

Table 4.2 The $k'^{f_{msr},f_{ref}}_{Q_{msr},Q_0}$ values and the slope a_{ch} of $k_{Q_{msr},Q_0}^{f_{msr},f_{ref}}$ vs electron density for all chamber types in parallel and perpendicular orientations determined with .

chamber type	parallel		perpendicular	
	$k'^{f_{msr},f_{ref}}_{Q_{msr},Q_0}$	a_{ch}	$k'^{f_{msr},f_{ref}}_{Q_{msr},Q_0}$	a_{ch}
Exradin A1SL	1.0070	0.4499	1.0070	0.4234
Exradin A14SL	1.0166	0.4487	1.0105	0.4299
Exradin A14	1.0175	0.4599	1.0148	0.4259
Exradin A16	1.0159	0.4248	1.0174	0.4352
IBA CC04	1.0115	0.4316	1.0112	0.4263
IBA CC01	1.0243	0.4400	1.0245	0.4354
PTW 31010	1.0041	0.4211	1.0188	0.4255
PTW 31014	1.0047	0.4293	1.0082	0.4275
PTW 31016	1.0044	0.4340	1.0072	0.4387

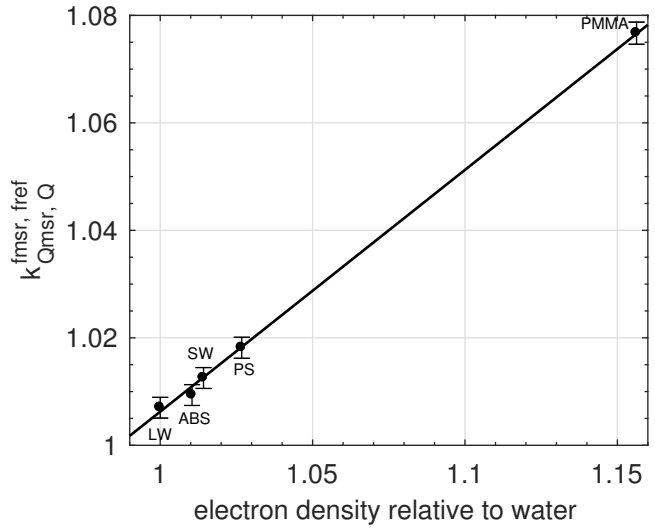

Figure 4.5 EGSnrc calculated $k_{Q_{msr},Q_0}^{f_{msr},f_{ref}}$ values as a function of electron density of the phantom materials for Exradin A1SL in parallel orientation. The uncertainty on $k_{Q_{msr},Q_0}^{f_{msr},f_{ref}}$ is type A and less than 0.2% (k = 1).

As discussed in section 4.3.2, the contribution of the phantom material can be disentangled from the contribution by the chamber itself, using the phantom dose conversion factor ($k^{w,\text{plastic}}_{Q_{\text{msr}}}$). Since $k^{w,plastic}_{Q_{\text{msr}}}$ is almost independent of chamber type, instead of using the chamber-dependent slope of $k^{f_{\text{msr}},f_{\text{ref}}}_{Q_{\text{msr}},Q_0}$ vs electron density (a_{ch}), an average slope of $k^{w,plastic}_{Q_{msr}}$-electron density over nine chamber types and orientations can be used in conjunction with $k^{'f_{\text{msr}},f_{\text{ref}}}_{Q_{\text{msr}},Q_0}$ values for different chamber types provided in table 4.2 and equation 4.14. With this second methodology, corrections for a given chamber type in an arbitrary plastic phantom material can be determined using the electron density of the phantom material only. For certified plastics, the electron density can be obtained from the manufacturer.

$$k^{f_{\text{msr}},f_{\text{ref}}}_{Q_{\text{msr}},Q_0} = k^{'f_{\text{msr}},f_{\text{ref}}}_{Q_{\text{msr}},Q_0} k^{w,\text{plastic}}_{Q_{\text{msr}}} = k^{'f_{\text{msr}},f_{\text{ref}}}_{Q_{\text{msr}},Q_0}[(\rho^{rel}_e - 1)b + 1] \tag{4.14}$$

In equation 4.14, b = 0.4284 $\pm$ 2.3% is the slope of $k^{w,\text{plastic}}_{Q_{msr}}$- electron density averaged over nine chamber types for both orientations of chamber: parallel and perpendicular. ρ^{rel}_e is the electron density of the phantom material relative to the electron density of water. In equation 4.14, the theoretical liquid water phantom was chosen as the reference phantom since $k^{w,\text{plastic}}_{Q_{\text{msr}}}$ is unity independent of chamber type. An estimated accuracy for this method was obtained by comparing $k^{f_{\text{msr}},f_{\text{ref}}}_{Q_{\text{msr}},Q_0}$ values predicted using equation 4.14 and $k^{f_{\text{msr}},f_{\text{ref}}}_{Q_{\text{msr}},Q_0}$ values calculated by using equation 4.3 (for data see Table 4.3 of Appendix). The average percentage difference between the predicted and calculated $k^{f_{\text{msr}},f_{\text{ref}}}_{Q_{\text{msr}},Q_0}$ values was found to be 0.16%.

4.4.5 Impact on Gamma Knife dosimetric intercomparisons

Figure 4.6 presents previously measured dose rates as part of a dosimetric intercomparison study between nine centres [3]. This study used the Exradin A16 and PTW 31010 chambers in half-sphere water, solid water and ABS phantoms and has been reanalyzed with and without the correction of this work (`EGSnrc`). The correction of Johansson et al. [1] study is also applied for the solid water phantom. Figure 4.6 shows the dose rate determined using TG-21 and ABS phantom as an arbitrary normalization.

The uncertainties reported in figure 4.6, include the type A uncertainty on the original measurement [3] combined with the overall standard uncertainty (type A and type B) on the correction factors discussed in this work. The uncertainties shown on dose rate measurement corrected with the Johansson et al. [1] correction only include a type A uncertainty on their Monte Carlo calculated $k^{f_{\text{msr}},f_{\text{ref}}}_{Q_{\text{msr}},Q_0}$ values and on the measured readings. It can be seen that

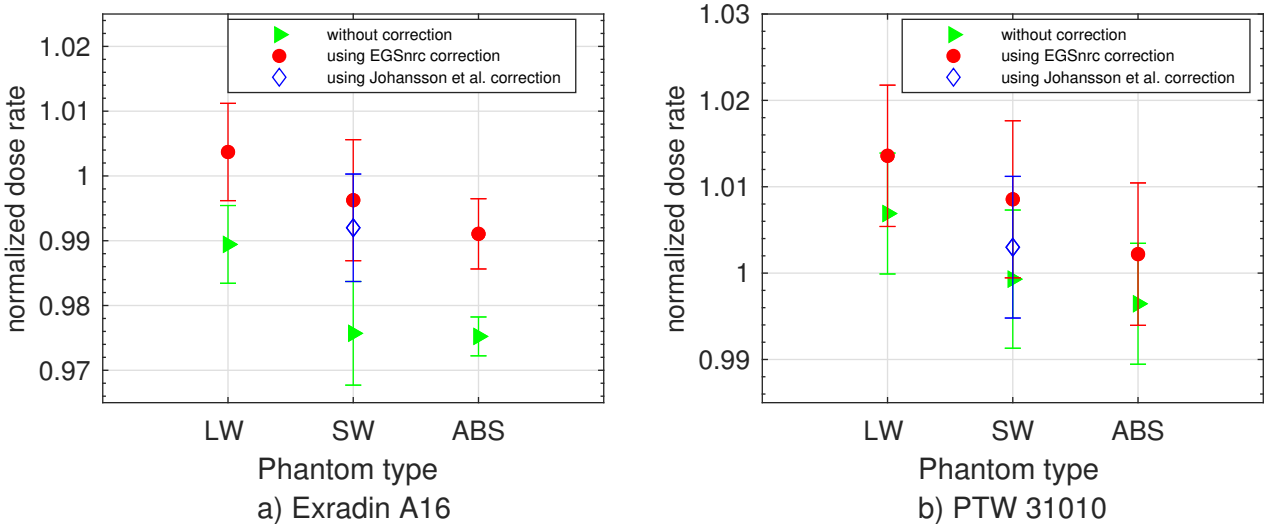

Figure 4.6 Measured dose-rate with Exradin A16 (a) and PTW 31010 (b) in half-sphere water phantom (LW), solid water (SW) and ABS phantoms [3] with and without the correction of `EGSnrc` calculated $k_{Q_{msr},Q_0}^{f_{msr},f_{ref}}$ values of this work normalized to the dose-rate measured with TG-21 protocol and ABS phantom. For solid water phantom, the corrections calculated by Johansson et al. [1] is also applied. The uncertainties on dose-rate measurement without the correction are due to the standard deviation on the measurement [3], the uncertainties on dose-rate measurement corrected with the correction of this study are due to the type A and B uncertainty on Monte Carlo calculated $k_{Q_{msr},Q_0}^{f_{msr},f_{ref}}$ values and the standard error on the measurement. The uncertainties shown on dose-rate measurement corrected with the Johansson et al. [1] correction are due to the type A uncertainty on Monte Carlo calculated $k_{Q_{msr},Q_0}^{f_{msr},f_{ref}}$ values and standard deviation on the measurement.

the sample standard deviation of the measured dose rates for both chambers and all three phantoms slightly improves from 1.29% to 0.8% after applying the EGSnrc calculated $k_{Q_{msr},Q_0}^{f_{msr},f_{ref}}$ values of this work to the measured dose-rates. Using the correction of Johansson et al. [1] for solid water phantom also lowers the standard deviation on dose rate from 1.29% to 0.8%. Therefore, the measured dose rate corrected with the $k_{Q_{msr},Q_0}^{f_{msr},f_{ref}}$ values determined in this work results in absorbed dose values that are consistent to within 0.8%.

4.5 Discussion

In all phantom materials, a larger $k_{Q_{msr},Q_0}^{f_{msr},f_{ref}}$ value is observed for Exradin A14SL and A14 when the chambers are placed parallel to the z-axis compared to the case where chambers are positioned perpendicular to the z-axis. The difference between $k_{Q_{msr},Q_0}^{f_{msr},f_{ref}}$ values for the parallel and perpendicular orientation is the largest for PTW-31010 (1.8%) in the ABS phantom. This can be attributed to the material of electrode of the chamber. Since the electrode is made of Aluminum in PTW-31010. $k_{Q_{msr},Q_0}^{f_{msr},f_{ref}}$ values in the parallel orientation are generally smaller than the $k_{Q_{msr},Q_0}^{f_{msr},f_{ref}}$ values in perpendicular orientation. This depends mainly on the specifications of the wall and cavity of the chambers and can be investigated further by performing a calculation of the individual perturbation effects.

The difference between the $k_{Q_{msr},Q_0}^{f_{msr},f_{ref}}$ values for Exradin A1SL calculated using the spectrum [13] and phase space files of ^{60}Co radiation unit of the secondary standard dosimetry laboratory [14] is found to be less than 0.03%.

The difference between the $k_{Q_{msr},Q_0}^{f_{msr},f_{ref}}$ values calculated in this study (EGSnrc) and Johansson et al. [1] study in ABS phantom is largest for PTW 31010 (0.91%) (data given in the Table 4.3 of Appendix). The main reason is that in Johansson et al. [1] study a simplified model of the PTW 31010 chamber was used whereas in the present work, the PTW 31010 is modeled in detail based on blueprints provided by the manufacturer. Additionally in the Monte Carlo calculation of this study, phantoms were considered to be ideally homogeneous without any air gaps. While in Johansson et al. [1] study, the actual drilled inserts were modeled. Moreover, unlike the Johansson et al. [1] study, the ABS phantom mounting adapter was not simulated in the present study. The ABS phantom adapter results in an underestimation of output by 0.97% [24]. However, this does only minimally affect the $k_{Q_{msr},Q_0}^{f_{msr},f_{ref}}$ values because of cancellation of ($D_{w,Q_{msr}}^{f_{msr}}$) and the mean absorbed dose to the air cavity of chamber in *msr* field ($D_{det,plastic,Q_{msr}}^{f_{msr}}$).

The $k^{f_{\mathrm{msr}},f_{\mathrm{ref}}}_{Q_{\mathrm{msr}},Q_0}$ values increases linearly with electron density of the phantom material because of the linear dependence of photon energy fluence ratios on electron density. Assuming transient electronic equilibrium at the depth of measurement and no depth scaling is applied, the factor $k^{w,\mathrm{plastic}}_{Q_{msr}}$ can be expressed as (for derivation see Seuntjens et al. [20]):

$$k^{w,\mathrm{plastic}}_{Q_{msr}} = \psi^{w}_{\mathrm{plastic}} \left(\frac{\bar{\mu}_{en}}{\rho}\right)^{w}_{\mathrm{plastic}} \beta^{w}_{\mathrm{plastic}} \left(\frac{\bar{L}}{\rho}\right)^{\mathrm{plastic}}_{w} \frac{P_{Q_{\mathrm{msr}},\mathrm{plastic}}}{P_{Q_{\mathrm{msr}},w}} \tag{4.15}$$

Where, $\psi^{w}_{\mathrm{plastic}}$ is the photon energy fluence ratio water to plastic, $\left(\frac{\bar{\mu}_{en}}{\rho}\right)^{w}_{\mathrm{plastic}}$ is the average mass-energy absorption coefficient of the water to plastic, $\beta^{w}_{plastic}$ is the ratio of absorbed dose and collision kerma at the given point in water to plastic, $\left(\frac{\bar{L}}{\rho}\right)^{\mathrm{plastic}}_{w}$ is the averaged restricted collision mass stopping power ratio plastic to water.

In equation 4.15, the $(\frac{\bar{L}}{\rho})$ depends linearly on Z/A of the material (see Andreo et al. [25]). The $(\frac{\bar{\mu}_{en}}{\rho})$ also depends linearly on the Z/A of the material since Compton interaction is the dominant process in the energy range studied here. Therefore in equation 4.15, $\left(\frac{\bar{L}}{\rho}\right)^{\mathrm{plastic}}_{w}$ and $\left(\frac{\bar{\mu}_{en}}{\rho}\right)^{w}_{\mathrm{plastic}}$ partially cancel out for the same phantom material in this energy region. Furthermore, the ratio of perturbation factors $\frac{P_{Q_{\mathrm{msr}},plastic}}{P_{Q_{\mathrm{msr}},w}}$ mostly depends on the ionization chamber components. This explains the small variation of a_{ch} for different chambers in Table 4.2. The ratio of perturbation factors does not vary significantly with the electron density of the phantom material. Therefore, the only linear factor in equation 4.15 is the photon energy fluence ratio water-to-plastic ($\psi^{w}_{plastic}$). Since the photon energy fluence ratios are linearly dependent on electron density, $k^{w,plastic}_{Q_{\mathrm{msr}}}$ and, as a result, the $k^{f_{\mathrm{msr}},f_{\mathrm{ref}}}_{Q_{\mathrm{msr}},Q_0}$ values are linearly dependent on electron density. In the realistic half-sphere water phantom, after applying the `EGSnrc`-calculated $k^{f_{\mathrm{msr}},f_{\mathrm{ref}}}_{Q_{\mathrm{msr}},Q_0}$ values to the measured dose rates normalized to the dose rate measured with TG-21 protocol and ABS phantom, the dose rate ratios are found to be 1.0037 $\pm$ 0.0075 for Exradin A16 and 1.0136 $\pm$ 0.0082 for PTW 31010 (see figure 4.6).

For the ABS phantom, the dose rates corrected with the `EGSnrc` $k^{f_{\mathrm{msr}},f_{\mathrm{ref}}}_{Q_{\mathrm{msr}},Q_0}$ values of this work normalized to the dose rate determined with TG-21 and ABS phantom are 0.9911 $\pm$ 0.0054 for Exradin A16 and 1.0022 $\pm$ 0.0082 for PTW 31010.

For the solid water phantom material, the corrected dose rate normalized to the TG-21 value using the correction factors determined in this study (`EGSnrc`) were found to be 0.9963 $\pm$ 0.0093 for Exradin A16 and 1.0085 $\pm$ 0.0091 for PTW 31010. In the present study, the solid

water phantom is considered perfectly homogeneous, while a realistic phantom does have some low-density regions [16]. The solid water aluminum mounting frame was also not considered in the present study. It is expected to have no significant effect on the results, for similar reasons as for the ABS phantom mounting frame. It has been also shown that the Elekta solid water phantom does not exhibit the issue of adapter attenuation as observed with the ABS phantom [16, 24].

4.6 Conclusion

The $k_{Q_{msr},Q_0}^{f_{msr},f_{ref}}$ factors were determined for nine commonly used chambers in the reference dosimetry of LGK Perfexion unit using Monte Carlo simulation. The influence of using different Monte Carlo codes (`EGSnrc` and `PEGASOS`/`PENELOPE`) is studied in a theoretical spherical liquid water phantom. The effect of chamber orientation with respect to the symmetry axis of the LGK is investigated in liquid water and realistic ABS, polystyrene and PMMA phantoms. The $k_{Q_{msr},Q_0}^{f_{msr},f_{ref}}$ factors for all chambers are provided as a function of electron density of the phantom materials. The $k_{Q_{msr},Q_0}^{f_{msr},f_{ref}}$ values for Exradin A16 and PTW 31010 chambers are applied to dose rates measured in different phantoms as part of a multi-institutional intercomparison [3].

Good agreement on $k_{Q_{msr},Q_0}^{f_{msr},f_{ref}}$ is observed between using different Monte Carlo codes in theoretical liquid water phantom where there is no uncertainties associated with the phantom composition, mass density, homogeneity, frames, air gaps and phantom inserts. The difference between $k_{Q_{msr},Q_0}^{f_{msr},f_{ref}}$ values in parallel and perpendicular orientations is largest for the PTW 31010 (1.8%) chamber. This is mainly due to the difference in the perturbation contribution of electrode (1.4%) and stem (0.4%) in parallel and perpendicular orientations. The %RMS deviation between `EGSnrc` and `PENELOPE` calculated $k_{Q_{msr},Q_0}^{f_{msr},f_{ref}}$ values is found to be 0.4%. The $k_{Q_{msr},Q_0}^{f_{msr},f_{ref}}$ values increases linearly with electron density for all chamber types mainly due to the linear dependence of photon energy fluence ratios on electron density. Using the correction of this work improves, the standard deviation on measured dose rate from the intercomparison study from 1.29% to 0.8%. Knowing the electron density of the phantoms, the calculated $k_{Q_{msr},Q_0}^{f_{msr},f_{ref}}$ values in this work will enable users to apply the appropriate correction for their own specific phantom material by only knowing the electron density of their phantom material.

Acknowledgments

LM acknowledge the financial support by the CREATE Medical Physics Research Training Network grant of the Natural Sciences and Engineering Research Council (Grant number: 432290) and NSERC RGPIN-2014-06475. The authors also acknowledge Compute Canada/Calcul Quebec for the computing resources and the ion chamber manufacturers: Standard Imaging (Regina Fulkerson), PTW (Jan Würfel) and IBA (David Menichelli) for providing the chambers blueprints and specifications. The authors thank Jonas Johansson for providing the phasespace data for the LGK unit and ^{60}Co unit.

Conflicts of Interest

The authors have no relevant conflicts of interest to disclose.

4.7 Appendix

The EGSnrc calculated $k_{Q_{\text{msr}},Q_0}^{f_{\text{msr}},f_{\text{ref}}}$ values for all chambers in the half-sphere water phantom (LW), solid water (SW), ABS, and polystyrene (PS) phantoms for the nominal electron density of the phantoms are given in Table 4.3. For ABS and polystyrene phantoms, data are provided for both possible orientations of chambers: parallel and perpendicular.

[a)] Author to whom correspondence should be addressed.
Electronic mail: lalageh.mirzakhanian@mail.mcgill.ca

Table 4.3 Monte Carlo determined $k_{Q_{msr},Q_0}^{f_{msr},f_{ref}}$ correction factors for nine chambers in parallel and perpendicular orientations with respect to the symmetry axis of the collimator block (z-axis) in half-sphere water phantom (LW), solid water (SW), acrylonitrile butadiene styrene (ABS) and polystyrene (PS) phantoms for LGK Perfexion^{TM} unit. The uncertainty on EGSnrc data is type A and less than 0.2% (k=1).

Chamber type	phantom type	chamber orientation	$k_{Q_{msr},Q_0}^{f_{msr},f_{ref}}$ EGSnrc (this study)	$k_{Q_{msr},Q_0}^{f_{msr},f_{ref}}$ Johansson et al. [1]
Exradin A1SL	LW	Parallel	1.0088	-
	SW	Parallel	1.0125	1.0046
	ABS	Parallel	1.0094	-
		Perpendicular	1.0130	1.0138
	PS	Parallel	1.0181	-
		Perpendicular	1.0221	-
Exradin A14	LW	Parallel	1.0208	-
	SW	Parallel	1.0270	-
	ABS	Parallel	1.0227	-
		Perpendicular	1.0177	-
	PS	Parallel	1.0310	-
		Perpendicular	1.0241	-
Exradin A14SL	LW	Parallel	1.0190	-
	SW	Parallel	1.0216	1.0154
	ABS	Parallel	1.0196	-
		Perpendicular	1.0135	1.0194
	PS	Parallel	1.0275	-
		Perpendicular	1.0203	-
Exradin A16	LW	Parallel	1.0144	-
	SW	Parallel	1.0211	1.0167
	ABS	Parallel	1.0162	-
		Perpendicular	1.0239	1.0295
	PS	Parallel	1.0244	-
		Perpendicular	1.0322	-
IBA CC04	LW	Parallel	1.0130	-
	SW	Parallel	1.0157	1.0107
	ABS	Parallel	1.0140	-
		Perpendicular	1.0186	1.0117
	PS	Parallel	1.0194	-
		Perpendicular	1.0260	-
IBA CC01	LW	Parallel	1.0251	-
	SW	Parallel	1.0311	1.0213
	ABS	Parallel	1.0253	-
		Perpendicular	1.0311	1.0292
	PS	Parallel	1.0329	-
		Perpendicular	1.0391	-
PTW 31010	LW	Parallel	1.0066	-
	SW	Parallel	1.0093	1.0037
	ABS	Parallel	1.0058	-
		Perpendicular	1.0240	1.0146
	PS	Parallel	1.0135	-
		Perpendicular	1.0327	-
PTW 31014	LW	Parallel	1.0081	-
	SW	Parallel	1.0109	-
	ABS	Parallel	1.0071	-
		Perpendicular	1.0145	-
	PS	Parallel	1.0130	-
		Perpendicular	1.0235	-
PTW 31016	LW	Parallel	1.0045	-
	SW	Parallel	1.0105	1.0040
	ABS	Parallel	1.0056	-
		Perpendicular	1.0142	1.0110
	PS	Parallel	1.0130	-
		Perpendicular	1.0207	-

Bibliography

[1] Johansson J, Gorka B, Novotny Jr., et al. In: *Plenary Oral Presentation at the 16th International Meeting of the Leksell Gamma Knife® Society;* 2012. p. 69.

[2] Andreo P, Benmakhlouf H. Improved reference and relative dosimetry of small radiation therapy photon beams. SSM Report 2014:26. Stockholm: Swedish Radiation Safety Authority.

[3] Drzymala R, Alvarez P, Bednarz G, et al. A round-robin gamma stereotactic radiosurgery dosimetry interinstitution comparison of calibration protocols. *Med Phys.* 2015;42:6745.

[4] Das IJ, Ding GX, Ahnesjö A. Small fields: nonequilibrium radiation dosimetry. *Med Phys.* 2008;35:206.

[5] International Atomic Energy Agency. *Dosimetry of small static fields used in external beam radiotherapy.* Technical Reports Series No. 483. Vienna: International Atomic Energy Agency; 2017.

[6] Alfonso R, Andreo P, Capote R, et al. A new formalism for reference dosimetry of small and nonstandard fields. *Med Phys.* 2008;35:5179.

[7] Lindquist C, Paddick I. The Leksell Gamma Knife Perfexion and comparisons with its predecessors. *Operative Neurosurgery* 2007;61(Suppl 3): ONS-130.

[8] Zoros E, Moutsatsos A, Pappas E, et al. Monte Carlo and experimental determination of correction factors for gamma knife perfexion small field dosimetry measurements. *Phys Med Biol.* 2017;62:7532.

[9] Kawrakow I, Mainegra-Hing E, Tessier F, Walters B. NRC Report PIRS-898 (rev A); 2009.

[10] Kawrakow I, Rogers D. The `EGSnrc` code system: Monte Carlo simulation of electron and photon transport, 2000. *NRCC Report PIRS-701.*(2000).

[11] Kawrakow I. Accurate condensed history Monte Carlo simulation of electron transport. I. `EGSnrc`, the new `EGS4` version. *Med Phys.* 2000;27:485.

[12] Salvat F, Fernández-Varea JM, Sempau J. In: *the workshop proceedings, June*; 2008.

[13] Mora G, Maio A, Rogers D. Monte Carlo simulation of a typical 60Co therapy source. *Med Phys.* 1999;26:2494.

[14] Tedgren ÅC, de Luelmo S, Grindborg J-E. Characterization of a 60Co unit at secondary standard dosimetry laboratory-Monte Carlo simulations compared to measurements and results from the literature. *Med Phys.* 2010;37:2777.

[15] Drzymala R, Wood R, Levy J. Calibration of the Gamma Knife using a new phantom following the AAPM. TG51 and TG21 protocols. *Med Phys.* 2008;35:514.

[16] McDonald D, Yount C, Koch N, Ashenafi M, Peng J, Vanek K. Calibration of the Gamma Knife Perfexion using TG-21 and the solid water Leksell dosimetry phantom. *Med Phys.* 2011;38:1685.

[17] Bhatnagar JP, Niranjan A, Kalend A, et al. Miniature Ion Chamber for Output Calibration of Stereotactic Radiosurgery Units. In: M. W. McDermott, ed. *Radiosurgery.* Vol. 7. Basel: Karger Publishers; 2010:66–74.

[18] Novotny J Jr., Bhatnagar JP, Chung H-T, et al. Assessment of variation in Elekta plastic spherical-calibration phantom and its impact on the Leksell Gamma Knife calibration. *Med Phys.* 2010;37:5066.

[19] Berger MJ, Coursey J, Zucker M, Chang J. *Stopping-power and range tables for electrons, protons, and helium ions.* Gaithersburg, MD: NIST Physics Laboratory; 1998.

[20] Seuntjens J, Olivares M, Evans M, Podgorsak E. Absorbed dose to water reference dosimetry using solid phantoms in the context of absorbed dose protocols. *Med Phys.* 2005;32:2945.

[21] Wulff J, Zink K, Kawrakow I. Efficiency improvements for ion chamber calculations in high energy photon beams. *Med Phys.* 2008;35:1328.

[22] Bouchard H, Seuntjens J, Carrier J-F, Kawrakow I. Ionization chamber gradient effects in nonstandard beam configurations. *Med Phys.* 2009;36:4654.

[23] Taylor BN. *Guidelines for Evaluating and Expressing the Uncertainty of NIST Measurement Results (rev).* Gaithersburg, MD: DIANE Publishing; 2009.

[24] Bhatnagar JP, Novotny J Jr., Quader MA, Bednarz G, Huq MS. Unintended attenuation in the Leksell Gamma Knife® Perfexion^{TM} calibration- phantom adaptor and its effect on dose calibration. *Med Phys.* 2009;36:1208.

[25] Andreo P, Burns D, Nahum A, Seuntjens J, Attix F. *Fundamentals of Ionizing Radiation Dosimetry.* Weinheim: Wiley; 2017.

Chapter 5

Experimental validation of recommended *msr*-correction factors for the calibration of Leksell Gamma Knife® Icon™ Unit following IAEA TRS-483

Lalageh Mirzakhanian, Arman Sarfehnia and Jan Seuntjens

Submitted to Physics in Medicine and Biology journal, August 2019

5.1 Preface

In this chapter, the $k_{Q_{msr},Q_0}^{f_{msr},f_{ref}}$ values calculated in chapter 4 for the calibration of LGK PerfeXion/Icon unit were validated experimentally. A comparison between the use of three calibration methodologies for reference dosimetry of LGK was also provided.

Abstract

Currently, the American Association of Physicists in Medicine (AAPM) TG-21 is the conventional protocol currently used for the calibration of the Leksell Gamma Knife® (LGK) (despite the publication of the AAPM TG-51 protocol). However, this protocol is based on

the air-kerma standards requiring an elaborate conversion process resulting in an increase in the possibility of errors in the clinic. The International Atomic Energy Agency (IAEA) Technical Reports Series (TRS)-483 Code of Practice provides new recommendations on the dosimetry of small static fields and correction factor data for the calibration of the LGK unit. The purpose of this study is to experimentally validate previously calculated $k_{Q_{msr},Q_0}^{f_{msr},f_{ref}}$ factors for the calibration of the LGK Perfexion/Icon unit in the context of the TRS-483 protocol. An experimental comparison between three protocols (TG-51, TG-21 and TRS-483 with the aforementioned correction factors) for calibration of the LGK unit is provided. Dose rate measurements were performed on a LGK Icon unit using three ionization chambers and three phantoms with different orientations of the chambers with respect to the LGK unit. The dose rate was determined following the three calibration protocols. The standard deviation on the mean dose rate over all phantoms and chambers in different orientations determined using TG-51, TG-21 and TRS-483 protocols were 0.9%, 0.5% and 0.4%, respectively. The mean dose rate calculated using TG-51 protocol was 1.6% and 1.2% lower comparing to the TG-21 and TRS-483 protocols respectively. Applying the $k_{Q_{msr},Q_0}^{f_{msr},f_{ref}}$ values calculated in Mirzakhanian et al. to the measured dose rates in LGK unit for all chambers and phantoms resulted in dose rates that are consistent to within 0.4%. The TRS-483 protocol improves the consistency of the results especially when the chamber was positioned in different orientations with respect to the LGK (from 1.6% when using TG-51 or TG-21 protocols to 0.2% when using TRS-483 protocol) since the other protocols do not correct for the different chamber orientations.

5.2 Introduction

The Leksell Gamma Knife® (LGK) Icon is an upgrade of the previous Gamma Knife Perfexion. Although the radiation delivery unit component as well as the patient positioning system are identical to the older Perfexion, the main difference is the additional cone-beam CT (CBCT) imaging device that is attached to the unit as well as the Intra-Fraction Motion Management system that is attached to the couch for patient positioning [1]. The most common and long established protocol used in calibration of the LGK unit is the American Association of Physicists in Medicine (AAPM) Task Group TG-21 protocol [2]. The TG-21 protocol is based on air-kerma standards. A conversion process, through the N_{gas} concept is used to obtain absorbed dose to water. This requires elaborate calculations, knowledge of interaction coefficients and correction factors increasing the possibility of errors in the clinic [3]. In

addition, the TG-21 protocol does not correct for the differences between the conditions of field size and geometry of the conventional reference and the Gamma Knife set-up.

Since two decades, absorbed dose to water standards-based dosimetry protocols were introduced such as the AAPM TG-51 protocol [3, 4] and the International Atomic Energy Agency (IAEA) Technical Reports Series (TRS) 398 Code of Practice [5]. Few multiplicative factors are used to convert the reading of an ionization chamber, calibrated in terms of absorbed dose to water into dose to water in the users beam. Compared to the TG-21 protocol, the TRS-398 and TG-51 protocols are considerably simpler to use and implement. In the last two decades, the TG-21 protocol has been largely replaced by the TG-51/TRS-398 protocols for external-beam radiotherapy. However the latter protocols cannot be applied for dosimetry of the LGK since the radiation field and phantoms used in the LGK do not meet the phantom material and reference condition requirements of the absorbed dose protocols.

The recently published TRS-483 protocol [6] provides recommendations for the dosimetry of small static fields used in radiotherapy. It also provides correction factors ($k_{Q_{\mathrm{msr}},Q_0}^{f_{\mathrm{msr}},f_{\mathrm{ref}}}$) for different ionization chambers based on the data available in the literature. The $k_{Q_{\mathrm{msr}},Q_0}^{f_{\mathrm{msr}},f_{\mathrm{ref}}}$ is a factor that corrects for the difference between the response of the ionization chamber in a conventional reference calibration field f_{ref} with beam quality Q_0 at the standards laboratory and the response of the ionization chamber in the machine specific reference field (*msr*) f_{msr} with beam quality Q_{msr} [6]. In the case of LGK reference dosimetry, the $k_{Q_{\mathrm{msr}},Q_0}^{f_{\mathrm{msr}},f_{\mathrm{ref}}}$ factors used in the TRS-483 protocol are based on a Monte Carlo (MC) study by Johansson et al. [7].

For the LGK, a recent comparison between the new protocol and the existing calibration methods has been made in a round robin study [8]: two ionization chambers and three phantoms, the Solid Water LGK Dosimetry Phantom [9], the Elekta Acrylonitrile Butadiene Styrene (ABS) phantom and the half-sphere water phantom provided by The Phantom Laboratory, Inc. (Salem, NY) were used in nine different institutes [8]. The LGK unit was calibrated according to different protocols. The reported dose-rates for each protocol and phantom were normalized to the dose-rate determined with the TG-21 protocol and the ABS phantom for each LGK unit. This study suggests that the TG-51 protocol is not reliable for the LGK calibration while the results obtained with the formalism proposed by Alfonso et al. [10] (which now is adopted in TRS-483 protocol) agreed with the results obtained using the TG-21 protocol (1.000 ± 0.006). This result is somewhat fortuitous since the TG-21 protocol has no mechanism to take into account the difference between the N_K chamber calibration geometry and the irradiation geometry during phantom dose delivery (i.e., the *msr* field). On the other

hand, however, the TG-21 protocol does explicitly take into account the potential fact that the phantom material may be plastic instead of water. Although the results of this study were promising further studies were needed to confirm that this new formalism performs as well or better for other ionization chambers commonly used in GK dosimetry. The MC calculated correction factors in Drzymala et al. [8] were also taken from the same single source [7]. Additionally, in Drzymala et al. [8] study, during the calibration the chambers were placed in parallel to the symmetry axis of the collimator block (z-axis). However in some clinics when performing calibrations the chamber is positioned in the ABS phantom with the chamber stem perpendicular to the z-axis [11, 7].

The goal of the present study is to evaluate the recommendation provided in the TRS-483 protocol and to experimentally validate our previously calculated $k_{Q_{\mathrm{msr}},Q_0}^{f_{\mathrm{msr}},f_{\mathrm{ref}}}$ values [12] for the LGK Perfexion/Icon Unit. We also studied the influence of calibration protocol, phantom material, chamber type and chamber orientations in calibration of the LGK unit. The data were compared to the results available in the literature.

5.3 Methods

5.3.1 Measurement and equipment

Dose-rate measurements were performed at the LGK Icon$^{\mathrm{TM}}$ unit at the Sunnybrook Health Sciences Center using three chambers Exradin-A1SL, A16 and PTW 31010 all paired with a Keithley 6517A electrometer with exposure calibration coefficient (N_X) and ^{60}Co absorbed dose to water calibration coefficient ($N_{D,w,Q_0}^{f_{\mathrm{ref}}}$) traceable to the National Research Council, Canada (NRC) standards lab. Three phantoms including the Solid Water, the Lucy and the ABS phantoms were used in the measurements. The phantoms had been placed in the treatment room overnight to reach ambient room temperature [13]. A treatment plan that involves all sources with collimation 16 mm diameter was created and used as *msr* field. The current was measured at the center of each phantom using the Keithley 6517A electrometer and the three ionization chambers. Measurements were performed with the electrometer in current mode and twenty values were averaged for each data point. The measurements in ABS and Lucy phantoms were performed for different orientations of the chambers with respect to the LGK unit (the phantoms and chamber orientations are shown in Figure 5.1). The chambers were pre-irradiated to achieve electronic stability. The temperature and pressure were measured for

each set-up before and after the measurements. The positioning of the chamber inside each phantom was verified using the Icon CBCT system (Figure 5.2). The dose-rate was determined following the TG-51, TG-21 and the TRS-483 protocols to study the effect of the different protocols used.

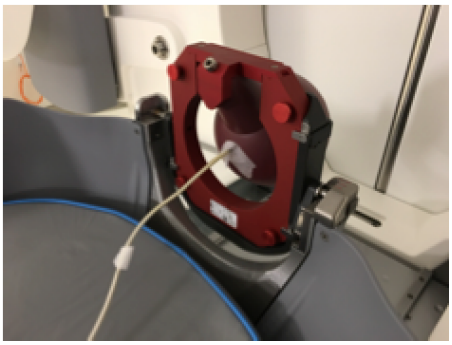

a) Solid Water

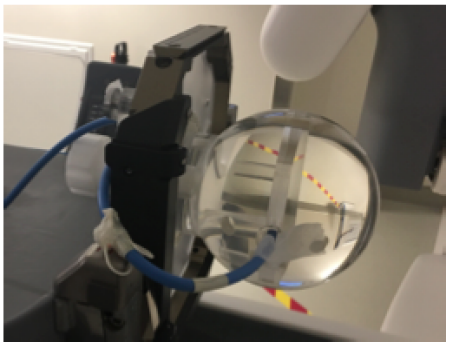

b) Lucy 0°

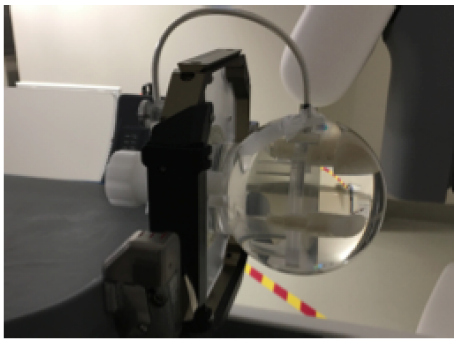

c) Lucy 270°

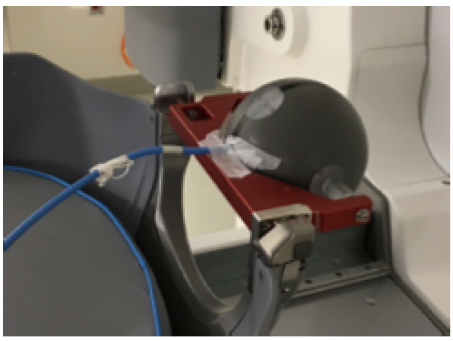

d) ABS parallel (|)

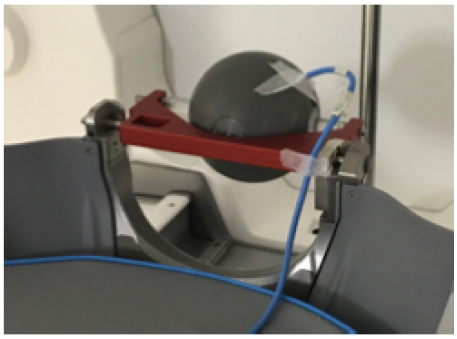

e) ABS perpendicular (⊥)

Figure 5.1 Experimental set-up for the Solid Water, Lucy and ABS phantoms at LGK Icon^{TM} Unit

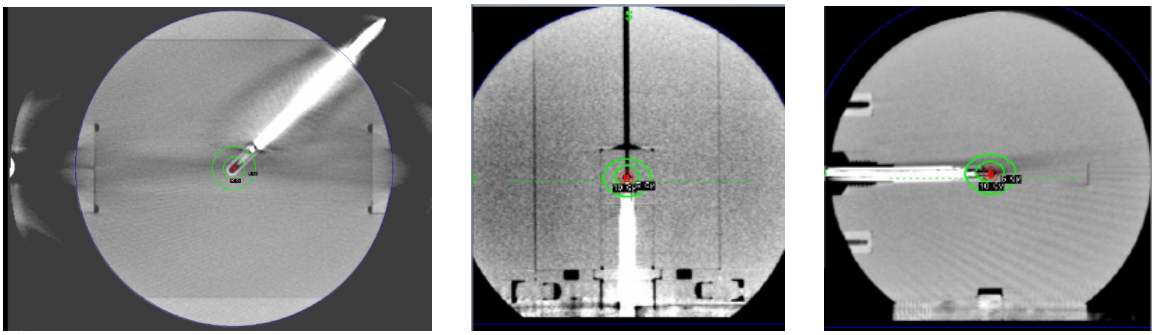

a) ABS b) SW c) Lucy

Figure 5.2 Cone-beam CT image of the chamber positioned inside the a) ABS, b) SW and c) Lucy phantom

5.3.2 Calibration protocols

In TG-21 protocol analyses, the charge per unit mass of air per unit exposure was taken to be k=2.58$\times$ 10^{-4} C/kg R, the average energy per unit charge W/e=33.7 J/C and β_{wall}=1.005 [2]. The other parameters used in the TG-21 dose calibration protocol for data analysis is provided in table 5.1. All the data is taken from TG-21 protocol [2] except the parameter for Solid Water which was taken from Seuntjens et al. [14] since TG-21 protocol did not provide values for Solid Water.

For the TRS-483 protocol analysis, the $k_{Q_{\text{msr}},Q_0}^{f_{\text{msr}},f_{\text{ref}}}$ factors for Exradin-A1SL, A16 and PTW 31010 in Solid Water and ABS phantoms (parallel and perpendicular orientations) were taken from table AI of the Mirzakhanian et al. [12] study. The parameters for the Lucy phantom have not been tabulated in the literature. In this study, the $k_{Q_{\text{msr}},Q_0}^{f_{\text{msr}},f_{\text{ref}}}$ factor for Lucy was determined using Eq. 14 of Mirzakhanian et al. [12]. An extra factor (exp(-μd)) was applied to Eq. 14 of Mirzakhanian et al. [12] to take into account the difference in beam attenuation of the PMMA with 7 cm radius used in this study and 8 cm radius used in the Mirzakhanian et al. [12] study as follows:

$$k_{Q_{\text{msr}},Q_0}^{f_{\text{msr}},f_{\text{ref}}} = k_{Q_{\text{msr}},Q_0}^{'f_{\text{msr}},f_{\text{ref}}}[(\rho_e^{rel}-1)b+1]\exp(-\mu d) \tag{5.1}$$

Table 5.1 Parameters for the Exradin-A1SL, Exradin-A16 and PTW-31010 ionization chambers in Solid Water (SW), PMMA and ABS phantoms used in this study for the TG-21 protocol dose calculation analysis.

parameter	Exradin-A1SL value [reference]	Exradin-A16 value [reference]	PTW-31010 value [reference]
N_X(R/nC)	61.77 [NRC calibration report]	336.8 [NRC calibration report]	30.63 [NRC calibration report]
A_{ion}	1 [NRC calibration report]	1 [NRC calibration report]	1 [NRC calibration report]
A_{wall}	0.992 [Standard Imaging Technical Note 4532-04]	0.994 [Standard Imaging Technical Note 4532-04]	0.992 [TG-21 protocol[2] Table III]
α	0.87 [TG-21 protocol[2] Figure 1]	0.63 [TG-21 protocol[2] Figure 1]	0.59 [TG-21 protocol[2] Figure 1]
$(\bar{L}/\rho)^{wall}_{air}$	1.000 [TG-21 protocol[2] Table I C-552]	1.000 [TG-21 protocol[2] Table I C-552]	1.103 [TG-21 protocol[2] Table I acrylic]
$(\bar{\mu}_{en}/\rho)^{air}_{wall}$	1.000 [TG-21 protocol[2] Table I C-552]	1.000 [TG-21 protocol[2] Table I C-552]	0.925 [TG-21 protocol[2] Table I acrylic]
$(\bar{L}/\rho)^{cap}_{air}$	1.000 [TG-21 protocol[2] Table I C-552]	1.000 [TG-21 protocol[2] Table I C-552]	1.103 [TG-21 protocol[2] Table I acrylic]
$(\bar{\mu}_{en}/\rho)^{air}_{cap}$	1.000 [TG-21 protocol[2] Table I C-552]	1.000 [TG-21 protocol[2] Table I C-552]	0.925 [TG-21 protocol[2] Table I acrylic]
$(\bar{\mu}_{en}/\rho)^{ABS}_{wall}$	1.072 [TG-21 protocol[2] (Table IX) polystyrene, C-552]	1.072 [TG-21 protocol[2] (Table IX) polystyrene, C-552]	0.994 [TG-21 protocol[2] (Table IX) polystyrene, acrylic]
$(\bar{\mu}_{en}/\rho)^{wall}_{SW}$	1.079 [Seuntjens et al. [14] Table II SW, C-552]	1.079 [Seuntjens et al. [14] Table II SW, C-552]	0.999 [Seuntjens et al. [14] Table II SW, PMMA]
$(\bar{\mu}_{en}/\rho)^{PMMA}_{wall}$	1.078 [TG-21 protocol[2] (Table IX) acrylic, C-552]	1.078 [TG-21 protocol[2] (Table IX) acrylic, C-552]	1.000 [TG-21 protocol[2] (Table IX) acrylic, acrylic]
N_{gas} (Gy/nC)	0.535 [TG-21 protocol[2] equation 6]	2.925 [TG-21 protocol[2] equation 6]	0.260 [TG-21 protocol[2] equation 6]
P_{wall} in ABS	0.968 [TG-21 protocol[2] equation 10]	0.977 [TG-21 protocol[2] equation 10]	0.991 [TG-21 protocol[2] equation 10]
P_{wall} in SW	0.975 [TG-21 protocol[2] equation 10]	0.983 [TG-21 protocol[2] equation 10]	0.995 [TG-21 protocol[2] equation 10]
P_{wall} in PMMA	0.987 [TG-21 protocol[2] equation 10]	0.991 [TG-21 protocol[2] equation 10]	1.000 [TG-21 protocol[2] equation 10]
P_{repl}	0.9947 [TG-21 protocol[2] Figure 5]	0.9968 [TG-21 protocol[2] Figure 5]	0.9928 [TG-21 protocol[2] Figure 5]
parameter	**med: SW**	**med: PMMA**	**med: ABS**
$(\bar{L}/\rho)^{med}_{air}$	1.1113 [Seuntjens et al. [14] Table I, Solid Water]	1.103 [TG-21 protocol[2] Table IV, acrylic]	1.113 [TG-21 protocol[2] Table IV, polystyrene]
$(\bar{\mu}_{en}/\rho)^{water}_{med}$	1.030 [Seuntjens et al. [14] Table II, Solid Water]	1.031 [TG-21 protocol[2] Table XII, acrylic]	1.036 [TG-21 protocol[2] Table XII, polystyrene]

From Eq. 5.1, $k'^{f_{msr},f_{ref}}_{Q_{msr},Q_0}$ values of 1.0070, 1.0174 and 1.0188 were applied for the Exradin-A1SL, A16, and PTW 31010 respectively. These data were obtained from table II of Mirzakhanian et al. [12] for perpendicular orientation. ρ_e^{rel} is the electron density of PMMA relative to the electron density of water and is taken to be 1.1563. b is a fitting parameter and is equal to 0.4284. The value for b is taken from Mirzakhanian et al. [12]. μ is the linear attenuation coefficient in PMMA for ^{60}Co (1.25 MeV) and is equal to 0.0725 cm^{-1}, and d =1 cm is the difference between the phantom radii used in Mirzakhanian et al. [12] (8 cm) and this study (7 cm).

We assumed that orientations 0° and 270° in the Lucy phantom had the same correction factor. Since in both cases, the chamber was positioned perpendicular to the symmetry axis of the LGK (Figure 5.1. d and e) and it was assumed that the source distribution was symmetric.

The $k^{f_{msr},f_{ref}}_{Q_{msr},Q_0}$ values for all the configurations discussed are listed in Table 5.2. The smallest calculated $k^{f_{msr},f_{ref}}_{Q_{msr},Q_0}$ factor was for Exradin A1SL in Lucy phantom (0.9993) and the largest correction was for PTW 31010 (1.0240) in the ABS phantom (perpendicular to the symmetry axis of the LGK).

5.3.3 Uncertainties

The sources of uncertainties are listed in table 5.3. The total uncertainty was estimated according to the uncertainty propagation method described in the Guide to the Expression of Uncertainty in Measurement (GUM) [15].

Table 5.2 $k^{f_{\text{msr}},f_{\text{ref}}}_{Q_{\text{msr}},Q_0}$ correction factors for Exradin-A1SL, A16 and PTW 31010 in LGK Solid Water (SW), Lucy and ABS phantoms for LGK Perfexion/Icon$^{\text{TM}}$ unit. The type A uncertainty on the EGSnrc data is less than 0.2% (k=1). The data for SW and ABS are taken from Table AI of Mirzakhanian et al. [12]. The data for Lucy is computed using Eq. 14 of Mirzakhanian et al. [12] and corrected for the differences in phantom size.

Chamber	**phantom**	**orientation**	$k^{f_{\text{msr}},f_{\text{ref}}}_{Q_{\text{msr}},Q_0}$
Exradin A1SL	SW	-	1.0125
	Lucy	0° and 270°	0.9993
	ABS	Parallel	1.0094
		Perpendicular	1.0130
Exradin A16	SW	-	1.0211
	Lucy	0° and 270°	1.0096
	ABS	Parallel	1.0162
		Perpendicular	1.0239
PTW 31010	SW	-	1.0093
	Lucy	0° and 270°	1.0110
	ABS	Parallel	1.0058
		Perpendicular	1.0240

Table 5.3 The estimated sources of uncertainties (%). The total combined estimate assumes that all sources of uncertainties are uncorrelated. The uncertainties on N_X and $\text{N}^{f_{\text{ref}}}_{D,w,Q_0}$ include contributions from establishing the source rates using the Canadian Primary Standards for exposure (a carbon walled cylindrical ionization chamber) and absorbed dose to water (a sealed water calorimeter) respectively, and short term statistical uncertainties observed during the measurements. These do not imply any long-term stability of the devices under test.

Source of uncertainty	TG-51	TG-21	TRS-483	references
Current	0.05	0.05	0.05	σ of consecutive measurements
P_{TP}	0.10	0.10	0.10	McEwen et al. [4]
P_{ion}	0.10	0.10	0.10	McEwen et al. [4]
P_{leak}	0.05	0.05	0.05	McEwen et al. [4]
P_{pol}	0.05	-	0.05	McEwen et al. [4]
Phantom diameter/density	0.30	0.30	0.30	Novotny Jr et al. [11]
$\text{N}^{f_{\text{ref}}}_{D,w,Q_0}$	0.43(A1SL)	-	0.43 (A1SL)	NRC calibration report
	0.46 (A16)	-	0.46 (A16)	NRC calibration report
	0.43 (31010)	-	0.43 (31010)	NRC calibration report
$k^{f_{\text{msr}},f_{\text{ref}}}_{Q_{\text{msr}},Q_0}$ type A	-	-	0.20	Mirzakhanian et al. [12]
$k^{f_{\text{msr}},f_{\text{ref}}}_{Q_{\text{msr}},Q_0}$ type B	-	-	0.40	Mirzakhanian et al. [12]
N_X	-	0.32 (A1SL)	-	NRC calibration report
	-	0.35 (A16)	-	NRC calibration report
	-	0.32 (31010)	-	NRC calibration report
P_{repl}	-	0.30	-	TRS-398[5]
P_{wall}	-	0.50	-	TRS-398[5]
$(\bar{L}/\rho)^{med}_{air}$	-	0.50	-	TRS-398[5]
$(\bar{\mu}_{en}/\rho)^{w}_{med}$	-	0.10	-	Andreo et al. [16]
$\text{N}_{gas}/\text{N}_X$	-	0.70	-	uncertainty propagation method described in GUM[15]
Total combined	0.55 (A1SL)	1.14 (A1SL)	0.71 (A1SL)	GUM[15]
	0.57 (A16)	1.15 (A16)	0.73 (A16)	GUM[15]
	0.55 (31010)	1.14 (31010)	0.71 (31010)	GUM[15]

5.4 Results

5.4.1 Influence of calibration protocol

Figure 5.3 shows the dose rates analyzed using TG-51, TG-21 and TRS-483 protocols for three chambers in different phantoms. The overall standard deviations on dose rate considering all phantoms and chambers in different orientations are 0.9%, 0.5% and 0.4% when using the TG-51, TG-21 and TRS-483 protocols respectively. Depending on the chamber and phantom used, the discrepancy in dose-rate between the TRS-483 and TG-21 protocols is found to range between 0.02% and 1.3%. However, the observed differences are within the combined standard uncertainty of the two protocols. The mean dose rate calculated using TRS-483 protocol (2.655 Gy/min) is 0.4% lower than TG-21 protocol (2.665 Gy/min) and the mean dose rate calculated using TG-51 protocol (2.624 Gy/min) is 1.2% and 1.6% lower compared to the TRS-483 and TG-21 protocols respectively.

5.4.2 Influence of phantom material

For each chamber, the standard deviation on measured dose rate across the three phantoms is less than 0.4% when using TRS-483 protocol (Figure 5.3.c) and 0.6% when using TG-51 and TG-21 protocols (Figure 5.3.a and Figure 5.3.b respectively). For all chambers, the TRS-483 protocol dose-rate is slightly higher in Solid Water phantom compared to the ABS and Lucy phantoms (Figure 5.3.c).

5.4.3 Influence of chamber type

For each phantom, the standard deviation on measured dose rate across the three chambers is less than 0.5% when using TRS-483 protocol (Figure 5.3.c), 0.7% when using TG-21 protocol (Figure 5.3.b) and 1.1% when using TG-51 protocol. In all phantoms, Exradin A1SL has the highest dose rate followed by PTW 31010 and Exradin A16 when calibrating using TRS-483 protocol. However, the differences are within uncertainties.

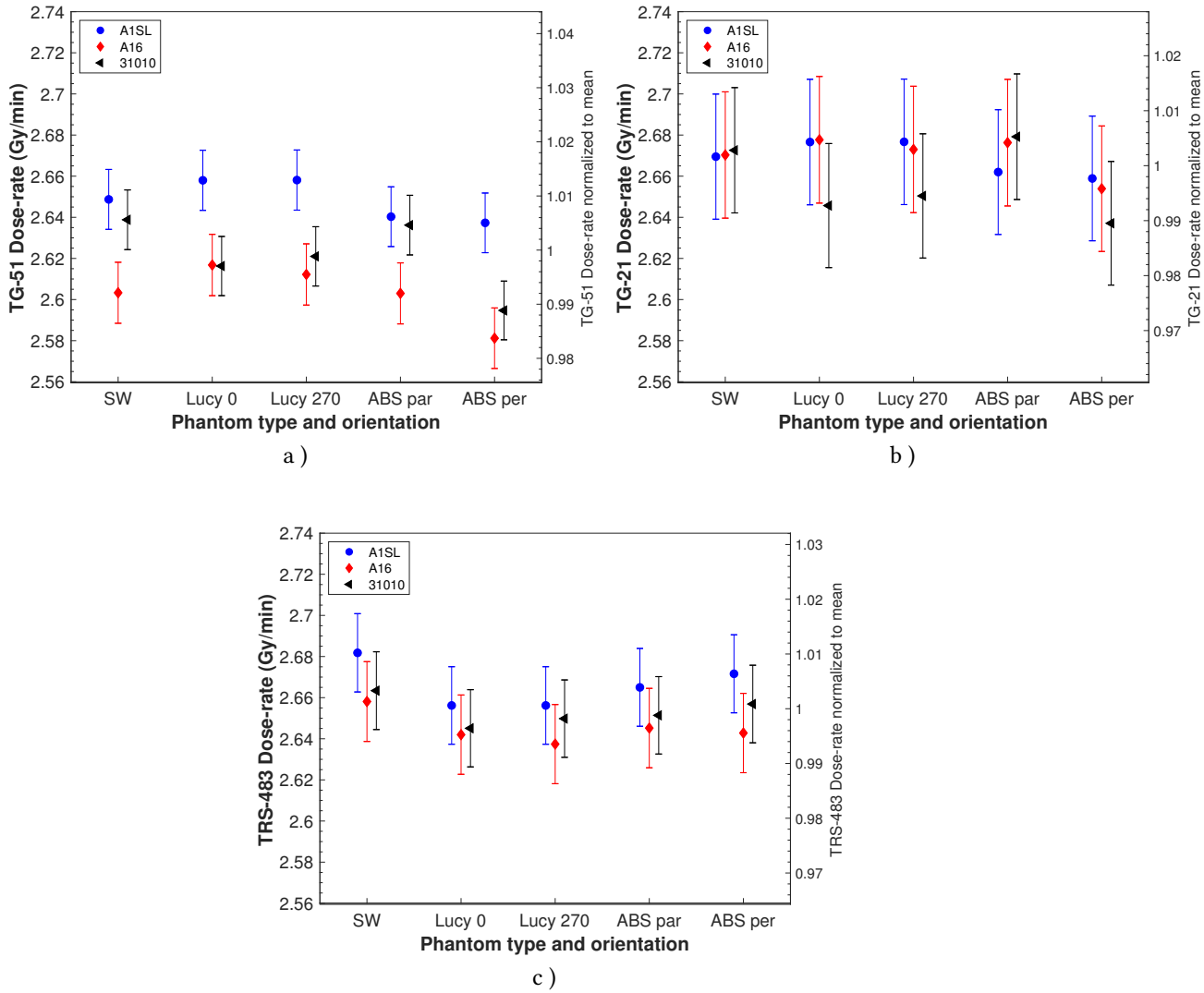

Figure 5.3 Dose rates calculated using a) TG-51, b) TG-21 and c) TRS-483 protocols for three chambers in different phantoms. The symbols $\perp$ and $\parallel$ represent the chambers orientations perpendicular and parallel to the z-axis respectively. The vertical axis on the right shows the values normalized to the mean dose rate calculated using each protocol.

5.4.4 Influence of chamber orientation

In the ABS phantom, the difference between dose-rate measured in parallel and perpendicular orientation was largest for PTW 31010 (1.6%) followed by Exradin A16 (0.8%) and Exradin A1SL (0.1%) when using TG-51 or TG-21 protocols. For all chambers, the TG-51 and TG-21 protocols dose-rate was larger in parallel orientation compared to the perpendicular orientation. A similar trend was observed in the Mirzakhanian et al. [12] study, where the differences in the MC calculated $k_{Q_{msr},Q_0}^{f_{msr},f_{ref}}$ values between parallel and perpendicular orientation were 1.8%, 0.8% and 0.4% for PTW 31010, Exradin-A16 and A1SL respectively. When the dose-rate was corrected using the MC $k_{Q_{msr},Q_0}^{f_{msr},f_{ref}}$ values [12], the differences between the dose-rate measured in parallel and perpendicular orientation in ABS phantom were reduced to 0.2% for all three chamber types.

In the Lucy phantom, the differences between the dose-rate measured at 0° and 270° orientations were negligible (less than 0.2%).

5.5 Discussion

Ideally, the measured dose-rate to water should be independent of the field size, chamber type, chamber orientation, phantom material and shape. Therefore the measured dose-rate to water should be identical for all the configurations shown in figure 5.1. Among the protocols used, the best level of agreement was observed for TRS-483 protocol (with the Mirzakhanian *et al* [12] correction factor data) and the worst for TG-51 protocol. This was expected since the $k_{Q_{msr},Q_0}^{f_{msr},f_{ref}}$ correction introduced in TRS-483 protocol takes into account the difference between the conditions of field size, geometry, phantom material of the conventional reference field and the LGK *msr* field. The TG-21 protocol does not take into account the conditions of field size and geometry, phantom shape nor different orientation of chamber, but there does take into account the composition of the phantom. The radiation field, phantom shape and material in LGK also do not meet the requirements of the TG-51 protocol. Despite the fact that TG-51 protocol is based on absorbed dose to water standards and is simpler to use, it has a lower stated combined uncertainty compared to TG-21 protocol for external beam reference dosimetry, the TG-51 protocol should not be used in reference dosimetry of LGK. This is mainly because water is the mandatory reference phantom material in the TG-51 protocol

(and does not correct for non-water phantom materials) while the TG-21 protocol allows and does take into account the use of non-water phantom material.

For all chambers, a slightly larger dose-rate was observed in Solid Water phantom relative to the ABS and Lucy phantoms when calibrating using TRS-483 protocol. This might be due to the non-uniformity of the phantoms, the phantom inserts, the air gaps around the chambers in Solid Water phantom (Figure 5.2) and the attenuation of the ABS frame (about 1.0%) [18] which have not been taken into account in this study. There might, also be heterogeneity in the phantom density and size [11]. Novotny Jr et al. [11] showed that the variations in terms of phantom size and mass density of the phantom [11] have 0.3% impact on dose-rate measurements. The 0.3% was also added to our uncertainty budget since the $k_{Q_{msr},Q_0}^{f_{msr},f_{ref}}$ factor used in this study corresponds to a nominal density of the phantom material [12].

For each phantom, the 0.5% standard deviation on dose rate determined using TRS-483 protocol across the three chambers is mainly due to the uncertainties in determination of absorbed dose to water calibration coefficient. Other factors are the uncertainties associated with $k_{Q_{msr},Q_0}^{f_{msr},f_{ref}}$ factor determination including type A and type B uncertainties (chamber material and dimensions) and differences in phantom inserts for each chamber. For TG-21 protocol, the 1.1% uncertainty on measured dose rate is due to uncertainties in determination of exposure calibration coefficient and the TG-21 protocol parameters listed in table 5.1.

The difference between the dose-rate measured in parallel and perpendicular orientations was noticeable for PTW 31010 (1.6%). This is due to the differences in electrode and stem perturbation factors in parallel and perpendicular orientations [12]. For the three chambers studied, the dose rate analyzed with TG-51 or TG-21 protocols was larger in parallel orientation compared to the perpendicular orientation. This was expected since some parts of the beam are attenuated by the chamber stem in the perpendicular orientation. The differences between the dose-rate measured in parallel and perpendicular orientations was reduced to 0.2% when using TRS-483 protocol with the orientation-dependent correction factor data of the Mirzakhanian *et al* [12] study. For the Lucy phantom, the differences between the dose-rate measured in 0° and 270° orientations were negligible since in the LGK unit the source distribution is approximately symmetric.

McDonald et al. [9] reported that TG-51 protocol resulted in 1.8% lower dose-rate compared to TG-21 protocol in Solid Water phantom for microchamber Exradin A14SL. This is comparable with our study, where the averaged TG-51 protocol dose-rate was 1.6% lower than

the average of TG-21 protocol dose rate. Drzymala et al. [8] also observed a lower dose rate when using TG-51 protocol compared to TG-21 protocol.

To compare our results with Drzymala et al. [17]'s data, we normalized the dose-rate obtained in the Solid Water phantom, analyzed using each protocols to the dose rate determined in the ABS phantom using TG-21 protocol (TG-21+ABS). The data is shown in figure 5.4.

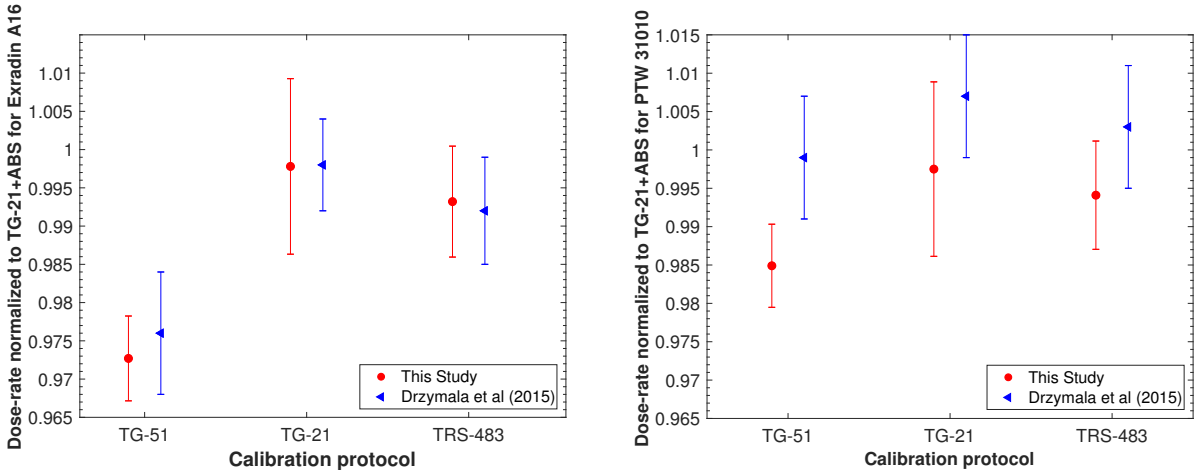

Figure 5.4 Dose rates measured using a) Exradin A16 and b) PTW 31010 in Solid Water phantom analyzed using TG-51, TG-21 and TRS-483 protocols using the Mirzakhanian *et al* [12] correction factor data, normalized to the dose rate measured in ABS phantom (parallel orientation) analyzed using TG-21 protocol (TG-21+ABS). It should be noted that the TG-21+ABS is not the reference in this study, it is chosen only for comparison with Drzymala et al. [8] study.

Figure 5.4 shows that our data in Solid Water phantom for Exradin A16 normalized to TG-21+ABS is in good agreement with Drzymala et al. [17] study (within 0.3%).

However, for PTW 31010, a difference of up to 1.4% was observed between our study and Drzymala et al. [17] when using TG-51 protocol.

Drzymala et al. [17] achieved a remarkably tight agreement between the mean dose-rate determined using the formalism introduced by Alfonso et al. [10] (current TRS-483 protocol) and TG-21+ABS (1.000$\pm$0.006). In contrast, in the present study we found a 0.4% difference between the mean dose rate calculated using TRS-483 protocol and same quantity determined

using TG-21 protocol. The difference between the dose rate analyzed using TG-21 and TRS-483 protocols was at most 1.3% (for the Exradin A16 in the Lucy phantom). This may be explained by the uncertainties involved in the measurements and the differences between the two studies. In this study we used three chambers instead of two and we used the Lucy phantom instead of the half-sphere water phantom used in Drzymala et al. [17] In addition, we studied different orientations of the chambers in ABS and Lucy phantom. We have also used the original TG-21 protocol parameters without data modification or updated values. In Drzymala et al. [17] study the $k_{Q_{msr},Q_0}^{f_{msr},f_{ref}}$ values were taken from Johansson et al. [7]; while in this study we used the $k_{Q_{msr},Q_0}^{f_{msr},f_{ref}}$ values calculated in Mirzakhanian et al. [12]. The Drzymala et al. [17] study was a multi-institutional comparison and the dose rate was determined with each protocol and compared to the dose rate measured using TG-21 protocol in ABS phantom since the measurements had been performed in different institutes. In this study, all the measurement were done at a single institute.

Our work is relevant in the context of the forthcoming AAPM TG-178 [19] protocol for GK which follows the same recommendations and data for reference dosimetry as TRS-483. Our work can be extended to include more chambers of different types provided the correction factors can be determined using MC calculations or experiments. Finally, direct calorimetric measurements using approaches based on small volume calorimeters could be used to put these results on an absolute basis[20, 21].

5.6 Conclusion

In this study, dose rate measurements were performed on a LGK Icon unit using three ionization chambers Exradin-A1SL, A16 and PTW 31010 in Solid Water, Lucy and ABS phantoms. The dose-rate was determined using three protocols: the TG-51, TG-21 and TRS-483. The $k_{Q_{msr},Q_0}^{f_{msr},f_{ref}}$ values (introduced in TRS-483 protocol) calculated in Mirzakhanian et al. [12] were validated through measurements. The influence of calibration protocol, phantom material, chamber type and orientation of chamber with respect to the LGK were also studied. Applying the $k_{Q_{msr},Q_0}^{f_{msr},f_{ref}}$ values to the measured dose rates in LGK Icon unit for three chambers and three phantoms resulted in dose rates that were consistent to within 0.4%.

Following the TRS-483 protocol using the correction factor data published in Mirzakhanian *et al* [12] improves consistency of the results compared to the TG-51 and TG-21 protocols especially when the chamber is positioned in different orientations with respect to the LGK

unit (from 1.6% in TG-51/TG-21 protocols to 0.2% in TRS-483 protocol).

Acknowledgments

This work was supported financially by the CREATE Medical Physics Research Training Network grant of the Natural Sciences and Engineering Research Council (Grant number: 432290) and NSERC RGPIN-2019-06746.

Bibliography

[1] M Zeverino, M Jaccard, D Patin, N Ryckx, M Marguet, C Tuleasca, L Schiappacasse, J Bourhis, M Levivier, FO Bochud, and R Moeckli. Commissioning of the Leksell Gamma Knife Icon^{TM}. *Medical physics*, 44(2):355–363, 2017.

[2] AAPM Task Group 21, Radiation Therapy Committee. A protocol for the determination of absorbed dose from high-energy photon and electron beams. *Medical Physics*, 10(6): 741–771, 1983.

[3] PR Almond, PJ Biggs, BM Coursey, WF Hanson, MS Huq, R Nath, and DWO Rogers. AAPM's TG-51 protocol for clinical reference dosimetry of high-energy photon and electron beams. *Medical physics*, 26(9):1847–1870, 1999.

[4] M McEwen, L DeWerd, G Ibbott, D Followill, DWO Rogers, S Seltzer, and J Seuntjens. Addendum to the AAPMs TG-51 protocol for clinical reference dosimetry of high-energy photon beams. *Medical physics*, 41(4), 2014.

[5] P Andreo, DT Burns, K Hohlfeld, M Huq, T Kanai, F Laitano, V Smyth, and S Vynckier. TRS-398: Absorbed dose determination in external beam radiotherapy: An international code of practice for dosimetry based on standards of absorbed dose to water. *International Atomic Energy Agency*, 420, 2001.

[6] H Palmans, P Andreo, K Christaki, MS Huq, and J Seuntjens. TRS-483: Dosimetry of small static fields used in external beam radiotherapy: an international code of practice for reference and relative dose determination. *International Atomic Energy Agency, Vienna*, 2017.

[7] J Johansson, B Gorka, J Novotny Jr, JD Bourland, J Bhatnagar, G Bednarz, RCM Best, L Persson, H Nordstrom, and O Svarm. Monte carlo calculated and experimentally verified correction factors for clinical reference dosimetry for the Leksell Gamma Knife: Application of a new IAEA dosimetry formalism. In *Plenary Oral Presentation at the 16th International Meeting of the Leksell Gamma Knife Society*, page 69, 2012.

[8] RE Drzymala, PE Alvarez, G Bednarz, JD Bourland, LA DeWerd, L Ma, SG Meltsner, G Neyman, J Novotny Jr, PL Petti, MJ Rivard, AS Shiu, and SJ Goetsch. A round-robin gamma stereotactic radiosurgery dosimetry interinstitution comparison of calibration protocols. *Medical physics*, 42(11):6745–6756, 2015.

[9] D McDonald, C Yount, N Koch, M Ashenafi, J Peng, and K Vanek. Calibration of the Gamma Knife Perfexion using TG-21 and the solid water Leksell dosimetry phantom. *Medical physics*, 38(3):1685–1693, 2011.

[10] R Alfonso, P Andreo, R Capote, MS Huq, W Kilby, P Kjäll, TR Mackie, H Palmans, K Rosser, J Seuntjens, W Ullrich, and S Vatnitsky. A new formalism for reference dosimetry of small and nonstandard fields. *Medical physics*, 35(11):5179–5186, 2008.

[11] JN Jr, JP Bhatnagar, HT Chung, J Johansson, G Bednarz, L Ma, and MS Huq. Assessment of variation in Elekta plastic spherical-calibration phantom and its impact on the Leksell Gamma Knife calibration. *Medical physics*, 37(9):5066–5071, 2010.

[12] L Mirzakhanian, H Benmakhlouf, F Tessier, and J Seuntjens. Determination of $k_{Q_{\mathrm{msr}},Q_0}^{f_{\mathrm{msr}},f_{\mathrm{ref}}}$ factors for ion chambers used in the calibration of Leksell Gamma Knife Perfexion model using EGSnrc and PENELOPE Monte Carlo codes. *Medical physics*, 45(4):1748–1757, 2018.

[13] MJ Butson, T Cheung, and KN Peter. Solid water phantom heat conduction: Heating and cooling rates. *Journal of Medical Physics/Association of Medical Physicists of India*, 33(1): 24, 2008.

[14] J Seuntjens, M Olivares, M Evans, and E Podgorsak. Absorbed dose to water reference dosimetry using solid phantoms in the context of absorbed-dose protocols. *Medical physics*, 32(9):2945–2953, 2005.

[15] BN Taylor, CE Kuyatt. Guidelines for Evaluating and Expressing the Uncertainty of NIST Measurement Results, [Online]. Available: http://physics.nist.gov/TN1297 [2007, May]. *National Institute of Standards and Technology,* Gaithersburg, MD.

[16] P Andreo, DT Burns, and F Salvat. On the uncertainties of photon mass energy-absorption coefficients and their ratios for radiation dosimetry. *Physics in Medicine & Biology*, 57(8): 2117, 2012.

[17] RE Drzymala, RC Wood, and J Levy. Calibration of the Gamma Knife using a new phantom following the AAPM TG51 and TG21 protocols. *Medical physics*, 35(2):514–521, 2008.

[18] JP Bhatnagar, J Novotny Jr, MA Quader, G Bednarz, and MS Huq. Unintended attenuation in the Leksell Gamma Knife Perfexion^{TM} calibration-phantom adaptor and its effect on dose calibration. *Medical physics*, 36(4):1208–1211, 2009.

[19] S Goetsch. SU-F-P-15: Report On AAPM TG 178 Gamma Knife Dosimetry and Quality Assurance. *Medical physics*, 43.6Part5, 3361-3361, 2016.

[20] J Renaud, A Sarfehnia A, J Bancheri J, J Seuntjens. Aerrow: A probe-format graphite calorimeter for absolute dosimetry of high-energy photon beams in the clinical environment. *Medical physics*, 45(1):414-428, 2018.

[21] B Cote, J Seuntjens, A Sarfehnia, J Renaud. Aerrow-Mini: A Probe-Format Graphite calorimeter for absolute dosimetry of small high-energy photon fields. *International Symposium on Standards, Applications and Quality Assurance in Medical Radiation Dosimetry (IDOS-2019).*

Chapter 6

Extending the IAEA-AAPM TRS-483 methodology for radiation therapy machines with field sizes down to 10×2 cm^2

Lalageh Mirzakhanian, Rostem Bassalow, Calvin Huntzinger and Jan Seuntjens

Submitted to Medical Physics journal, July 2019

6.1 Preface

In this chapter, the methodology for reference dosimetry of small static fields described in IAEA-AAPM TRS-483 was extended to field sizes down to 2 cm on a side. The motivation of this work was to provide a methodology for the reference dosimetry of the new RefleXion BgRT machine where the field size closest to the conventional reference field is 10×2 cm^2 or 10×3 cm^2. In this chapter, two approaches were provided for calibration of generic machines with 6 MV FFF beams and field sizes down to 10×2 cm^2 (similar to RefleXion BgRT). The results of two methodologies were compared.

Abstract

Purpose: The purpose of this study is to provide a calibration methodology for radiation therapy machines where the closest field to the conventional reference field may not meet the lateral charged particle equilibrium (LCPE) condition of the machine specific reference (*msr*) field. We provided two methodologies by extending the International Atomic Energy Agency (IAEA) and the American Association of Physicists in Medicine (AAPM) TRS-483 code of practice (COP) [1] methodology for the calibration of radiation therapy machines with 6 MV flattening filter free (FFF) beam and with field sizes down to 10×2 cm^2.

Methods: Two methods of calibration were provided following the TRS-483. In calibration Method I, the generic correction factors $k_{Q_A,Q_0}^{f_A,f_{ref}}$ were calculated using MC for seven detectors and rectangular field sizes ranging from 10×1.5 cm^2 to 10×10 cm^2. In calibration Method II, we extended TRS-483s table 16 for equivalent uniform square *msr* field size of rectangular fields down to 10×2 cm^2. The beam quality specifier for a hypothetical 10×10 cm^2 field was derived from the beam quality specifier determined for the field dimensions between 2 and 10 cm by extending the Eq. 28 and 29 provided in the TRS-483 to 2 cm field widths. Since the $k_Q^{f_{ref}}$ values tabulated in table 28 of TRS-483 are provided only for large reference chambers, we calculated the $k_Q^{f_{ref}}$ values analytically for our beam quality specifier and chambers used, using the data in TRS-398 [2].

Results: The correction factors calculated using the first method for chambers with electrode made of C552 almost did not vary across the different field sizes studied (within 0.1%) while it varied by 1.6% for IBA CC01 with electrode made of steel. Extending the equivalent field and beam quality specifier determination methodology of TRS-483 resulted in a maximum error of 1.3% on the beam quality specifier for the 2×2 cm^2 field size. However this had a negligible impact on the correction factor $k_{Q_A,Q_0}^{f_A,f_{ref}}$ (less than 0.1%). For chambers with C552 and Al electrode material, the correction factors determined using the two methods of calibration were the same to within 0.5%. However, for the chambers with electrode made of higher atomic number (Z), the difference between the two methodologies could be as large as 1.6%. It was shown that this difference can be reduced to 0.4% if central electrode perturbation effects and $k_{Q_A^{FFF},Q^{FFF}}^{f_A,f_{ref}}$ values introduced in TRS-483 were taken into account.

Conclusions: In this study, applying the correction calculated using the calibration Method I to the chamber reading improved the consistency on a absorbed dose determination from 0.57% to 0.06% standard deviation (except for the Exradin A16). For this reason we recommend using calibration Method I. If the $k_{Q_A,Q_0}^{f_A,f_{ref}}$ values are not available for the user's detector,

calibration Method II can be used to predict the correction factors. However, the second methodology should not be used for chambers with electrode made of high Z material unless the electrode perturbation effects and $k_{Q_A^{FFF},Q^{FFF}}^{f_A,f_{ref}}$ values are taken into account.

6.2 Introduction

Small fields in radiation therapy (RT) are characterized by one or more of three conditions: the size of the ionization chamber comparable to the beam dimensions, partial source occlusion of the primary photon source or a loss of lateral charged particle equilibrium (LCPE) on the beam axis [1, 3]. Charged particle equilibrium (CPE) occurs when the charged particles of a given energy from regions outside the beam central axis are scattered toward the central region and compensate for charged particles of the same energy leaving the central region. LCPE is a qualitative term given to CPE when associated with the lateral (perpendicular to beam axis) movement of charged particles in laterally limited beam conditions [4]. The number of radiation therapy machines that make use of small fields have increased significantly in recent years. Dosimetric uncertainties in small fields have led to special calibration protocols that differ from conventional radiation therapy protocols such as the TRS-398 COP [2] and AAPM TG-51 Protocol [5, 6].

A general formalism for reference dosimetry of small fields is provided in the recently published TRS-483 COP [1] and its summary [7]. The TRS-483 COP deals with two issues in contemporary RT dosimetry: (1) specialized machines cannot realise the standard reference calibration conditions and extra factors are involved in the formalism and (2) small field output measurements using detectors require correction factors, and these are provided in the protocol. This formalism introduces the machine specific reference field (*msr*) [1, 8], defined as the field size that has dimensions as close as possible to those of conventional reference fields and extends at least a distance r_{LCPE} beyond the outer boundaries of the reference ionization chamber [1]. The r_{LCPE} can be defined as the minimum radius of a circular field for which the absorbed dose to water in the center of the field is related by a constant factor to electronic kerma in water [1, 4].

Three different methods are suggested in the IAEA TRS-483 COP for reference dosimetry of *msr* fields [1, 7].

In the first approach, the standards dosimetry laboratory provides the user with a calibration coefficient for an ion chamber measured specifically for their *msr* field. This is the preferred, as yet theoretical approach, as these calibrations are currently not available.

The second approach is the more common approach. The standards laboratory provides the user with a calibration coefficient for an ionization chamber determined in a calibration beam of quality (Q_0) for a conventional 10×10 cm^2 reference field. In this approach, a beam quality correction factor ($k_{Q_{\mathrm{msr}},Q_0}^{f_{\mathrm{msr}},f_{\mathrm{ref}}}$) is needed to correct the chamber response for the difference between the *msr* field (f_{msr}) with beam quality of Q_{msr} and the reference field (f_{ref}) with beam quality (Q_0). The $k_{Q_{\mathrm{msr}},Q_0}^{f_{\mathrm{msr}},f_{\mathrm{ref}}}$ is defined as

$$k_{Q_{\mathrm{msr}},Q_0}^{f_{\mathrm{msr}},f_{\mathrm{ref}}} = \frac{D_{\mathrm{w},Q_{\mathrm{msr}}}^{f_{\mathrm{msr}}} / M_{Q_{\mathrm{msr}}}^{f_{\mathrm{msr}}}}{D_{\mathrm{w},Q_0}^{f_{\mathrm{ref}}} / M_{\mathrm{w},Q_0}^{f_{\mathrm{ref}}}}, \tag{6.1}$$

In Eq. 6.1, the $D_{\mathrm{w},Q_{\mathrm{msr}}}^{f_{\mathrm{msr}}}$ and $D_{\mathrm{w},Q_0}^{f_{\mathrm{ref}}}$ are the absorbed dose to water at a point in *msr* and reference fields, respectively. $M_{Q_{\mathrm{msr}}}^{f_{\mathrm{msr}}}$ and $M_{\mathrm{w},Q_0}^{f_{\mathrm{ref}}}$ are the readings of chamber in the *msr* and reference fields, respectively, both corrected for influence quantities.

A third approach is recommended when correction factors in the second method for the ionization chamber used are not available. In this approach, the beam quality specifier for a hypothetical 10×10 cm^2 field is derived from a beam quality specifier measurement performed directly in the *msr* field. This method is based on a model proposed by Palmans [9] where BJR Suppl 25 tissue phantom ratio (TPR) data were used and fitted for square field sizes ranging from 4 cm to 40 cm and photon energies from 4 MV to 12 MV. For the determination of the beam quality the equivalent *msr* field is determined by equating the amount of photon scatter in-phantom. The beam quality conversion factor corresponding to the hypothetical 10×10 cm^2 field is used to look up the beam quality conversion factor in standard reference dosimetry protocols. If the beam is an FFF beam, the beam quality conversion factor should be corrected for the difference in response of the chamber due to the different secondary charged particle spectra of both beam qualities changing the stopping-power ratios, perturbation correction ratios. The volume averaging effect due to the non-uniformity of the lateral beam profile of the FFF beam [1] should also be corrected for. With these extra corrections, the absorbed dose to water at the reference depth in a water phantom irradiated by a beam quality $Q_{\mathrm{msr}}^{\mathrm{FFF}}$ in the *msr* field and FFF beams ($D_{\mathrm{w},Q_{\mathrm{msr}}^{\mathrm{FFF}}}^{f_{\mathrm{msr}}}$) is determined using Eq. 6.2.

$$D_{\mathrm{w},Q_{\mathrm{msr}}^{\mathrm{FFF}}}^{f_{\mathrm{msr}}} = M_{Q_{\mathrm{msr}}^{\mathrm{FFF}}}^{f_{\mathrm{msr}}} N_{D,\mathrm{w},Q_0}^{f_{\mathrm{ref}}} k_{Q^{\mathrm{WFF}},Q_0}^{f_{\mathrm{ref}}} k_{Q^{\mathrm{FFF}},Q^{\mathrm{WFF}}}^{f_{\mathrm{ref}}} k_{Q_{\mathrm{msr}}^{\mathrm{FFF}},Q^{\mathrm{FFF}}}^{f_{\mathrm{msr}},f_{\mathrm{ref}}} \tag{6.2}$$

where, the $N_{D,\mathrm{w},Q_0}^{f_{\mathrm{ref}}}$ is the absorbed dose to water calibration coefficient of the ionization chamber measured at the standards laboratory for a conventional 10×10 cm^2 reference field in beam quality (Q_0). The $k_{Q^{\mathrm{WFF}},Q_0}^{f_{\mathrm{ref}}}$ is the beam quality correction factor for a "with flattening filter" (WFF) beam that correct for the difference between the response of the ionization chamber in a conventional reference calibration field with beam quality Q_0 at the standards laboratory and the response of the ionization chamber in a conventional 10×10 cm^2 reference field with beam quality Q at the same machine as the *msr* field. The $k_{Q^{\mathrm{WFF}},Q_0}^{f_{\mathrm{ref}}}$ is obtained from TRS-398 or TG-51 for a WFF beam with the same beam quality specifier as the one determined for FFF beam. The $k_{Q^{\mathrm{FFF}},Q^{\mathrm{WFF}}}^{f_{\mathrm{ref}}}$ factor takes into account the difference in response of the ionization chamber between WFF and FFF beams. The $k_{Q_{\mathrm{msr}}^{\mathrm{FFF}},Q^{\mathrm{FFF}}}^{f_{\mathrm{msr}},f_{\mathrm{ref}}}$ corrects for the different response of ionization chamber in a hypothetical 10×10 cm^2 field with beam quality Q^{FFF} using the same machine as *msr* field and the response of the ionization chamber in the *msr* field with beam quality $Q_{\mathrm{msr}}^{\mathrm{FFF}}$.

The calibration of radiation therapy machines where the field size closest to the conventional reference field size does not meet the *msr* condition is challenging. One example is the new RefleXion$^{\mathrm{TM}}$ biology-guided radiotherapy (BgRT) machine (Hayward, CA, USA). The design of the RefleXion BgRT machine restricts the maximum field size to 2 or 3 cm in the Y dimension (along the axis of the bore) and 40 cm in the X dimension (40×2 cm^2 or 40×3 cm^2) at a source-to-axis distance (SAD) of 85 cm. The field dimensions closest to the conventional reference field in this machine will thus be 10×2 cm^2 or 10×3 cm^2. The beam is nominally 6 MV and is flattening filter free (FFF). The calibration of this machine can become challenging since the TRS-483 cannot be directly used for the calibration of this system. First of all, the 10×2 cm^2 field size may not meet the LCPE condition of *msr* fields depending on the detector used. Secondly, when using the third approach of TRS-483, the Eq. 28 and 29 provided in the TRS-483 for deriving the beam quality specifier are limited to 4 cm field size. The equivalent field size given in table 16 of the CoP is also limited to 3 cm field size. Furthermore, the beam quality correction factor ($k_Q^{f_{\mathrm{ref}}}$) values tabulated in table 28 and 29 are provided only for large reference chambers not suitable for fields as small as 2 or 3 cm.

Our hypothesis is that even if the *msr* condition (the field size has to extend at least a distance r_{LCPE} beyond the outer boundaries of the reference ionization chamber) is not preserved, depending on the detector used, appropriate correction factors determined for reference detectors can still be applied for the purpose of reference dosimetry. This hypothesis is supported by the well-established practice, recommended in TRS-483 for the Leksell Gamma

Knife®(LGK) unit (Elekta Instruments, Stockholm, Sweden). Value of r_{LCPE} for the LGK (^{60}Co) has been estimated to be 0.6 cm [10]. In that case, depending on the detector used the collimator field sizes of 1.6 cm (Perfexion$^{\mathrm{TM}}$) or 1.8 cm (4C) may not meet the LCPE conditions. Further support for this hypothesis stems from the fact that the literature and TRS-483 has published highly accurate field output correction factors for small fields for a wide variety of ionization chambers (and other detectors), supporting the idea that for fields comparable or slightly below LCPE conditions accurate absorbed dose determination is possible.

We introduce a "sub-r_{LCPE} reference field" termed *A* and the purpose of this study is to test whether the TRS-483 COP [1] methodology can be extended to calibrating radiation therapy machines with rectangular fields down to to 10×2 cm^2 (for 6 MV FFF). In this study, we vary the small side of the field size from 1.5 to 10 cm (i.e., 10×1.5 cm^2, 10×2 cm^2, 10×3 cm^2, 10×5 cm^2 and 10×10 cm^2 field sizes at source-to-detector distance (SDD) 85 cm) on the Varian TrueBeam 6 MV FFF beam. We verify whether measurements with four different chamber types in the 10×1.5 cm^2, 10×2 cm^2 and 10×3 cm^2 field sizes lead to consistent absorbed doses in the TrueBeam 6 MV FFF system.

We follow two calibration approaches (the second and third approaches specified in TRS-483). In the first method, the generic correction factors ($k_{Q_{\mathrm{msr}},Q_0}^{f_{\mathrm{msr}},f_{\mathrm{ref}}}$) are calculated using MC for several chambers and validated through measurements. In a second method, we expand the method for equivalent field widths down to 2 cm following the same methodology as described in the TRS-483. We also extend Eq. 28 and 29 provided in the TRS-483 for deriving the beam quality specifier down to field widths of 2 cm. Since the $k_Q^{f_{\mathrm{ref}}}$ values tabulated in table 28 are provided only for reference chambers with volume over 0.3 cm^2, we calculate values of $k_Q^{f_{\mathrm{ref}}}$ for our beam quality specifier and chambers used from data in TRS-398 [2]. As per TRS-483, volume averaging and water-to-air stopping power ratio corrections are also applied to the values to correct for the differences between the WFF and FFF beams. The accuracy of method II is assessed by comparing to direct MC data from method I.

6.3 Materials and Methods

6.3.1 Monte Carlo beam models and beam quality index

The Varian TrueBeam linear accelerator was modeled using BEAMnrc [11] MC code. The beam model has been previously validated for 6 MV FFF [12] and 10 MV FFF beam energies by

comparing the calculated beam profile, percent depth dose and field output factor values with the measurements. In the MC simulation, the electron (ECUT) and photon (PCUT) cut-off values were set to 700 keV and 10 keV respectively. Directional bremsstrahlung splitting [13] (DBS) was used as the variance reduction method in BEAMnrc with the splitting number of 1000.

For the $TPR_{20,10}(10)$ calculations, the averaged absorbed dose to a small volume of water (0.15 cm radius sphere) was calculated at depths of 10 and 20 cm in a water phantom ($30 \times 30 \times 30$ cm^3) with SDD 100 cm using EGSnrc `egs_chamber` user code [14]. The BEAMnrc 6 MV FFF and 10 MV FFF beam models were used as a shared library in `egs_chamber` calculations. The number of histories in `egs_chamber` varied to achieve a 1-sigma type A uncertainty of 0.05% or less on the absorbed dose in the small volume. Similarly, the $TPR_{20,10}(S)$ for square field sizes of S: 2, 2.5, 3, 3.5, 4, 6, 8 and 10 cm at SDD 100 cm was calculated for the TrueBeam 6 MV FFF. The dependency of $TPR_{20,10}(S)$ on distance SDD was also studied by repeating the calculations for three square field size of 2, 4 and 10 cm at SDD 85 cm. We expect the $TPR_{20,10}(10)$ to be almost insensitive to SDD [9]. The $TPR_{20,10}(S)$ was also measured in a Varian STX TrueBeam 6 MV FFF beam using the Exradin A1SL chamber for square field sizes of 2, 2.5, 3, 3.5, 4, 6, 8 and 10 cm defined by jaws for SDD 100 cm.

BEAMnrc was used to create the phase space files for a 10×10 cm^2 field size at an source-to-surface (SSD) of 100 cm for the 6 MV FFF and 10 MV FFF beams. The phase space file was used as an input for the DOSXYZnrc user-code [15]. Value of $\%dd(10,10)_x$ was calculated using DOSXYZnrc with only the photon part of phase space file. The mean absorbed dose to water was calculated along the central axis of a cubic phantom ($30 \times 30 \times 30$ cm^3) with the scoring voxel size of $1 \times 1 \times 0.1$ cm^3 (0.1 cm along the depth). The number of primary particles was adjusted to achieve a 1-sigma type A uncertainty of better than 0.1% on the absorbed dose at 10 cm depth and at depth of maximum dose (z_{max}). Both the $\%dd(10,S)$ and $\%dd(10,S)_x$ for equivalent square field sizes of S: 2, 2.5, 3, 3.5, 4, 6, 8 and 10 cm at SSD 100 cm were also calculated using all and the photon part of phase space file in DOSXYZnrc, respectively, for the 6 MV FFF beam. The size of the scoring voxel also varied for different field sizes: $0.5 \times 0.5 \times 0.1$ cm^3 (for fields smaller than 3.5×3.5 cm^2), $0.6 \times 0.6 \times 0.1$ cm^3 (for 4×4 cm^2 and 6×6 cm^2) and $0.8 \times 0.8 \times 0.1$ cm^3 (for 8×8 cm^2). The dependency of $\%dd(10,S)_x$ on distance SSD was studied by repeating the calculations for square field sizes of 2, 4 and 10 cm at SSD 85 cm.

6.3.2 Machine specific reference condition

In order for a field to be a machine-specific reference field, its full width at half maximum (FWHM) has to satisfy the following condition [1].

$$FWHM \geq 2r_{\mathrm{LCPE}} + d \tag{6.3}$$

Where d is the greatest distance between two points on the edges of the sensitive volume of detector. r_{LCPE} is the lateral charge particle equilibrium range.

In-plane (Y) profile measurements were performed using a TrueBeam 6 MV FFF machine. Field sizes of 10×3 cm^2, 10×2 cm^2 and 10×1.5 cm^2 were studied. The field sizes were defined by the jaws at SSD 85 cm. Four chambers including Exradin-A1SL, A26, IBA CC01 and PTW 31010 were placed at a depth of 10 cm and SSD of 85 cm using the IBA blue water phantom (IBA, Belgium). The chambers were oriented with their major axis parallel to the long axis of the beam (X). In-plane profile measurements were taken for each field size. The FWHM of the in-plane beam profile was measured for all three field sizes and chambers.

The parameter d in Eq. 6.3 was estimated for the four chambers by comparing the longitudinal and radial dimensions as per TRS-483.

To determine the r_{LCPE}, TRS-483 provides an expression for r_{LCPE} as a function of beam quality index (Eq. 3 and 4 of TRS-483). These equations are based on a MC study by Papaconstadopoulos [16] where the r_{LCPE} was determined as a function of the beam quality index in the open beam. However, Eq. 3 and 4 of TRS-483 were derived only for WFF beams and were not verified for FFF beams. Therefore, in this study we determined the r_{LCPE} directly using MC for the TrueBeam 6 FFF and 10 FFF using a methodology similar as in Papaconstadopoulos [16] and we verified the accuracy of Eq. 3 and 4 of TRS-483 for r_{LCPE} in FFF beams.

6.3.3 Determination of r_{LCPE}

The DOSRZnrc [17] user code was used in this study to calculate the central axis absorbed dose and kerma to water similar to the approach used in Papaconstadopoulos [16] study. In the DOSRZnrc simulation, the ECUT and PCUT values were set to 521 and 10 keV respectively. Photon forcing was used as variance reduction technique. A water phantom was modeled as a cylinder with radius 15 cm and a thickness of 30 cm. The incident beam was a point source and defined at the surface of the phantom at a SSD 100 cm on the central axis. The beam radius was varied between 0.25 and 1.8 cm at SSD 100 cm. The absorbed dose and kerma to

water were scored at depth 5.25 cm in a cylinder with 0.5 cm thickness and 0.05 cm radius. The TrueBeam 6 MV FFF and 10 MV FFF spectra were used in the DOSRZnrc simulations and these spectra were obtained from the phase space data [18]. Electronic (collision) kerma K_{el} was be determined from kerma K and the radiative fraction g ($K_{\mathrm{el}} = K(1-g)$). The beam radius at which the ratio of absorbed dose to electronic kerma becomes constant was chosen as r_{LCPE}. Since g is constant over all field sizes, we determined the ratio of absorbed dose to kerma to establish r_{LCPE} [10].

Using $\mathrm{TPR}_{20,10}(10)$ and $\%dd(10,10)_{\mathrm{x}}$ (calculated in section 6.3.1) for the TrueBeam 6 MV FFF and 10 MV FFF beams along with Eq. 3 and 4 of TRS-483 respectively, r_{LCPE} was calculated and compared to the value of r_{LCPE} determined from the absorbed dose to electronic kerma ratio to verify the fit provided in TRS-483 (Eq. 3 and 4).

Using the measured FWHM, the estimated d and the r_{LCPE} determined from MC, the condition of Eq. 6.3 was verified for the three field sizes and four chamber types studied.

6.3.4 Calibration method I and experimental validation: Chamber calibrated for a conventional reference field, with generic beam quality correction factors ($k^{f_{\mathbf{A}},f_{\mathbf{ref}}}_{Q_{\mathbf{A}},Q_{\mathbf{0}}}$) available

This method is equivalent to calibration method (b) in the TRS-483 protocol but extended to field sizes near LCPE. To this end, we calculated $k^{f_{\mathrm{msr}},f_{\mathrm{ref}}}_{Q_{\mathrm{msr}},Q_0}$ correction factors independently. Assuming that the chamber reading is proportional to the absorbed dose in the chamber Eq. 6.1 can be calculated using MC as

$$k^{f_{\mathrm{msr}},f_{\mathrm{ref}}}_{Q_{\mathrm{msr}},Q_0} = \frac{D^{f_{\mathrm{msr}}}_{\mathrm{w},Q_{\mathrm{msr}}} / D^{f_{\mathrm{msr}}}_{cav,Q_{\mathrm{msr}}}}{D^{f_{\mathrm{ref}}}_{\mathrm{w},Q_0} / D^{f_{\mathrm{ref}}}_{cav,Q_0}}, \tag{6.4}$$

where $D^{f_{\mathrm{msr}}}_{cav,Q_{\mathrm{msr}}}$ and $D^{f_{\mathrm{ref}}}_{cav,Q_0}$ are mean absorbed dose to the sensitive volume of the chamber in the *msr* and reference fields respectively. The field A has dimensions as close as possible to those of the conventional reference field, however, A may or may not meet the LCPE condition (Eq. 6.3). Assuming there is no effects in intrinsic response of the chamber, the correction factor to determine absorbed dose in field A is:

$$k^{f_{\mathrm{A}},f_{\mathrm{ref}}}_{Q_{\mathrm{A}},Q_0} = \frac{D^{f_{\mathrm{A}}}_{\mathrm{w},Q_{\mathrm{A}}} / D^{f_{\mathrm{A}}}_{cav,Q_{\mathrm{A}}}}{D^{f_{\mathrm{ref}}}_{\mathrm{w},Q_0} / D^{f_{\mathrm{ref}}}_{cav,Q_0}}, \tag{6.5}$$

This work provides Monte Carlo calculated values of $k_{Q_A,Q_0}^{f_A,f_{ref}}$ for fields $10 \times y$ cm^2 with y = 1.5 cm, 2 cm, 3 cm, 5 cm and 10 cm. The types and specifications of the detectors investigated in this work are summarized in Table 6.1. These chambers (except Exradin A26) are recommended in the TRS-483 protocol [1] for reference dosimetry of *msr* fields smaller than 6×6 cm^2. Some of them do not meet the reference chamber criteria but have been used in the calibration of Gamma Knife. The ionization chambers were modeled in this study using blue prints provided by manufacturers using EGSnrc `egs++` [19]'s geometry package [20, 21].

Table 6.1 Summary of chambers and their characteristics used in this study. The electrode materials are air equivalent plastic (C552), silver-plated copper covered steel (SPC), steel and aluminum (Al).

chamber type	sensitive volume (cm^3)	cavity radius (mm)	electrode material
Exradin A1SL[a]	0.057	2.1	C552
Exradin A14SL[a]	0.016	2.1	SPC
Exradin A14[a]	0.016	2.0	SPC
Exradin A16[a]	0.007	1.2	SPC
Exradin A26[b]	0.015	1.65	C552
IBA CC01[a]	0.010	1.0	Steel
PTW 31010	0.125	2.8	Al

[a] Chambers that do not meet the criteria for the reference class chambers [22] but have been proven to be suitable for reference dosimetry of Gamma Knife [23, 1].
[b] This is a new chamber and it is not listed in the TRS-483 protocol.

In the MC simulation, the chambers were located with their centre at 10 cm depth in a water phantom ($30 \times 30 \times 30$ cm^3) with the field sizes of 10×2 cm^2, 10×3 cm^2, 10×5 cm^2 and 10×10 cm^2 defined at SSD 85 cm in the TrueBeam 6 MV FFF beam. The reference (^{60}Co) beam was modeled using the tabulated spectrum of Mora et al. [24]. The source was a point source collimated onto a 10×10 cm^2 field size at SSD of 100 cm. The chamber was located at 5 cm depth in the water phantom. The mean absorbed dose to the sensitive volume of all chambers required in Eq. 6.5 were calculated using EGSnrc `egs_chamber` user code in both *msr* (or *A*) and reference set-ups. The mean absorbed dose to water in a small volume in *msr* and reference field was also calculated.

The calculations were experimentally validated by comparing absorbed dose determination under *msr* conditions using $N_{D,\mathrm{w},Q_0}^{f_{\mathrm{ref}}}$ standard reference calibration and $k_{Q_{\mathrm{msr}},Q_0}^{f_{\mathrm{msr}},f_{\mathrm{ref}}}$ factors from the calculations for detector readings in different field sizes. This absorbed dose determination should lead to a single *msr*-specific absorbed dose to water ($D_{\mathrm{w},Q_{\mathrm{msr}}}^{f_{\mathrm{msr}}}$) regardless of the detector used. To remove the uncertainty of the common $N_{D,\mathrm{w},Q_0}^{f_{\mathrm{ref}}}$ coefficient, the calculations were referenced to experiments using the standard reference field at the nominal radiation quality, i.e., 10×10 cm^2 at 6 MV FFF instead of ^{60}Co, (beam quality Q, instead of Q_0). Formally:

$$D_{\mathrm{w},Q_{\mathrm{msr}}}^{f_{\mathrm{msr}}} = M_{Q_{\mathrm{msr}}}^{f_{\mathrm{msr}}} \left[N_{D,\mathrm{w},Q_0}^{f_{\mathrm{ref}}} k_{Q,Q_0}^{f_{\mathrm{ref}}} \right] k_{Q_{\mathrm{msr}},Q}^{f_{\mathrm{msr}},f_{\mathrm{ref}}} \tag{6.6}$$

The term inside the square bracket in Eq. 6.6 represents the $N_{D,\mathrm{w},Q}^{f_{\mathrm{ref}}}$, the ionization chamber's calibration coefficient at beam quality Q and is a constant for a given chamber type in the experimental validation of the correction factors calculated in this work. It is defined as the ratio of the absorbed dose to water in beam quality Q (D_{w}^{Q}) and the fully corrected chamber reading in the beam quality Q ($M_Q^{f_{\mathrm{ref}}}$), therefore:

$$D_{\mathrm{w},Q_{\mathrm{msr}}}^{f_{\mathrm{msr}}} = M_{Q_{\mathrm{msr}}}^{f_{\mathrm{msr}}} N_{D,\mathrm{w},Q}^{f_{\mathrm{ref}}} k_{Q_{\mathrm{msr}},Q}^{f_{\mathrm{msr}},f_{\mathrm{ref}}} = M_{Q_{\mathrm{msr}}}^{f_{\mathrm{msr}}} (D_{\mathrm{w}}^{Q} / M_Q^{f_{\mathrm{ref}}}) k_{Q_{\mathrm{msr}},Q}^{f_{\mathrm{msr}},f_{\mathrm{ref}}}, \tag{6.7}$$

where $k_{Q_{\mathrm{msr}},Q}^{f_{\mathrm{msr}},f_{\mathrm{ref}}}$ is a factor that corrects for the difference between the response of the ionization chamber in a conventional 10×10 cm^2 reference field f_{ref} with beam quality Q using the same machine as the *msr* field f_{msr} and the response of the ionization chamber in the *msr* field f_{msr} with beam quality Q_{msr}. $k_{Q_{\mathrm{msr}},Q}^{f_{\mathrm{msr}},f_{\mathrm{ref}}}$ is calculated in MC as:

$$k_{Q_{\mathrm{msr}},Q}^{f_{\mathrm{msr}},f_{\mathrm{ref}}} = \frac{D_{\mathrm{w},Q_{\mathrm{msr}}}^{f_{\mathrm{msr}}} / D_{cav,Q_{\mathrm{msr}}}^{f_{\mathrm{msr}}}}{D_{\mathrm{w},Q}^{f_{\mathrm{ref}}} / D_{cav,Q}^{f_{\mathrm{ref}}}}. \tag{6.8}$$

From Eq. (6.7) and (6.8), the ratio of $D_{\mathrm{w},Q_{\mathrm{msr}}}^{f_{\mathrm{msr}}}$ for two chambers (denoted as ch$_i$ where i=1,2) can be expressed as:

$$\frac{(D_{\mathrm{w},Q_{\mathrm{msr}}}^{f_{\mathrm{msr}}})_{\mathrm{ch}_1}}{(D_{\mathrm{w},Q_{\mathrm{msr}}}^{f_{\mathrm{msr}}})_{\mathrm{ch}_2}} = 1 = \underbrace{\frac{(M_{Q_{\mathrm{msr}}}^{f_{\mathrm{msr}}} / M_Q^{f_{\mathrm{ref}}})_{\mathrm{ch}_1}}{(M_{Q_{\mathrm{msr}}}^{f_{\mathrm{msr}}} / M_Q^{f_{\mathrm{ref}}})_{\mathrm{ch}_2}}}_{\text{measurement}} \underbrace{\frac{(k_{Q_{\mathrm{msr}},Q}^{f_{\mathrm{msr}},f_{\mathrm{ref}}})_{\mathrm{ch}_1}}{(k_{Q_{\mathrm{msr}},Q}^{f_{\mathrm{msr}},f_{\mathrm{ref}}})_{\mathrm{ch}_2}}}_{\text{MC}} \tag{6.9}$$

where $M_{Q_{\mathrm{msr}}}^{f_{\mathrm{msr}}}$ is the fully corrected chamber reading in the *msr* field f_{msr} and beam quality Q_{msr}. $M_Q^{f_{\mathrm{ref}}}$ is the the fully corrected chamber reading in the reference field f_{ref} and beam

quality Q using the same machine as the *msr* field. Absorbed dose to water ($D^{f_{\mathrm{msr}}}_{\mathrm{w},Q_{\mathrm{msr}}}$) on the left-hand side should be independent of chamber type and Eq. (6.9) should ideally be one. This is studied in this work by calculating the $(k^{f_{\mathrm{msr}},f_{\mathrm{ref}}}_{Q_{\mathrm{msr}},Q})_{\mathrm{chi}}$ using MC for each chamber type (i) and taking the measured chamber readings $(M^{f_{\mathrm{msr}}}_{Q_{\mathrm{msr}}}/M^{f_{\mathrm{ref}}}_{Q})_{\mathrm{chi}}$. Eq. 6.9 is independent of $N^{f_{\mathrm{ref}}}_{D,\mathrm{w},Q_0}$ and any uncertainties associated with it.

The measurements were performed in the TrueBeam 6 MV FFF STX machine using the IBA blue water phantom. The different field sizes of 10×1.5 cm^2, 10×2 cm^2, 10×3 cm^2, 10×5 cm^2 and the 10×10 cm^2 were defined at SSD of 85 cm using the jaws. Four chambers including Exradin-A1SL, A26, IBA CC01 and PTW 31010 were placed in the water phantom. The in-plane (Y) and cross-plane (X) profiles were taken for each field sizes. The scanning water phantom software checks the symmetry of both profiles and the gantry tilt. It applies a shift to align the detector with the central axis. After centering the chamber, the detector was positioned at 10 cm depth in water with the positioning accuracy of 0.1 mm. All chambers were irradiated by 200 MU with dose-rate of 600 MU min^{-1}. The charge was collected using the Keithley 6517A electrometer for each field sizes. The stability of the detectors was checked by pre-irradiation. The measurements were repeated to reach a standard deviation of less than 0.03%. The charge was corrected for temperature-pressure, leakage, ion recombination and polarity according to Almond et al. [5]. The corrected charge reading in each field size of 10×1.5 cm^2, 10×2 cm^2, 10×3 cm^2 and 10×5 cm^2 ($M^{f_{\mathrm{A}}}_{Q_{\mathrm{A}}}$) was normalized to the charge reading in the field size of 10×10 cm^2 ($M^{f_{\mathrm{ref}}}_{Q}$) at the same beam quality Q. The $k^{f_{\mathrm{A}},f_{\mathrm{ref}}}_{Q_{\mathrm{A}},Q}$ factors determined by MC is applied to the corrected charged ratio of $(M^{f_{\mathrm{A}}}_{Q_{\mathrm{A}}}/M^{f_{\mathrm{ref}}}_{Q})$ for each chamber and compared to each other.

The linearity of ion recombination was also studied for two chambers PTW 31010 and Exradin A16. The voltage was varied between 50 V and 300 V. The charge measurement was done in the water phantom at SSD of 100 cm, 10×10 cm^2 field size using the two chambers. The dose per pulse was varied by changing the energy and depth. The measurements were performed for both energies 6 FFF and 10 FFF at the depth of maximum and 10 cm. The dose per pulse was obtained by taking the ratio of dose rate at the depth of maximum dose and the accelerator pulse repetition frequency. The pulse repetition frequency for the two beam energies 6 FFF and 10 FFF were measured by connecting the accelerator target to an oscilloscope. Knowing the PDD at 10 cm for 6 FFF and 10 FFF, the dose per pulse for the 10 cm depth can be easily calculated.

6.3.5 Calibration Method II: Chamber calibrated for the conventional reference field, without generic beam quality correction factors available

Calibration Method II can be used when generic type-dependent beam quality correction factors are not available. In this work we provide a hybrid methodology inspired from TRS-398 and TRS-483 to determine the three factors from Eq. 6.2, applied to reference field A, $k_{Q^{\mathrm{WFF}},Q_0}^{f_{\mathrm{ref}}}$, $k_{Q^{\mathrm{FFF}},Q^{\mathrm{WFF}}}^{f_{\mathrm{ref}}}$ and $k_{Q_{\mathrm{A}}^{\mathrm{FFF}},Q^{\mathrm{FFF}}}^{f_{\mathrm{A}},f_{\mathrm{ref}}}$.

The $k_{Q^{\mathbf{WFF}},Q_0}^{f_{\mathbf{ref}}}$ factor

To determine the $k_{Q^{\mathrm{WFF}},Q_0}^{f_{\mathrm{ref}}}$, the beam quality Q of the hypothetical 10×10 cm^2 field and ultimately the square equivalent field must be quantified. The data for equivalent uniform square *msr* field size of rectangular field with dimensions X and Y (X=3: 12 cm and Y=3: 12 cm) for 6 MV FFF beams are provided in the Table 16 of TRS-483. The equivalent uniform square was determined using the Eq. 58 of TRS-483 based on the condition that the scatter component is equalized. However, the IAEA-AAPM data is limited to a minimum field of 3×3 cm^2. In this work, we extended this methodology to square fields with 2 cm on a side and we study the effect and possible error that can have on beam quality specifier value and beam quality conversion factors. The scatter component using Eq. 58 for FFF beams was calculated by integration over rectangular fields of $10 \times y$ cm^2 (y =2 to 10 cm) with a measured lateral beam profile for the Varian TrueBeam 6 MV FFF specified for depth of maximum dose in water (1.5 cm) for the open field (40×40 cm^2). Similarly as in Ref. [9] equivalent fields were determined for field sizes A studied here (10×2 cm^2, 10×3 cm^2 and 10×5 cm^2) (See table 6.3).

$\mathrm{TPR}_{20,10}(10)$ or $\%dd(10,10)_{\mathrm{x}}$ were derived from $\mathrm{TPR}_{20,10}(\mathrm{S})$ and $\%dd(10,\mathrm{S})_{\mathrm{x}}$ (calculated in section 6.3.1) using Eq. 28 and 29 of TRS-483, respectively. Since SSD was 85 cm, the $\%dd(10,S)_{\mathrm{x}}$ was corrected using the Eq. 31 of TRS-483 where the TMR (the tissue maximum ratio) and NPSF (the normalized peak-scatter factor) ratios of Eq. 31 were neglected [25, 1]. However, Eq. 28 and 29 are valid for fields S between 4 and 12 cm. In this study, Eq. 28 and 29 are investigated further for 6 MV FFF beam and fields A as small as 2 cm on a side.

Only MC data were used since SSD of 65 cm for $TPR_{20,10}(S)$ measurements was not possible at the TrueBeam machine. Knowing the $TPR_{20,10}(S)$, the $TPR_{20,10}(10)$ of the hypothetical 10×10 cm^2 field was calculated using Eq. 28 of TRS-483.

Knowing the $TPR_{20,10}(10)$ of the hypothetical conventional reference field, the tabulated quality conversion factor (denoted by $k_Q^{f_{\text{ref}}}$ in TRS-483, or k_Q in TRS-398 and k_Q in TG-51 and its addendum) can be looked up. The quality conversion factor corrects for the effects of the difference between the reference beam quality Q_0 and the user beam quality Q. However, the tabulated beam quality correction factors provided in Andreo et al. [2] are for larger chambers not suitable for use in small fields. Therefore, in this study the beam quality correction factors were determined following the procedure in TRS 398 [2]. The parameters used are provided in the supplementary material. For this part only the beam quality specifier $TPR_{20,10}(10)$ was used.

The $k_{Q^{\text{FFF}},Q^{\text{WFF}}}^{f_{\text{ref}}}$ factor

The correction $k_{Q^{\text{FFF}},Q^{\text{WFF}}}^{f_{\text{ref}}}$ corrects for the difference between WFF and FFF beams. Two effects contribute to $k_{Q^{\text{FFF}},Q^{\text{WFF}}}^{f_{\text{ref}}}$. One is the difference between the charged particle spectra of both beam qualities FFF and WFF. This changes the water-to-air stopping power ratio and ionization chamber perturbation correction factors. The second effect is the volume averaging correction factor ($(k_{\text{vol}})_Q^{f_{ref}}$) which corrects for the nonuniformity of the lateral beam profile in the FFF beam. The $(k_{\text{vol}})_Q^{f_{ref}}$ is defined as the absorbed dose averaged over a volume of water in homogeneous water where the water volume coincides with the volume displaced by the ionization chamber [1].

We used the fit provided in TRS-398 (Figure-C.1 of TRS-398) for determining the water to air stopping power ratios for WFF beams $(s_{\text{w,air}})_{\text{TPR}_{20,10}(10)}^{\text{WFF}}$. For the TrueBeam 6 MV FFF, we calculated the water to air stopping-power ratios using the SPRRZnrc [17] user-code of the EGSnrc system using a spectrum derived from the TrueBeam 6 MV FFF phase space. The phantom defined in SPRZnrc was cylindrical with 20 cm height and 15 cm radius. The scoring region was a column with 1 cm radius at 10 cm depth. The electron production threshold and cutoff used in SPRZnrc were 521 keV and no range rejection was used. The ratio of water to air stopping-power ratios for FFF and WFF is used as the correction $\left((s_{\text{w,air}})_{\text{TPR}_{20,10}(10)}^{\text{FFF}} / (s_{\text{w,air}})_{\text{TPR}_{20,10}(10)}^{\text{WFF}}\right)$.

As in TRS-483, in the present study, it was assumed that the dependence of ionization chamber perturbation correction factors on the beam quality indices for the FFF beams is the same as for WFF beams. However, we noted that for chambers with high Z electrode, this effect represents an important contribution. Therefore this assumption was revisited for the central electrode correction factor (P_{cel}). We studied P_{cel} for all seven chambers in the TrueBeam 6 MV FFF and reference ^{60}Co beam. P_{cel} is defined as the ratio of absorbed dose to the sensitive volume of the detector but with the electrode parts close to the sensitive volume of the detectors replaced by air ($D_{\text{no cel}}$) to the absorbed dose in the sensitive volume of air in the fully modeled chamber (D).

$$P_{\text{cel}} = \frac{D_{\text{no cel}}}{D} \tag{6.10}$$

TrueBeam field size was 10×10 cm^2 at SSD 100 cm and the detector placed at 10 cm depth. The ^{60}Co source was modeled as a point source collimated to a 10×10 cm^2 field size at SSD 100 cm and the detector was placed at 5 cm depth. For the WFF, we assumed that the ratio of central electrode correction in WFF beam and ^{60}Co was unity [1].

The volume averaging correction ($(k_{vol})_Q^{f_{ref}}$) was determined in this study by using the Eq. 54 of the TRS-483 using the chamber's cavity lengths and the beam quality index $\text{TPR}_{20,10}(10)$.

The $k^{f_{\mathbf{A}},f_{\mathbf{ref}}}_{Q_{\mathbf{A}}^{\mathbf{FFF}},Q^{\mathbf{FFF}}}$ factor

As in TRS-483, in this study, it was assumed that $k^{f_{\text{A}},f_{\text{ref}}}_{Q_{\text{A}}^{\text{FFF}},Q^{\text{FFF}}}$ is unity [1]. This assumption was verified in the present study for the seven chamber types used and the possible error was estimated. $k^{f_{\text{A}},f_{\text{ref}}}_{Q_{\text{A}}^{\text{FFF}},Q^{\text{FFF}}}$ is defined as

$$k^{f_{\text{A}},f_{\text{ref}}}_{Q_{\text{A}}^{\text{FFF}},Q^{\text{FFF}}} = \frac{D^{f_{\text{A}}}_{\text{w},Q_{\text{A}}^{\text{FFF}}} / D^{f_{\text{A}}}_{cav,Q_{\text{A}}^{\text{FFF}}}}{D^{f_{\text{ref}}}_{\text{w},Q^{\text{FFF}}} / D^{f_{\text{ref}}}_{cav,Q^{\text{FFF}}}}. \tag{6.11}$$

$D^{f_{\text{A}}}_{cav,Q_{\text{A}}^{\text{FFF}}}$ and $D^{f_{\text{A}}}_{\text{w},Q_{\text{A}}^{\text{FFF}}}$ represent the mean absorbed dose to the cavity of chamber and a small volume respectively calculated for all fields A: 10×2 cm^2, 10×3 cm^2 and 10×5 cm^2 at SSD 85 cm depth of 10 cm in water. $D^{f_{\text{ref}}}_{cav,Q^{\text{FFF}}}$ and $D^{f_{\text{ref}}}_{\text{w},Q^{\text{FFF}}}$ are the mean absorbed dose to the cavity of chamber and a small volume respectively in the reference 10×10 cm^2 field defined at SSD of 100 cm and depth of 10 cm in water at the same beam quality (TrueBeam 6 MV FFF). All four parameters in Eq. 6.11 were calculated using the EGSnrc `egs_chamber` user code.

Using Eq. 6.11 and mentioned quantities, $k^{f_A,f_{ref}}_{Q_A^{FFF},Q^{FFF}}$ for the seven ionization chamber types was calculated.

6.4 Results

6.4.1 r_{LCPE} data in FFF beam

In the supplementary data section, we show that the r_{LCPE} for FFF beams is approximately the same as that for the WFF beams of the same nominal energy, despite the lower prediction by applying Eq. 3 and 4 in TRS-483. The $2r_{LCPE}$+d values for four chambers in the TrueBeam 6 MV FFF are listed in table 6.2. FWHM determined from measurements for all chambers and three rectangular field sizes of 10×1.5 cm^2, 10×2 cm^2 and 10×3 cm^2 are also provided in table 6.2. Table 6.2 shows that for all chambers, the FWHM for 10×1.5 cm^2 and 10×2 cm^2 is smaller than the $2r_{LCPE}$+d. For 10×3 cm^2 field size, the condition of *msr* is fulfilled for all chambers except the largest chamber PTW 31010.

Table 6.2 Measured in-plane FWHM and values of 2 r_{LCPE} + d for four chamber types and 10 $\times$ y cm^2 (y= 1.5, 2 and 3) TrueBeam 6 MV FFF field sizes.

Chamber type	FWHM y:1.5 cm	FWHM y:2 cm	FWHM y:3 cm	$2r_{LCPE}$+d (cm)
Exradin A1SL	1.96	2.54	3.60	3.47
Exradin A26	1.92	2.49	3.55	3.23
IBA CC01	1.75	2.32	3.36	3.21
PTW 31010	1.77	2.34	3.38	3.52

6.4.2 Calibration Method I $k^{f_A,f_{ref}}_{Q_A,Q_0}$ data

Figure 6.1 shows the $k^{f_A,f_{ref}}_{Q_A,Q_0}$ factors for all chambers as a function of field side. The $k^{f_A,f_{ref}}_{Q_A,Q_0}$ values for Exradin A1SL changes by less than 0.1% over all fields studied. Larger variations when changing the field size from 10×10 cm^2 to 10×1.5 cm^2 are found for the Exradin A16 (0.63%) and for chambers with high Z electrodes IBA CC01 (1.58%).

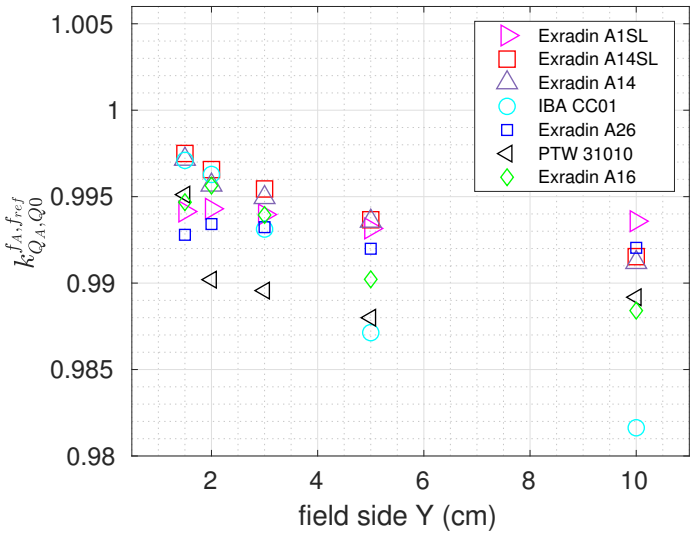

Figure 6.1 The $k_{Q_A,Q_0}^{f_A,f_{ref}}$ factors as a function of field size for seven chamber types modeled in this study. The type A uncertainty is 0.1% (k=1) and not shown for visibility

6.4.3 Calibration Method I $k_{Q_A,Q}^{f_A,f_{ref}}$ data and experimental validation

Figure 6.2 shows the $k_{Q_A,Q}^{f_A,f_{ref}}$ values for seven chamber types as a function of field side. The $k_{Q_A,Q}^{f_A,f_{ref}}$ values for Exradin-A1SL and A26 are almost unity (within 0.1%). However, for PTW 31010 the $k_{Q_A,Q}^{f_A,f_{ref}}$ value increases from 0.1% to 0.6% when the field size is decreased from 10×2 cm^2 to 10×1.5 cm^2. For Exradin A16, A14 and A14SL the $k_{Q_A,Q}^{f_A,f_{ref}}$ value changes by 0.6% for the 10×1.5 cm^2. For IBA CC01, the correction changes by 1.6% for the smallest field.

Figure 6.3 presents the absorbed dose to water $D_{w,Q_A}^{f_A}$ determined for Exradin A26, PTW 31010, IBA CC01 and Exradin A16 chambers normalized to the absorbed dose to water using a reference chamber (Exradin A1SL). The corrected absorbed dose ratio for all chambers except Exradin A16 and all fields sizes are within 0.1%. The corrected absorbed dose measured with Exradin A16 is 2.2% lower than the corrected absorbed dose measured with Exradin A1SL and all other chambers for the smallest field (1.5 cm). The sources of uncertainties are the SSD setting (0.10% [6]), depth setting (0.17% [6]), field size setting (0.10% [6]), charge measurements (0.03%), P_{TP} (0.10% [6]), P_{ion} (0.10% [6]), P_{pol} (0.05% [6]) and $k_{Q_A,Q}^{f_A,f_{ref}}$ correction factor ((0.10%). The overall standard uncertainty is estimated using uncertainty propagation as per the Guide to the Expression of Uncertainty in Measurement (GUM) [26] and is found to

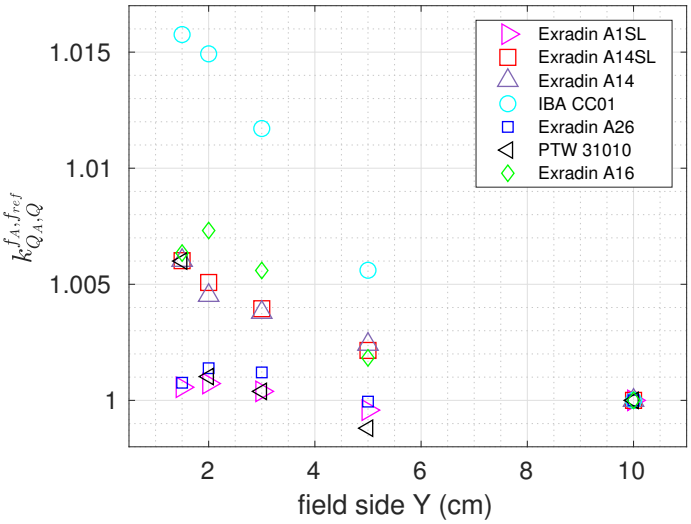

Figure 6.2 The $k_{Q_A,Q}^{f_A,f_{ref}}$ factors as a function of field size for seven chamber types modeled in this study. The field sizes 10×1.5 cm^2, 10×2 cm^2, 10×3 cm^2, 10×5 cm^2 and 10×10 cm^2 are defined at SSD 85 cm. The uncertainty is type A 0.1% (k=1) and not shown for visibility

be 0.41%. We conclude that with the exception of the Exradin A16 chamber, applying MC calculated correction factors leads to a consistent reference field absorbed dose for all fields ranging from 10×1.5 cm^2 to 10×10 cm^2.

6.4.4 Calibration Method II: $k_{Q^{WFF},Q_0}^{f_{ref}}$ data

The equivalent uniform square field

The equivalent field sizes for the TrueBeam 6 FFF needed to apply calibration method II are provided in table 6.3. These equivalent square msr field size is in agreement with the Table 16 of TRS-483 for fields larger than 3 cm (within$\pm$1 mm). For the 2 cm field width new data is provided using the same approach.

For the field sizes 10×2 cm^2, 10×3 cm^2, 10×5 cm^2 and 10×10 cm^2 the equivalent square field sizes are 3.6 cm, 4.7 cm, 6.6 cm and 9.5 cm, respectively.

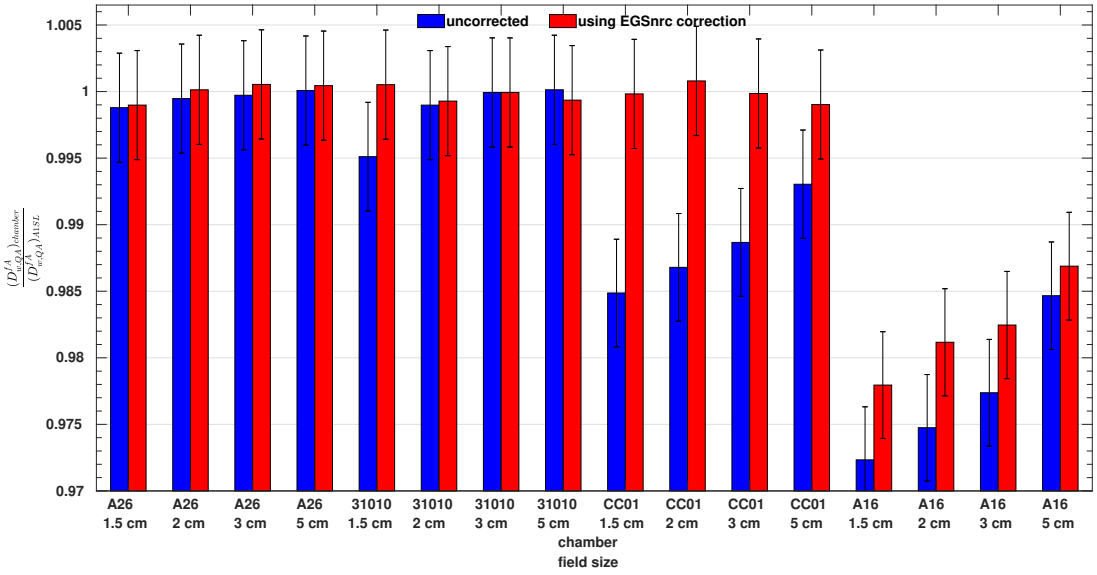

Figure 6.3 The absorbed dose to water $D^{f_{\text{msr}}}_{w,Q_{\text{msr}}}$ determined for Exradin A26, PTW 31010, IBA CC01 and Exradin A16 chambers normalized to the absorbed dose to water in reference chamber (Exradin A1SL). The overall standard uncertainty is 0.41% (k=1).

The beam quality specifier of the hypothetical 10×10 cm^2 field

In figure 6.4, the MC calculated $\text{TPR}_{20,10}$(S) values are plotted as a function of square field sizes between 2 and 10 cm for the TrueBeam 6 MV FFF. The MC values are compared to the measured values of this study and Huq et al. [27]. Good agreement is observed between the MC and measured $\text{TPR}_{20,10}$(S) values of this study (within 0.1% for fields larger than 3 cm and 0.5% for fields smaller than 3 cm). The measured $\text{TPR}_{20,10}$(S) values of Huq et al. [27] study also agree with our MC values (within 0.3%). The fit shown in figure 6.4 was determined using Eq. 24 of TRS-483 and was extended to field widths as small as 2 cm. The difference between the predicted $\text{TPR}_{20,10}(10)$ of a 4×4 cm^2 and 10×10 cm^2 field size is 0.7% similar to the difference of 0.6% found by Huq et al. [27]. The difference reaches a maximum of 1.3% at the smallest field (2×2 cm^2). As expected, the $\text{TPR}_{20,10}$(S) values are found to be insensitive to the SDD. The difference between $\text{TPR}_{20,10}$(S) values calculated at SDD 100 cm and 85 cm are less than 0.1% for all three field sizes tested (2×2 cm^2, 4×4 cm^2 and 10×10 cm^2).

Values of $\%dd(10,S)$ and $\%dd(10,S)_x$ as a function of field width ranging from 2 to 10 cm for the TrueBeam 6 MV FFF is shown in Figure 6.5. Good agreement is obtained between the

Table 6.3 The equivalent uniform square *msr* field size of rectangular fields (dimensions X × Y) for 6 FFF TrueBeam calculated in this study

x(cm) \ $y(cm)$	10	9	8	7	6	5	4	3	2
10	9.5	9.2	8.6	8.0	7.3	6.6	5.7	4.7	**3.6**
9		8.7	8.2	7.6	7.0	6.3	5.5	4.6	**3.5**
8			7.7	7.3	6.7	6.1	5.3	4.4	**3.4**
7				6.8	6.3	5.7	5.1	4.2	**3.3**
6					5.9	5.4	4.7	4.0	**3.1**
5						4.9	4.4	3.7	**2.9**
4							3.9	3.4	**2.7**
3								3.0	**2.4**
2									**2.0**

MC calculated $\%dd$(10,S) and reference values (myVarian.com) (within 0.2%). However, the percent difference between $\%dd$(10,S) values calculated in this study and measured values by Huq et al. [27] is 0.4% for 10 × 10 cm^2 field size and 1.2% for 3 × 3 cm^2 field size. The difference between $\%dd$(10,S) and $\%dd(10,S)_x$ both calculated using MC is 0.55% for the largest field (10 × 10 cm^2) and it becomes negligible for the smaller fields (0.01% for 2 × 2 cm^2 field size). The fit was determined according to Eq. 29 of TRS-483 and was extended to smaller fields (2 × 2 cm^2). The difference between the predicted $\%dd(10,S)_x$ of a 4 × 4 cm^2 and 10 × 10 cm^2 field size is 0.6% compared to 0.4% reported by Huq et al. [27]. A maximum difference of almost 2% is observed at 2 × 2 cm^2 field size. As expected, the $\%dd(10,S)_x$ depends on the SSD. The $\%dd(10,S)_x$ converted from SSD = 85 cm using Eq. 31 in TRS-483 is in good agreement with the $\%dd(10,S)_x$ determined at 100 cm SSD (within 0.07% and 0.20% for the largest (10 × 10 cm^2) and smallest field (2 × 2 cm^2) respectively.)

For 6 MV FFF field sizes 10 × 2 cm^2, 10 × 3 cm^2, 10 × 5 cm^2 and 10 × 10 cm^2 the MC calculated $TPR_{20,10}$(S) values are 0.6056±0.0004, 0.6089±0.0005, 0.6171±0.0005 and 0.6303±0.0005, respectively. Using the equivalent field size and Eq. 28 of TRS-483 resulted in $TPR_{20,10}$(10) values of 0.6425, 0.6397, 0.6370 and 0.6332 for the hypothetical 10 × 10 cm^2 field of 10 × 2 cm^2, 10 × 3 cm^2, 10 × 5 cm^2 and 10 × 10 cm^2 field sizes, respectively. The $k^{f_{ref}}_{Q^{WFF},Q_0}$ corresponding to these $TPR_{20,10}$(10) values were calculated analytically using TRS-398.

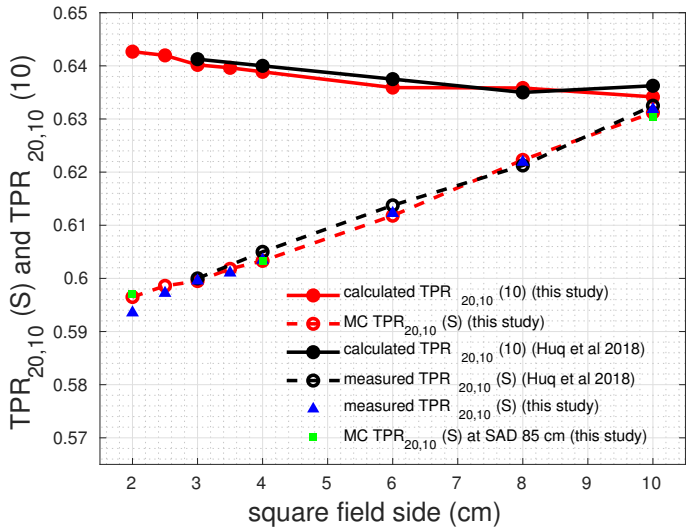

Figure 6.4 The measured $TPR_{20,10}$(S), MC $TPR_{20,10}$(S) and calculated $TPR_{20,10}$(10) (using Eq. 28 of TRS-483) values as a function of the side of the square field size for the TrueBeam 6 MV FFF beam. The uncertainty on the MC $TPR_{20,10}$(S) values is type A, less than 0.1% (k=1) and not shown. The data is compared to the measured $TPR_{20,10}$(S) and calculated $TPR_{20,10}$(10) values of Huq et al. [27]. In Huq et al. [27] study the horizontal axis is the field FWHM.

6.4.5 Calibration Method II: $k^{f_{\mathrm{ref}}}_{Q^{\mathrm{FFF}},Q^{\mathrm{WFF}}}$ data

The $k^{f_{\mathrm{ref}}}_{Q^{\mathrm{FFF}},Q^{\mathrm{WFF}}}$ factor is the product of water to air stopping-power ratio correction, perturbation correction factors and volume averaging correction. Water to air stopping power ratio for the TrueBeam 6 MV FFF 10×10 cm^2 field defined at SSD 100 cm ($(s_{\mathrm{w,air}})^{\mathrm{FFF}}_{\mathrm{TPR}_{20,10}(10)}$) were 1.1231±0.0003 within 0.1% of the value reported by Dalaryd et al. [28] (1.1243). The water to air stopping power ratio for the WFF beam ($(s_{\mathrm{w,air}})^{\mathrm{WFF}}_{\mathrm{TPR}_{20,10}(10)}$) was 1.1263 for a $TPR_{20,10}$(10) of 0.6312±0.0005. Therefore, the correction $((s_{\mathrm{w,air}})^{\mathrm{FFF}}_{\mathrm{TPR}_{20,10}(10)}/(s_{\mathrm{w,air}})^{\mathrm{WFF}}_{\mathrm{TPR}_{20,10}(10)})$ is 0.9972. The ionization chamber perturbation correction factors were assumed unity. The volume averaging correction calculated using Eq. 54 of the TRS-483 for the seven chambers studied here was at most 0.03% from unity for the largest chamber (PTW 31010).

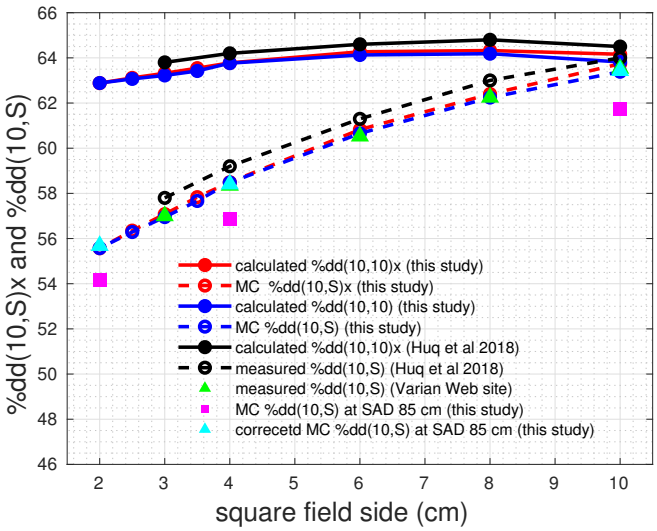

Figure 6.5 The measured $\%dd(10,S)$, MC $\%dd(10,S)_x$, MC $\%dd(10,S)$ and calculated $\%dd(10,10)_x$ (using Eq. 29 of TRS-483) values as a function of the square field size for the TrueBeam 6 MV FFF beam. The type A uncertainty on the MC calculated values amounted to less than 0.2% (k=1) and is not shown. The data is compared to the measured $\%dd(10,S)_x$ and calculated $\%dd(10,10)_x$ values of Huq et al. [27]. In Huq et al. [27] study the horizontal axis is the field FWHM.

6.4.6 Comparison between calibration Method I and Method II

Figure 6.6 shows a comparison between the MC calculated $k^{f_A,f_{ref}}_{Q_A,Q_0}$ values (Calibration Method I) and the $k^{f_{ref}}_{Q^{WFF},Q_0}$ $k^{f_{ref}}_{Q^{FFF},Q^{WFF}}$ $k^{f_A,f_{ref}}_{Q_A^{FFF},Q^{FFF}}$ factors determined following Calibration Method II.

The percent difference between the corrections calculated using the two approaches is less than 0.24%, 0.28%, 0.78% and 1.49% for the chambers studied here in the 10×2 cm^2, 10×3 cm^2, 10×5 cm^2 and 10×10 cm^2 field sizes, respectively (Figure 6.6.a to d). The discrepancy was largest (1.49%) for the IBA CC01 chamber with high Z material in the largest field (10×10 cm^2). However, if the data is further corrected for the $k^{f_A,f_{ref}}_{Q_A^{FFF},Q^{FFF}}$ and P_{cel} values the differences would reduce to less than 0.5% for all chambers and field sizes (see supplementary material Table 6.5).

In Figure 6.6, it appears as though the agreement between the two methodologies deteriorates at larger fields from 0.24% to 1.49%. However, when the data is corrected for the $k^{f_A,f_{ref}}_{Q_A^{FFF},Q^{FFF}}$ and P_{cel} values, the difference between the two methodologies is almost constant (0.2-0.5%) over the field sizes (supplementary material Table Table 6.5).

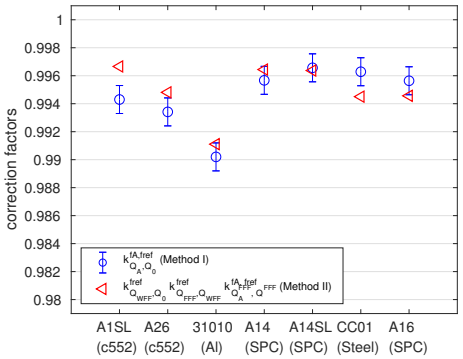

a) 10×2 cm^2 field size at SSD 85 cm

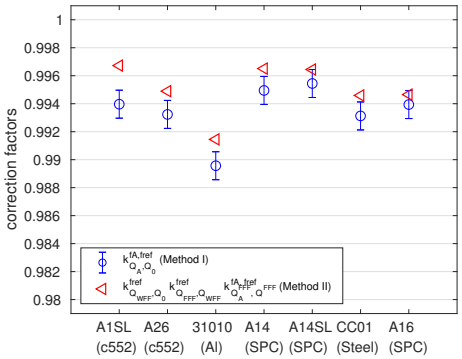

b) 10×3 cm^2 field size at SSD 85 cm

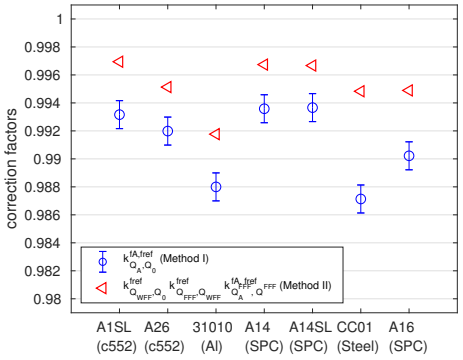

c) 10×5 cm^2 field size at SSD 85 cm

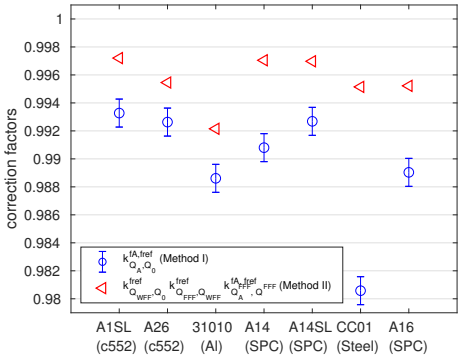

d) 10×10 cm^2 field size at SSD 100 cm

Figure 6.6 A comparison between the correction calculated using the method I ($k_{Q_A,Q_0}^{f_A,f_{ref}}$) and the method II ($k_{Q^{WFF},Q_0}^{f_{ref}} k_{Q^{FFF},Q^{WFF}}^{f_{ref}} k_{Q_A^{FFF},Q^{FFF}}^{f_A,f_{ref}}$) for all field sizes studied. In the second approach the $k_{Q_A^{FFF},Q^{FFF}}^{f_A,f_{ref}}$ and perturbation corrections are assumed to be unity. The uncertainty on the MC calculated $k_{Q_A,Q_0}^{f_A,f_{ref}}$ values is type A and less than 0.1% (k=1). The estimated uncertainty on the $k_{Q^{WFF},Q_0}^{f_{ref}} k_{Q^{FFF},Q^{WFF}}^{f_{ref}} k_{Q_A^{FFF},Q^{FFF}}^{f_A,f_{ref}}$ values is assumed to be 1% and not shown.

The type A uncertainty on the $k_{Q_A,Q_0}^{f_A,f_{ref}}$ factor is less than 0.1% (k=1). The estimated overall standard uncertainty on the $k_{Q^{WFF},Q_0}^{f_{ref}}$ $k_{Q^{FFF},Q^{WFF}}^{f_{ref}}$ $k_{Q_A^{FFF},Q^{FFF}}^{f_A,f_{ref}}$ values is 1%. This includes an uncertainty on $k_{Q^{WFF},Q_0}^{f_{ref}}$ value (1% taken from TRS-398 [2]), the generic volume averaging correction factors (0.2% [1]), water to air stopping power ratio as a function of $TPR_{20,10}(10)$ (0.2%[1]), the variation of other correction factors with beam quality (0.1% [1]) and the variation of water-to-air stopping power difference between WFF and FFF (0.15% [1]).

6.5 Discussion

Values of r_{LCPE} of 6 FFF and 10 FFF photon beams are comparable to the r_{LCPE} of 6 WFF and 10 WFF photon beams, respectively despite having a significantly lower beam quality (supplementary material figure 6.7). Users should be aware that when using the beam quality specifier ($TPR_{20,10}(10)$ or $\%dd(10,0)_x$) along with Eq. 3 and 4 of TRS-483 to estimate the r_{LCPE} of 6 FFF beam, r_{LCPE} is underestimated by 5 mm.

In the TrueBeam 6 FFF beam without considering the detector, the FWHM of the beam has to be greater than 2.8 cm ($2\times r_{LCPE}$) to preserve the LCPE condition. Table 6.2 shows that the 10×3 cm^2 can be considered a *msr* field when using the Exradin-A1SL, A26 and IBA CC01. However, the largest chamber (PTW 31010) does not meet the *msr* conditions requirement. The 10×1.5 cm^2 and 10×2 cm^2 also do not satisfy the *msr* conditions for any chambers listed here. Therefore, there is a need to extend the calibration protocols for radiation therapy machines where the maximum field size achievable may not necessarily meet the *msr* condition.

In the present study, Exradin A1SL was chosen as the reference chamber with MC calculated $k_{Q_A,Q_0}^{f_A,f_{ref}}$ values of less than 0.1% for all fields studied. The larger variation for IBA CC01 (1.58%) is due to it's electrode made of high Z material (figure 6.1).

The $k_{Q_{msr},Q}^{f_{msr},f_{ref}}$ values for Exradin-A1SL and A26 (with electrodes made of plastic and relatively small chambers) are almost unity even for the smallest field 10×1.5 cm^2 where the condition of *msr* was not met for any of the chambers studied here (see table 6.2). This is confirming our hypothesis that even if the condition of *msr* is not met depending on the chamber used the corrections factors in these reference fields might be minor. The 0.5% increase in $k_{Q_A,Q}^{f_A,f_{ref}}$ value for PTW 31010 when the field size is decreased from 10×2 cm^2 to 10×1.5 cm^2 is because of volume averaging. For IBA CC01 that has the highest-Z electrode (Steel), the correction changes by maximum 1.6% for the smallest field followed by chambers with relatively high Z

material such as Exradin A16, A14 and A14SL (0.6%). In general, chambers that use electrode material with higher-Z such as IBA CC01 (steel), Exradin-A16, A14, and A14SL (silver-plated copper covered electrodes) have larger central electrode correction factors compared to Exradin A1SL (C552) and PTW 31010 (Aluminum) [29].

Figure 6.3 shows that applying the $k_{Q_A,Q}^{f_A,f_{ref}}$ factors to chamber charge readings except Exradin A16 improves the standard deviation from 0.57% to 0.06% validating the MC calculated $k_{Q_A,Q}^{f_A,f_{ref}}$ values. However, a 2.2% difference is observed for Exradin A16 compared to Exradin A1SL for the smallest field size. Further investigation showed that non-linearity is observed in the Jaffé plots for the Exradin A16 (supplementary material figure 6.8), which might be due to the presence of strong electric field in the cavity of this microchamber [22, 30] and this might invalidate the ion recombination correction applied for the A16. We repeated the measurements with a different Exradin A16 and same behaviour was observed. Radiograph images were taken for both Exradin A16 chambers confirming there is no defect in the chambers. It remains unclear why Exradin A16 response is 2.2% different compared to the other chambers and more work taking into account the detailed electric field distribution in the chamber is recommended.

The equivalent square *msr* field size provided in table 6.3 is in agreement with table 16 of TRS-483 for fields larger than 3 cm (within$\pm$1 mm). The small difference is due to the slightly different lateral beam profile used in our calculations. For fields smaller than 3 cm our work provides new data following the same approach. However, it should be noted that the Eq. 58 of TRS-483 and the parameters μ and λ have not been validated for fields smaller than 3 cm and this should in principle be properly validated versus measurements [31]. In this work we have just extended the Eq. 58 of TRS-483 using the same parameter to 2 cm field size to study how much it would affect the beam quality specifier value and the resulting generic beam quality correction factors.

Figure 6.4 and 6.5 show that the Eq. 28 and 29 of TRS-483 can be used to derive the $TPR_{20,10}(10)$ and $\%dd(10,10)_x$ from $TPR_{20,10}(S)$ and $\%dd(10,S)_x$ within a maximum difference of 1.3% and 2% respectively for the 2×2 cm^2 field size. The 1.3% difference on the $TPR_{20,10}(10)$ has a negligible impact on the $k_{Q_A,Q_0}^{f_A,f_{ref}}$ factors (less than 0.1% for all chambers studied here). This justifies the use of equivalent field size and the beam quality specifier calculated in this study to determine the beam quality correction factors for smaller fields.

The $\left((s_{w,air})^{FFF}_{TPR_{20,10}(10)}/(s_{w,air})^{WFF}_{TPR_{20,10}(10)}\right)$ correction value is in agreement with the average value reported by Dalaryd et al. [28] (0.3%). The volume averaging correction is practically

unity for all chamber studied here (maximum 0.03% for PTW 31010) and this was expected since all the chambers studied here have cavity lengths smaller than the 0.7 cm.

The difference between correction factor calculated using Calibration Method I ($k^{f_A,f_{ref}}_{Q_A,Q_0}$) and Calibration Method II ($k^{f_{ref}}_{Q^{WFF},Q_0} k^{f_{ref}}_{Q^{FFF},Q^{WFF}} k^{f_A,f_{ref}}_{Q_A^{FFF},Q^{FFF}}$) is less than 0.4% for chambers with electrodes made of c552 (Exradin-A1SL and A26) and Al (PTW 31010), less than 0.6% for chambers with electrodes made of SPC (Exradin-A14, A14SL and A16) and 1.5% for IBA CC01 (electrode made of Steel) considering all field sizes.

The $k^{f_A,f_{ref}}_{Q_A^{FFF},Q^{FFF}}$ factor is assumed unity in TRS-483. We have verified this value by doing direct calculation since the 10×10 cm^2 field size is achievable in TrueBeam machine. This assumption was found to be true for all chambers studied here ($k^{f_A,f_{ref}}_{Q_A^{FFF},Q^{FFF}}$ are less than 0.7%) except for the IBA CC01 (1.6%) (supplementary material figure 6.10) which has a high Z electrode.

If in Calibration Method II, the data is corrected for P_{cel} and MC calculated $k^{f_A,f_{ref}}_{Q_A^{FFF},Q^{FFF}}$ values, the differences become less than 0.5% for all chamber types and field sizes. This is a reasonable agreement and confirming our hypothesis that even if the condition of *msr* is not met, Method II can still be used to determine correction factor data for chambers for which Method I correction factor data is not available provided that chamber's electrode is not made of high Z material.

6.6 Conclusion

In this study we extended the TRS-483 methodology for the calibration of radiation therapy machines with field widths down to 2 cm. We changed the lateral field size from 1.5 cm to 10 cm in the Varian TrueBeam 6 MV FFF beam. We observed that the 10×2 cm^2 field size does not preserve the *msr* condition for the chambers studied in the TrueBeam 6 MV FFF machine. We investigated two calibration methodologies following the TRS-483. In calibration method I, the generic correction factors were calculated directly using MC for seven chamber types (corresponding to Route 2 in TRS-483). We found that the correction factors for relatively small chambers with electrode made of plastic (Exradin-A1SL and A26) almost did not change with field size even for the smallest field the 10×1.5 cm^2 where the *msr* condition is not met. The corrections were verified through measurements and very good agreement was observed for all chambers (within 0.1%) except for the Exradin A16. In calibration method II (corresponding to Route 3 in TRS-483), we extended the methodology provided in the TRS-483 with the goal

to provide users with a mechanism of accurately estimating beam quality correction factors when MC correction factors following calibration method I are not available. We extended the TRS-483 equivalent field size and the beam quality specifier down to 2 cm field widths. For the 2×2 cm^2 field size, this resulted in maximum difference of 1.3% in the $\mathrm{TPR}_{20,10}(10)$ value which has a negligible impact on the beam quality correction factors. Knowing the beam quality specifier, the $k_{Q^{\mathrm{WFF}},Q_0}^{f_{\mathrm{ref}}}$ was calculated analytically using data from TRS-398. The difference between the WFF and FFF beam was corrected using the water-to-air stopping power ratio correction and the volume averaging. We found that calibration method II can predict the correction factors within 0.4% for chambers with electrode made of low Z material. However, for chambers with higher-Z electrodes the correction can be overestimated by 1.5%.

We recommend to use calibration method I for calibration of this type of machines. If the $k_{Q_{\mathrm{A}},Q_0}^{f_{\mathrm{A}},f_{\mathrm{ref}}}$ data are not available users can apply calibration method II to predict the correction factors for their own detector. The second methodology should not be used for chambers with electrode made of high Z material unless all the proper perturbation correction factors and the $k_{Q_{\mathrm{A}}^{\mathrm{FFF}},Q^{\mathrm{FFF}}}^{f_{\mathrm{A}},f_{\mathrm{ref}}}$ values can be evaluated and applied. The user should be aware of the higher uncertainties using calibration method II comparing to the first approach; the combined standard uncertainty on the beam quality correction factors reported in the TRS-398 values is 1% (table B.III. of TRS-398).

Acknowledgments

This work was supported financially by the CREATE Medical Physics Research Training Network grant of the Natural Sciences and Engineering Research Council (Grant number: 432290), NSERC RGPIN-2019-06746 and RefleXion Medical. The authors acknowledge Compute Canada/Calcul Quebec for the computing resources and the ion chamber manufacturers Standard Imaging, PTW and IBA for providing the chambers blueprints and specifications. We also like to thank Frédéric Tessier, Saiful Huq and Pavlos Papaconstadopoulos for the helpful comments and Kyle O'Grady and Marc-André Renaud for providing the beam models.

Disclosure of Conflicts of Interest

This study was partially supported by funds from RefleXion Medical.

Bibliography

[1] H Palmans, P Andreo, K Christaki, MS Huq, and J Seuntjens. TRS-483: Dosimetry of small static fields used in external beam radiotherapy: an international code of practice for reference and relative dose determination. *International Atomic Energy Agency, Vienna*, 2017.

[2] P Andreo, DT Burns, K Hohlfeld, MS Huq, T Kanai, F Laitano, V Smyth, and S Vynckier. TRS-398: Absorbed dose determination in external beam radiotherapy: an international code of practice for dosimetry based on standards of absorbed dose to water. *International Atomic Energy Agency*, 420, 2001.

[3] IJ Das, GX Ding, and A Ahnesjö. Small fields: nonequilibrium radiation dosimetry. *Medical physics*, 35(1):206–215, 2008.

[4] P Andreo, DT Burns, AE Nahum, J Seuntjens, and FH Attix. Fundamentals of ionizing radiation dosimetry. *Wiley-VCH Verlag GmbH & Co, KGaA, Boschstr*, 12:69469, 2017.

[5] PR Almond, PJ Biggs, BM Coursey, WF Hanson, MS Huq, R Nath, and DWO Rogers. AAPM's TG-51 protocol for clinical reference dosimetry of high-energy photon and electron beams. *Medical physics*, 26(9):1847–1870, 1999.

[6] M McEwen, L DeWerd, G Ibbott, D Followill, DWO Rogers, S Seltzer, and J Seuntjens. Addendum to the AAPMs TG-51 protocol for clinical reference dosimetry of high-energy photon beams. *Medical physics*, 41(4), 2014.

[7] H Palmans, P Andreo, MS Huq, J Seuntjens, KE Christaki, and A Meghzifene. Dosimetry of small static fields used in external photon beam radiotherapy: Summary of TRS-483, the IAEA-AAPM international Code of Practice for reference and relative dose determination. *Medical physics*, 45(11):e1123–e1145, 2018.

[8] R Alfonso, P Andreo, R Capote, MS Huq, W Kilby, P Kjäll, TR Mackie, H Palmans, K Rosser, J Seuntjens, W Ullrich, and S Vatnitsky. A new formalism for reference dosimetry of small and nonstandard fields. *Medical physics*, 35(11):5179–5186, 2008.

[9] H Palmans. Determination of the beam quality index of high-energy photon beams under nonstandard reference conditions. *Medical physics*, 39(9):5513–5519, 2012.

[10] XA Li, M Soubra, J Szanto, and LH Gerig. Lateral electron equilibrium and electron contamination in measurements of head-scatter factors using miniphantoms and brass caps. *Medical physics*, 22(7):1167–1170, 1995.

[11] DWO Rogers, BA Faddegon, GX Ding, CM Ma, J We, and TR Mackie. Beam: a monte carlo code to simulate radiotherapy treatment units. *Medical physics*, 22(5):503–524, 1995.

[12] K O'Grady, S Davis, and J Seuntjens. Tu-ab-brc-05: Creation of a monte carlo truebeam model by reproducing varian phase space data. *Medical physics*, 43(6Part32):3730–3730, 2016.

[13] I Kawrakow, DWO Rogers, and BRB Walters. Large efficiency improvements in beamnrc using directional bremsstrahlung splitting. *Medical physics*, 31(10):2883–2898, 2004.

[14] J Wulff, K Zink, and I Kawrakow. Efficiency improvements for ion chamber calculations in high energy photon beams. *Medical physics*, 35(4):1328–1336, 2008.

[15] BRB Walters, I Kawrakow, DWO Rogers, et al. Dosxyznrc users manual. *Nrc Report Pirs*, 794:31, 2005.

[16] P Papaconstadopoulos. On the detector response and the reconstruction of the source intensity distribution in small photon fields. *PhD thesis, McGill University Libraries*, 2016.

[17] DWO Rogers, I Kawrakow, JP Seuntjens, BRB Walters, and E Mainegra-Hing. Nrc user codes for egsnrc. *NRCC Report PIRS-702 (Rev. B)*, 2003.

[18] CM Ma and DWO Rogers. Beamdp users manual. *NRC Report PIRS-0509 (D)*, 1995.

[19] I Kawrakow, E Mainegra-Hing, F Tessier, and BRB Walters. The egsnrc c++ class library. *NRC Report PIRS-898 (rev A)*, 2009.

[20] I Kawrakow and DWO Rogers. The egsnrc code system: Monte carlo simulation of electron and photon transport. 2000.

[21] I Kawrakow. Accurate condensed history monte carlo simulation of electron transport. i. egsnrc, the new egs4 version. *Medical physics*, 27(3):485–498, 2000.

[22] MR McEwen. Measurement of ionization chamber absorbed dose kq factors in megavoltage photon beams. *Medical physics*, 37(5):2179–2193, 2010.

[23] J Johansson, B Gorka, J Novotny Jr, JD Bourland, J Bhatnagar, G Bednarz, RCM Best, L Persson, H Nordstrom, and O Svarm. Monte carlo calculated and experimentally verified correction factors for clinical reference dosimetry for the leksell gamma knife®: Application of a new iaea dosimetry formalism. In *Plenary Oral Presentation at the 16th International Meeting of the Leksell Gamma Knife® Society*, page 69, 2012.

[24] GM Mora, A Maio, and DWO Rogers. Monte carlo simulation of a typical 60co therapy source. *Medical physics*, 26(11):2494–2502, 1999.

[25] EB Podgorsak. Radiation oncology physics. *Vienna: International Atomic Energy Agency*, pages 123–271, 2005.

[26] BN Taylor. *Guidelines for Evaluating and Expressing the Uncertainty of NIST Measurement Results (rev)*. DIANE Publishing, 2009.

[27] MS Huq, Min-Sig Hwang, TP Teo, Si Y Jang, DE Heron, and RJ Lalonde. A dosimetric evaluation of the iaea-aapm trs 483 code of practice for dosimetry of small static fields used in conventional linac beams and comparison with iaea trs-398, aapm tg 51, and tg 51 addendum protocols. *Medical physics*, 45(9):4257–4273, 2018.

[28] M Dalaryd, T Knöös, and C Ceberg. Combining tissue-phantom ratios to provide a beam-quality specifier for flattening filter free photon beams. *Medical physics*, 41(11), 2014.

[29] BR Muir and DWO Rogers. The central electrode correction factor for high-z electrodes in small ionization chambers. *Medical physics*, 38(2):1081–1088, 2011.

[30] J Snow and L DeWerd. Th-e-brb-06: Characterization of microionization chambers for small-field reference dosimetry. *Medical Physics*, 39(6Part31):4010–4010, 2012.

[31] W Lechner, P Kuess, D Georg, and H Palmans. Equivalent (uniform) square field sizes of flattening filter free photon beams. *Physics in Medicine & Biology*, 62(19):7694, 2017.

6.7 Supplementary material

6.7.1 *msr* condition

Figure 6.7 shows the ratio of dose and total kerma for different beam qualities of ^{60}Co to 24 MV as a function of the beam radius. For the ^{60}Co and WFF beams the data is taken from Papaconstadopoulos [1]/ Palmans et al. [2]. The data for the TrueBeam 6 MV FFF and 10 MV FFF are calculated in this study. An exponential function $b+(a-b)\exp(-r/c)$ with fit parameters a, b and c is fitted to the data for each beam quality, the beam radius for which the dose to total kerma ratio reaches 99.9% of the saturation are determined as r_{LCPE}. The r_{LCPE} is 1.4 cm for the TrueBeam 6 MV FFF and 2.2 cm for the TrueBeam 10 MV FFF. However, using the calculated beam quality specifiers for the TrueBeam 6 MV FFF ($\mathrm{TPR}_{20,10}(10)$=0.6312±0.0005 and $\%dd(10,10)_x$=%63.74±0.0010) and Eq. 3 and 4 of TRS-483 result in r_{LCPE} of 0.9 cm.

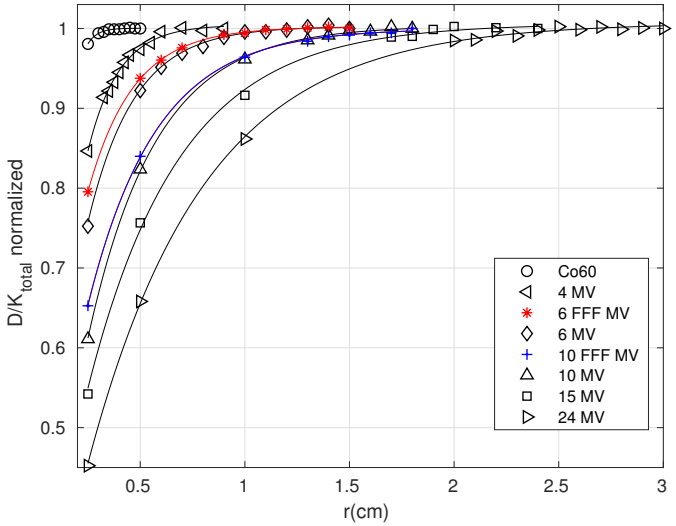

Figure 6.7 Ratio of dose and total kerma for beam qualities of ^{60}Co to 24 MV as a function of the field radius. For the ^{60}Co and WFF beams the data is taken from Papaconstadopoulos [1]/ Palmans et al. [2]. The data for the FFF beams (the TrueBeam 6 MV FFF and 10 MV FFF) is calculated in this study. The SSD is 100 cm for the high-energy photon beams and 80 cm for the ^{60}Co. The dose to total kerma ratio is scored at 5.25 cm depth in water. The data is normalized to the saturation point. The uncertainty on the data calculated in this study (6 FFF and 10 FFF) is type A, less than 0.15% (k=1) and not shown.

Table 6.4 Parameters used in this study for determining of the k_{Q,Q_0}.

parameter	^{60}Co	Q
$S_{w,air}$	1.133 (Andreo [4])	a+b $TPR_{20,10}(10)$ + c $TPR_{20,10}(10)^2$ + d $TPR_{20,10}(10)^3$ (Andreo et al. [2]) a=1.3614, b=-1.2963, c= 2.5302 and d=-1.6896
W_{air} (JC^{-1})	33.97 (Andreo et al. [2])	33.97 (Andreo et al. [2])
p_{cav}	1 (Andreo et al. [2])	1 (Andreo et al. [2])
p_{dis}	1-0.004 r_{cyl} (Andreo et al. [2])	1- δr_{cyl} δ tabulated as a function of $TPR_{20,10}(10)$ (TRS-277)
p_{wall}	$\frac{\alpha s_{wall,air}(\mu_{en}/\rho)_{w,wall}+\tau s_{sleeve,air}(\mu_{en}/\rho)_{w,sleeve}+(1-\alpha-\tau)s_{w,air}}{s_{w,air}}$ (Andreo et al. [2])	$\frac{\alpha s_{wall,air}(\mu_{en}/\rho)_{w,wall}+\tau s_{sleeve,air}(\mu_{en}/\rho)_{w,sleeve}+(1-\alpha-\tau)s_{w,air}}{s_{w,air}}$ (Andreo et al. [2])
$\alpha(t_w)$	1-$e^{-11.88t_w}$ (Andreo et al. [2])	tabulated as a function of wall thickness and $TPR_{20,10}(10)$ (TRS-277)
$\tau(t_s)$	$e^{-11.88t_w}(1-e^{-11.88t_s})$ (Andreo et al. [2])	$e^{-11.88t_w}(1-e^{-11.88t_s})$ (Andreo et al. [2])
$(\mu_{en}/\rho)_{w,med}$	tabulated for different material [5]	tabulated as a function of $TPR_{20,10}(10)$ for different material [5]
$s_{med,air}$	tabulated for different material [5]	tabulated as a function of $TPR_{20,10}(10)$ for different material [5]

6.7.2 Adopting the beam quality correction factors from TRS-398

The beam quality correction factors k_{Q,Q_0} are determined theoretically using Eq. 6.12 [2].

$$k_{Q,Q_0} = \frac{(s_{w,air})_Q (W_{air})_Q P_Q}{(s_{w,air})_{Q_0} (W_{air})_{Q_0} P_{Q_0}} \tag{6.12}$$

$$P_Q = P_{cav} P_{dis} P_{wall} P_{cel} \tag{6.13}$$

Where, $s_{w,air}$ is the water to air stopping power ratios, the W_{air} is the mean energy expended in air per ion pair formed and P_Q is the overall perturbation factor includes the cavity correction (P_{cav}), the displacement correction (P_{dis}), the wall correction (P_{wall}) and the central electrode correction (P_{cel}) in beam qualities Q and Q_0 [2]. All the parameters and references used in this study are summarized in table 6.4. Knowing the inner radius of the chamber cavity (r_{cyl}), the thickness of the wall (t_w), the thickness of the sleeve (t_s if applicable), the wall material, the electrode material, the sleeve material (if applicable) and the $TPR_{20,10}(10)$ of the hypothetical conventional reference field, the k_{Q,Q_0} values are determined using Eq. 6.12, 6.13 and the parameters provided in table 6.4.

6.7.3 Jaffé plot for the PTW 31010 and Exradin A16

The dose per pulse for the TrueBeam 6 FFF and 10 FFF beams at the depth of maximum dose are found out to be 0.065 cGy/Pulse and 0.111 cGy/Pulse respectively. Figure 6.8 shows the Jaffé plot (1/chamber reading against 1/applied voltage) for the PTW 31010 and Exradin A16

for four different dose per pulses. A linear relation is observed for the PTW 31010, however Exradin A16 shows nonlinearity.

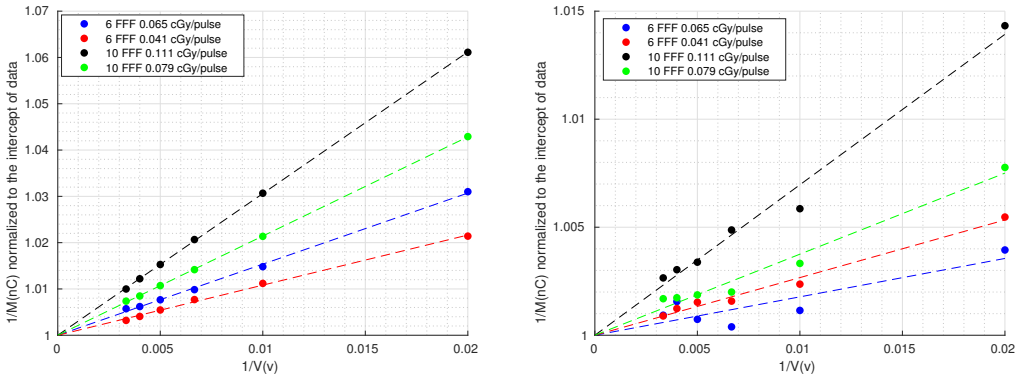

Figure 6.8 1/M vs 1/V (Jaffé plots) for the PTW 31010 (left) and Exradin A16 (right)

6.7.4 Central electrode correction

The P_{cel} ratio in the TrueBeam 6 MV FFF and in cobalt-60 for all chambers studied here is plotted in figure 6.9. Deviation from one is largest for IBA CC01 (1.04%) followed by Exradin-A16 and A14. It is unity (less than 0.07%) for chambers with electrode made of plastic.

6.7.5 $k^{f_A,f_{ref}}_{Q_A^{FFF},Q^{FFF}}$

The $k^{f_A,f_{ref}}_{Q_A^{FFF},Q^{FFF}}$ calculated in MC for seven chamber types is shown in figure 6.10. For all chambers the $k^{f_A,f_{ref}}_{Q_A^{FFF},Q^{FFF}}$ is less than 0.07%. However for IBA CC01, it is as large as 1.6% for the 10×2 cm^2 field size.

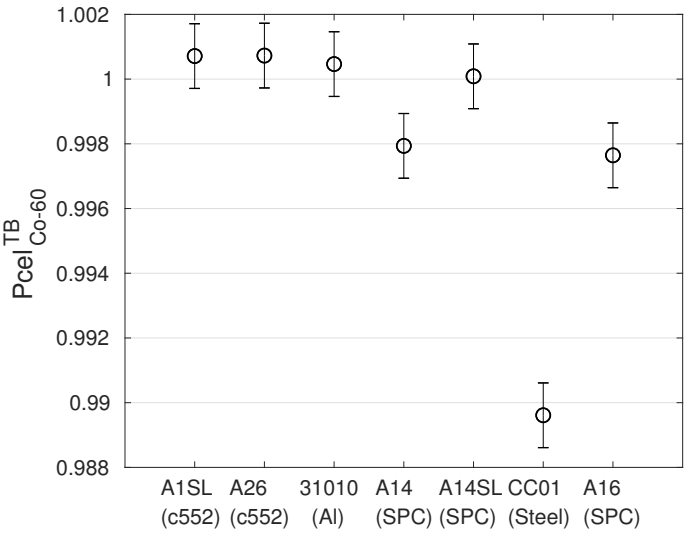

Figure 6.9 The P_{cel} ratio in the TrueBeam 6 MV FFF and in cobalt-60 for seven chamber types studied here

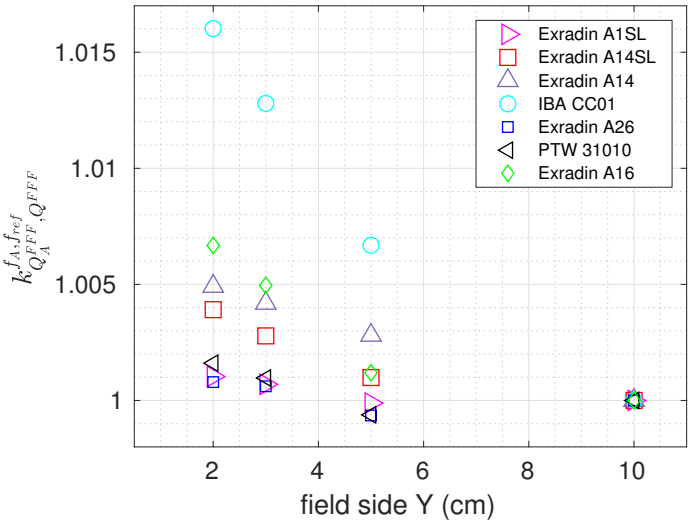

Figure 6.10 The $k_{Q_A^{FFF},Q^{FFF}}^{f_A,f_{ref}}$ factors calculated in MC for seven chamber types studied here for 10×2 cm^2, 10×3 cm^2 and 10×5 cm^2 field sizes defined at SSD 85 cm and 10×10 cm^2 defined at SSD 100 cm. The uncertainty is type A and less than 0.1% (k=1)

Table 6.5 Generic beam quality conversion factors for different chamber types in four different field sizes determined using both approaches and corrected for the MC calculated values of $k_{Q_A^{FFF},Q^{FFF}}^{f_A,f_{ref}}$ and P_{cel}. Uncertainty on $k_{Q_{msr},Q_0}^{f_{msr},f_{ref}}$ (1st approach) is type A and 0.1%. Uncertainty on the $k_{Q^{WFF},Q_0}^{f_{ref}} k_{Q^{FFF},Q^{WFF}}^{f_{ref}} k_{Q_A^{FFF},Q^{FFF}}^{f_A,f_{ref}}$ values is estimated to be 1%.

Chamber type	Field cm^2	$k_{Q_A,Q_0}^{f_A,f_{ref}}$	$(k_{Q^{WFF},Q_0}^{f_{ref}} k_{Q^{FFF},Q^{WFF}}^{f_{ref}} k_{Q_A^{FFF},Q^{FFF}}^{f_A,f_{ref}})$ using MC $k_{Q_A^{FFF},Q^{FFF}}^{f_A,f_{ref}}$ and P_{cel} values	diff (%)
Exradin A1SL	10×2	0.9943	0.9984	0.41
Exradin A1SL	10×3	0.9940	0.9981	0.42
Exradin A1SL	10×5	0.9932	0.9975	0.44
Exradin A1SL	10×10	0.9933	0.9979	0.47
Exradin A26	10×2	0.9934	0.9961	0.27
Exradin A26	10×3	0.9932	0.9950	0.18
Exradin A26	10×5	0.9920	0.9953	0.33
Exradin A26	10×10	0.9926	0.9962	0.36
Exradin A16	10×2	0.9956	0.9988	0.32
Exradin A16	10×3	0.9939	0.9972	0.33
Exradin A16	10×5	0.9902	0.9937	0.36
Exradin A16	10×10	0.9890	0.9929	0.39
Exradin A14SL	10×2	0.9966	1.0004	0.38
Exradin A14SL	10×3	0.9954	0.9993	0.39
Exradin A14SL	10×5	0.9937	0.9977	0.41
Exradin A14SL	10×10	0.9927	0.9971	0.44
Exradin A14	10×2	0.9957	0.9993	0.36
Exradin A14	10×3	0.9949	0.9986	0.37
Exradin A14	10×5	0.9936	0.9975	0.39
Exradin A14	10×10	0.9908	0.9950	0.42
PTW 31010	10×2	0.9902	0.9932	0.30
PTW 31010	10×3	0.9896	0.9929	0.33
PTW 31010	10×5	0.9880	0.9916	0.37
PTW 31010	10×10	0.9886	0.9926	0.40
IBA CC01	10×2	0.9963	0.9999	0.37
IBA CC01	10×3	0.9931	0.9969	0.38
IBA CC01	10×5	0.9871	0.9911	0.40
IBA CC01	10×10	0.9806	0.9848	0.43

Bibliography

[1] P Papaconstadopoulos. On the detector response and the reconstruction of the source intensity distribution in small photon fields. *PhD thesis, McGill University Libraries*, 2016.

[2] H Palmans, P Andreo, K Christaki, MS Huq, and J Seuntjens. TRS-483: Dosimetry of small static fields used in external beam radiotherapy: an international code of practice for reference and relative dose determination. *International Atomic Energy Agency, Vienna*, 2017.

[3] P Andreo, DT Burns, K Hohlfeld, MS Huq, T Kanai, F Laitano, V Smyth, and S Vynckier. TRS-398: Absorbed dose determination in external beam radiotherapy: an international code of practice for dosimetry based on standards of absorbed dose to water. *International Atomic Energy Agency*, 420, 2001.

[4] P Andreo. Chamber-dependent wall correction factors in dosimetry. *Physics in Medicine & Biology*, 31(11),1986.

[5] TRS-277 : Absorbed dose determination in photon and electron beams. An international Code of Practice, *International Atomic Energy Agency*, 1997.

Chapter 7

IAEA-AAPM TRS-483-based reference dosimetry of the new RefleXion^{TM} biology-guided radiotherapy (BgRT) machine

Lalageh Mirzakhanian, Rostem Bassalow, Daniel Zaks, Calvin Huntzinger and Jan Seuntjens

Submitted to Medical Physics journal, July 2019

7.1 Preface

In this chapter, the RefleXion BgRT machine was calibrated using the two methodologies described in chapter 6. The data for reference dosimetry of RefleXion BgRT was provided in this chapter.

Abstract

Purpose: The recent RefleXion^{TM} biology-guided radiotherapy (BgRT) machine (Hayward, CA, USA) combines stereotactic radiotherapy with positron-emission tomography (PET) and computed tomography (CT) imaging systems (PET/CT). The closest possible field size to a conventional reference field in this system is 10×2 cm^2 or possibly 10×3 cm^2 at the isocenter.

For a 6 MV FFF beam, a 10×2 cm^2, and for Farmer type chambers, a 10×3 cm^2 field do not meet the lateral charged particle equilibrium (LCPE) condition of a machine-specific reference (*msr*) field introduced in the International Atomic Energy Agency (IAEA) and the American Association of Physicists in Medicine (AAPM) TRS-483 Code of Practice (COP) [1]. Consequently, TRS-483 cannot be directly used for the calibration of this system. However, in a recent study we extended the methodology provided in TRS-483 to be applicable to fields of the nature as produced by the RefleXion BgRT machine [2] . The purpose of this study is to provide data for the calibration of the RefleXion BgRT machine following the TRS-483 and Mirzakhanian et al. [2].

Methods: The RefleXion BgRT machine was calibrated using two methodologies described in TRS-483 and Mirzakhanian et al. [2] In the first approach (Approach 1), the generic beam quality conversion factor $k_{Q_A,Q_0}^{f_A,f_{ref}}$ was calculated using an accurate Monte Carlo (MC) model of the beam and of six ionization chamber types, where field A represents the reference calibration field that does not fulfill *msr* conditions. In the second approach (Approach 2), a square equivalent field size was determined for field A of 10×2 cm^2 and 10×3 cm^2. Knowing the equivalent field size, the beam quality specifier for the hypothetical 10×10 cm^2 field size was derived. This was used to calculate the beam quality correction factor analytically for the six chamber types using the TRS-398 [3]. The accuracy of Approach 2 is studied in comparison to Approach 1.

Results: Among the chambers, the PTW 31010 had the largest $k_{Q_A,Q_0}^{f_A,f_{ref}}$ correction due to the volume averaging effect. The smallest-volume chamber (IBA CC01) had the smallest correction followed by the other micro chambers Exradin-A14 and A14SL. The equivalent square fields sizes were found to be 3.6 cm and 4.8 cm for the 10×2 cm^2 and 10×3 cm^2 field sizes respectively. The beam quality conversion factors calculated using the two approaches were within 0.27% for all chambers except IBA CC01. The latter chamber has an electrode made of steel and the differences between the correction calculated using the two approaches was the largest, i.e., 0.5%.

Conclusions: In this study we provided the $k_{Q_A,Q_0}^{f_A,f_{ref}}$ values as a function of the beam quality specifier at the RefleXion BgRT setup ($TPR_{20,10}$(S) and $\%dd(10,S)_x$) for six chamber types. We suggest using the first approach for calibration of the RefleXion BgRT machine. However, if the MC correction is not available for a user's detector, the user can use the second approach for estimating the beam quality conversion factor to sufficient accuracy (0.3%) provided the

chamber electrode is not made of high Z material.

7.2 Introduction

The RefleXion BgRT machine combines stereotactic radiotherapy with Positron Emission Tomography (PET) and fan-beam computed tomography (CT) imaging systems for better localization and tracking of the tumor during the treatment delivery. It delivers a high dose of radiation to the tumor while sparing the healthy tissue based on the patient's individual biology guided during the treatment (intra-fraction) using PET emissions in real-time. The energy of the beam is 6 MV and the beam is FFF. The maximum field size achievable in this machine is 2 or 3 cm in the IEC 61217 Y dimension and 40 cm in the X dimension at the source-to-axis distance (SAD) of 85 cm. The closest field to the conventional reference field size is 10×2 cm^2 or 10×3 cm^2 at the isocenter.

Similar to any other radiotherapy machine, the clinical application of the RefleXion BgRT machine for external beam radiation therapy needs the accurate calibration of absorbed dose per monitor unit of delivered radiation. The current protocols for the reference dosimetry of conventional photon beams the AAPM TG-51 [4], its addendum [5] and the TRS-398 Code of Practice [3]) cannot be used for the reference dosimetry of this machine since the conventional reference condition of 10×10 cm^2 field size and source-to-surface distance (SSD) of 100 cm cannot be realized in the RefleXion BgRT machine. Recently, the TRS-483 [1] report proposes a formalism for the dosimetry of small static fields in external beam radiotherapy. However as explained in Mirzakhanian et al. [2] this formalism cannot be directly used for the reference dosimetry of the RefleXion BgRT machine. Firstly, the 10×2 cm^2 and 10×3 cm^2 field sizes of the RefleXion BgRT machine do not meet the LCPE condition of the *msr* field. Secondly, the methodology for deriving the beam quality specifier for the hypothetical 10×10 cm^2 field provided in the TRS-483 is restricted to a 4 cm equivalent field size. Additionally, the tabulated data for the equivalent uniform square field size is limited to a 3-cm field size. A third issue is that the tabulated values of beam quality correction factors are provided only for larger chambers not suitable for calibration of the RefleXion BgRT machine. A solution to these issues was addressed in Mirzakhanian et al. [2]. They extended the TRS-483 methodology to fields as small as 2 cm on a side and utilizing data from the Varian TrueBeam machine

emulating a setup as in the RefleXion BgRT machine: 6 FFF beam energy, field size of 10×3 cm^2 and 10×2 cm^2 at Source to Detector Distance (SDD) of 85 cm.

The RefleXion BgRT is a new machine and there is no available data on its reference dosimetry. The purpose of this study is to provide these data for the calibration of the RefleXion BgRT machine following the two methodologies described in Mirzakhanian et al. [2] and TRS-483. In the first method, the $k_{Q_A,Q_0}^{f_A,f_{ref}}$ factors were calculated *ab initio* using MC with an accurate beam model and for six different chamber models and three different beam qualities. In the second method, the beam quality specifier for the hypothetical 10×10 cm^2 field size was derived from the beam quality specifier at the 10×2 cm^2 and 10×3 cm^2 field sizes. The square equivalent field size was also determined for the 10×2 cm^2 and 10×3 cm^2 field sizes. Afterwards, the beam quality specifier for the hypothetical 10×10 cm^2 field size was used to determine the beam quality correction factor using the TRS-398 for the six chamber types. The beam quality correction factor was corrected for the differences between FFF and WFF beams. The results of two methods are compared. Recommendations are made on the calibration of the RefleXion BgRT machine.

7.3 Materials and Methods

For the calibration of the RefleXion BgRT machine, similar to Mirzakhanian et al. [2] the following two calibration methods were used.

7.3.1 Calibration approach I: Using the generic beam quality correction factor $k_{Q_A,Q_0}^{f_A,f_{ref}}$

The absorbed dose to water for the field A ($D_{w,Q_A}^{f_A}$) which is 10×2 cm^2 or 10×3 cm^2 in the RefleXion BgRT machine is given by equation 7.1.

$$D_{w,Q_A}^{f_A} = M_{Q_A}^{f_A} N_{D,w,Q_0}^{f_{ref}} k_{Q_A,Q_0}^{f_A,f_{ref}} \tag{7.1}$$

In which $M_{Q_A}^{f_A}$ is the chamber response in the A field corrected for influence quantities, such as pressure, temperature, ion recombination, polarity effects, etc. The $N_{D,w,Q_0}^{f_{ref}}$ is the calibration coefficient in terms of absorbed dose to water of the ionization chamber measured at the standards laboratory for a conventional 10×10 cm^2 reference calibration field (f_{ref})

with beam quality Q_0. The $k_{Q_A,Q_0}^{f_A,f_{ref}}$ factor corrects for the differences between the conditions of field size, phantom material, geometry, and beam quality of the conventional reference field (f_{ref}) and the A field (f_A). It is defined as below:

$$k_{Q_A,Q_0}^{f_A,f_{ref}} = \frac{D_{w,Q_A}^{f_A}/M_{Q_A}^{f_A}}{D_{w,Q_0}^{f_{ref}}/M_{w,Q_0}^{f_{ref}}}, \tag{7.2}$$

where, the $D_{w,Q_A}^{f_A}$ and $D_{w,Q_0}^{f_{ref}}$ are the mean absorbed dose to water over a small volume in A and reference fields respectively. $M_{Q_A}^{f_A}$ and $M_{w,Q_0}^{f_{ref}}$ are the response of the chamber in field A and reference field corrected for influence quantities respectively. Since in the MC simulations the chamber response is assumed to be proportional to the mean absorbed dose to the sensitive volume of the detector, equation 7.2 can be written as:

$$k_{Q_A,Q_0}^{f_A,f_{ref}} = \frac{D_{w,Q_A}^{f_A}/D_{det,Q_A}^{f_A}}{D_{w,Q_0}^{f_{ref}}/D_{det,Q_0}^{f_{ref}}} \tag{7.3}$$

where $D_{det,Q_A}^{f_A}$ and $D_{det,Q_0}^{f_{ref}}$ are the mean absorbed dose to the sensitive volume of the detector in the A and reference fields respectively. The four parameters $D_{w,Q_A}^{f_A}$, $D_{det,Q_A}^{f_A}$, $D_{w,Q_0}^{f_{ref}}$ and $D_{det,Q_0}^{f_{ref}}$ were calculated in MC as explained below.

Six chamber models including Exradin-A1SL, A26, A14, A14SL, IBA CC01, and PTW 31010 were simulated in the `egs++` geometry package [6] of `EGSnrc` [7, 8] MC code using the blueprints provided by the manufacturers. These are the same chamber types used in Mirzakhanian et al. [2]. Generic specifications of the chambers can be found in table I of Mirzakhanian et al. [2].

The RefleXion BgRT machine was modeled using the `BEAMnrc` [9]/`EGSnrc` MC code. The collimation system consisted of the primary collimator, the split-jaw (upper and lower jaws) and the multileaf collimator (MLC) which was sandwiched between the upper and lower jaws. The directional bremsstrahlung splitting [10] was used as the variance reduction technique with a splitting number of 1000 in `BEAMnrc`. For the 10×2 cm^2 and 10×3 cm^2 field sizes, the radius of the DBS splitting field was set to 10 cm at 85 cm distance. The electron source was modeled as a parallel circular beam. The electron cut-off energy (ECUT) and photon cut-off energy (PCUT) values were set to 700 keV and 10 keV respectively. In `BEAMnrc`, the primary electron kinetic energy and the radius of the electron beam were used to tune the beam to

achieve agreement between MC calculated and measured depth, cross-plane and in-plane profiles.

To calculate the profiles using MC, the beam model was compiled as a shared library to the `DOSXYZnrc` user code [11]. The depth, cross-plane and in-plane profiles were calculated using `EGSnrc/DOSXYZnrc`. The mean absorbed dose to water was calculated in a cubic phantom ($30 \times 30 \times 30$ cm^3) with the scoring voxel size of $0.25 \times 0.25 \times 0.1$ cm^3 at three different depths: 1.5 cm, 10 cm and 20 cm for both fields 10×2 cm^2 and 10×3 cm^2. The number of primary particles varied to achieve a statistical uncertainty better than 0.1% on the dose at 10 cm depth. In the `DOSXYZnrc` simulations, the ECUT and PCUT values were set to 700 keV and 10 keV respectively.

The profile measurements were performed using Exradin A14SL ion chamber in a scanning water tank. The cross-plane and in-plane profiles were measured for both fields 10×2 cm^2 and 10×3 cm^2 at three different depths: 1.5 cm, 10 cm and 20 cm with SSD 85 cm. The percent depth dose at 10 cm depth at SSD of 85 cm was measured using the Exradin A14SL in both field sizes.

To model the field *A* setup, the RefleXion BgRT beam model was used as a shared library in `egs_chamber` calculations. The field size was 10×2 cm^2 and 10×3 cm^2 defined at SSD 85 cm. The reference point of the detector was placed at 10 cm depth in a $30 \times 30 \times 30$ cm^3 water phantom. The average absorbed dose to the sensitive volume of the detector ($D^{f_A}_{det,Q_A}$) was calculated. The average absorbed dose to a small volume of water (scoring sphere with diameter 3 mm) at 10 cm depth in the water box was also calculated ($D^{f_A}_{w,Q_A}$).

To model the reference setup, the Co^{60} spectrum calculated by Mora et al. [12] was used in this study as an input for the `egs_chamber` calculations. The source was a point source collimated into a 10×10 cm^2 field size at SSD 100 cm. The detector and small scoring volume (3 mm diameter spherical volume) were placed at 5 cm depth in the water phantom. The averaged dose to the sensitive volume of the detector ($D^{f_{ref}}_{det,Q_0}$) and small volume ($D^{f_{ref}}_{w,Q_0}$) were calculated in `egs_chamber`.

In both set-ups the *A* and ref, the symmetry axis of the chamber was perpendicular to the beam axis. In all `egs_chamber` calculations, the ECUT and PCUT values were set to 521 keV (including electron rest mass) and 10 keV respectively. The production threshold for electrons (AE) was set to 521 keV and for photons (AP) to 10 keV. The number of primary particles was chosen to realise a statistical uncertainty of better than 0.05% on the dose. Photon cross section enhancement (XCSE) was used as the variance reduction technique in `EGSnrc/egs_chamber`.

The photon cross section was enhanced by a XCSE factor of 256 within a one cm cylindrical water shell surrounding the chamber. Default transport parameters were used in `EGSnrc` except for the use of XCOM photon cross section. The calculations of $D^{f_A}_{det,Q_A}$ and $D^{f_A}_{w,Q_A}$ were repeated for two other kinetic energies of the incident beam (5.2 and 6 MeV).

The beam quality specifier $TRP_{20,10}$(10,S) was calculated using `egs_chamber` for both field sizes 10×2 cm^2 and 10×3 cm^2 and for three beam incident energies 5.2 MeV, 5.6 MeV (the nominal) and 6 MeV. Three beam incident energies were chosen to report the corrections as a function of beam quality since like any other linear accelerator each RefleXion BgRT machine might have a slightly different beam quality specifier. The `BEAMnrc` was used as a shared library in `egs_chamber`. The average dose to a small volume of water (0.15 cm radius sphere) was calculated at depths of 10 cm and 20 cm in a water phantom ($30 \times 30 \times 30$ cm^3) with SAD 85 cm using `EGSnrc` `egs_chamber` user code [13].

To determine the beam quality specifier $\%dd(10,S)_X$, `BEAMnrc` was used to create phase space files for both 10×2 cm^2 and 10×3 cm^2 field sizes at an SSD of 85 cm. The phase space file was used as an input for the `DOSXYZnrc` user-code [11]. In the `DOSXYZnrc` calculation only the photon part of phase space file was used. The mean absorbed dose to water was calculated along the central axis of a cubic phantom ($30 \times 30 \times 30$ cm^3) with the scoring voxel size of $0.30 \times 0.30 \times 0.15$ cm^3. The number of primary particles was tuned to achieve a statistical uncertainty of better than 0.1% on the dose at 10 cm depth and depth at maximum dose (z_{max}). The $\%dd(10,S)$ was also calculated in this work using all particles of the phase space file to study the difference between the total percentage depth dose and the photon component of the percentage depth dose.

The $k^{f_A,f_{ref}}_{Q_A,Q_0}$ corrections were then provided as a function of $TRP_{20,10}$(10,S) and $\%dd(10,S)_X$.

7.3.2 Calibration approach II: Using the theoretical approach without a generic correction factor $k^{f_A,f_{ref}}_{Q_A,Q_0}$ available

The absorbed dose to water for the A field (f_A), in a beam of quality Q_A for a FFF beam, at the reference depth in water and in the absence of the ionization chamber is given by (See also, Mirzakhanian et al. [2]):

$$D^{f_A}_{w,Q^{FFF}_A} = M^{f_A}_{Q^{FFF}_A} N^{f_{ref}}_{D,w,Q_0} k^{f_{ref}}_{Q^{WFF},Q_0} k^{f_{ref}}_{Q^{FFF},Q^{WFF}} k^{f_A,f_{ref}}_{Q^{FFF}_A,Q^{FFF}} \tag{7.4}$$

where, $N_{D,\mathrm{w},Q_0}^{f_{\mathrm{ref}}}$ is the absorbed dose to water calibration coefficient of the ionization chamber determined at the standards laboratory for a conventional 10×10 cm^2 reference field in beam quality Q_0. The $k_{Q^{\mathrm{WFF}},Q_0}^{f_{\mathrm{ref}}}$ is the beam quality correction factor from TRS-398 or TG-51 for a WFF beam with the same beam quality specifier as the one determined for FFF beam. This requires knowledge of the beam quality Q of the hypothetical 10×10 cm^2 field and the square equivalent field. The $k_{Q^{\mathrm{FFF}},Q^{\mathrm{WFF}}}^{f_{\mathrm{ref}}}$ factor corrects for the difference in response of the ionization chamber in WFF and FFF beams. It includes the water-to-air stopping-power ratio, ionization chamber perturbation corrections and the volume averaging correction. The $k_{Q_{\mathrm{msr}}^{\mathrm{FFF}},Q^{\mathrm{FFF}}}^{f_{\mathrm{msr}},f_{\mathrm{ref}}}$ corrects for the difference in response of the chamber in a hypothetical 10×10 cm^2 field in the RefleXion BgRT machine with beam quality $\mathrm{Q}^{\mathrm{FFF}}$ and the response of chamber in the same RefleXion BgRT machine with beam quality $\mathrm{Q}_A^{\mathrm{FFF}}$ but in the A field.

The square equivalent field of 10×2 cm^2 and 10×3 cm^2 was calculated using equation 58 of TRS-483 using the lateral beam profile ($F(r)$) measured at RefleXion BgRT machine. Mirzakhanian et al. [2] showed that the square equivalent field of 10×2 cm^2 can be determined using the same approach as described in TRS-483 without introducing significant errors in the beam quality conversion values. Similarly, $\mathrm{TPR}_{20,10}(10)$ can be calculated using equation 28 of TRS-483 and $\mathrm{TPR}_{20,10}(\mathrm{S})$ for both fields 10×2 cm^2 and 10×3 cm^2. Knowing the $\mathrm{TPR}_{20,10}(10)$, the $k_{Q^{\mathrm{WFF}},Q_0}^{f_{\mathrm{ref}}}$ factor was calculated analytically using TRS-398.

To determine the $k_{Q^{\mathrm{FFF}},Q^{\mathrm{WFF}}}^{f_{\mathrm{ref}}}$ factor for RefleXion BgRT machine, the water-to-air stopping-power ratio correction was assumed to be 0.997 [14, 2]. The ionization chamber perturbation correction factor differences were assumed to be unity [1] and the volume averaging was calculated using equation 54 of TRS-483.

The $k_{Q_{\mathrm{A}},Q}^{f_{\mathrm{A}},f_{\mathrm{ref}}}$ factor was assumed to be unity in this study similar as in TRS-483 [1]. It was not possible to determine the $k_{Q_{\mathrm{A}},Q}^{f_{\mathrm{A}},f_{\mathrm{ref}}}$ factor directly using MC because in order to create the hypothetical 10×10 cm^2 reference field in the RefleXion BgRT MC beam model, the primary collimator in the RefleXion BgRT machine would need to be modified and this would modify the beam quality significantly.

7.4 Results

The depth dose calculated using MC was compared to the measurement in the 10×2 cm^2 and 10×3 cm^2 field sizes. The agreement was within 0.5% past 5 mm depth. For the cross-plane and in-plane profiles, the agreement was within 1% in the center, 5% in the penumbra and

about 10% in the umbra region (figure 7.3 in supplementary material). Further tuning of the beam model could reduce these differences but the impact on the parameters calculated in this work would not be significant. The nominal kinetic energy of the incident beam was 5.6 MeV. This value was chosen by comparing the MC calculated and measured profiles.

The measured $\%dd(10,S)$ for the 10×2 cm^2 and 10×3 cm^2 were 57.1% and 58.7% respectively within 0.3% of the MC calculated values (57.3% for 10×2 cm^2 and 58.7% for 10×3 cm^2). The difference between the photon-only $\%dd(10,S)_X$ and $\%dd(10,S)$ both calculated using MC was found be less than 0.15% for both fields showing that electron contamination has no meaningful effect on beam quality correction factors for this machine.

The $k_{Q_A,Q_0}^{f_A,f_{ref}}$ factors for six chamber types as a function of beam quality $TPR_{20,10}$(S) and $\%dd(10,S)_X$ for both fields 10×2 cm^2 and 10×3 cm^2 is plotted in figure 7.1. Among the six chamber types for the 10×2 cm^2 field size and the nominal beam quality, the smallest-volume chamber (IBA CC01) has the smallest correction (0.9996) followed by the other micro chambers Exradin-A14 (0.9973) and A14SL (0.9965). The intermediate-volume scanning chamber Exradin A1SL and the microchamber Exradin A26 have larger correction factors (0.9941 and 0.9940 respectively). The largest-volume chamber (PTW 31010) has the largest $k_{Q_A,Q_0}^{f_A,f_{ref}}$ factor (0.9919). A similar trend is observed for the 10×3 cm^2 field size. Figure 7.1.b also shows that changing the beam quality specifier by about 3% changes the $k_{Q_A,Q_0}^{f_A,f_{ref}}$ factors by at most 0.3% (for the largest chamber, PTW 31010 in 10×3 cm^2 field size).

The equivalent square fields sizes for the RefleXion BgRT machine were found to be 3.6 cm and 4.8 cm for the 10×2 cm^2 and 10×3 cm^2 field sizes respectively.

Figure 7.2 shows a comparison between the $k_{Q_A,Q_0}^{f_A,f_{ref}}$ correction calculated using the Approach I and the $k_{Q^{WFF},Q_0}^{f_{ref}}$ $k_{Q^{FFF},Q^{WFF}}^{f_{ref}}$ $k_{Q_A^{FFF},Q^{FFF}}^{f_A,f_{ref}}$ values determined from the Approach II. Overall, aside from the IBA CC01 chamber, a good agreement was observed between the correction calculated using the two methodologies for all chambers in both fields (less than 0.3 %). However for the IBA CC01 the differences between the correction calculated using the two methodologies was 0.5%. The uncertainty shown on $k_{Q_{msr},Q_0}^{f_{msr},f_{ref}}$ is of type A and is less than 0.1%. The type B uncertainty for similar type of calculations is estimated to be 0.4% [16, 15]. The combined type A and B uncertainty on $k_{Q_{msr},Q_0}^{f_{msr},f_{ref}}$ values is expected to be between 0.40-0.49% [15, 16]. The estimated uncertainty on the $k_{Q^{WFF},Q_0}^{f_{ref}}$ $k_{Q^{FFF},Q^{WFF}}^{f_{ref}}$ $k_{Q_A^{FFF},Q^{FFF}}^{f_A,f_{ref}}$ values is estimated to be 1% [1, 3, 2].

The data for the nominal beam quality of the 10×2 cm^2 and 10×3 cm^2 field sizes for all chambers determined using both approaches is also provided in table 7.1.

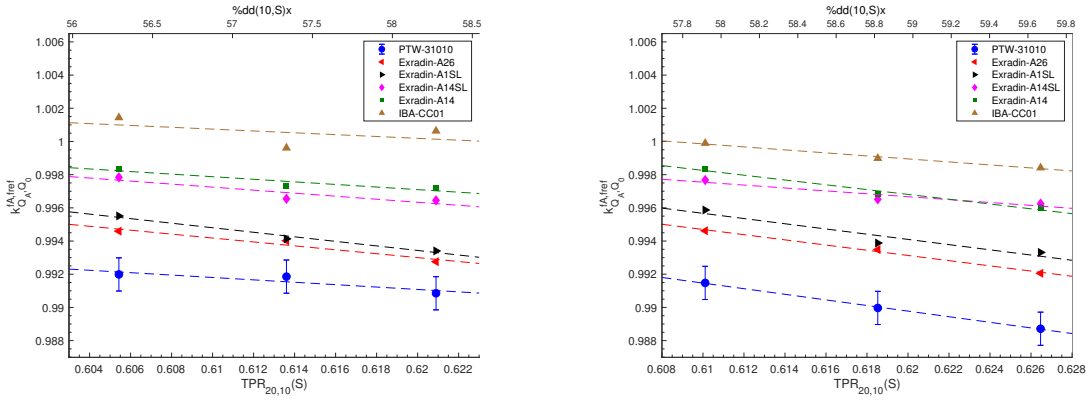

a) 10×2 cm^2 field size b) 10×3 cm^2 field size

Figure 7.1 Monte Carlo calculated $k_{Q_A,Q_0}^{f_A,f_{ref}}$ factors as a function of beam quality specifiers $TPR_{20,10}(S)$ and $\%dd(10,S)_X$ for both field sizes 10×2 cm^2 and 10×3 cm^2 at RefleXion BgRT machine. The Type A uncertainty on the MC calculated $k_{Q_A,Q_0}^{f_A,f_{ref}}$ values is less than 0.1% (k=1). It is shown only for PTW 31010 for visibility.

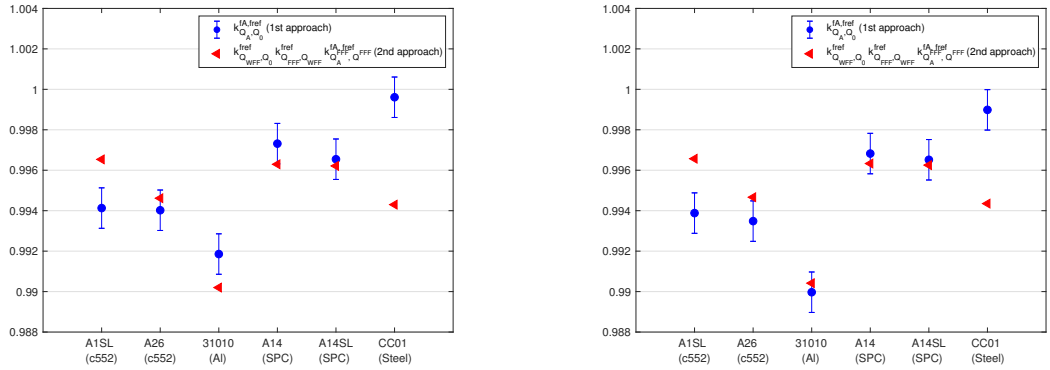

a) 10×2 cm^2 field size b) 10×3 cm^2 field size

Figure 7.2 Comparison between the $k_{Q_A,Q_0}^{f_A,f_{ref}}$ factors calculated using the Approach I and the $k_{Q^{WFF},Q_0}^{f_{ref}} k_{Q^{FFF},Q^{WFF}}^{f_{ref}}$ $k_{Q_A^{FFF},Q^{FFF}}^{f_A,f_{ref}}$ values determined using Approach II for both field sizes a) 10×2 cm^2 and b) 10×3 cm^2 in the RefleXion BgRT machine. The uncertainty on the MC calculated $k_{Q_A,Q_0}^{f_A,f_{ref}}$ values is of type A and is less than 0.1% (k=1). The estimated uncertainty on the $k_{Q^{WFF},Q_0}^{f_{ref}} k_{Q^{FFF},Q^{WFF}}^{f_{ref}}$ $k_{Q_A^{FFF},Q^{FFF}}^{f_A,f_{ref}}$ values is assumed to be 1% [3] and is not shown.

Table 7.1 Generic beam quality conversion factors for different chamber types for the nominal beam quality of the 10×2 cm^2 and 10×3 cm^2 field sizes determined using both approaches. Type A uncertainty on $k_{Q_{msr},Q_0}^{f_{msr},f_{ref}}$ (1st approach) is 0.1%. Uncertainty on the $k_{Q^{WFF},Q_0}^{f_{ref}}$ $k_{Q^{FFF},Q^{WFF}}^{f_{ref}}$ $k_{Q_A^{FFF},Q^{FFF}}^{f_A,f_{ref}}$ values (2nd approach) is estimated to be 1%.

chamber type	field cm^2	Method I	Method II	diff (%)
Exradin-A1SL	10×2	0.9941	0.9965	-0.24
Exradin-A1SL	10×3	0.9939	0.9966	-0.27
Exradin-A26	10×2	0.9940	0.9946	-0.06
Exradin-A26	10×3	0.9935	0.9947	-0.12
Exradin-A14SL	10×2	0.9965	0.9962	+0.03
Exradin-A14SL	10×3	0.9965	0.9963	+0.03
Exradin-A14	10×2	0.9973	0.9963	+0.10
Exradin-A14	10×3	0.9968	0.9963	+0.05
PTW-31010	10×2	0.9919	0.9902	+0.17
PTW-31010	10×3	0.9900	0.9904	-0.05
IBA-CC01	10×2	0.9996	0.9943	+0.53
IBA-CC01	10×3	0.9990	0.9944	+0.46

7.5 Discussion

A good agreement was observed between the Monte Carlo calculated and the measured beam quality specifier ($\%dd(10,S)$) for the RefleXion BgRT machine.

The larger correction for PTW 31010 is dominated by volume averaging over its larger cavity volume. The microchambers IBA CC01, Exradin-A14 and A14SL have the smallest correction due to their small cavity volume. A similar trend was also observed in Mirzakhanian et al. [2] where a similar setup (10×2 cm^2 and 10×3 cm^2 field sizes at SDD 85 cm) was emulated using the 6 FFF Varian TrueBeam machine.

Although the microchambers (Exradin-A14, A14SL and IBA CC01) exhibit smaller correction factors, one should be careful when using these microchambers. At normal operating voltages the electric field strength in the microchambers might be too high causing charge multiplication [17] which can be observed in anomalous polarity and ion recombination corrections. For this reason, these detectors are not recommended for reference dosimetry in high-dose-rate photon beams (FFF) [18]. Hyun et al. [18] has shown, however, that the microchamber Exradin-A26 and the intermediate-volume scanning chamber Exradin-A1SL meet the reference-class chamber requirements with respect to ion recombination and polarity

in the high dose rate linac beams [18]. However, Exradin-A26 is a new chamber and is not listed in the TRS-483 and further measurements are needed to confirm the use of this chamber for calibration. Furthermore, in TRS-483, the Exradin-A1SL is also only recommended for use in calibration of Gamma Knife. Overall, as expected, the $k_{Q_A,Q_0}^{f_A,f_{ref}}$ factors decrease by increasing the beam quality specifier for most chambers. Also, increasing the field size from 10×2 cm^2 to 10×3 cm^2 increases the beam quality specifier resulting in a slight decrease in the $k_{Q_A,Q_0}^{f_A,f_{ref}}$ factors for most chambers.

We found that, from the perspective of reference dosimetry, electron contamination is negligible in the RefleXion BgRT machine for both field sizes and is less than 0.15%. This is consistent with the observation by Mirzakhanian et al. [2] for TrueBeam and for smaller fields. We can assume that $\%dd(10,S)$ is equal to $\%dd(10,S)_X$ and there is therefore no need to use the lead foil for this FFF beam.

The equivalent uniform square field sizes of 3.6 cm for 10×2 cm^2 field size and 4.8 cm for 10×3 cm^2 field size obtained in this study are in agreement with the equivalent uniform square *msr* field size of 10×2 cm^2 in Table III of Mirzakhanian et al. [2] and 10×3 cm^2 in Table 16 of TRS-483 [1] respectively.

Reasonable agreement is observed between the corrections calculated using the two approaches for chambers with electrode made of low or intermediate Z material with differences between the approaches of less than 0.3%. This is also consistent with the magnitude of differences reported in Mirzakhanian et al. [2] for the 6 FFF Varian TrueBeam machine in 10×2 cm^2 and 10×3 cm^2 field sizes. The larger difference (0.5%) for the IBA CC01 is due to the larger differences in the central electrode perturbation factors for IBA CC01 in WFF and FFF beam since the chamber has an electrode made of high Z material (Steel) [19, 2]. Also we have assumed that $k_{Q_A^{FFF},Q^{FFF}}^{f_A,f_{ref}}$ was unity following the TRS-483. Mirzakhanian et al. [2] have shown that for IBA CC01 the $k_{Q_A^{FFF},Q^{FFF}}^{f_A,f_{ref}}$ can be as large as 1.6%.

For the chambers investigated in this work, the user could measure the beam quality specifier $TPR_{20,10}$(S) or $\%dd(10,S)_X$ at SAD or SSD 85 cm respectively and use figure 7.1 to interpolate the $k_{Q_A,Q_0}^{f_A,f_{ref}}$ values for their own beam quality. However, given the modest beam quality dependence of $k_{Q_A,Q_0}^{f_A,f_{ref}}$ one could use the correction factors corresponding to the *nominal* beam energy reported here since the factor varies by less than 0.3% when changing the beam quality specifier by 3%.

In case the correction for the user's chamber is not available, the second approach can be used to estimate the correction factor to within 0.3%. However, this methodology should

not be used for chambers with electrodes made of high Z material and for these chambers an explicit Monte Carlo calculation or measurement should be performed. The overall combined standard uncertainty on the correction factors calculated using the second approach is more significant (1%) compared to the first method (combined type A and B of 0.40-0.49% [15].).

7.6 Conclusion

In this study, the RefleXion BgRT machine was calibrated using two approaches following the TRS-483 [1] and Mirzakhanian et al. [2]. Data on the $k_{Q_A,Q_0}^{f_A,f_{ref}}$ factors was provided for six chamber types as a function of beam quality in the RefleXion BgRT machine for both field sizes 10×2 cm^2 and 10×3 cm^2. An agreement to within 0.3% was observed on the correction factors determined using the two approaches, except for the chamber with the steel electrode. If the MC $k_{Q_A,Q_0}^{f_A,f_{ref}}$ factors are not available for the user's ionization chamber, the user can use the second approach to estimate the beam quality conversion factors provided that the chamber electrode is not made of high Z material. Although the results of this study are promising, further measurements are required using the RefleXion BgRT machine to validate the correction factors calculated in this study.

Acknowledgments

This work has been partially supported by RefleXion Medical, the CREATE Medical Physics Research Training Network grant of the Natural Sciences and Engineering Research Council (Grant number: 432290) and NSERC RGPIN-2019-06746. The authors acknowledge Compute Canada/Calcul Quebec for the computing resources and the ion chamber manufacturers Standard Imaging, PTW and IBA for providing the chambers blueprints.

Disclosure of Conflicts of Interest

This study was partially supported by funds from RefleXion Medical.

Bibliography

[1] H Palmans, P Andreo, K Christaki, MS Huq, and J Seuntjens. TRS-483: Dosimetry of small static fields used in external beam radiotherapy: an international code of practice for

reference and relative dose determination. *International Atomic Energy Agency, Vienna*, 2017.

[2] L Mirzakhanian, R Bassalow, C Huntzinger, and J Seuntjens. Extending IAEA-AAPM TRS-483's methodology for radiotherapy machines with field sizes down to 10×2 cm^2. *Submitted to Medical Physics*

[3] P Andreo, DT Burns, K Hohlfeld, M Huq, T Kanai, F Laitano, V Smyth, and S Vynckier. TRS-398: Absorbed dose determination in external beam radiotherapy: An international code of practice for dosimetry based on standards of absorbed dose to water. *International Atomic Energy Agency*, 420, 2001.

[4] PR Almond, PJ Biggs, BM Coursey, WF Hanson, MS Huq, R Nath, and DWO Rogers. AAPM's TG-51 protocol for clinical reference dosimetry of high-energy photon and electron beams. *Medical physics*, 26(9):1847–1870, 1999.

[5] M McEwen, L DeWerd, G Ibbott, D Followill, DWO Rogers, S Seltzer, and J Seuntjens. Addendum to the AAPMs TG-51 protocol for clinical reference dosimetry of high-energy photon beams. *Medical physics*, 41(4), 2014.

[6] I Kawrakow, E Mainegra-Hing, F Tessier, and BRB Walters. The egsnrc c++ class library. *NRC Report PIRS-898 (rev A)*, 2009.

[7] I Kawrakow and D Rogers. The egsnrc code system: Monte carlo simulation of electron and photon transport. 2000.

[8] I Kawrakow. Accurate condensed history monte carlo simulation of electron transport. i. egsnrc, the new egs4 version. *Medical physics*, 27(3):485–498, 2000.

[9] DWO Rogers, BA Faddegon, GX Ding, C-M Ma, J We, and TR Mackie. Beam: a monte carlo code to simulate radiotherapy treatment units. *Medical physics*, 22(5):503–524, 1995.

[10] I Kawrakow, DWO Rogers, and BRB Walters. Large efficiency improvements in beamnrc using directional bremsstrahlung splitting. *Medical physics*, 31(10):2883–2898, 2004.

[11] BRB Walters, I Kawrakow, DWO Rogers, et al. `Dosxyznrc` users manual. *Nrc Report Pirs*, 794:31, 2005.

[12] GM Mora, A Maio, and DWO Rogers. Monte carlo simulation of a typical 60Co therapy source. *Medical physics*, 26(11):2494–2502, 1999.

[13] J Wulff, K Zink, and I Kawrakow. Efficiency improvements for ion chamber calculations in high energy photon beams. *Medical physics*, 35(4):1328–1336, 2008.

[14] M Dalaryd, T Knöös, and C Ceberg. Combining tissue-phantom ratios to provide a beam-quality specifier for flattening filter free photon beams. *Medical physics*, 41(11), 2014.

[15] BR Muir, MR McEwen, and DWO Rogers. Measured and monte carlo calculated kq factors: Accuracy and comparison. *Medical physics*, 38(8):4600–4609, 2011.

[16] L Mirzakhanian, H Benmakhlouf, F Tessier, and J Seuntjens. Determination of $k_{Q_{\mathrm{msr}},Q_0}^{f_{\mathrm{msr}},f_{\mathrm{ref}}}$ factors for ion chambers used in the calibration of leksell gamma knife perfexion model using `EGSnrc` and PENELOPE Monte Carlo codes. *Medical physics*, 45(4):1748–1757, 2018.

[17] MR McEwen. Measurement of ionization chamber absorbed dose kq factors in megavoltage photon beams. *Medical physics*, 37(5):2179–2193, 2010.

[18] MA Hyun, JR Miller, JA Micka, and LA DeWerd. Ion recombination and polarity corrections for small-volume ionization chambers in high-dose-rate, flattening-filter-free pulsed photon beams. *Medical physics*, 44(2):618–627, 2017.

[19] BR Muir and DWO Rogers. The central electrode correction factor for high-z electrodes in small ionization chambers. *Medical physics*, 38(2):1081–1088, 2011.

7.7 Supplementary material

The percent depth dose, crossplane and inplane comparison of the MC beam model to the measurement in the 10×2 cm^2 and 10×3 cm^2 field sizes are shown in figure 7.3.

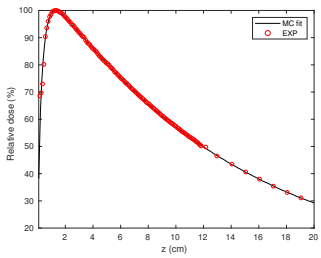

a) Z profile in 10×2 cm^2

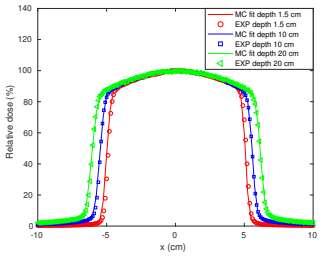

b) X profile in 10×2 cm^2

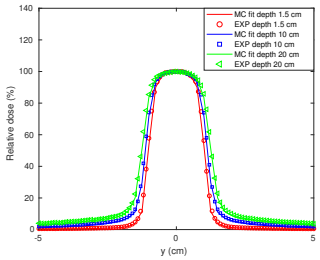

c) Y profile in 10×2 cm^2

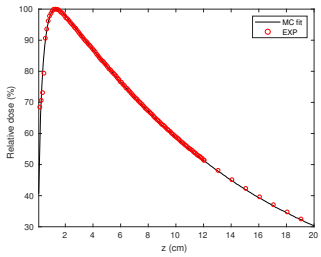

d) Z profile in 10×3 cm^2

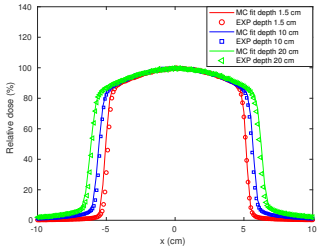

e) X profile in 10×3 cm^2

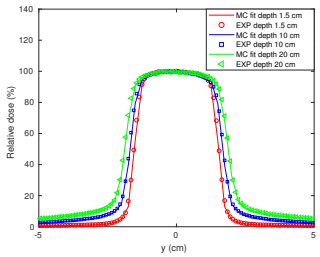

f) Y profile in 10×3 cm^2

Figure 7.3 Calculated and measured percent depth dose and crossplane and inplane profiles at three depths in the RefleXion BgRT machine under the condition of SSD 85 cm, 10×2 cm^2 and 10×3 cm^2 field sizes. The uncertainty on the MC is type A and less than 0.2%. The uncertainty on the measurements is 0.5%.

Chapter 8

Summary and future directions

This thesis focused on reference dosimetry of two nonstandard radiotherapy machines, the Leksell Gamma Knife® (LGK) (Elekta Instruments AB, Stockholm, Sweden) and the RefleXion™ biology-guided radiotherapy (BgRT) (Hayward, CA, USA). This chapter summarizes the previous work published by other groups on reference dosimetry of LGK and the main findings in this study for both radiotherapy machines LGK and RefleXion BgRT followed by some future directions.

8.1 Reference dosimetry of LGK

Currently, in most hospitals TG-21 [1] is used as the reference dosimetry protocol of the LGK. TG-21 is a well established protocol, however as reviewed in section 3.3.1, there are many parameters involved in TG-21 which make the analysis complex and increases the possibility of error in the clinic. Additionally, TG-21 is based on exposure (air-kerma) standards. As discussed in section 3.3.4, TRS-483 [2] is a recent protocol providing guidelines for reference and relative dosimetry of small static fields. For applications in LGK, there are few available data on $k_{Q_{msr},Q_0}^{f_{msr},f_{ref}}$ correction values (introduced in TRS-483) in the literature [3, 4]. Johansson et al. [3] calculated the $k_{Q_{msr},Q_0}^{f_{msr},f_{ref}}$ values for seven chamber types in three phantom materials using `PEGASOS` (a MC system based on `PENELOPE`) in LGK unit. The data has later been applied in a Round Robin study [5] and tabulated in TRS-483. However, these corrections were not calculated and verified for all possible phantom materials, chamber types and orientations.

In this thesis, as discussed in chapter 4, we calculated the $k_{Q_{msr},Q_0}^{f_{msr},f_{ref}}$ correction factors for nine chamber types and six phantom materials in LGK Perfexion unit using `EGSnrc` and

PENELOPE MC codes. We were able to provide the first independent comparison of EGSnrc and PENELOPE based $k_{Q_{msr},Q_0}^{f_{msr},f_{ref}}$ factors. We studied the influence of MC codes, chamber type, chamber orientation and phantom electron density on $k_{Q_{msr},Q_0}^{f_{msr},f_{ref}}$ values.

In our results, we observed a good agreement between our EGSnrc calculated $k_{Q_{msr},Q_0}^{f_{msr},f_{ref}}$ values and the values determined by Johansson et al. [3] using PEGASOS/PENELOPE in the liquid water phantom. We chose liquid water for comparison because there were no uncertainties associated with phantom composition, mass density, homogeneity, frames, air gaps and phantom inserts in the liquid water phantom.

We concluded that chambers with electrode made of high Z material when placed in parallel and perpendicular orientations with respect to the LGK symmetry axis (z-axis) have different $k_{Q_{msr},Q_0}^{f_{msr},f_{ref}}$ values (up to 1.8% for PTW 31010).

We were also able to estimate the type B uncertainty on $k_{Q_{msr},Q_0}^{f_{msr},f_{ref}}$ values by using the percentage root-mean-square (%RMS) deviation between EGSnrc and PENELOPE calculated $k_{Q_{msr},Q_0}^{f_{msr},f_{ref}}$ values.

Based on our results, we concluded that the $k_{Q_{msr},Q_0}^{f_{msr},f_{ref}}$ values increased linearly with electron density of the phantom material for all chamber types mainly due to the linear dependency of photon energy fluence ratios on electron density. Therefore, we were able to derive a relationship between the $k_{Q_{msr},Q_0}^{f_{msr},f_{ref}}$ factors and electron density of the phantom material. This confirmed our hypothesis that the correction factors ($k_{Q_{msr},Q_0}^{f_{msr},f_{ref}}$) for different ionization chamber in calibration of LGK can be predicted for any phantom material from a base value of the correction factor for water and only knowing the electron density of the phantom material.

It should be mentioned that in parallel to our study, another group also published the $k_{Q_{msr},Q_0}^{f_{msr},f_{ref}}$ values for different detector types in three phantom materials in LGK using EGSnrc [4]. Later in 2018, another group used GEANT4 MC code to calculate the $k_{Q_{msr},Q_0}^{f_{msr},f_{ref}}$ factors in LGK Perfexion and reported the $k_{Q_{msr},Q_0}^{f_{msr},f_{ref}}$ factors for three ionization chambers and five different phantom materials [6].

In chapter 5, we experimentally validated our calculated $k_{Q_{msr},Q_0}^{f_{msr},f_{ref}}$ values for three chamber types in three phantom materials with different orientations of the chambers with respect to the LGK unit. We analyzed the dose-rate using three protocols: the TG-51, TG-21 and TRS-483 using our calculated correction factors to study the effect of the use of different protocols. We also studied the influence of phantom material, chamber type and orientation of chamber with respect to the LGK.

When we applied our calculated $k_{Q_{msr},Q_0}^{f_{msr},f_{ref}}$ values to the measured dose rates in LGK Icon unit for three chambers and three phantom materials, it resulted in dose rates that were consistent to within 0.4%.

We found that the use of TRS-483 protocol with our calculated $k_{Q_{msr},Q_0}^{f_{msr},f_{ref}}$ values improved the consistency of the results compared to the TG-21 and TG-51 protocols especially when the chamber was positioned in different orientations (parallel and perpendicular to the symmetry axis of the LGK unit). We expected this, since the $k_{Q_{msr},Q_0}^{f_{msr},f_{ref}}$ factor corrects for the difference between the conditions of field size, geometry, chamber orientation, phantom material of the conventional reference field and the LGK *msr* field.

8.2 Reference dosimetry of RefleXion BgRT

As reviewed in section 1.6.2, the RefleXion BgRT is a new type of radiation therapy machine which combines stereotactic radiotherapy with PET and CT imaging systems. The field size closest to the conventional field in this machine is 10×2 cm^2 or 10×3 cm^2. The reference dosimetry of this machine is challenging since TRS-483 cannot be directly used for its calibration. First, the the 10×2 cm^2 field size does not meet the *msr* condition. Secondly, the methodology provided in TRS-483 to derive the beam quality specifier is limited to a field size larger than 4 cm on a side. The equivalent field size tabulated in TRS-483 is also limited to 3 cm field size. Additionally, the tabulated beam quality correction factor ($k_Q^{f_{ref}}$) in TRS-483 are provided only for large reference chambers.

First we extended the methodology provided in TRS-483 for the calibration of general radiotherapy machines with 6 MV flattening filter free (FFF) beam and with field sizes down to 2 cm on a side (chapter 6). We provided two calibration approaches following TRS-483. In the first method, we calculated the $k_{Q_A,Q_0}^{f_A,f_{ref}}$ factors for several detectors in a 6 FFF generic Varian TrueBeam machine in field sizes ranging from 10×1.5 cm^2 to 10×10 cm^2. We validated these results experimentally on the Varian TrueBeam machine. In the second method, we extended the beam quality specifier and equivalent field size data to smaller fields (2 cm). We calculated the beam quality correction factor $k_Q^{f_{ref}}$ analytically and compared the results of two methodologies.

Based on our results, we concluded that for chamber with electrode made of low Z material the $k_{Q_A,Q_0}^{f_A,f_{ref}}$ factors did not vary significantly across the different field sizes studied while for chambers with electrode made of high Z material they varied up to 1.6% (for IBA CC01). When

we applied the calculated corrections to the measurements, it improved the consistency on the dose determination (from 0.576% to 0.06%). This confirmed our hypothesis that even if the *msr* condition is not preserved, depending on the detector used, appropriate correction factors determined for reference detectors can still be applied for the purpose of reference dosimetry.

We showed that the methodology in TRS-483 for determination of beam quality specifier and equivalent field size can be extended to 2 cm field size without introducing a significant error.

We found out that for chambers with electrodes made of low Z material, the correction factors determined using the two methods of calibration were the same (within 0.5%). While for chambers with electrode made of high Z materials, the difference was larger (1.6%).

In Chapter 7, we used the two methodologies provided in chapter 6 and applied them to the RefleXion BgRT machine. We produced the $k_{Q_A,Q_0}^{f_A,f_{ref}}$ data for several chamber types as a function of the beam quality specifier at the RefleXion BgRT machine.

We concluded that the beam quality conversion factors calculated using the two approaches at RefleXion BgRT were in good agreement for chambers with electrode made of low Z material. This was similar to our observation in chapter 6.

In summary, we recommended using the first approach for reference dosimetry of RefleXion BgRT. However, if the correction factors are not available one can use the second method which provides highly accurate results provided that the chamber electrode is not made of a high Z material.

This thesis contributed to improving the reference dosimetry of LGK and provided the data and methodology for reference dosimetry of the new RefleXion BgRT machine.

8.3 Future work

8.3.1 LGK

In this study we assumed that the phantoms were ideally uniform and the phantom compositions and densities were well known. However, the phantoms used in the clinic sometimes do not have a well defined mass density or composition. There are also air gaps and heterogeneities in the phantom. One can model the air gaps, the phantom inserts and the mounting frames in MC in details and study their impact on $k_{Q_A,Q_0}^{f_A,f_{ref}}$ factors.

It would be also interesting to compare the dose measured with ion chambers corrected for the $k_{Q_{msr},Q_0}^{f_{msr},f_{ref}}$ values to the dose measured with other techniques such as alanine or the Aerrow-Mini, a small probe-format graphite calorimeter currently being developed at McGill [7, 8], for the 16 mm diameter *msr* field size in LGK.

8.3.2 RefleXion BgRT

Although the simulation studies described in chapter 7 were promising, further measurements are required at the RefleXion BgRT machine to validate the correction factors calculated in this study.

As described in Chapter 3, reference dosimetry measurements (TG-21, TG-51 and TRS-483) are performed in a static reference field (10×10 cm^2) or in the *msr* field if the reference field is not achievable on the machine. While this formalism is well established, the practical implementation for small *msr* fields creates additional sources of uncertainties due to the ionization chamber positioning and high dose gradients. The absorbed dose can be also measured in a plan-class specific reference field (*pcsr*). *pcsr* is a reference field that is close to the final clinical delivery scheme but delivers a homogeneous absorbed dose to a geometrically simple target volume using dynamic or step-and shoot delivery fields, or combinations of fields [9]. Some of the advantages of using *pcsr* over *msr* is that the condition of LCPE is met when using the *pcsr* field size, the *pcsr* is closer to the clinical delivery field and the positioning errors would be reduced when using the *pcsr* field size. One can determine and validate the *pcsr* correction factors for the common chamber types in RefleXion BgRT machine and study the feasibility of using *pcsr* field for BgRT or machines similar to BgRT that have small and challenging *msr* field sizes. However, the use of *pcsr* might be challenging since the treatment planning system has to have the ability to use the new *pcsr* field as a reference field.

Bibliography

[1] AAPM Task Group 21, Radiation Therapy Committee. A protocol for the determination of absorbed dose from high-energy photon and electron beams. *Medical Physics*, 10(6): 741–771, 1983.

[2] Palmans H, Andreo P, Christaki K, Huq MS, Seuntjens J. TRS-483: Dosimetry of small static fields used in external beam radiotherapy: an international code of practice for

reference and relative dose determination. *International Atomic Energy Agency, Vienna*, 2017.

[3] Johansson J, Gorka B, Novotny J, Bourland JD, Bhatnagar J, Bednarz G, Best RCM, Persson L, Nordström H, Svarm O. *Plenary Oral Presentation at the 16th International Meeting of the Leksell Gamma Knife® Society;* 2012. p. 69.

[4] Zoros E, Moutsatsos A, Pappas EP, Georgiou E, Kollias G, Karaiskos P, Pantelis E. Monte Carlo and experimental determination of correction factors for gamma knife perfexion small field dosimetry measurements. *Physics in Medicine Biology*, 62(18):7532, 2017.

[5] Drzymala RE, Alvarez PE, Bednarz G, Bourland JD, DeWerd LA, Ma L, Meltsner SG, Neyman G, Novotny Jr J, Petti PL, Rivard MJ. A round-robin gamma stereotactic radiosurgery dosimetry interinstitution comparison of calibration protocols. *Medical physics*, 42(11), 6745-6756, 2015.

[6] Schaarschmidt T, Kim TH, Kim YK, Yang HJ, Chung HT. GEANT4-based Monte Carlo Simulation of Beam Quality Correction Factors for the Leksell Gamma Knife® Perfexion™. *Journal of the Korean Physical Society*, 73(12):1814-20, 2018.

[7] Renaud J. On the development of absorbed dose calorimeter systems for absolute clinical dosimetry. *Doctoral dissertation, McGill University Libraries*, 2017.

[8] Cote B, Seuntjens J, Sarfehnia A, Renaud J. Aerrow-Mini: A Probe-Format Graphite calorimeter for absolute dosimetry of small high-energy photon fields. *International Symposium on Standards, Applications and Quality Assurance in Medical Radiation Dosimetry (IDOS-2019).*

[9] Alfonso R, Andreo P, Capote R, Huq MS, Kilby W, Kjäll P, Mackie TR, Palmans H, Rosser K, Seuntjens J, Ullrich W. A new formalism for reference dosimetry of small and nonstandard fields. *Medical physics*, 35(11), 5179–5186, 2008.